

RICE UNIVERSITY

**Observation of antiferromagnetic correlations in the Fermi-Hubbard
model**

by

Pedro M Duarte

A THESIS SUBMITTED
IN PARTIAL FULFILLMENT OF THE
REQUIREMENTS FOR THE DEGREE

Doctor of Philosophy

APPROVED, THESIS COMMITTEE:

Randall G. Hulet, *Chair*
Fayez Sarofim Professor of Physics and
Astronomy

Thomas. C. Killian
Professor of Physics and Astronomy

Peter Wolynes
Bullard-Welch Foundation Professor of Science
Professor of Chemistry and
Materials Science & NanoEngineering
Professor of Physics and Astronomy

HOUSTON, TEXAS
OCTOBER 2014

ABSTRACT

Observation of antiferromagnetic correlations in the Fermi-Hubbard model

by

Pedro M Duarte

The Hubbard model contains only the essential ingredients to describe the behavior of strongly interacting electrons moving in a periodic lattice. It describes particles that can tunnel between sites in the lattice and that acquire an on-site interaction energy when two of them occupy the same lattice site. This simple model is a prominent example of how strongly correlated phases emerge from simple Hamiltonians. It gives rise to a Mott-metal insulator transition, and at a density of one particle per site shows an antiferromagnetic ground state. It is also considered to contain the essence of high-temperature superconductivity as observed in the cuprates, a question that remains open due to the difficulty in numerically accessing the solutions of the model at densities different than one particle per site.

In this work we have realized the Hubbard model with a spin mixture of ultracold atoms in a simple cubic optical lattice. Atoms in lattices have emerged in the last decade as promising systems in which to perform quantum simulations of condensed matter Hamiltonians. In the laboratory we can create defect-free optical lattice potentials with laser light, and we can control the interactions between the atoms using a magnetic Feshbach resonance.

For this work we implemented a novel compensated optical lattice setup, which allows us to control the density of the sample and mitigate the non-adiabaticity in the lattice loading process which often leads to heating of the sample or to out of equilibrium distributions. Using the compensated optical lattice we are able to get closer to the ground state of the Hubbard model than anybody before us has been able to do so with ultracold atoms.

To demonstrate this achievement we use spin-sensitive Bragg scattering of light to mea-

sure the spin-structure factor, a measure of the antiferromagnetic correlations in the collection of spins. Measurements of the spin-structure factor are compared to theoretical calculations to establish precise thermometry of the atoms in the lattice. We have also studied the *in-situ* density distribution of the system, which confirms that the temperature of our sample is in a regime where most of the remaining entropy in the system resides in the spin degree of freedom.

The results presented here represent an important step in the field of quantum simulation with ultracold atoms. In the future, we expect to further explore and exploit the experimental possibilities opened up by the compensated lattice potential and by light scattering thermometry, with the ultimate goal of addressing the existence of *d*-wave superfluidity in the Hubbard model.

Table of Contents

1 Many body physics with ultracold atoms	1
1.1 Motivation: Strongly correlated materials	1
1.2 Quantum simulations with ultracold atoms	4
1.3 Quantum magnetism with ultracold atoms	6
1.4 This thesis	9
1.4.1 Outline	10
2 Ultracold atoms in optical lattices	11
2.1 One-dimensional optical lattice potential	11
2.1.1 Band structure	13
2.1.2 Eigenstates	14
2.1.3 Wannier states	15
2.2 Three-dimensional optical lattice potential	16
2.3 Hubbard Hamiltonian	18
2.3.1 Second quantization	19
2.3.2 Operators in second quantization	21
2.3.3 Second quantized Hubbard Hamiltonian	24
2.4 Parameter regimes for a valid description using a single band Hubbard model	31
3 The Hubbard model	33
3.1 A bit of history	33
3.2 Hubbard model for a single lattice site, $t = 0$	35

Chapter	Page
3.3 Particle-hole symmetry	38
3.4 Exact diagonalization	38
3.5 High-temperature series expansion	46
3.6 Local density approximation	50
3.7 Latest developments in numerical techniques	51
4 Overview of the experimental setup	55
4.1 Vacuum system	57
4.2 671 nm laser cooling system	58
4.2.1 Laser system	58
4.2.2 Zeeman slower	60
4.2.3 2DMOT and MOT	61
4.3 323 nm laser cooling system	63
4.3.1 Laser system	63
4.3.2 UVMOT	64
4.3.3 Transfer from MOT to UVMOT	66
4.4 Optical dipole trap	67
4.5 Magnetic field	70
4.6 Loading the ODT	71
4.7 Compensated optical lattice	76
4.7.1 Optical lattice and dimple	76
4.7.2 Compensation	77
4.8 Diagnostics	78
4.9 Control, automation, and data analysis	80
5 Compensated optical lattice potential	83

Chapter	Page
5.1 Form of the potential	86
5.2 General aspects	87
5.3 Local density approximation	94
5.3.1 Format for presentation of LDA results	94
5.3.2 Entropy redistribution	100
5.4 Results	101
5.4.1 Atom number	104
5.4.2 Timescales for locking the lattice	105
5.5 Comparison between different kinds of traps	106
6 Diagnostic tools I: Polarization phase-contrast imaging	111
6.1 Polarization phase-contrast imaging	112
6.1.1 Transmission of light through a polarized gas	114
6.1.2 Polarization of the cloud	116
6.1.3 Susceptibility for ${}^6\text{Li}$ atoms at high magnetic field	119
6.1.4 Change in field parameters due to atomic column density	123
6.1.5 Experimental setup for PPCI	124
6.1.6 Results	126
7 Diagnostic tools II: Fermi gas thermometry	129
7.0.7 Density distributions of a trapped Fermi gas	130
7.0.8 Time-of-flight	132
7.0.9 Column density and imaging geometry	133
7.0.10 Fitting functions	135
8 Diagnostic tools III: Double occupancy	137
8.1 ${}^6\text{Li}$ Feshbach resonances	138
8.2 Measurement procedure	140

Chapter	Page
8.3 Measurements in a compensated lattice	142
8.4 <i>In-situ</i> measurement of double occupancies	143
8.5 Measurement systematics	143
9 Diagnostic tools IV: Bragg scattering of light	147
9.1 Coherent light scattering by an array of atoms.	149
9.1.1 Incoherent scattering	152
9.1.2 Coherent scattering	153
9.1.3 Crystal structure	153
9.1.4 Magnetic structure	154
9.1.5 Time-of-flight	155
9.2 Experimental setup	157
9.2.1 Diffuse background	159
9.3 Measurement of the crystal structure factor	160
9.3.1 Angular dependence of the scattering	161
10 Experimental procedures	165
10.1 Production of a deeply degenerate ${}^6\text{Li}$ spin mixture in a dimple potential	166
10.1.1 Optimized trajectory for evaporation in the ODT	166
10.1.2 Modifications to the trajectory for evaporating into the dimple	170
10.2 Lattice alignment procedure	172
10.3 Lattice loading ramps	175
11 Mott insulating state in a simple cubic lattice	179
11.1 Summary	185
12 Antiferromagnetic correlations in the Hubbard model	187

Chapter	Page
12.1 Technical details	187
12.1.1 Momentum transferred from the probe to the atoms.	189
12.1.2 Optical density.	190
12.1.3 Light collection.	191
12.1.4 Data averaging.	191
12.2 Time-of-flight	192
12.3 Number variation	192
12.4 Calculations using the LDA	195
12.4.1 Extraction of the temperature	196
12.5 Summary	199
13 Conclusion	201
A Compensated optical lattice potential	205
A.1 Dipole potential and scattering rate	205
A.2 Compensated lattice potential: definitions and simplified expressions	206
A.2.1 Electric field	207
A.2.2 Lattice depth	208
A.2.3 Lattice and dimple radial frequencies	209
A.2.4 Compensation beams	210
A.3 Fermi temperature for a compensated dimple	211
A.4 Heating	212
A.5 Heating due to optical lattice beams	214
A.6 Heating due to green compensation beams	216
A.7 Total heating rate in the compensated lattice	216
A.8 Total heating rate in the compensated lattice	217

Chapter

Page

BIBLIOGRAPHY

219

1. Many body physics with ultracold atoms

1.1 Motivation: Strongly correlated materials

Most of our experiences in the physical world can, in principle, be explained by considering the description of the collections of positively charged nuclei and negatively charged electrons that make up ordinary matter. From high to low energy this includes: neutral plasmas, free atoms, free molecules, and atoms and molecules that have condensed into liquid or glassy phases or crystallized to form solids. At lower energies more exotic phenomena take place, starting with magnetism and going further to superfluidity, superconductivity and the novel examples of modern condensed matter physics such as the fractional quantum Hall effect, heavy electrons, high-temperature superconductors and topological insulators.

In principle, the correct description of all the above phenomena is contained in the Schrödinger equation for the interacting system of electrons and nuclei, where the interaction is given by the Coulomb potential. In practice, we know that even though stating the equation is easy, there is not sufficient computing power available in the world to solve it for systems of more than just a few particles. Xiao-Gang Wen, in the introduction to his textbook on many-body physics [1], points out that back in the 80's a computer with 32 MB of RAM could solve a system of 11 interacting electrons. In this century, while computing power has increased more than 100 times, this allows for the addition of only two more electrons to the system.

Despite the above, the use of the Schrödinger equation and perturbation theory for the description of systems of electrons and nuclei has been very successful over the past century. The most prominent example of this success is our understanding of semiconductors, which are at the root of the electronic devices that permeate all aspects of our lives. The remarkable success of condensed matter physics can be traced back to the principle of adiabatic

continuity [2]. This principle states that the low-energy excitations of an interacting system are **non-interacting quasiparticles** which can be closely related to the actual particles that form the interacting system. This last sentence may sound confusing, but think about a hole in the valence band of a semiconductor. The hole corresponds to a collective arrangement of all the electrons in the system, but we typically do not think about it that way. The hole is a low energy excitation of the collection of electrons, and thus we think about it as a **quasiparticle**, with properties that are remarkably similar to those of a free electron albeit with a positive rather than a negative charge. The fact that an electron and a hole behave so similarly is not at all intuitive, especially if one stops to think about any effects due to the Coulomb interaction between electrons. However, adiabatic continuity guarantees that for practical purposes we can think of the hole simply as a positively charged electron.

The practical consequence of adiabatic continuity is that interactions seemingly do not play an important role in the low-energy description of the system. For this reason, the free electron model of Drude and Sommerfeld [3] is relatively successful in explaining electrical and thermal conductivity in metals, and also in explaining the Hall effect. In 1957, Landau formulated the theory of the Fermi-Liquid [4] and gave a solid basis to the notion of adiabatically connected quasiparticles. To this day, the Fermi-Liquid theory is the default starting point for the study of Fermi systems such as conventional metals, helium-3, and ultracold atomic Fermi gases.

But, just as Fermi-Liquid theory is celebrated for its success, it is also known for the phenomena that it fails to explain. Starting in the mid 70's and going through the 80's, the discoveries of heavy electron superconductivity [5, 6], the fractional quantum Hall effect [7, 8], and high-temperature superconductors [9] sparked a revolution in condensed matter physics [10]. These materials, in which the electron behavior cannot be described effectively in terms of non-interacting electron-like quasiparticles came to be known as **strongly correlated materials**. Strongly correlated materials, and the concept of emergence, brought to the forefront by P.W. Anderson in his famous essay "More is Different" [11], are at the center of modern condensed matter physics.

The behavior of strongly correlated materials is emergent because the low-energy excitations of the system bear no resemblance to its constituent particles. This disconnect should not be so surprising, after all we are familiar with this definition of emergence whenever a system undergoes a phase transition. For example, when a liquid cools down to form a crystalline solid, continuous translational symmetry is broken. By going across the liquid-to-solid phase transition, adiabatic continuity is violated; nevertheless, it is easy to mathematically identify the low energy excitations of the new phase and ascribe them the character of quasiparticles. In the case of the crystalline solid this involves finding the normal modes of a set of coupled oscillators; the normal modes are the quasiparticles known as phonons. Phonons are emergent because they bear no direct resemblance to the constituent ions that form the crystal lattice.

Strongly correlated materials are examples of emergent phenomena in which the origin and properties of the low-energy excitations are not as straightforward as those of phonons in a crystalline solid. The fractional quantum Hall state, in which the quasiparticles carry a rational fraction of the electron charge serves to illustrate this point. The strong interactions between the electrons in the quantum Hall system (electrons confined in a plane in the presence of a very high magnetic field) make the problem intractable from the perturbative point of view and thus **the connection between the microscopic degrees of freedom and the collective low-energy excitations is very difficult to establish**; certainly not as easy as the connection between small displacements of ions about their equilibrium points in a crystal lattice and the collective phonon modes. It was Laughlin's insight that led him to postulate the correct wavefunction for the quantum Hall state [8], but the microscopic origin of the state is still under debate.

The challenge posed by strongly correlated materials has led to great discoveries in condensed matter physics, such as the concepts of topological order [12] and quantum criticality [13, 14], but also many questions remain unanswered. Furthermore, the problem of strongly correlated materials is only scratching the surface of what is possible and what remains to be discovered. New materials are being synthesized constantly. Among the

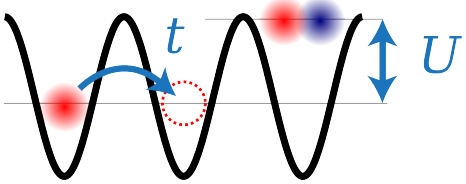


Figure 1.1: Illustration of the Hubbard model

myriad of possible materials and compounds yet to be explored by materials scientists, one can only expect that there will be new states of matter to be found; states with technological implications that will revolutionize life on earth.

1.2 Quantum simulations with ultracold atoms

We have seen that, even though the Schrödinger equation in principle contains a full description of a solid, its solution is practically impossible to compute using a classical computer due to the large amount of memory required to represent a many-body quantum state. The approach in condensed matter theory, rather than directly aim to solve the complete Schrödinger equation, is to introduce simplified effective models, which should capture the essential features of the system under study. Solving the effective model leads to an understanding of the low-energy excitations of the system and gives clues to their microscopic origin.

The Hubbard model, formulated half a century ago [15] contains only the essential ingredients necessary to describe the behavior of strongly interacting electrons moving in a periodic lattice. It describes electrons that can hop between sites in a lattice (with probability amplitude t), and which acquire an interaction energy (U) when two electrons are on the same site, see Figure 1.1. The Hubbard model is an extension of the tight-binding model, with the interactions between electrons incorporated as the on-site energy U . After its inception, it was shortly realized [16] that the model could explain the Mott metal-insulator transition, which was observed in the transition metal oxides even though conventional band theory predicted them to be conductors. Beyond its early success, the Hubbard model is

now the quintessential model for strongly correlated systems. It is widely accepted as the most viable candidate to explain high- T_c superconductors from first principles. Despite this fact, its exact solution in more than one dimension has evaded theorists for more than four decades [17].

It is at this point that ultracold atoms enter the picture. It turns out that ultracold atoms in an optical lattice provide a faithful realization of the Hubbard model [18], thus the properties exhibited by the collection of atoms are in fact the solutions of the model. In this way, such systems can be used to map the phase diagram of the Hubbard model in what is known as **quantum simulation**, an idea that was first proposed by Richard Feynman in 1982 [19].

In a seminal paper [18], Jaksch and collaborators showed that Bose-Einstein condensates of atoms loaded into optical lattices could be used as simulators of the Bose-Hubbard model. A few years later, the superfluid (SF) to Mott insulator (MI) phase transition, the hallmark of the Bose-Hubbard model, was realized experimentally [20], and several detailed studies of this system have followed since then [21–25]. For bosonic systems, the properties of the ground state are well understood theoretically [26–28]; however, experiments of atoms in lattices are starting to shed light into the dynamics of these systems [29], which are more difficult to address for theorists.

Despite the remarkable advances with bosonic systems, the ultimate goal of quantum simulation with ultracold atoms is to find the ground states of theoretically intractable fermionic models, to see if these models can reproduce the measured properties of strongly correlated electron systems. In this prescription for quantum simulation, the subject of most interest is whether or not the Hubbard model can exhibit a *d*-wave superfluid state which would validate it as the prime model for high- T_c superconductors [30, 31]. In pursuit of this goal, experiments have realized the Hubbard model with spin mixtures of fermionic atoms, where two hyperfine levels of the atomic ground state play the role of spin-up and spin-down states of the spin- $\frac{1}{2}$ electrons in real compounds. Experiments with this kind of

realization of the Hubbard model are the subject of this thesis.

A quantum degenerate spin-mixture of fermionic atoms is prepared in a harmonic potential and then transferred adiabatically into an optical lattice potential. The lattice depth and the contact interactions between the atoms, which together set the values for the Hubbard parameters t and U , can be controlled almost at will by the experimenter. The tunneling rate t is controlled by adjusting the intensity of the lattice lasers. The interaction strength U is controlled by setting the external magnetic field and making use of a magnetically tunable Feshbach resonance, which offers the possibility of realizing non-interacting samples, or samples with, arbitrarily, large attractive or repulsive interactions¹. The unprecedented control over the system parameters has allowed the realization of band insulating states [33] and Mott insulating states [34, 35] with spin-mixtures of ultracold fermionic atoms. However, the possibility of exploring the strongly correlated phases of the Hubbard model has not yet been realized because the required temperatures are out of reach for current experiments.

1.3 Quantum magnetism with ultracold atoms

Even though temperatures as low as $T \simeq 0.04 T_F$ can be reached with ultracold Fermi gases in a harmonic trap, these temperatures are not low enough to allow exploration of the strongly correlated phases of the Hubbard model. To get an idea of the temperature scales involved, we will examine a qualitative temperature-doping phase diagram, shown in Fig. 1.2, which is based on experimental results obtained for the cuprate high- T_c superconductors², see Fig. 1.2.

The qualitative phase diagram shows that the cuprates exhibit various interesting phases besides the superconducting (SC) dome at intermediate doping. Most importantly, the un-

¹In practice it is observed that, for some values of the interaction strength, significant three-body losses and the associated heating rates prevent studying the equilibrium physics of the quantum gas [32].

²See [36] for a review of cuprate superconductors, [37] for a study of the onset of superconductivity at optimal hole-doping, [38] for the phase diagram of hole-doped cuprate superconductors and [39] for a more accessible report on the subject.

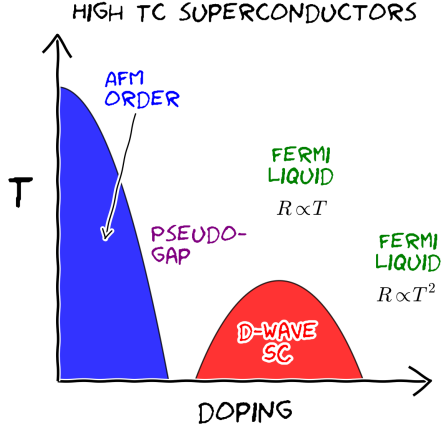


Figure 1.2: Cartoon phase diagram for cuprate high- T_c superconductors. The antiferromagnetic insulator (AFM) and the Fermi liquid with quadratic resistivity are well understood by theory, however the strange Fermi liquid with linear resistivity and the interplay between the pseudogap regime and the superconducting dome are issues still under debate [39].

doped parent compound is an antiferromagnetic (AFM) Mott insulator with a Néel ordering temperature that is higher than any value of the critical temperature T_c along the SC dome.

The onset of AFM ordering in the cuprate parent compounds is driven by the magnetic exchange interaction [40], where a spin can lower its energy if it can tunnel virtually to a neighboring site. For a single band model, the Pauli exclusion principle dictates that this is only possible if neighboring sites have opposing spins, as in the Néel AFM state. The Néel temperature T_N is then of the order of the exchange energy $4t^2/U$, which is the second-order correction (due to virtual tunneling) to the ground state energy of a two-site model in which the interaction U is treated as a perturbation. The undoped parent compounds, at temperatures several times larger than T_N , will be Mott insulators with exactly one electron per lattice site but without any spin ordering. As T_N is approached, AFM correlations between the spins start to develop.

To put some estimates on the values of T_N and T_c , let's consider the most common high- T_c superconductor [41], $\text{YBa}_2\text{Cu}_3\text{O}_{6+x}$, usually referred to as YBCO. The critical temperature for YBCO can be as large as $T_c \simeq 93$ K, obtained for optimal hole-doping [42]. In the absence of doping, the YBCO parent compound is antiferromagnetic with a Néel

temperature $T_N \simeq 500K$ [43]. The Fermi energy for YBCO is on the order of ~ 1 eV [44], which corresponds to ~ 10000 K. In units of the Fermi temperature T_F , we have $T_C \simeq 0.01 T_F$, and $T_N \simeq 0.05 T_F$.

We immediately see that, in units of T_F , the relevant temperature for d -wave superconductivity is much lower than state-of-the-art temperatures for ultracold fermionic atoms. On the other hand T_N may be just within reach. The Mott insulator state (without spin ordering) was first realized with fermionic atoms in a simple cubic lattice in 2008 [34, 35]. Immediately after that, the race started to see which group could be the first to observe the AFM state and take the next step in the roadmap of quantum simulation.

Recently in 2013, the Esslinger group, at ETH Zürich, has demonstrated the use of a dimerized optical lattice to measure the nearest-neighbor spin correlations that start to develop, as a consequence of the exchange interaction, at temperatures a few times larger than the Néel temperature for AFM ordering [45]. They observe significant spin-spin correlations in arrays of one-dimensional chains, and they can detect the spin-spin correlations that form on the approach to AFM order in a simple cubic lattice. Prior to the work of the Esslinger group, the Bloch group used a similar optical super-lattice to study exchange interactions with bosons in isolated double-wells [46] and isolated four-site plaquettes [47].

Other experiments have realized AFM states in engineered Ising Hamiltonians, using trapped ions [48, 49], or by mapping motional degrees of freedom to effective Ising models [50, 51]. In Ising type models, the magnetic coupling (anti or ferromagnetic) is put in by hand in the Hamiltonian, and thus they realize what is referred to as “classical” magnetism. In the Hubbard model, on the other hand, magnetism arises from the exchange interaction, like it does in condensed matter systems such as the transition metal oxides or the cuprate parent compounds. Realizations of classical magnetism are excellent systems to study magnetic frustration, or the dynamics of quenching the system across a phase-transition [52]. Systems of trapped ions can help understand models with long range interactions [53], and

also emerge as good candidates to realize universal quantum computers [49]. However, despite their advantages in other areas, these systems do not directly address the long-standing open question of superconductivity in the Hubbard model.

Approximately eight years ago, the Hulet lab started an experiment to study strongly correlated matter using ultracold atoms in optical lattices; our main goal being the achievement of temperatures below the Néel transition temperature. The Néel state in the Hubbard model, besides being the natural stepping stone in the quest to simulating strongly correlated systems, offers the added benefit that it is well understood by theory [54, 55]. The ability to compare experimental results with theory offers a test bed for quantum simulation and also a way to establish absolute thermometry for ultracold atoms in optical lattices, which is another major challenge in this field [56].

1.4 This thesis

Over the course of this work we have used a compensated lattice potential, which allows excellent control over the density distribution of the atoms in the lattice. The compensated lattice also helps mitigate heating of the atoms as they are loaded into the lattice and has allowed us to reach temperatures as low as $1.4 T_N$, which is a factor of 2 colder than previous experiments [57]. We measure the temperature of the atoms in the lattice using Bragg scattering of light off of the magnetic sublattices that start forming on the approach to the Néel transition. This technique has been discussed before [58], but only until now implemented. A very important aspect of our work is the comparison to *ab initio* numerical simulations of the Hubbard model. We have used results from determinantal quantum Monte Carlo (DQMC) [54] and from numerical linked-cluster expansion (NLCE) [59] calculations, along with the local density approximation to establish the link between light scattering and absolute thermometry of the sample.

1.4.1 Outline

The approach taken in this thesis is to first provide a detailed description of the condensed matter physics background which motivates our experiments, before describing the experimental procedures and results.

- Chapter 2 explains how ultracold atoms in an optical lattice can be an almost ideal realization of the Hubbard model.
- Chapter 3 explores the physics of the Hubbard model and gives the reader a flavor of the physics that will be explored later on when discussing the results of our experiments.
- Chapter 4 introduces the experimental setup, to provide the context for the more detailed explanations that will follow.
- Chapter 5 discusses the optical lattice potential in which our experiments are carried out. We designed this potential with a few ideas in mind regarding how it may help us reach lower temperatures with atoms in a lattice. Suggestions for future improvements of the setup will be given there.
- Chapters 6-9 describe the diagnostic tools that we have improved and developed, over the course of this work, to access the physical observables in our system.
- Chapter 10 gives details of a few crucial experimental steps required to produce an ultracold gas of atoms in an optical lattice.
- Chapters 11 and 12 discuss the main results of this thesis: the observation of an incompressible Mott insulator of ultracold atoms in an optical lattice, and the observation of antiferromagnetic correlations using Bragg scattering of light.
- Chapter 13 concludes this thesis and discusses possible directions for future experiments.

2. Ultracold atoms in optical lattices

In this chapter we consider the description of cold atoms in an optical lattice potential. Second quantization is introduced, and the many-body Hubbard Hamiltonian is derived, thus making the case for ultracold atoms as a nearly ideal realization of the Hubbard model. We discuss the requirements necessary for the ultracold atom system to be well described by a single band Hubbard model.

The computer code used to generate all of the plots in this chapter and to calculate the Hubbard parameters t and U can be downloaded from [60].

2.1 One-dimensional optical lattice potential

The contents of this section follow the derivation found in § IV.A of the review article by Morsch and Oberthaler. [61]. The Hamiltonian for an atom moving in a one-dimensional (1D) sinusoidal potential, such as that produced by an optical lattice, is

$$H_{\text{single},1\text{D}} = -\frac{\hbar^2}{2m} \frac{\partial^2}{\partial x^2} + V_0 \sin^2(kx) \quad (2.1)$$

where $k = 2\pi/\lambda$, λ is the wavelength of the lattice laser, and m is the mass of an atom. The lattice depth V_0 is naturally expressed in units of the recoil energy: $E_r = \frac{\hbar^2 k^2}{2m}$. Defining $v_0 = V_0/E_r$ the Hamiltonian reduces to

$$\begin{aligned} H_{\text{single},1\text{D}} &= -\frac{1}{k^2} \frac{\partial^2}{\partial x^2} + v_0 \sin^2(kx) \\ &= -\frac{1}{k^2} \frac{\partial^2}{\partial x^2} + \frac{v_0}{4} (2 - e^{2ikx} - e^{-2ikx}) \end{aligned} \quad (2.2)$$

The solutions to the time independent Schrödinger equation for this Hamiltonian are Bloch states, which are labeled by their quasimomentum q and their band index n , and can be

written in general form as

$$\psi_q^n(x) = e^{iqx} \sum_{l \in \mathbb{Z}} c_{ql}^n e^{ilGx} \quad (2.3)$$

The lattice translation invariant function that accompanies e^{iqx} in a Bloch state has been written here, with no loss of generality, as a sum of plane waves with momenta lG , where l is an integer, $G = 2k = 2\pi/a$ is the magnitude of the primitive vector of the reciprocal lattice, and $a = \lambda/2$ is the lattice spacing.

Acting with the Hamiltonian on the Bloch states and then rearranging some of the terms in the infinite sum, we get

$$\begin{aligned} H_{\text{single,1D}} \psi_q(x) &= \sum_l \left[(q/k + 2l)^2 + \frac{v_0}{4} (2 - e^{2ikx} - e^{-2ikx}) \right] c_{ql}^n e^{iqx + il2kx} \\ &= \sum_l \left[\left((q/k + 2l)^2 + \frac{v_0}{2} \right) c_{ql}^n - \frac{v_0}{4} c_{q,l-1}^n - \frac{v_0}{4} c_{q,l+1}^n \right] e^{iqx + il2kx} \end{aligned} \quad (2.4)$$

The quasimomentum is restricted to the first Brillouin zone, which can be taken to be $[-\frac{\pi}{a}, \frac{\pi}{a}]$. The natural unit for the quasimomentum is $2\pi/a$ ($= 2k$). Defining $q' = q/(2k)$, we can then write the time-independent Schrödinger equation as

$$\left((2q' + 2l)^2 + \frac{V_0}{2} \right) c_{ql}^n - \frac{V_0}{4} c_{q,l-1}^n - \frac{V_0}{4} c_{q,l+1}^n = E_q c_{ql}^n \quad (2.5)$$

We then have an infinite linear system of equations which determines the c_{ql}^n . For our practical purposes we truncate the set of equations such that $|l| \leq \mathcal{N}$. The resulting equations can be written in matrix form, for example if we select $\mathcal{N} = 2$

$$\begin{bmatrix} \frac{1}{2}V_0 + 4(q-2)^2 & -\frac{1}{4}V_0 & 0 & 0 & 0 \\ -\frac{1}{4}V_0 & \frac{1}{2}V_0 + 4(q-1)^2 & -\frac{1}{4}V_0 & 0 & 0 \\ 0 & -\frac{1}{4}V_0 & \frac{1}{2}V_0 + 4q^2 & -\frac{1}{4}V_0 & 0 \\ 0 & 0 & -\frac{1}{4}V_0 & \frac{1}{2}V_0 + 4(q+1)^2 & -\frac{1}{4}V_0 \\ 0 & 0 & 0 & -\frac{1}{4}V_0 & \frac{1}{2}V_0 + 4(q+2)^2 \end{bmatrix} \cdot \begin{bmatrix} c_{q,-2}^n \\ c_{q,-1}^n \\ c_{q,0}^n \\ c_{q,1}^n \\ c_{q,2}^n \end{bmatrix} = E_q^n \begin{bmatrix} c_{q,-2}^n \\ c_{q,-1}^n \\ c_{q,0}^n \\ c_{q,1}^n \\ c_{q,2}^n \end{bmatrix} \quad (2.6)$$

These equations can be solved to obtain the eigenvectors c_{ql}^n and the eigenvalues E_q^n . In the numerical solution that we implemented we truncated the infinite set at $\mathcal{N} = 5$. We find that, to accurately obtain the dispersion relationship for the n^{th} band, you need $\mathcal{N} \geq n + 1$.

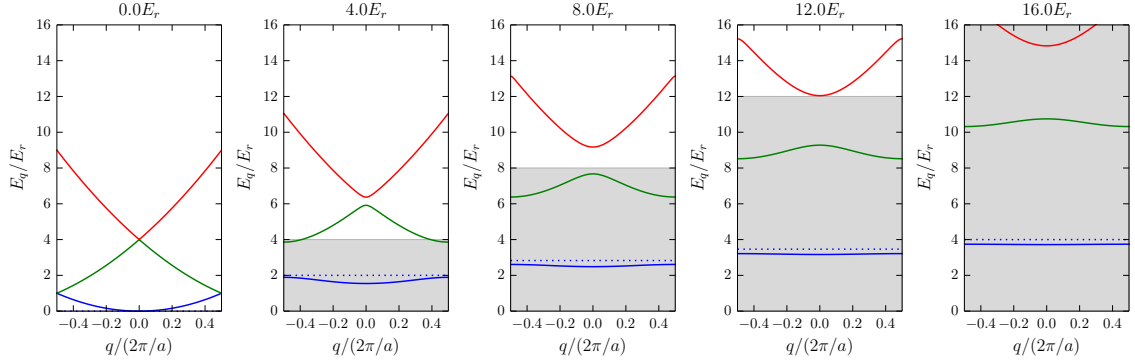


Figure 2.1: Band structure in a 1D optical lattice. The depth of the lattice is indicated by the shaded area, and the energy of the harmonic oscillator ground state in a single lattice site is shown as a dotted line.

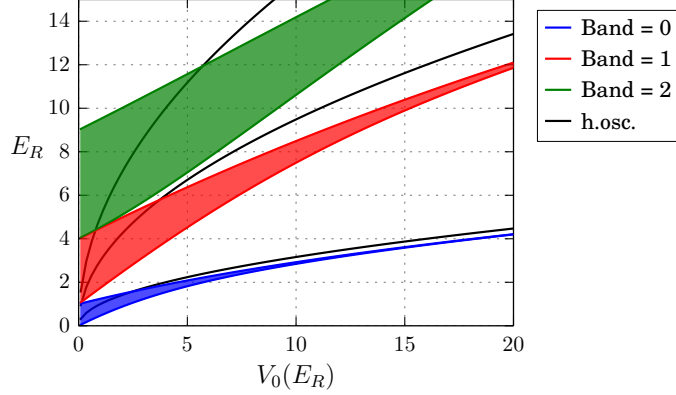


Figure 2.2: Band structure in a 1D optical lattice. Each band is indicated by the colored area, the harmonic oscillator states in an isolated lattice site are shown as black lines.

2.1.1 Band structure

The eigenvalues obtained from the solutions to Eq. 2.6 correspond to the energies E_q^n as a function of quasimomentum q and band index n and are referred to as the band structure. We show the band structure for a 1D lattice as a function of q in Fig. 2.1, and also as a function of lattice depth in Fig. 2.2

The time independent Schrödinger equation for the Hamiltonian in Eq. 2.1, can also be solved using Mathieu functions. One can then calculate the band structure by using the known properties of the Mathieu functions, which are available on tables or as functions in

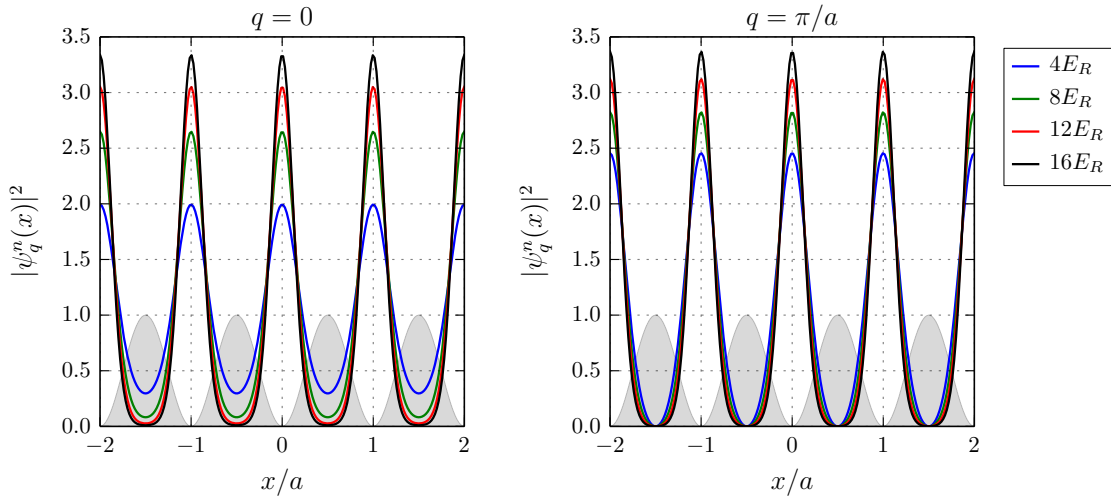


Figure 2.3: Eigenstates of the Hamiltonian in a 1D optical lattice shown for $q = 0$ (left) and $q = \pi/a$ (right) for various lattice depths. The states are normalized so that the integral of the probability density over one lattice site is equal to one. The gray shaded region is shown to indicate the variation of the lattice potential.

some software packages (e.g. Mathematica), see for instance the treatment in [62].

2.1.2 Eigenstates

For each energy eigenvalue we have an associated eigenstate which is defined in terms of the c_{ql}^n by Eq. 2.3. Typically, numerical diagonalization routines return the normalized eigenvectors of the matrix in question, and for us this means that the coefficients c_{ql}^n will satisfy

$$\sum_l |c_{ql}^n|^2 = 1 \quad (2.7)$$

This has the implication that the states obtained from Eq. 2.3 will be normalized over a lattice site. In Fig. 2.3. we show the probability density for a lowest band eigenstate as a function of position in the lattice for various lattice depths. One can see how, as the lattice gets deeper, the state becomes more localized around the center of each lattice site.

2.1.3 Wannier states

It is useful to define a basis of states that are localized around a single lattice site. We will see later on that, when using such a basis, the Hamiltonian for the Hubbard model takes its most familiar form. In a finite sized lattice with L sites, the localized state centered around the j^{th} site(at x_j) can be constructed as the following superposition of eigenstates of the Hamiltonian¹:

$$w^n(x - x_j) = \frac{1}{L} \sum_q e^{-iq2\pi x_j} \psi_q^n(x) \quad (2.8)$$

Here the sum runs over the set of quasimomenta $q \in \left\{ \frac{2\pi u}{aL} \mid u \in \{0, 1, \dots, L-1\} \right\}$. Inserting the expansion of $\psi_q^n(x)$ in plane waves into the definition of the Wannier state we obtain

$$w^n(x - x_j) \equiv w_j^n(x) = \frac{1}{L} \sum_q \sum_{l \in \mathbb{Z}} c_{ql}^n e^{-i2\pi q x_j} e^{i2\pi(q+l)x} \quad (2.9)$$

We will set $x_j = 0$ for the calculation of the Wannier function, Wannier states centered at different lattice sites can be obtained by translation of the $x_j = 0$ solution.

$$w_0^n(x) = \frac{1}{L} \sum_q \sum_{l \in \mathbb{Z}} c_{ql}^n e^{i2\pi(q+l)x} \quad (2.10)$$

Since the Hamiltonian commutes with the parity operator, it is required that $\psi_q^n(-x) = \pm \psi_q^n(x)$, which implies that $c_{ql}^n = \pm c_{pl}^n$ if $(q + l) = -(p + l')$. Using this symmetry, the Wannier state can be written as

$$w_0^n(x) = \frac{1}{L} \left(c_{00}^n + \sum_{q>0} \sum_{l>0} c_{ql}^n [e^{i2\pi(q+l)x} \pm e^{-i2\pi(q+l)x}] \right) \quad (2.11)$$

It is shown in [64] that the maximally localized Wannier states are obtained if the plus sign is chosen for even bands and the minus sign is chosen for odd bands. So, the $x_j = 0$ Wannier state is symmetric for the even bands and antisymmetric for the odd bands.

$$w_0^n(x) = \frac{c_{00}^n}{L} + \frac{2}{L} \sum_{q>0} \sum_{l>0} c_{ql}^n \begin{cases} \cos[2\pi(q+l)x] & \text{if } n \text{ even} \\ \sin[2\pi(q+l)x] & \text{if } n \text{ odd} \end{cases} \quad (2.12)$$

¹In some treatments (for instance [63]) the Wannier function is defined with a normalization factor of \sqrt{L} rather than L as shown here. Those treatments consider eigenfunctions $\psi_q^n(x)$ which are normalized when integrating over the full extent in the lattice. We stick to the L normalization factor, without the square root, since the eigenfunctions that are obtained numerically come out normalized over a lattice site, as was explained in the previous section.

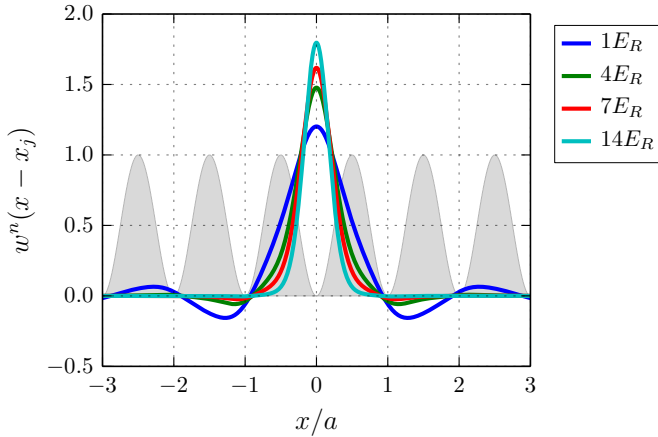


Figure 2.4: Wannier states localized at $x_j = 0$ in a 1D optical lattice for various lattice depths. The gray shaded region is shown to indicate the spatial variation of the lattice potential.

After defining the way to construct the Wannier states starting from the c_{ql}^n , we can now proceed to add up the plane waves to obtain the states, as shown in Fig. 2.4 for various lattice depths. As the lattice depth is increased, the Wannier states become more localized, which leads to less overlap between states in adjacent sites, and results in a reduction of the probability amplitude for a particle to tunnel from one site to the neighboring one. More localized states also imply that the on-site interaction will be larger, since, on average, two particles in the same site will be closer to each other.

We also show, in Fig. 2.5, the Wannier functions for the first three bands in a $4E_R$ lattice.

2.2 Three-dimensional optical lattice potential

The Hamiltonian for an atom moving in a 3D lattice can be separated in the three spatial coordinates. So we can use the solutions that were obtained in the previous section for the 1D lattice and obtain the band structure and the Wannier states for the 3D lattice. The 3D band structure is shown in Fig. 2.6.

The Wannier states in a 3D lattice are simply products of the Wannier states in each of

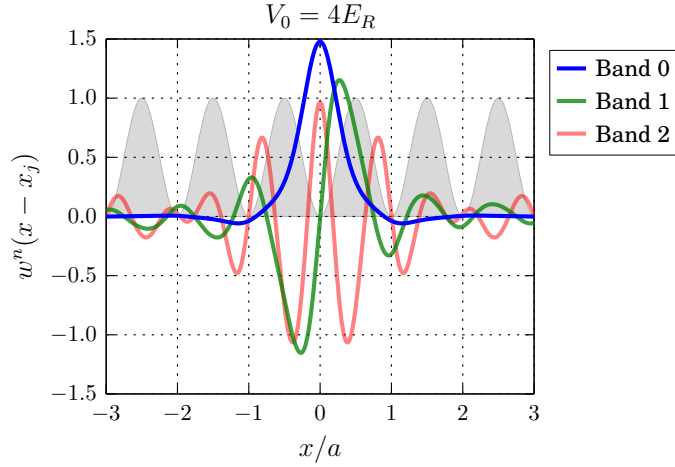


Figure 2.5: Wannier states localized at $x_j = 0$ in a $4E_R$ 1D optical lattice for the first three energy bands. The gray shaded region is shown to indicate the spatial variation of the lattice potential.

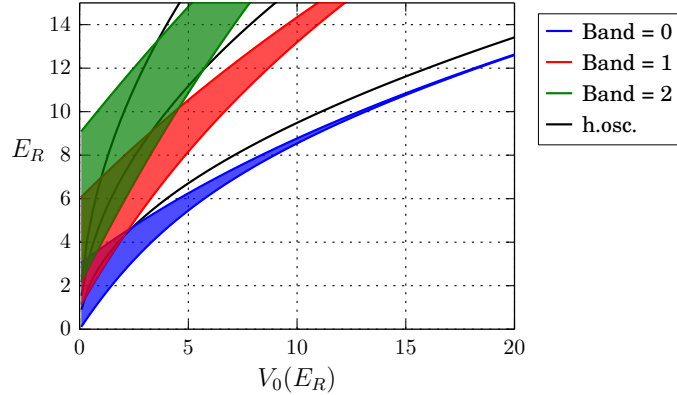


Figure 2.6: Band structure in a 3D optical lattice. Each band is indicated by the colored area, the harmonic oscillator states in an isolated lattice site are shown as black lines.

the three spatial coordinates. They are defined as

$$w^n(\mathbf{r} - \mathbf{r}_j) = \frac{1}{L^3} \sum_{\mathbf{q}} e^{-i\mathbf{q} \cdot \mathbf{r}_j} \prod_{u=x,y,z} \psi_{qu}^{n_u}(u) \quad (2.13)$$

where L^3 is the total number of sites in the lattice.

2.3 Hubbard Hamiltonian

The many-body Hubbard Hamiltonian is

$$H = -t \sum_{\langle ij \rangle, \sigma} a_{i\sigma}^\dagger a_{j\sigma} + U \sum_i n_{i\uparrow} n_{i\downarrow} \quad (2.14)$$

where i, j are indices that run over lattice sites, $\langle ij \rangle$ denotes nearest-neighbors, and σ denotes the spin state of the particles. The particle creation and annihilation operators, $a_{j\sigma}$ and $a_{i\sigma}^\dagger$, along with the number operator $n_{i\sigma}$ arise naturally in the second quantization formalism. In what follows, we will see how to obtain this many-body form of the Hamiltonian, starting from the first quantized version for a system of N particles moving in a periodic lattice.

The Hamiltonian for a single atom in a 3D optical lattice is given by

$$H_{\text{single,3D}} = -\frac{\hbar^2}{2m} \left(\frac{\partial^2}{\partial x^2} + \frac{\partial^2}{\partial y^2} + \frac{\partial^2}{\partial z^2} \right) + V_0 (\cos^2(kx) + \cos^2(ky) + \cos^2(kz)) \quad (2.15)$$

and when N particles are considered, along with their interactions it takes a more complicated form

$$\begin{aligned} H &= \sum_l^N \left[-\frac{\hbar^2}{2m} \left(\frac{\partial^2}{\partial x_l^2} + \frac{\partial^2}{\partial y_l^2} + \frac{\partial^2}{\partial z_l^2} \right) + V_0 (\cos^2(kx_l) + \cos^2(ky_l) + \cos^2(kz_l)) \right] \\ &\quad + \frac{1}{2} \sum_{l,n,l \neq n}^N V_{\text{int}}(\mathbf{r}_l, \mathbf{r}_n) \\ &\equiv H_0 + H_{\text{int}} \end{aligned} \quad (2.16)$$

where the particles are labeled by indices l, n and V_{int} is the potential energy of interaction between two particles. In the last line we have defined a more concise notation that splits the Hamiltonian into the non-interacting (H_0) and interacting (H_{int}) parts. Solving this problem is a daunting task primarily for two reasons:

1. The Bose or Fermi statistics of the identical particles under consideration require the solutions to be fully symmetric or antisymmetric with respect to particle exchange.

2. The interactions between the particles prevent a straightforward reformulation of the problem as a collection of easier-to-solve single particle Hamiltonians.

The formalism of many-body theory encapsulates a series of methods to deal with the two issues mentioned above. First, the reformulation of the Schrodinger equation in the language of second quantization provides the advantage that the statistics are automatically taken into account by the notation, so one can essentially forget about the (anti)symmetrization of the many-particle wave functions. The small price to pay is that one needs to be very careful and consistent about the order in which operators show up in the notation, since the symmetry properties of the resulting states are contained in the commutation relations defined between the operators. Furthermore, second quantization makes it easy to consider the extended Hilbert space where the number of particles is not fixed, known as the Fock space.

For weak interactions, many-body theory provides a solution to the problem in terms of perturbation expansions for the physical quantities of interest. The theoretical formalism also reduces most of the important physical quantities in terms of certain matrix elements (Green's functions). This allows the user to concentrate on obtaining such matrix elements, which serve as a starting point for the exploration of the properties of any system. The complication arises when the interactions are not weak, and the perturbative approach of the many-body formalism breaks down.

2.3.1 Second quantization

Let us start with a complete orthonormal set of single particle states $\{|i\rangle\} \equiv \{|1\rangle, |2\rangle, \dots\}$, using these states we can write the basis states for the N -particle system as

$$|i_1, \dots i_\alpha, \dots i_N\rangle \equiv |i_1\rangle_1 \dots |i_\alpha\rangle_\alpha \dots |i_N\rangle_N , \quad (2.17)$$

which represents a state in which particle 1 is in state $i_1 \in \{|i\rangle\}$, particle α is in state i_α and so on. These product states are not eigenstates of the permutation operator P_{ij} which

interchanges particles i and j . However, starting from the product states we can obtain the completely (anti)symmetrized basis states for bosons (fermions), which are eigenstates of any possible permutation of the particle labels.

For bosons, the normalized completely symmetric states are

$$|n_1, n_2, \dots\rangle = \frac{1}{\sqrt{N!n_1!n_2!\dots}} \sum_P P|i_1, i_2, \dots i_N\rangle \quad (2.18)$$

where the P 's are elements of the permutation group² In this expression, n_i is the number of times that the state $|i\rangle$ occurs among the N particles, also called the occupation number of state $|i\rangle$. The sum of all occupation numbers n_i must equal the total number of particles, but otherwise there is no restriction in the occupation number for bosons.

For fermions the normalized completely antisymmetric states have an extra factor $(-1)^P$, which denotes the parity of the permutation P . They can be written in the form of Slater determinants:

$$\begin{aligned} |n_1, n_2, \dots\rangle &= \frac{1}{\sqrt{N!}} \sum_P (-1)^P P|i_1, i_2, \dots i_N\rangle \\ &= \frac{1}{\sqrt{N!}} \begin{vmatrix} |i_1\rangle_1 & |i_1\rangle_2 & \cdots & |i_1\rangle_N \\ \vdots & \vdots & \ddots & \vdots \\ |i_N\rangle_1 & |i_N\rangle_2 & \cdots & |i_N\rangle_N \end{vmatrix} \end{aligned} \quad (2.19)$$

If a single particle state appears more than once in the product state, the resulting totally antisymmetric state is zero, i.e. the occupation numbers n_i can only take the values 0 or 1, a consequence of the Pauli exclusion principle.

For bosons (fermions), we can combine the (anti)symmetric states for $N = 0, 1, 2, \dots$ particles to obtain a complete orthonormal set of states for arbitrary particle number. This “number states” are the basis of the Fock space.

We will concentrate in the case of fermions, and define the creation operators such that the number state can be written as

$$|n_1, n_2, \dots\rangle = (a_1^\dagger)^{n_1} (a_2^\dagger)^{n_2} \dots |0\rangle \quad (2.20)$$

²For N particles there are $N!$ possible permutations and thus $N!$ elements in the permutation group.

where $|0\rangle$ is the vacuum state, in which there are no particles. By definition, the number state is completely antisymmetric, but what does this imply for the creation operators? Going back to Eq. 2.19, which defines the number states, we see that the sign of the number state depends on the particular ordering of the single particle states in the Slater determinant. Suppose $n_1 = n_2 = 1$, changing the labels on states 1 and 2 corresponds to exchanging two rows in the Slater determinant and thus a minus sign comes out:

$$(a_2^\dagger)^{n_2} (a_1^\dagger)^{n_1} \dots |0\rangle = -|n_1, n_2, \dots\rangle \quad (2.21)$$

Comparing with Eq. 2.20 we notice that the creation operators must then satisfy the following anticommutation relation

$$a_1^\dagger a_2^\dagger + a_2^\dagger a_1^\dagger \equiv \{a_1^\dagger, a_2^\dagger\} = 0 \quad (2.22)$$

Notice that this anticommutation relation implies $(a_i^\dagger)^2 = 0$, which is yet another manifestation of the Pauli exclusion principle.

When dealing with fermions, one must decide first on a particular ordering of the single particle states and then stick to it, noticing that to produce the number states (without a minus sign) all the creation operators must be applied to the vacuum state in the chosen order. The action of a creation operator on a number state is

$$a_i^\dagger | \dots, n_i, \dots \rangle = (-1)^{\sum_{k < i} n_k} | \dots, n_i + 1, \dots \rangle \quad (2.23)$$

where the factor $(-1)^{\sum_{k < i} n_k}$ takes care of the number of anticommutations needed to place the a_i^\dagger operator in the correct position. The action of the fermion annihilation operators can be inferred by taking the adjoint of Eq. 2.23. One can then obtain all of the anticommutation rules for fermions:

$$\{a_i, a_j\} = 0 \quad \{a_i^\dagger, a_j^\dagger\} = 0 \quad \{a_i, a_j^\dagger\} = \delta_{ij} \quad (2.24)$$

2.3.2 Operators in second quantization

So far two great leaps have been taken:

-
1. We have swept antisymmetrization under the rug by introducing the number states, defined from the vacuum in terms of creation operators which satisfy the Fermi anti-commutation rules.
 2. We started from an N particle Hamiltonian, but we have now defined number states that can handle the description of systems with an arbitrary number of particles

The two ideas mentioned are related to the states used to describe the system, now we will turn to the problem of the observables and see how they are handled in the second quantization.

Let us consider the sum $\sum_{\alpha} |i\rangle_{\alpha}\langle j|_{\alpha}$ where $|i\rangle$ and $|j\rangle$ are single particle states, and α runs over all particles in the system. We apply the sum to the number states using the definition in Eq. 2.19:

$$\left(\sum_{\alpha} |i\rangle_{\alpha}\langle j|_{\alpha} \right) |n_1, n_2, \dots\rangle = \frac{1}{\sqrt{N!}} \sum_P (-1)^P P \left(\sum_{\alpha} |i\rangle_{\alpha}\langle j|_{\alpha} |i_1, i_2, \dots, i_N\rangle \right) \quad (2.25)$$

For the term in the right not to vanish, the initial number state must have a particle in state $|j\rangle$, i.e. it must have $n_j = 1$. Also, n_i must be $n_i = 0$, or else the completely antisymmetric state will vanish. If the particle initially in state $|j\rangle$ is labeled as J we can write

$$\begin{aligned} \left(\sum_{\alpha} |i\rangle_{\alpha}\langle j|_{\alpha} \right) |n_1, n_2, \dots\rangle &= \frac{1}{\sqrt{N!}} \sum_P (-1)^P P \left(|i_1\rangle_1 |i_2\rangle_2 \dots \underbrace{|i\rangle_J}_{\text{instead of } |j\rangle_J} \dots |i_N\rangle_N \right) \\ &= \frac{1}{\sqrt{N!}} \begin{vmatrix} |i_1\rangle_1 & |i_1\rangle_2 & \cdots & |i_1\rangle_N \\ \vdots & \vdots & & \vdots \\ |i\rangle_1 & |i\rangle_2 & \cdots & |i\rangle_N \\ \vdots & \vdots & & \vdots \\ |i_N\rangle_1 & |i_N\rangle_2 & \cdots & |i_N\rangle_N \end{vmatrix} \end{aligned} \quad (2.26)$$

In the determinant of the left, the state $|i\rangle$ appears in the j^{th} row, so a few rows need to be exchanged to put it in the correct place, in accordance with our sign convention for the

number states:

$$\left(\sum_{\alpha} |i\rangle_{\alpha} \langle j|_{\alpha} \right) |n_1, n_2, \dots\rangle = \begin{cases} (-1)^{\sum_{k < j} n_k + \sum_{k < i} n_k} |n_1, n_2, \dots, n_i + 1, \dots, n_j - 1, \dots\rangle & \text{if } i \leq j, \\ (-1)^{\sum_{k < j} n_k + \sum_{k < i} n_k - 1} |n_1, n_2, \dots, n_j - 1, \dots, n_i + 1, \dots\rangle & \text{if } i > j \end{cases} \quad (2.27)$$

Checking the definition of the creation and annihilation operators we obtain the important result

$$\left(\sum_{\alpha} |i\rangle_{\alpha} \langle j|_{\alpha} \right) |n_1, n_2, \dots\rangle = a_i^{\dagger} a_j |n_1, n_2, \dots\rangle \Rightarrow \sum_{\alpha} |i\rangle_{\alpha} \langle j|_{\alpha} = a_i^{\dagger} a_j \quad (2.28)$$

Now, consider an operator T that is a sum over single particle operators

$$T = \sum_{\alpha} t_{\alpha} \quad (2.29)$$

If we insert the completeness relation for the single particle states twice in this sum, we have

$$\begin{aligned} T &= \sum_{\alpha} \left(\sum_i |i\rangle_{\alpha} \langle i|_{\alpha} \right) t_{\alpha} \left(\sum_j |j\rangle_{\alpha} \langle j|_{\alpha} \right) \\ &= \sum_{ij} \langle i | t | j \rangle \sum_{\alpha} |i\rangle_{\alpha} \langle j|_{\alpha} \\ &= \sum_{ij} \langle i | t | j \rangle a_i^{\dagger} a_j \equiv \sum_{ij} t_{ij} a_i^{\dagger} a_j \end{aligned} \quad (2.30)$$

This is the other big leap provided by the second quantization: an operator that was written as a sum over particles becomes a sum of creation and annihilation operators. We will apply this prescription to the non-interacting part of the Hamiltonian for N particles moving in a lattice.

Operators like the potential energy, $\frac{1}{2} \sum_{l,n,l \neq n}^N V_{\text{int}}(\mathbf{r}_l, \mathbf{r}_n)$, which are a sum over two-particle (or many-particle) operators, can be similarly expressed as sums of creation and annihilation operators [65]. For a two-body operator we have the expression

$$\begin{aligned} F &= \frac{1}{2} \sum_{\alpha \neq \beta} f(\mathbf{r}_{\alpha}, \mathbf{r}_{\beta}) \\ &= \frac{1}{2} \sum_{ijkm} \langle ij | f | km \rangle a_i^{\dagger} a_j^{\dagger} a_m a_k \end{aligned} \quad (2.31)$$

2.3.3 Second quantized Hubbard Hamiltonian

The Hubbard Hamiltonian in Eq. 2.16 is a sum of two single-particle operators and one two-particle operator. These are, respectively: the kinetic energy, the energy of the atoms in the lattice potential, and the interactions between the atoms. In this section we will express the Hubbard Hamiltonian in second quantized form. As a single-particle basis we will use the Wannier states that were derived in Section. 2.1.3

Tunneling matrix element, t . H_0 is a single particle operator of the kind defined in Eq. 2.29:

$$H_0 = \sum_{l=1}^N H_{\text{single,3D}}^l \quad (2.32)$$

where

$$H_{\text{single,3D}}^l = -\frac{\hbar^2}{2m} \left(\frac{\partial^2}{\partial x_l^2} + \frac{\partial^2}{\partial y_l^2} + \frac{\partial^2}{\partial z_l^2} \right) + V_0 \left(\cos^2(kx_l) + \cos^2(ky_l) + \cos^2(kz_l) \right) \quad (2.33)$$

Its second quantized form can be written as

$$\begin{aligned} H_0 &= \sum_{ij} \langle i | H_{\text{single,3D}} | j \rangle a_i^\dagger a_j \\ &\equiv - \sum_{ij} t_{ij} a_i^\dagger a_j \end{aligned} \quad (2.34)$$

Note that the sign of t_{ij} was picked rather arbitrarily to follow the usual conventions. We now proceed to find the value of the matrix element t_{ij} . We use the definition of the Wannier states given in Eq. 2.13 to find

$$\begin{aligned} -t_{ij} &= \frac{1}{L^6} \int d\mathbf{r} \sum_{\mathbf{q}'} e^{i\mathbf{q}' \cdot \mathbf{r}_i} \prod_{u'=x,y,z} \psi_{q'_u u'}^{n'_{u'}}(u') (H_{\text{single,3D}}) \sum_{\mathbf{q}} e^{-i\mathbf{q} \cdot \mathbf{r}_j} \prod_{u=x,y,z} \psi_{q_u u}^{n_u}(u) \\ &= \sum_{\mathbf{q}\mathbf{q}'} \frac{E_{\mathbf{q}}^n}{L^6} e^{i\mathbf{q}' \cdot \mathbf{r}_i} e^{-i\mathbf{q} \cdot \mathbf{r}_j} \int d\mathbf{r} \prod_{u'=x,y,z} \psi_{q'_u u'}^{n'_{u'}}(u') \prod_{u=x,y,z} \psi_{q_u u}^{n_u}(u) \\ &= \sum_{\mathbf{q}\mathbf{q}'} \frac{E_{\mathbf{q}}^n}{L^6} e^{i\mathbf{q}' \cdot \mathbf{r}_i} e^{-i\mathbf{q} \cdot \mathbf{r}_j} \delta_{\mathbf{q}\mathbf{q}'} \delta_{nn'} L^3 \\ &= \frac{1}{L^3} \sum_{\mathbf{q}} E_{\mathbf{q}}^n e^{i\mathbf{q} \cdot (\mathbf{r}_i - \mathbf{r}_j)} \delta_{nn'} \end{aligned} \quad (2.35)$$

We observe that there is no amplitude to go between states that are in two different bands, as is indicated by the appearance of $\delta_{nn'}$. In what follows, we will consider only the lowest

band, $n = 0$, so we will drop the band index, n , altogether. For this simplification to be valid, the following two requirements must be satisfied by the system:

1. **The temperature and the Fermi energy need to be small compared to the energy gap between the lowest and first excited band.**
2. **The interaction energy scale must also be small compared to the energy gap between the lowest and first excited band.**

In the 3D lattice, the total energy $E_{\mathbf{q}}$ is the sum of the energy associated with each quasimomentum component, $E_{\mathbf{q}} = \sum_{u=x,y,z} E_{q_u}$. By inserting this into the sum for t_{ij} above we find

$$\begin{aligned} -t_{ij} &= \frac{1}{L^3} \left[\left(\sum_{q_x} E_{q_x} e^{iq_x x_{ij}} \right) \sum_{q_y} e^{iq_y y_{ij}} \sum_{q_z} e^{iq_z z_{ij}} \right. \\ &\quad \left. + \sum_{q_x} e^{iq_x x_{ij}} \left(\sum_{q_y} E_{q_y} e^{iq_y x_{ij}} \right) \sum_{q_z} e^{iq_z z_{ij}} + \sum_{q_x} e^{iq_x x_{ij}} \sum_{q_y} e^{iq_y y_{ij}} \left(\sum_{q_z} E_{q_z} e^{iq_z z_{ij}} \right) \right] \end{aligned} \quad (2.36)$$

We make use of the identity $\sum_{q_u} e^{iq_u(u_i - u_j)} = L\delta_{u_i u_j}$ to obtain

$$-t_{ij} = \frac{1}{L} \left[\left(\sum_{q_x} E_{q_x}^{1D} e^{iq_x x_{ij}} \right) \delta_{y_i y_j} \delta_{z_i z_j} + \left(\sum_{q_y} E_{q_y}^{1D} e^{iq_y x_{ij}} \right) \delta_{x_i x_j} \delta_{z_i z_j} + \left(\sum_{q_z} E_{q_z}^{1D} e^{iq_z z_{ij}} \right) \delta_{x_i x_j} \delta_{y_i y_j} \right] \quad (2.37)$$

If $i = j$ we have

$$-t_{ii} = \frac{3}{L} \sum_q E_q \quad (2.38)$$

Since q runs over the L different values in the set $q \in \left\{ \frac{2\pi u}{aL} \mid u \in \{0, 1, \dots, L-1\} \right\}$ (as explained above following Eq. 2.8), $-t_{ii}$ is nothing more than the mean energy of the 3D energy band, which we will refer to as \bar{E} , $-t_{ii} \equiv \bar{E}$

If $i \neq j$, tunneling can only occur along one of the lattice directions as can be seen from the different Kronecker delta terms that show up in Eq. 2.37. In other words, for the simple cubic potential, diagonal tunneling events are second order processes. If we write

the distance between sites i, j as Δ_{ij} , the tunneling matrix element simplifies to

$$-t_{ij} = \frac{1}{L} \sum_q E_q e^{iq\Delta_{ij}} \quad (2.39)$$

Formula 2.39 is how we regularly calculate the tunneling matrix element³. Starting from the lattice depth we solve for E_q and then carry out the sum over q .

In the tight-binding approximation, terms for which $|\Delta_{ij}| > a$ are neglected, and Δ_{ij} can only take the values $-a$ or a , where a is the lattice spacing. In this case we use $t_{ij} \equiv t$, where t is given by

$$-t = \frac{1}{L} \sum_q E_q e^{iqa} \quad (2.41)$$

We can then go ahead and write the second quantized form of H_0 in the tight-binding approximation

$$H_0 = \bar{E} \sum_i a_i^\dagger a_i - t \sum_{\langle ij \rangle} a_i^\dagger a_j \quad (2.42)$$

The first term in this expression is constant for a system with a conserved number of particles, since $\sum_i a_i^\dagger a_i = N$. Usually this energy offset is neglected, but when dealing with inhomogeneous systems which have a position dependent lattice depth it will be important to take it into account, as we will see later on.

We can go ahead and invert the Fourier series in Eq. 2.39 to obtain

$$E_q = - \sum_{\Delta_{ij}} t_{ij} e^{-iq\Delta_{ij}} \quad (2.43)$$

which in the tight-binding approximation reduces to

$$E_q = -2t \cos(qa) \quad (2.44)$$

This explicit form for the dispersion relation allows us to relate the bandwidth, W_{1D} , to the tunneling matrix element as $W_{1D} = 4t$, which in 3D becomes $W_{3D} = 12t$.

³This derivation has used the Wannier states, constructed as a sum of plane waves, to obtain the tunneling matrix element. It can also be obtained directly from the Wannier states' wavefunctions as:

$$-t_{ij} = \int d\mathbf{r} w_i(\mathbf{r}) H_{\text{single},3D} w_j(\mathbf{r}) \quad (2.40)$$

Calculating the tunneling matrix element by computing the overlap integral of the Wannier wavefunctions is computationally more expensive than obtaining it as a sum over the energy eigenvalues of the band.

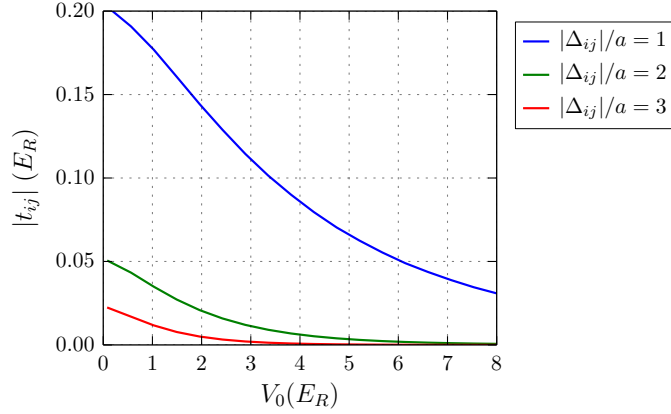


Figure 2.7: Tunneling matrix element in an optical lattice as a function of lattice depth. Nearest-neighbor and beyond nearest-neighbor matrix elements are shown to illustrate the range of lattice depths for which the tight-binding limit is a good approximation. Δ_{ij} corresponds to the distance between initial and final lattice sites in the tunneling matrix element. For $V_0 \gtrsim 5 E_r$ we can safely neglect tunneling beyond nearest neighbors.

It is useful to find out the range of lattice depths for which the tight-binding approximation is valid in the optical lattice potential. To do this we just need to look at the tunneling matrix elements for beyond nearest-neighbor tunneling, as shown in Fig. 2.7. It is seen in the figure that, for lattice depths $\gtrsim 5 E_r$ we can safely ignore beyond nearest-neighbor tunneling, see also Fig. 2.10.

Yet another way of estimating the tunneling matrix element [66] is by using the relationship $t = W_{1D}/4$, valid in the tight-binding limit, and then working backwards. An analytical form for the bandwidth can be obtained from the known properties of the Mathieu functions, which are solutions to the Schrodinger equation in a 1D lattice. This approach yields the analytic result

$$t/E_r \simeq \frac{4}{\sqrt{\pi}} v_0^{3/4} \exp(-2\sqrt{v_0}) \quad (2.45)$$

where v_0 is the lattice depth in units of the recoil energy. This formula appears in a popular review of the subject [66] and is thus widely used. The comparison between the result from Eq. 2.39 and Eq. 2.45 is shown in Fig. 2.8.

Notice that, up to now, we have ignored the spin part of the wavefunction. We can include it easily by noticing that H_0 does not act on the spin at all, so the states $|i\rangle$ and $|j\rangle$

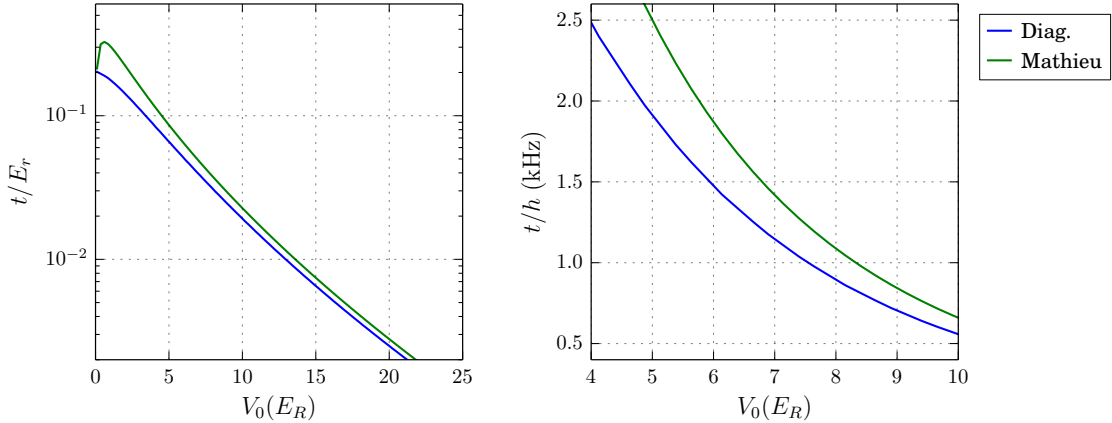


Figure 2.8: Nearest neighbor tunneling matrix element in an optical lattice as a function of lattice depth. Comparison between the result from Eq. 2.39 (blue line) and the one obtained from the Mathieu functions, Eq. 2.45 (green line). The right panel shows the tunneling rate in kHz for the mass of a ${}^6\text{Li}$ atom. At $7 E_r$, where we perform most of our experiments, the discrepancy can be significant.

that we have used in the derivation above need to have the same spin. If two spin states are available, our basis set is twice as large, which can be taken care of by including a sum over spin states in the second quantized form of the Hamiltonian:

$$H_0 = \bar{E} \sum_i a_i^\dagger a_i - t \sum_{\langle ij \rangle, \sigma=\uparrow\downarrow} a_{i\sigma}^\dagger a_{j\sigma} \quad (2.46)$$

On-site interaction energy, \mathbf{U} . The interaction part of the Hamiltonian for N particles is given by

$$H_{\text{int}} = \frac{1}{2} \sum_{l,m,l \neq m}^N V_{\text{int}}(\mathbf{r}_l, \mathbf{r}_m) \quad (2.47)$$

This is a two-particle operator, and its second quantized form is given by

$$H_{\text{int}} = \frac{1}{2} \sum_{i,j,k,m} \langle ij | V_{\text{int}} | km \rangle a_i^\dagger a_j^\dagger a_m a_k \quad (2.48)$$

where

$$\langle ij | V_{\text{int}} | km \rangle = \int d\mathbf{r}_1 \int d\mathbf{r}_2 \varphi_i^*(\mathbf{r}_1) \varphi_j^*(\mathbf{r}_2) V_{\text{int}}(\mathbf{r}_1, \mathbf{r}_2) \varphi_k(\mathbf{r}_1) \varphi_m(\mathbf{r}_2) \quad (2.49)$$

and the φ 's correspond to the wavefunctions of the single particle basis states chosen.

The interaction between ultracold atoms can be described in terms of the *s*-wave scattering length, a_s , and a pseudo-potential [67, 66] given by⁴

$$V_{\text{int}}(\mathbf{r}_1, \mathbf{r}_2) = \frac{4\pi\hbar^2 a_s}{m} \delta(\mathbf{r}_1 - \mathbf{r}_2) \quad (2.50)$$

so the matrix element above can be written as

$$\langle ij|V_{\text{int}}|km\rangle = \frac{4\pi\hbar^2 a_s}{m} \int d\mathbf{r} \varphi_i^*(\mathbf{r}) \varphi_j^*(\mathbf{r}) \varphi_k(\mathbf{r}) \varphi_m(\mathbf{r}) \quad (2.51)$$

Our basis states, φ , are the 3D Wannier states defined in Eq. 2.13, which are separable in the three spatial coordinates. We recall that the Wannier states are labeled by the lattice site around which they are centered, and by their band index. If we explicitly write out the two labels in the expression above, we obtain

$$\langle ij|V_{\text{int}}|km\rangle = \frac{4\pi\hbar^2 a}{m} \prod_{v=x,y,z} \int dv w_i^{n_i}(v) w_j^{n_j}(v) w_k^{n_k}(v) w_m^{n_m}(v) \equiv U_{ijkm} \quad (2.52)$$

In general i, j, k, m can represent any lattice sites. We will restrict our treatment to on-site interactions by enforcing $i = j = k = m$, furthermore, we consider only Wannier states in the lowest band. With this considerations, and also explicitly writing down the spin quantum number, we find

$$H_{\text{int}} = \frac{U}{2} \sum_i (a_{i\uparrow}^\dagger a_{i\downarrow}^\dagger a_{i\downarrow} a_{i\uparrow} + a_{i\downarrow}^\dagger a_{i\uparrow}^\dagger a_{i\uparrow} a_{i\downarrow}) \quad (2.53)$$

where we have defined $U \equiv U_{ijkm}$ for $i = j = k = m$, with U is given by

$$U/E_r = \frac{8}{\pi} \frac{a_s}{a} \prod_{v=x,y,z} \int w(v)^4 dv \quad (2.54)$$

Defining the number operator as $n_{i\sigma} = a_{i\sigma}^\dagger a_{i\sigma}$

$$\begin{aligned} H_{\text{int}} &= \frac{U}{2} \sum_i (n_{i\downarrow} n_{i\uparrow} + n_{i\uparrow} n_{i\downarrow}) \\ &= U \sum_i n_{i\uparrow} n_{i\downarrow} \end{aligned} \quad (2.55)$$

⁴This is a good approximation as long as the *s*-wave scattering lengths is small compared to the single-site harmonic oscillator length [68]. This condition is typically satisfied, and other concerns such as collisional losses or coupling to higher bands become more important well before the *s*-wave scattering length is comparable to the harmonic oscillator length. For reference, the harmonic oscillator length in a lattice site is $\ell = a/(\pi v_0^{1/4})$, which for a 7 E_r lattice with $a = 532$ nm is $\ell \approx 2000 a_0$, where a_0 is the Bohr radius.

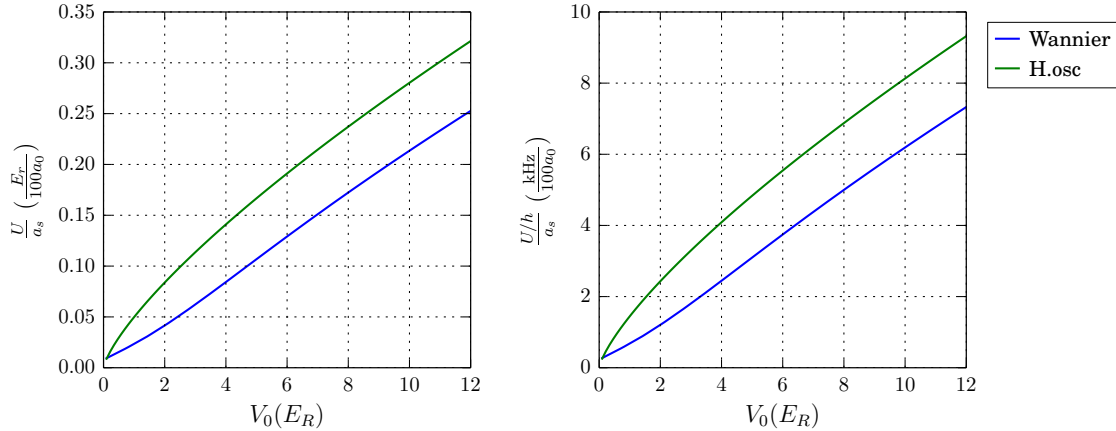


Figure 2.9: On-site interactions in a 3D lattice ($\lambda = 1064\text{ nm}$) as a function of lattice depth. Numerical calculation using Wannier functions (blue line) compared to the approximation using harmonic oscillator states (green line). The lattice depth is the same in all three directions of the lattice. The left panel shows uses E_r for the units of U and the right panel uses kHz for U/h .

where i runs over all of the lattice sites.

To calculate the value of U we use the Wannier states obtained in Sec. 2.1.3. Alternatively, one can approximate the Wannier state by the Gaussian ground state in the local oscillator potential of one lattice site and carry out the integral analytically to obtain [66]

$$U = \sqrt{8\pi} \frac{a_s}{a} v_0^{3/4} \quad (2.56)$$

Figure 2.9 shows a comparison of the exact result and the Gaussian approximation to the Wannier state for a lattice with $\lambda = 1064\text{ nm}$.

If the on-site interaction term is comparable to the energy spacing between the lowest and first excited bands, the single band approximation presented here breaks down. Corrections to the tunneling rate and the on-site interactions are necessary, which may depend on the lattice site occupation [69–71].

2.4 Parameter regimes for a valid description using a single band Hubbard model

Throughout this chapter we have mentioned the possible scenarios for which the single band Hubbard model is not an accurate description of ultracold atoms in an optical lattice. The two most important ones are:

- The on-site interaction U is comparable to the band gap Δ . The band gap is the energy difference between the highest energy state in the lowest band and the lowest energy state in the first excited band, see Fig. 2.6.
- Tunneling beyond nearest-neighbor (rate $t_2 \equiv t_{ij}$ for $\Delta_{ij} = 2a$, see Fig. 2.7) is not negligible compared to nearest-neighbor tunneling (rate t), i.e. the tight-binding approximation does not hold.

In Fig. 2.10 we have represented these two conditions as a function of the lattice depth and the s -wave scattering length. For more details on the validity of the single band Hubbard Hamiltonian see Ref. [69].

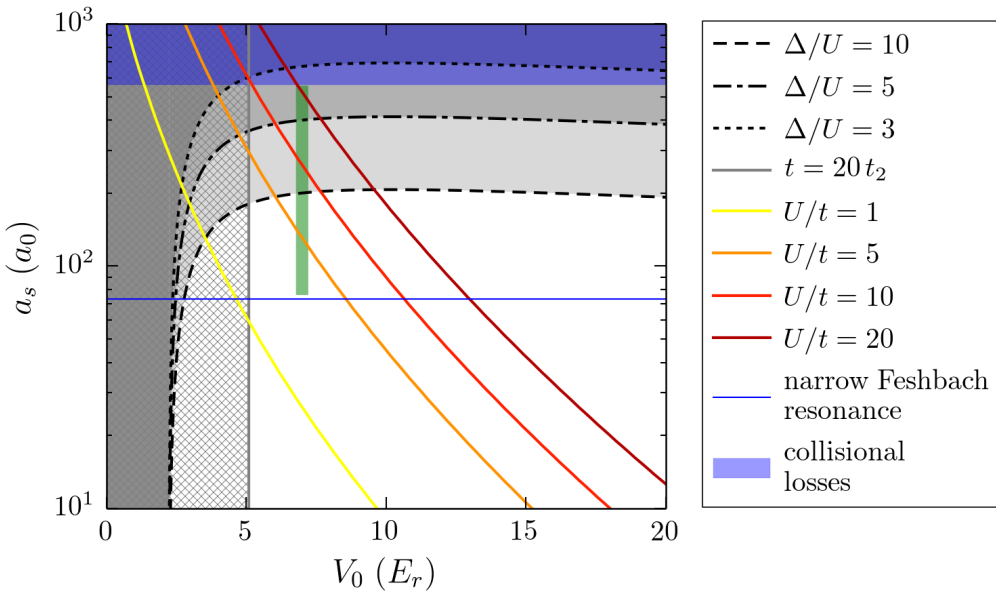


Figure 2.10: Regimes of validity for the single band Hubbard Hamiltonian. The dashed black lines show curves at constant Δ/U . As U approaches Δ , higher bands have to be taken into account to describe the system accurately [69]. The vertical gray line indicates the lattice depth at which $t = 20t_2$, which delimits the region of validity of the tight-binding approximation. Yellow to brown hued lines indicated curves at constant U/t . The thin blue line indicates the background s -wave scattering length in the vicinity of the narrow Feshbach resonance of ${}^6\text{Li}$ [72, 73]. The shaded blue area indicates the range of scattering lengths over which we see significant collisional losses and heating of the sample. The shaded green area denotes the parameter regime covered by the experiments carried out in this thesis.

3. The Hubbard model

In Chapter 2 we saw how ultracold atoms, under a large range of values for the lattice depth and the *s*-wave scattering length are a nearly ideal realization of the single band Hubbard model. The Hubbard model, nevertheless, was not originally formulated with these kind of systems in mind; it originated as an overly simplified picture for the description of electrons in solids. In this chapter we start by providing a brief historical perspective of the Hubbard model. We then go on to introduce simplified treatments of the model which will allow us to gain insight into its physics. We conclude by describing some of the latest advances in numerical simulations.

3.1 A bit of history

At the end of the 1920's, when the foundations of quantum mechanics were almost all formally laid out, there were quite a few phenomena begging for a touch of quantum mechanics to elucidate the physics behind them. One of those problems was ferromagnetism. Ferromagnetism was first understood classically within the Weiss picture of a molecular field, in which a ferromagnet is treated as a paramagnet under the influence of a fictitious magnetic field (the molecular field), which is postulated to be proportional to the magnetization. It was Heisenberg in 1928 [74] who realized that the exchange interaction, as used by Heitler and London to explain the singlet and triplet energy level splitting of the Helium atom, was responsible for the existence and magnitude of Weiss's molecular field. This motivated the Heisenberg model for ferromagnetism

$$H = - \sum_{ij} J_{ij} \mathbf{S}_i \cdot \mathbf{S}_j \quad (3.1)$$

where J_{ij} is the exchange constant between spins that are localized at sites i and j in a crystal lattice. Under the assumption that only nearest neighboring spins affect each other, the Heisenberg model can account for the Curie temperature of ferromagnets, with reasonable values of J as an input. However, even though Heisenberg's theory of ferromagnetism had the correct physical basis, a formal calculation of the exchange term, J , for a large system of interacting electrons is too difficult to carry out.

The problem of d electrons in ferromagnetic metals was still of much interest in the early 1960's. A lot of attention had been given in the previous decade to the issue of considering the consequences of interactions between electrons (correlations) in a free electron gas. This was very important for the description of electrons in conduction bands, but not satisfactory when considering partially filled d or f bands, such as those present in the transition and rare-earth metals. In particular, the d electrons of the transition metals were of major interest at the time because they are not as localized as f electrons, but also not as "free" as s -electrons in a conduction band.

Hubbard realized, in the early 60's, that the problem of d -electrons could be thought of as a problem of electrons in a conduction band, where the effects of interactions between electrons (correlations) give rise to behavior more consistent with an atomic picture of localized electrons. He then postulated a model [75], now known as the Hubbard model, as an extension of the tight-binding model (the simplest model for an energy band) on which the effects of correlations are simplified at maximum without removing them altogether. The hope was to see the behavior of electrons as localized moments, i.e. ferromagnetism or an insulating state, emerge solely as a consequence of electron correlations in a conduction band.

To simplify the role of correlations, Hubbard neglected all of the terms due to interactions, except the one where two electrons are on the same site. As we saw in Chapter 2, this approximation is easy to express in the second quantized formalism using Wannier states as a single particle basis. The on-site interaction term for the Coulomb energy between two

electrons is then:

$$U = \int w^*(\mathbf{x} - \mathbf{R}_i)w(\mathbf{x} - \mathbf{R}_k) \left(\frac{e^2}{|\mathbf{x} - \mathbf{x}'|} \right) w^*(\mathbf{x}' - \mathbf{R}_j)w(\mathbf{x}' - \mathbf{R}_l) \, d\mathbf{x}d\mathbf{x}' \quad (3.2)$$

where w are the Wannier states, introduced in Chapter 2, and $\mathbf{R}_i = \mathbf{R}_j = \mathbf{R}_k = \mathbf{R}_l$. In the same year as Hubbard, Gutzwiller [76] and Kanamori [77], independently formulated essentially the same model for d electrons.

Another thing to point out about the Hubbard model is that even though it was conceived with the problem of d -electrons in mind, the band considered in the model is an s -band. In a d -band there are 10 different levels that an electron can occupy, however in an s -band there are only two, spin up and spin down. Hubbard himself commented on this point and said: “one may nevertheless hope to obtain some results of general application” [75],.

3.2 Hubbard model for a single lattice site, $t = 0$

In the Hubbard model, the limit of no interactions, $U = 0$, takes us simply back to the tight-binding model. In this case the properties of the system can be well understood in terms of a single particle picture, where electrons occupy the single particle energy levels of the Hamiltonian according to the Fermi-Dirac distribution. The dispersion relation of the tight-binding model determines the density of states, and the thermodynamics at low temperature can be obtained from the value of the Fermi energy and the temperature by making use of Sommerfeld’s approach for approximating Fermi-Dirac integrals [3].

On the other hand, the limit of no tunneling [78], $t = 0$, will allow us to gain some insight into the thermodynamics of the Hubbard model. In this case the lattice sites can be considered to be completely independent of each other, and the partition function of the total system is simply a product of the partition function for a system with a single lattice site.

We recall the Hubbard Hamiltonian:

$$H = -t \sum_{\langle ij \rangle, \sigma} a_{i\sigma}^\dagger a_{j\sigma} + U \sum_i n_{i\uparrow} n_{i\downarrow} - \mu \sum_i (n_{i\uparrow} + n_{i\downarrow}) \quad (3.3)$$

where μ is the chemical potential, and the term $-\mu \sum_i (n_{i\uparrow} + n_{i\downarrow})$ is included to work in the grand canonical ensemble, where the particle number is allowed to vary.

The grand canonical partition function is given by

$$Z = \text{Tr} e^{-\beta H} = z^N \quad (3.4)$$

where z is the partition function for an individual site given by

$$z = 1 + 2e^{\beta\mu} + e^{2\beta\mu - \beta U} \quad (3.5)$$

With the partition function in hand we can obtain the thermodynamic quantities as derivatives of the grand canonical potential, $\Omega = -\ln Z/\beta$. We have for the density, double occupancy, and entropy per lattice site:

$$n = -\frac{1}{N} \frac{\partial \Omega}{\partial \mu} \quad d = \frac{1}{N} \frac{\partial \Omega}{\partial U} \quad s = -\frac{1}{N} \frac{\partial \Omega}{\partial T} \quad (3.6)$$

For example, the explicit expression for the density can be derived:

$$n = 2 \frac{e^{\beta\mu} + e^{2\beta\mu - \beta U}}{1 + 2e^{\beta\mu} + e^{2\beta\mu - \beta U}} \quad (3.7)$$

An important physical quantity in the Hubbard model is the local moment, defined as

$$\langle m^2 \rangle = \langle (n_\uparrow - n_\downarrow)^2 \rangle = n - 2d \quad (3.8)$$

If there is no probability of having doubly occupied sites, $d = 0$ and the local moment simply becomes equal to the density n . From the grand potential we obtain the expression

$$\langle m^2 \rangle = 2 \frac{e^{\beta\mu}}{1 + 2e^{\beta\mu} + e^{2\beta\mu - \beta U}} \quad (3.9)$$

In Fig. 3.1 we show plots of the density and the local moment versus chemical potential for various temperatures. As we mentioned above, the Hubbard model describes an s -band

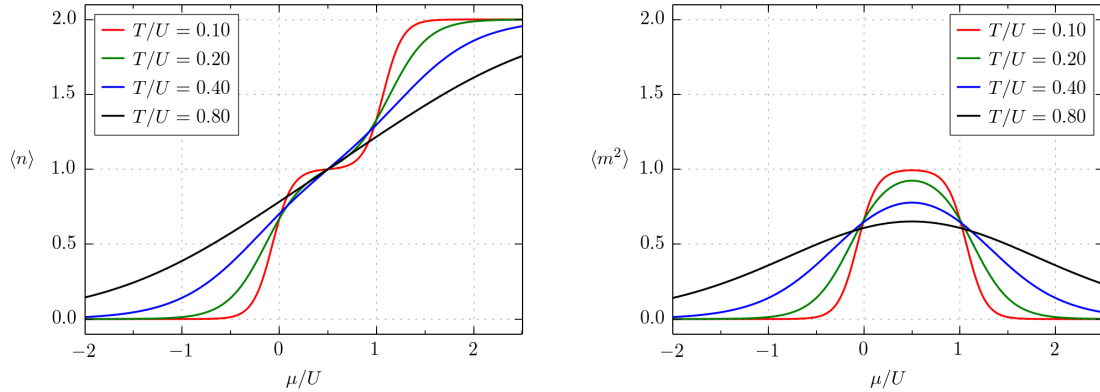


Figure 3.1: Density and local moment versus chemical potential in the Hubbard model for $t = 0$. In this limit the Hubbard model represents a collection of uncorrelated lattice sites. For a temperature, T , significantly lower than the on-site interaction, U , the density shows a plateau as a function of chemical potential, representative of the Mott insulating gap. At the same time the local moment goes to 1, indicating the absence of doubly occupied sites, and the suppression of fluctuations on the number of atoms per site, two indicators of an insulating state.

with a maximum capacity of two electrons per lattice site. When the average number of particles per site in the Hubbard model is $n = 1$, the system is said to be at half-filling. Figure 3.1 shows us that there is a plateau in the density as a function of chemical potential which occurs at half-filling for sufficiently low temperatures. This plateau is an indication of the Mott insulating gap, it can be interpreted as a discontinuous jump in the energy necessary to add an extra particle to the system. At the same time we see that the local moment goes to 1, equal to the density at half filling, which tells us that in the Mott insulating plateau the probability of finding doubly occupied sites goes to zero, as well as the fluctuations in the number of particles per site

In the previous paragraph we suggested that the plateau in n vs. μ is indicative of an energy gap. In more formal terms, to establish the presence of a gap in the spectrum of a many-body system, one should calculate the pseudo-particle density of states (also known as the spectral function). This was done by Hubbard on the third of the series of papers that followed his introduction of the Hubbard model [16], and he showed that his model predicted the existence of the Mott-Hubbard insulating gap. In 1949, Mott had suggested that the Coulomb interaction was responsible for the insulating properties of nickel monoxide (NiO),

a material with a partially filled band that should be a conductor according to conventional band theory [79]. The treatment by Hubbard was the first formal treatment of the Mott metal-insulator transition [80] and the first big success of the Hubbard model.

3.3 Particle-hole symmetry

The reader may have noticed, by looking at Fig. 3.1, that all of the plotted curves have a symmetry about $\mu = U/2$. All of the thermodynamic properties of the Hubbard model exhibit this symmetry, a consequence of the particle-hole symmetry of the Hamiltonian, and one only needs to obtain them for densities $0 \leq n \leq 1$, as they can be inferred for $1 \leq n \leq 2$ by reflection about $\mu = U/2$. In some theoretical treatments it is desirable to have the reflection point be independent of U , so a shift is introduced in the chemical potential $\mu' = \mu - U/2$ which results in the “particle-hole symmetric” form of the Hubbard Hamiltonian:

$$H' = -t \sum_{\langle ij \rangle, \sigma} a_{i\sigma}^\dagger a_{j\sigma} + U \sum_i \left(n_{i\uparrow} - \frac{1}{2} \right) \left(n_{i\downarrow} - \frac{1}{2} \right) - \mu' \sum_i (n_{i\uparrow} + n_{i\downarrow}) \quad (3.10)$$

This form produces the same physical results as the non-shifted one.

3.4 Exact diagonalization

The treatment of the single-site limit of the Hubbard model was very simple and we showed how to obtain an expression for the grand potential, from which all of the thermodynamic properties can be obtained. From this simple treatment we saw how the Mott insulating gap opens up at low temperatures, and a Mott insulator, with exactly one particle per lattice site, can exist at half-filling. At even lower temperatures it is well known that the localized moments of the Mott insulator order themselves into an AFM ordered state.

In what follows we will obtain the exact solution for the ground state of models with 2

sites and 4 sites. These solutions are going to motivate the antiferromagnetic character of the ground state of the Hubbard model, and give us a glimpse of the connection between the Hubbard model and high- T_c superconductivity.

Exact diagonalization for 2 sites

The full Hilbert space for a two-site model has dimension 16. To do an exact diagonalization we will restrict to a sector at half-filling with a balanced spin-mixture (equal number of up and down spins). The basis states are:

$$|\uparrow\downarrow, 0\rangle = a_{1\uparrow}^\dagger a_{1\downarrow}^\dagger |0\rangle \quad (3.11)$$

$$|\downarrow\uparrow, 0\rangle = a_{1\downarrow}^\dagger a_{2\uparrow}^\dagger |0\rangle \quad (3.12)$$

$$|\uparrow\downarrow, 0\rangle = a_{1\uparrow}^\dagger a_{2\downarrow}^\dagger |0\rangle \quad (3.13)$$

$$|0, \uparrow\downarrow\rangle = a_{2\uparrow}^\dagger a_{2\downarrow}^\dagger |0\rangle \quad (3.14)$$

$$(3.15)$$

Notice that we have chosen the ordering convention for fermion creation operators in which lower site indices are leftmost and spin up is to the left of spin down. Calculating the matrix elements of the Hubbard Hamiltonian in this basis is an exercise in tracking minus signs when commuting fermion creation and annihilation operators. We have automated that procedure by writing a python program which is available online [81].

The resulting matrix for the Hamiltonian is

$$H = \begin{pmatrix} U & 0 & -t & -t \\ 0 & U & -t & -t \\ -t & -t & 0 & 0 \\ -t & -t & 0 & 0 \end{pmatrix} \quad (3.16)$$

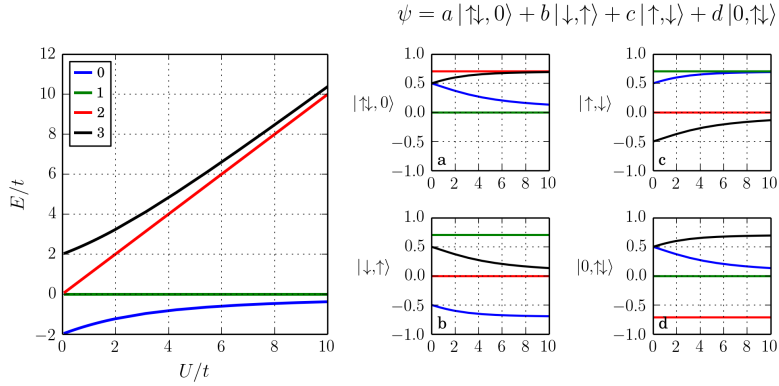


Figure 3.2: Energy eigenvalues and eigenstates for a two lattice site system. The coefficients a, b, c, d , which define the energy eigenstates are shown in the four panels at the right. We see that the ground state has an antiferromagnetic character.

which can be analytically diagonalized to obtain the eigenvalues

$$\begin{aligned} & \frac{1}{2} \left(U - \sqrt{16t^2 + U^2} \right) \\ & 0 \\ & U \\ & \frac{1}{2} \left(U + \sqrt{16t^2 + U^2} \right) \end{aligned} \tag{3.17}$$

For large U/t the energy of the ground state goes to $\approx -4t^2/U$, which is the value of the AFM exchange energy. In Fig. 3.2 we show plots of the energy eigenvalues as a function of U/t and also show the composition of the energy eigenstates in terms of our basis states. In the two-site system, we can see the opening of the Mott-Hubbard gap in the spectrum as U/t is increased, in agreement with the single site treatment. We can now also see the antiferromagnetic character of the ground state. In the limit of large U/t , the ground state is given by

$$\frac{1}{\sqrt{2}} |\uparrow, \downarrow\rangle - \frac{1}{\sqrt{2}} |\downarrow, \uparrow\rangle \tag{3.18}$$

Exact diagonalization for 4 sites

In the case of four lattice sites (a 2×2 plaquette), the basis set in the half-filling spin-balanced sector grows to contain 36 states. The Hamiltonian matrix is a 36×36 matrix,

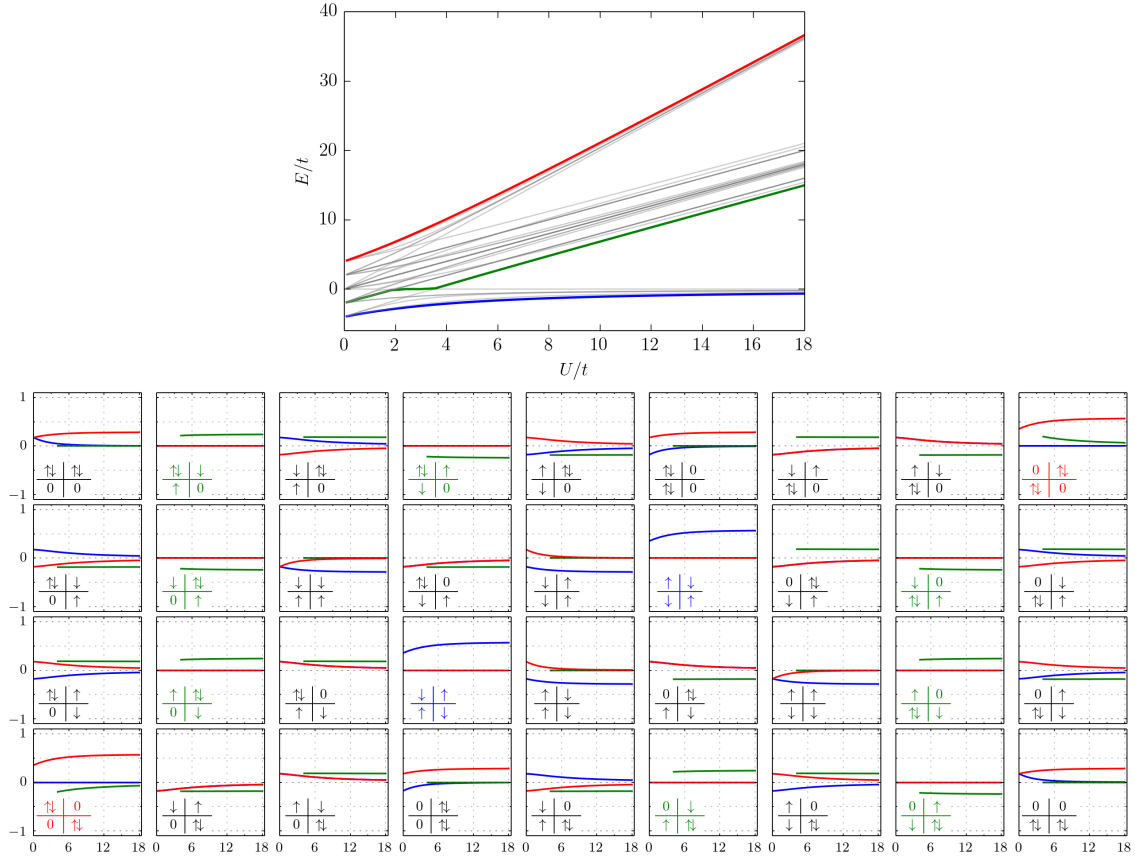


Figure 3.3: Energy eigenvalues and eigenstates for a 4-site plaquette. In the top panel we show the energy eigenvalues for all of the 36 different eigenstates. We highlight the ground state (blue), the first state above the Mott-Hubbard gap (green) and the highest energy state (red). In the lower panels we show the projections of each of the three highlighted states onto the basis states. Each panel corresponds to a basis state as indicated by the diagram on the lower left corner of the panels. We have colored the state labels indicating which states have the largest contribution to the eigenstates.

which can be readily diagonalized numerically. The results for the eigenvalues and the coefficients of three of the eigenvectors are shown in Fig. 3.3.

In the 4-site plaquette, the largest contribution to the ground state comes from states

$$\left| \frac{\downarrow\uparrow}{\uparrow\downarrow} \right\rangle = a_{1\downarrow}^\dagger a_{2\uparrow}^\dagger a_{3\uparrow}^\dagger a_{4\downarrow}^\dagger |0\rangle \quad \text{and} \quad \left| \frac{\uparrow\downarrow}{\downarrow\uparrow} \right\rangle = a_{1\uparrow}^\dagger a_{2\downarrow}^\dagger a_{3\downarrow}^\dagger a_{4\uparrow}^\dagger |0\rangle \quad (3.19)$$

where we have used the numbering convention $\frac{1|2}{3|4}$ to label the lattice sites.

There is something very important to notice in this case, though. Going back to the 2×1 lattice we saw there was a minus sign between the two antiferromagnetic configurations. In

this case, if we examine the panels in Fig. 3.3 we notice that the ground state has the largest contributions from the antiferromagnetic configurations, and that both configurations show up with the same sign:

$$|\phi_a\rangle = a_{1\downarrow}^\dagger a_{2\uparrow}^\dagger a_{3\uparrow}^\dagger a_{4\downarrow}^\dagger |0\rangle \quad |\phi_b\rangle = a_{1\uparrow}^\dagger a_{2\downarrow}^\dagger a_{3\downarrow}^\dagger a_{4\uparrow}^\dagger |0\rangle \quad (3.20)$$

As we will show, this is a consequence of the *d*-wave character of the ground state of the 4-site plaquette at half filling.

The problem of a 4-site plaquette lattice should evidently be invariant to 90 degree rotations of the system about the vector normal to the lattice plane. Four of such rotations bring the system back to the same spot, so there is an operator \hat{U} , such that $\hat{U}^4 = \mathbb{1}$. The eigenvalues of \hat{U} must therefore be $1, -1, i, -i$, each of these eigenvalues corresponding to a different orbital symmetry. We give an expression for \hat{U} in terms of operators that permute fermions [82]:

$$\hat{U} = \prod_{\sigma=\downarrow,\uparrow} K_{12\sigma} K_{24\sigma} K_{43\sigma} \quad (3.21)$$

The K operators, which permute fermions between two sites act as shown in the following example:

$$K_{43\uparrow} \left| \begin{array}{c} \uparrow \\ \downarrow \end{array} \middle| \begin{array}{c} \uparrow \\ \downarrow \end{array} \right\rangle = - \left| \begin{array}{c} \uparrow \\ \downarrow \end{array} \middle| \begin{array}{c} \uparrow \\ 0 \end{array} \right\rangle \quad (3.22)$$

$$K_{24\uparrow} K_{43\uparrow} \left| \begin{array}{c} \uparrow \\ \downarrow \end{array} \middle| \begin{array}{c} \uparrow \\ \downarrow \end{array} \right\rangle = + \left| \begin{array}{c} \uparrow \\ \downarrow \end{array} \middle| \begin{array}{c} \downarrow \\ \uparrow \end{array} \right\rangle \quad (3.23)$$

$$K_{12\uparrow} K_{24\uparrow} K_{43\uparrow} \left| \begin{array}{c} \uparrow \\ \downarrow \end{array} \middle| \begin{array}{c} \uparrow \\ \downarrow \end{array} \right\rangle = - \left| \begin{array}{c} 0 \\ \downarrow \end{array} \middle| \begin{array}{c} \uparrow \\ \uparrow \end{array} \right\rangle \quad (3.24)$$

$$(3.25)$$

It is seen that the combination $K_{12\uparrow} K_{24\uparrow} K_{43\uparrow}$ rotates all spin ups clockwise, which motivates the definition in Eq. 3.21: first rotate the \downarrow spins and then rotate the \uparrow spins to effect a full rotation. A formal expression for $K_{ij\sigma}$ is given by

$$K_{ij\sigma} = 1 - a_{i\sigma}^\dagger a_{i\sigma} - a_{j\sigma}^\dagger a_{j\sigma} + a_{i\sigma}^\dagger a_{j\sigma} + a_{j\sigma}^\dagger a_{i\sigma} \quad (3.26)$$

With the exact form for the 90 degree rotation operator in hand, we can go ahead and apply it to the antiferromagnetic states of the 4-site plaquette to obtain

$$\hat{U}|\phi_a\rangle = -|\phi_a\rangle \quad \hat{U}|\phi_b\rangle = -|\phi_b\rangle, \quad (3.27)$$

thus proving the *d*-wave character of these states. The full ground state of the 4-site plaquette also has some contributions from states with double-occupancies and some smaller contributions from non-AFM configurations. A complete analytical expression for the ground state, and all eigenstates in the 4-site plaquette can be found in [83]. It can then be verified that the exact ground state is an eigenstate of \hat{U} with eigenvalue -1, and thus a *d*-wave state [83].

4-site plaquette: the connection between the Hubbard model and *d*-wave superconductors

The present understanding of cuprate superconductors generally accepts a few facts [84]:

- Cooper pairing is responsible for superconductivity.
- Cooper pairs are singlet pairs with $d_{x^2-y^2}$ symmetry.
- Pairing occurs within the copper oxide CuO_2 planes (these planes are a common trait of all cuprate materials).
- Superconductivity occurs for a moderate amount of hole or electron doping on a parent compound that is an antiferromagnetic Mott insulator.

The fact that the pairs are singlet forces their spatial wavefunction to have even parity. This, and the symmetry of the underlying CuO_2 square lattice, constrains the possible orbital symmetry of the spatial part of the wavefunction. Experiments with Josephson junctions formed by two superconductors have established the $d_{x^2-y^2}$ character of the spatial part of the pair wave function [85, 86].

The simple model of a 4-site plaquette, which we saw has an antiferromagnetic ground state with a *d*-wave orbital symmetry serves to motivate the postulate that the Hubbard model is a very plausible model for the high- T_c cuprates, as we will explain below. Considering doping on the 4-site plaquette, we can obtain the solutions at quarter-filling, with only two electrons in the plaquette. Using exact diagonalization to obtain the ground state, or looking it up the analytical solution tables [83], we find that the ground state in this case, $|\psi_{0,2}\rangle$ is an *s*-state, which obeys

$$\hat{U}|\psi_{0,2}\rangle = +|\psi_{0,2}\rangle \quad (3.28)$$

If we start out with a system of 4 particles in a plaquette, which has a *d*-state antiferromagnetic ground state, $|\psi_{0,4}\rangle$, and want to create a pair of holes, then the hole-pair creation operator, $\hat{\Delta}$ must satisfy

$$\langle\psi_{0,2}|\hat{\Delta}|\psi_{0,4}\rangle \neq 0 \quad (3.29)$$

In other words the pairing operator must have a *d*-wave orbital symmetry, to satisfy orbital angular momentum selection rules. The orbital symmetry of the pair creation operator in a 4-site plaquette is thus consistent with the orbital symmetries of pairing observed in the high- T_c cuprates. This argument, which uses the orbital symmetry of the hole-pair in a 4-site plaquette to motivate the role of the Hubbard model in high- T_c superconductivity, was first presented in [87].

Another glimpse at the importance of an antiferromagnetic background for high- T_c superconductivity can be obtained by considering the energy of a pair of holes in an antiferromagnetic background. Consider the situation shown in Fig. 3.4, with one pair of holes. The figure illustrates that the energy cost of hopping, for a pair of holes, can be limited if the hopping is correlated (the energy cost is then proportional to the separation between holes). Since hopping reduces the energy by delocalizing the holes, then it is possible for the ground state of the system to be related to these correlated hole-pairs.

The arguments shown so far, regarding the symmetry of the ground states in a 4-site plaquette, and the effective attraction (or correlation) between holes in an antiferromagnetic

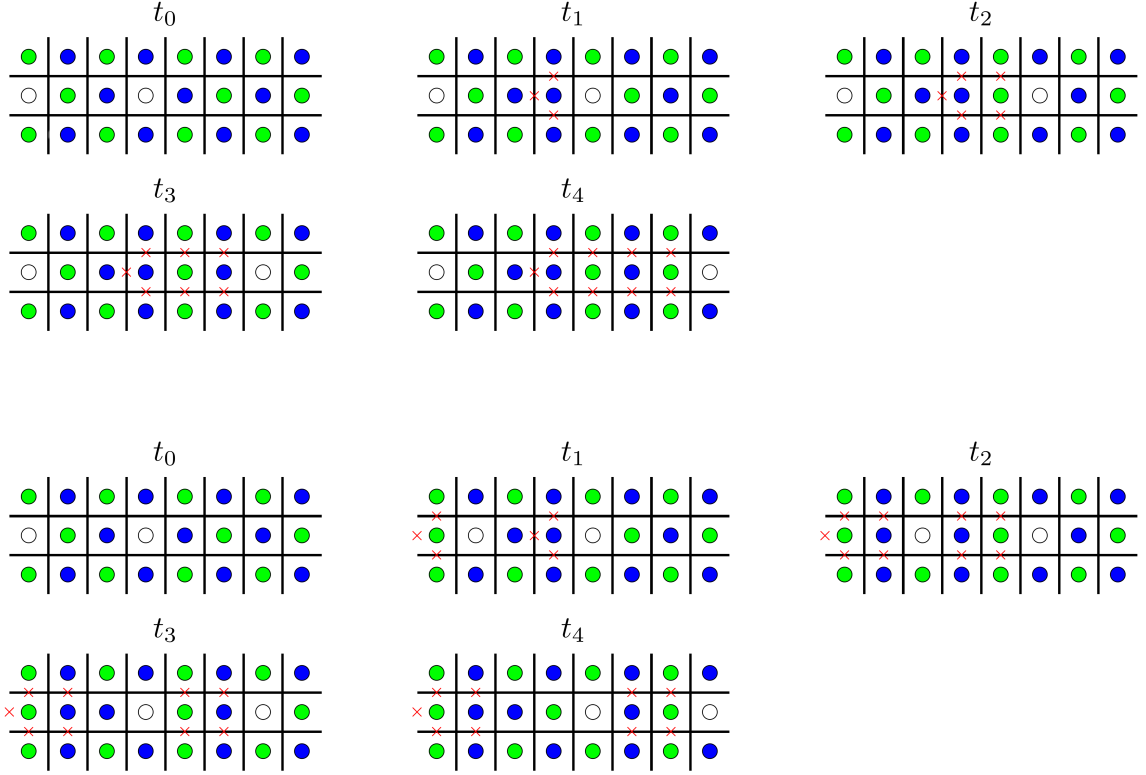


Figure 3.4: Energy consideration for a pair of holes hopping in an antiferromagnetic background. Spins up and down are represented as green and blue circles, holes are represented as empty circles, and broken antiferromagnetic (AF) bonds are shown as red crosses. In the top series, every time the hole tunnels to an adjacent site it breaks more AF bonds, which cost an energy $\approx -4t^2/U$ per bond. As the hole continues to hop, the total energy cost will be proportional to the number of sites it has traveled. In the bottom series, hopping is correlated for the two holes; they hop together in the same direction. In this case, the energy cost of hopping will be proportional to the separation between holes, and it will not continue to grow as the holes move along further. One can see that the number of broken bonds is the same in going from t_3 to t_4 . In the hole-doped antiferromagnet, if the kinetic energy decrease from hole delocalization (tunneling) exceeds the cost of the broken AF bonds, an insulating state may be able to lower its energy via the formation of hole-pairs,

background, signal the close relationship between antiferromagnetism and superconductivity. To balance out the perspective on this highly debated issue, we point out that in the phase diagram of high- T_c cuprates the phase transition does not occur directly from an AFM phase to a superconducting phase (the system must go through the pseudo-gap regime as hole-doping is increased). So if there is an AFM background in high temperature superconductors, it may be of a different nature than the Mott insulator type of AFM state which arises naturally in the Hubbard model.

We hope that the simplified treatments of the Hubbard model presented so far illustrate the richness of behaviors that emerge from it. We have seen the appearance of the Mott-Hubbard gap both in a single site, a double well, and a 4-site plaquette. In the plaquette scenario we motivated the role of the Hubbard model as one of the strongest candidates to describe the physics of *d*-wave superconductivity in the cuprates.

3.5 High-temperature series expansion

After exploring a few of the properties of the Hubbard model with overly simplified approaches, we now turn to a method that will prove very useful in comparing with experimental measurements. The high-temperature series expansion (HTSE) deals with tunneling as a perturbation on the on-site interactions, and is thus the natural next step beyond the single site treatment.

The partition function for the system is expanded as a series in the small parameter t/T . Clearly, this approach will work down to temperatures that approach the tunneling rate, $T \gtrsim t$. We will see that this limits its applicability to the calculation of thermodynamic quantities that involve the charge degree of freedom, i.e. the density, double-occupancy, and their derivatives. The spin degree of freedom becomes relevant only at temperatures below the antiferromagnetic exchange energy, which is much lower than t .

We start by writing down the Hubbard Hamiltonian as

$$\begin{aligned} H &= \left(U \sum_i n_{i\uparrow} n_{i\downarrow} - \mu \sum_i (n_{i\uparrow} + n_{i\downarrow}) \right) - t \sum_{\langle ij \rangle, \sigma} a_{i\sigma}^\dagger a_{j\sigma} \\ &= H_0 + H_1 \end{aligned} \tag{3.30}$$

We have already seen (in our treatment of the single-site model) that the partition function for the unperturbed part, $Z_0 = \text{Tr} e^{-\beta H_0}$, factorizes as $Z_0 = z_0^k$, for a system with k sites. The single site partition function is easy to calculate because the trace runs over the only four possible states in a single site $\{|0\rangle, |\uparrow\rangle, |\downarrow\rangle, |\uparrow\downarrow\rangle\}$.

$$z_0 = 1 + 2e^{\beta\mu} + e^{\beta(2\mu-U)} = 1 + 2z + z^2 u \tag{3.31}$$

where we have defined $z = e^{\beta\mu}$ and $u = e^{-\beta U}$

For the full Hamiltonian, the grand canonical partition function Z can be expanded in a perturbation series [88, 89]

$$\begin{aligned} Z &= \text{Tr}e^{-\beta H} \\ &= Z_0 \left[1 + \sum_{n=1}^{\infty} (-1)^n \int_0^{\beta} d\tau_1 \int_0^{\tau_1} d\tau_2 \cdots \int_0^{\tau_{n-1}} d\tau_n \langle \tilde{H}_1(\tau_1) \tilde{H}_1(\tau_2) \cdots \tilde{H}_1(\tau_n) \rangle \right] \end{aligned} \quad (3.32)$$

where the thermal expectation value inside the integrals is taken with the unperturbed part of the Hamiltonian

$$\langle A \rangle = \text{Tr}(e^{\beta H_0} A) / Z_0, \quad (3.33)$$

and the tilde means that the operator is evaluated in the interaction picture for the imaginary time in parenthesis:

$$\tilde{H}_1(\tau) = e^{\tau H_0} H_1 e^{-\tau H_0} \quad (3.34)$$

Given the series expansion for Z , the grand potential is

$$-\beta\Omega = Z_0 + \sum_{n=1}^{\infty} (-1)^n \int_0^{\beta} d\tau_1 \int_0^{\tau_1} d\tau_2 \cdots \int_0^{\tau_{n-1}} d\tau_n \langle \tilde{H}_1(\tau_1) \tilde{H}_1(\tau_2) \cdots \tilde{H}_1(\tau_n) \rangle \quad (3.35)$$

One can see that the n^{th} term in the expansion has n copies of the tunneling part of the Hamiltonian. In the thermal average, each application of H_1 results in a particle tunneling to a neighboring site. We see that there will be a contribution to the expansion only if after n tunneling events all the particles come back to their original sites. A direct consequence of this is that the first order term in the expansion vanishes (you cannot recover the same lattice configuration after a single tunneling event). The second order in the expansion corresponds to particles tunneling one site over and then coming back. Higher order terms can be represented by diagrams, to make them easier to keep track off. The contribution from orders up to $n = 9$ is shown in [89]. Here we will use up to the second order term to illustrate the phases that appear in the system.

The grand potential to second order is [89, 70]

$$-\beta\Omega_2 = k \ln z_0 + k \left(\frac{\beta t}{z_0} \right)^2 m \left(z + z^3 u + 2z^2 \frac{1-u}{\beta U} \right) \quad (3.36)$$

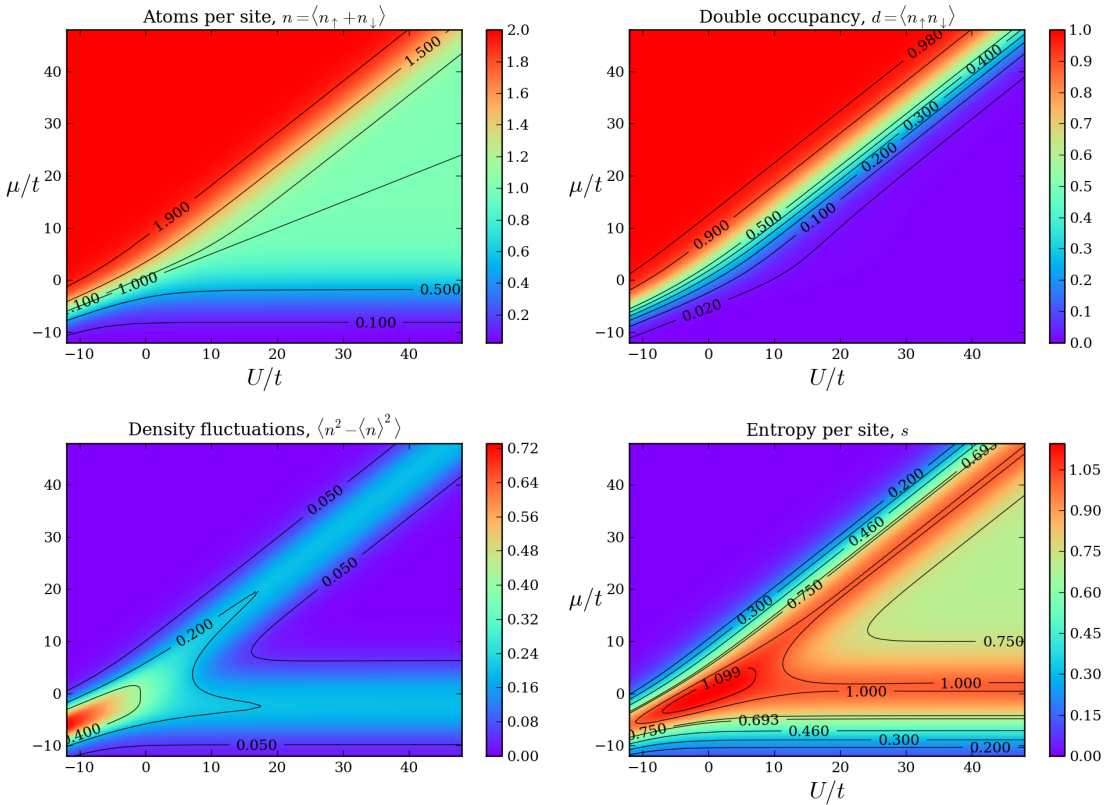


Figure 3.5: HTSE state diagram of the Fermi-Hubbard model calculated up to second order in the perturbation series.

where m is the number of nearest neighbors for each lattice site, which in the simple cubic case is $m = 6$. We see that the grand potential is proportional to the number of lattice sites, so we will obtain all the thermodynamic quantities per lattice site.

From the grand potential to second order we can calculate a state diagram for the Hubbard model. In Fig. 3.5, the results are shown at a temperature $T = 2.5t$. Constant T/t cuts are shown for different temperatures in Fig. 3.6.

From the figures, we see that the HTSE up to second order exhibit the main features of the Mott insulating regime:

- The density as function of chemical potential has a plateau at $n = 1$ centered around $\mu = U/2$, Fig. 3.6a.

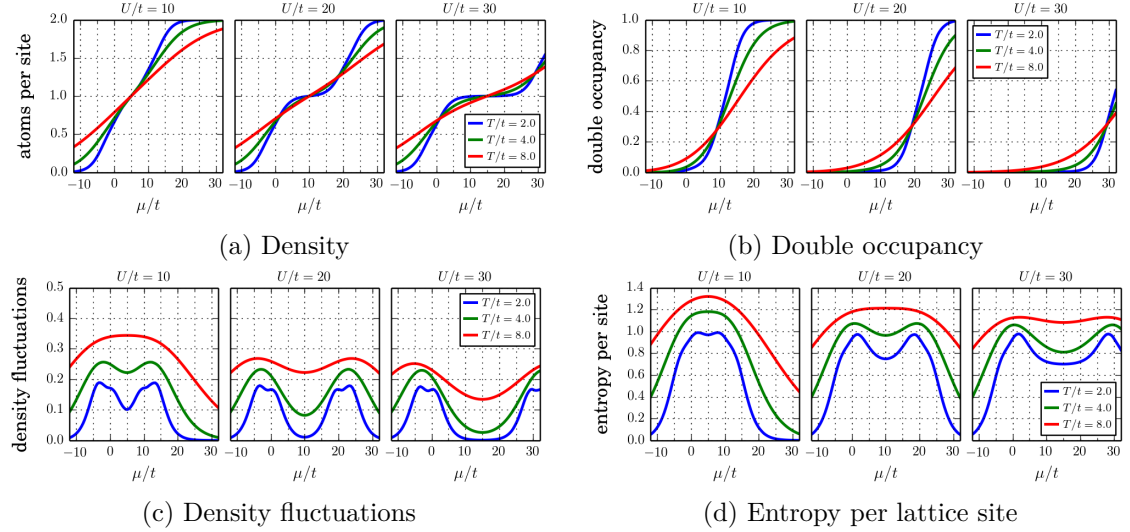


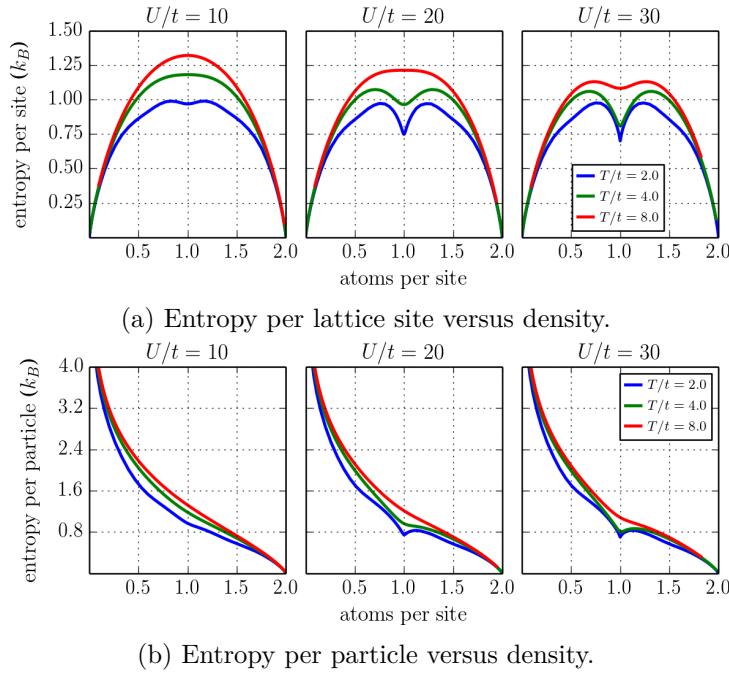
Figure 3.6: Thermodynamic quantities as a function of chemical potential calculated using the HTSE.

- At $n = 1$ the double occupancy is suppressed for lower temperatures, Fig. 3.6b.
- At $n = 1$ the density fluctuations are suppressed, Fig. 3.6c.
- At $n = 1$ the entropy per site is lowered, Fig. 3.6d.

For very large values of U/t , where at $T = 2.5t$ we have $T \ll U$, the system is deep in the Mott insulator regime. The system has exactly one atom per site, and the only remaining entropy is the spin entropy. With two spin states available per lattice site, the entropy per lattice site is $s = \ln 2 \approx 0.7$, as can be seen in the third panel of Fig. 3.6d.

We can also plot the HTSE result for the entropy as a function of density, as shown in Fig. 3.7a. Dividing the entropy per lattice site by the density, we obtain the entropy per particle, shown in Fig. 3.7b. The entropy per particle rises significantly at lower densities, which indicates the large entropy capacity of the metallic phase.

In a finite trapped system which inevitably has a shell with density $n < 1$, a large part of the total entropy of the system is carried by particles in the low density shell. This **entropy redistribution** allows the core to be at an effectively lower entropy per particle. The core can then locally access lower entropy phases, such as the AFM state, even if the



overall value of the entropy per particle is larger than the Néel entropy for a homogeneous system¹. We will elaborate more on this later on when we describe our trapping potential.

3.6 Local density approximation

The results presented above consider a homogeneous lattice potential. In experiments with ultracold atoms, a confining potential is a necessity since the samples created have a finite number of atoms. The presence of an inhomogeneous overall trapping potential presents a major challenge when comparing the results of experiment to theory. A useful technique, which works for systems without long range correlations, is the local density approximation (LDA). In the LDA, we consider each point in the potential as an homogeneous system and we set the condition that all of these local homogeneous systems are in thermal equilibrium with each other at some temperature T . If the trapping potential is properly characterized, at each point we can obtain a local value of the lattice depth, which along with the scattering length (set for the whole system via a Feshbach resonance),

¹ For the homogeneous system the Néel entropy per particle (at which the Mott insulator becomes AFM ordered) is $s_{\text{Néel}} = 0.4k_B$

determines the local values of the Hubbard parameters t and U . With the Hubbard parameters in hand, we can use a known solution to the homogeneous Hubbard model and obtain local values for the thermodynamic quantities, such as density, double occupancy, entropy, etc. We can then plot the local thermodynamic quantities as a function of trap position to obtain trap profiles. Alternatively, one can also integrate the results of the LDA over the trap and compare them to bulk measurements.

The validity of the LDA in lattice systems has been addressed before [90–92], proving that it yields very good agreement with exact calculations of the trap for quantities such as density profiles and momentum distributions and only slight discrepancies with quantities like the spectral function of the many-body excitations. In the work carried out for this thesis, all the comparisons with theory were done within the framework of the LDA.

3.7 Latest developments in numerical techniques

When performing the LDA one needs to have available a set of results for a homogeneous model with data available at low enough temperatures to match those of the experiment. In our experiment the temperature can be as low as $T/t \approx 0.4$ locally, just above T_N and so we need to make use of the latest developments in numerical techniques to access this regime. The hope is that one day ultracold atoms will greatly exceed the capabilities of numerical calculations, such that open questions like that of d -wave superconductivity in the Hubbard model can be put to rest.

Going down to temperatures comparable to the tunneling rate ($T < t$), analytical methods such as the HTSE up to second order fall short in their ability to describe the thermodynamics of the Hubbard model. Below these temperatures a variety of more sophisticated approaches has been used in the literature. Below we provide a non-exhaustive list of the main methods that have been applied to ultracold atoms in optical lattices:

- **DMFT.** Dynamical mean field theory. It considers a single site of the lattice, $H_1 =$

$Un_{\uparrow}n_{\downarrow} - \mu(n_{\uparrow} + n_{\downarrow})$, immersed in a bath of non-interacting electrons which represents the rest of the system. The interaction between the bath and the impurity is mapped onto what is referred to as a single-impurity Anderson model. The resulting impurity model is solved with a self-consistency condition, i.e. the resulting dynamics of the bath must be consistent with the dynamics of the impurity since, after all, the bath is made of a bunch of other sites, just like the one under consideration. Of course, this is easier said than done; nevertheless, the problem reduces to solving the problem for a single-impurity. There are several techniques available for that task. Ref. [91] uses the numerical renormalization group (NRG), for example.

- **DCA.** Dynamical cluster approximation. This is an extension of DMFT, where the impurity is not a single site but a cluster of sites. As the number of sites in the cluster, N_c goes to infinity one should recover the exact solution, and for $N_c = 1$ the method reduces to DMFT. The DCA was used to calculate the thermodynamics of the Fermi-Hubbard in a 3D lattice in Ref. [55].
- **DQMC.** Determinantal quantum Monte Carlo. In general, the Monte Carlo method reduces the calculation of the full quantum partition function as a sum over all possible configurations in some product space basis set (where the basis states are products of single particle states). In DQMC [93, 94], an exact simplification is used where the partition function is reduced to a sum over the determinant of the Hamiltonian matrix (in the chosen basis). So the name “determinantal” QMC. This simplification holds if the Hamiltonian is quadratic. The on-site interaction term in the Hubbard model is quartic instead of quadratic, but there is a way to handle this using what is called a Hubbard-Stratonovich transformation. A problem with applying this method to fermions is that the determinant of the resulting matrices can be negative sometimes, which affects the convergence of the Monte Carlo evaluation of the sum. This is known as the sign problem, it can be avoided completely for calculations at half-filling ($\mu = U/2$) and it is not so significant for small values of U at arbitrary filling. However, for large values of $U \gtrsim 12$ it prevents calculations for values of $T/t \lesssim 1$.

- **NLCE.** Numerical linked-cluster expansion. The NLCE is a series expansion in powers of t/T , which reminds one of the HTSE. In the HTSE, different contributions are grouped solely by the power of t/T , whereas in the NLCE clusters of sites are exactly diagonalized (numerically) and added to the series according to a weight that can be obtained by considering all possible subclusters in the cluster [95]. The region of convergence of the NLCE can be extended for $T/t < 1$ via numerical resummations [96], although results for $T/t < 0.8$ in a 3D lattice can get rather noisy, as we will see.

As part of this thesis we have closely collaborated with the following condensed matter theorists:

- Thereza Paiva at Universidade Federale de Rio de Janeiro
- Ehsan Khatami at San Jose State University
- Richard Scalettar at UC Davis
- David Huse at Princeton University
- Nandini Trivedi at Ohio State University

Our collaborators are experts in the use of DQMC and NLCE and so all of the modeling of our experimental results is restricted to these two techniques.

4. Overview of the experimental setup

In this chapter we will give a brief description of the experimental setup used for this thesis. The idea is to make the reader familiar with the experimental steps required to produce an ultracold Fermi gas and the different systems associated with each step, before explaining concepts in more detail in later chapters. We will assume familiarity with the use of light to cool and trap atoms [97–99], and with the use of magnetic fields to control the strength of the interactions between atoms [100].

For the non-expert, it will suffice to know that light that is near resonant to an atomic transition can result in dissipative forces, which can be used to reduce the velocity of atoms (cooling). Light detuned far from an atomic transition produces a conservative force, which changes the potential energy of an atom. If the far detuned light is detuned to the red of the atomic transition, atoms will be attracted to intensity maxima of the light field (trapping), whereas if the light is red detuned they will be repelled from the intensity maxima.

It takes about 15 seconds to produce a degenerate cloud of ${}^6\text{Li}$ atoms. It then takes only a few tens of milliseconds to load this cold sample into an optical lattice and perform a measurement on it. Measurements are destructive, so we must repeat the process over and over again. Most of the time in the lab is spent optimizing the setup and finding out the right way to carry out the experiments. Final data can then consist of only a few tens to a few hundred shots, depending on the statistics needed for the particular experiment.

In Fig. 4.1 we show a schematic of the vacuum system where the experiments are carried out. This will give the reader a spatial setting in which to visualize the descriptions given below. The experimental cycle proceeds in the following way:

1. A thermal beam of ${}^6\text{Li}$ atoms, which originates at the oven, is decelerated by the Zeeman slower and cooled transversally by the two-dimensional magneto-optical trap (2DMOT).
2. The magneto-optical trap (MOT) captures the slowed atoms at the center of the chamber, where they reach a temperature as low as $\approx 300 \mu\text{K}$.
3. We transfer the atoms from the MOT to a narrow linewidth magneto-optical trap, which operates on the ultraviolet $2S_{1/2} \rightarrow 3P_{3/2}$ transition (UVMOT). In the UVMOT the atoms are cooled down to $\approx 60 \mu\text{K}$.
4. We load a balanced mixture of atoms in the two lowest energy hyperfine states into a crossed-beam optical dipole trap (ODT)
5. Once in the ODT, a magnetic field is used to control the scattering cross section between atoms in the two different hyperfine states, via a magnetic Feshbach resonance [101]. Setting a large scattering cross section allows efficient evaporative cooling to quantum degeneracy. Cooling is forced by reducing the depth of the optical potential.
6. As the power in the ODT is reduced for evaporation, the atoms are left in a dimple trap, which was ramped up prior to the start of evaporation. The dimple trap is the starting point in all of our experiments.
7. At this point, the trapping potential is slowly transformed into an optical lattice potential, where the Hubbard model is realized. We then proceed to measure the properties of the system.

In the following sections we briefly describe the different systems involved in the realization of the experimental cycle.

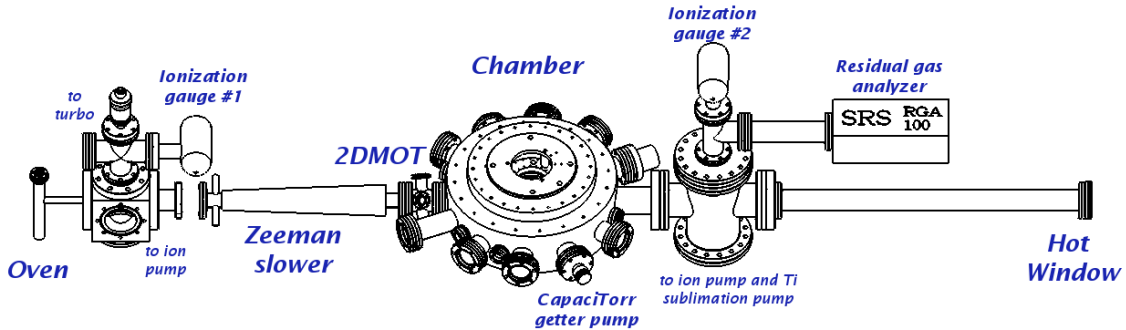


Figure 4.1: Main components of the vacuum system.

4.1 Vacuum system

During operation, the oven section of the vacuum system (see Fig. 4.1) is heated to 450°C to produce a collimated beam of lithium atoms. The Zeeman slower (described later in Sec. 4.2.2) is constructed with a narrow tube and provides a low conductance (0.5 L/s) that can help maintain up to a factor of 10 pressure differential between the oven and the main chamber sections. The pressure¹ in the oven section is 4×10^{-9} Torr, and in the chamber section² is 5×10^{-10} Torr.

Lithium atoms that are not captured by the MOT eventually hit a sapphire window at the far end of the setup, which we refer to as the ‘hot window’ because it is heated up to around 290°C to avoid coating it with the lithium metal. The long tube between the chamber and the hot window serves a differential pumping purpose; the tube inside is lined with a helical strip of non-evaporable getter material³.

The vacuum is maintained by two ion pumps and a non-evaporable getter pump. A Vacion Plus Starcell (150 L/s) from Varian vacuum technologies is connected to the cross between the chamber and the hot window sections. A titanium sublimation cartridge is attached to this pump. A smaller Vacion Plus Starcell (55 L/s) is connected to the cube on

¹Measured with Bayard-Alpert type ionization gauge (Varian Type 571) labeled #1 in Fig. 4.1

²Measured with ion gauge #2

³SAES St 707/CTAM/30D, 30 mm wide strip.

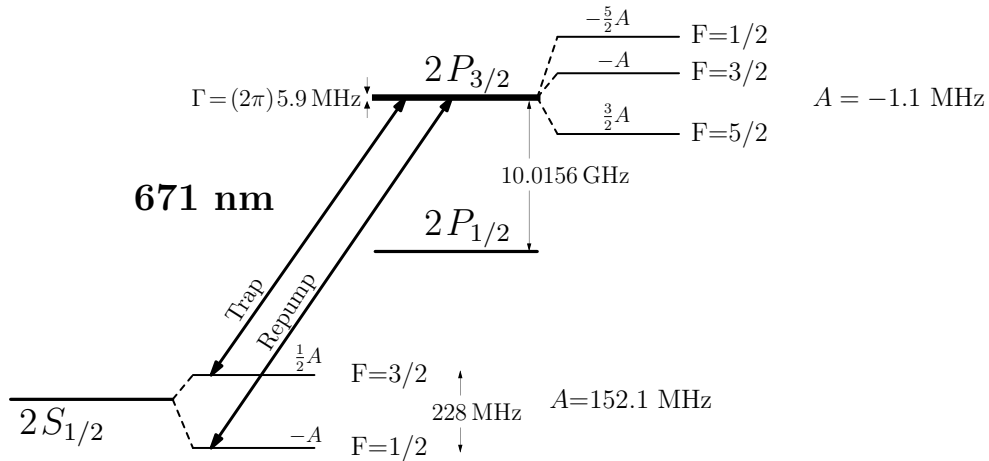


Figure 4.2: Energy level diagram showing transitions relevant for laser cooling ^6Li using the $2S_{1/2} \rightarrow 2P_{3/2}$ transition.

the oven section. A CapaciTorr B200 getter pump (90 L/s for H_2) is attached directly to one of the chamber viewports. Due to the close proximity of this getter pump to the atoms (8 cm) we expect the background pressure to be lower in the center of the chamber than the 5×10^{-10} Torr measured with ion gauge #2.

4.2 671 nm laser cooling system

For the Zeeman slower, 2DMOT and MOT we perform laser cooling using the $2S_{1/2} \rightarrow 2P_{3/2}$ transition in ^6Li (see level diagram in Fig. 4.2) which has a wavelength of 671 nm. The light is produced in a separate optical table and transferred to the apparatus table via optical fibers. In this section we give a description of the different parts of the 671 nm laser cooling system.

4.2.1 Laser system

Efficient laser cooling relies on continuous scattering of photons by the atom. To avoid optical pumping to a dark hyperfine ground state we use two frequencies of light, tuned to the $2S_{1/2}, F=3/2$ and $2S_{1/2}, F=1/2$ states. We refer to these as trap and repump,

respectively, as shown in Fig. 4.2.

The laser system that is used to produce the trapping and repumping MOT light, as well as the Zeeman slower and imaging probe light, was described in detail in my Master's thesis [102]. We have two home-built extended cavity diode lasers, which we refer to as MOT Master and ZS Master. The MOT Master is stabilized to the $2S_{1/2}, F=3/2 \rightarrow 2P_{3/2}$ transition via saturated absorption spectroscopy and the ZS Master is offset locked (red detuned) to the MOT Master using the side-of-filter technique [103].

MOT Master

Light from the MOT Master is split up for producing the trap and repump frequencies; each path is passed through a double-pass acousto-optic modulator (AOM) and injection-locks a slave laser diode for amplification. The light from the trap and repump slaves is overlapped on a beamsplitter before injecting a tapered amplifier. The output from the tapered amplifier is fiber coupled to the apparatus table. After passing through an AOM and splitting ten percent of the light for the 2DMOT, we can get as much as 90 mW of power for the MOT. Due to the small splitting between trap and repump frequencies, 22 mW of light are produced by the tapered amplifier in unwanted sidebands at $f_{\text{trap}} - 228 \text{ MHz}$ and $f_{\text{repump}} + 228 \text{ MHz}$ [104]. This results in a net 53 mW of trapping light and 16 mW of repumping light that are dedicated to the MOT.

ZS Master

Light from the ZS Master is split up into two paths. The first path is used as the probe light in Bragg scattering experiments. It is passed through AOMs for power control and switching purposes and coupled into an optical fiber. Approximately 5 mW are available for the experiment at the output end. The second path is used to inject a slave laser diode for amplification. The output of the slave passes through an AOM, which selects whether

the light is used for Zeeman slowing or imaging. The zeroth order of the AOM is used for Zeeman slowing and the 1st order is used as the imaging probe. Approximately 30 mW (20 mW) of light are available for Zeeman slowing (imaging) after the light is coupled into an optical fiber.

4.2.2 Zeeman slower

The Zeeman slower reduces the speed of atoms coming out of the oven to less than the capture velocity of our MOT, $v_c \simeq 5\Gamma/k = 20$ m/s, where 5Γ is the red detuning from resonance at which we operate the MOT during loading. The Zeeman slower works by using red detuned laser light propagating opposite to the lithium atomic beam. Due to the Doppler shift, the laser light is resonant with atoms coming out of the oven, and via repeated photon scattering can produce a maximum deceleration given by $a_{\max} = \frac{\hbar\Gamma}{2\lambda m}$. As the atoms get slowed they shift out of resonance, but the spatially dependent magnetic field of the Zeeman slower shifts the transition to the red keeping the atoms resonant with the light as they travel through the slower.

The Zeeman slower operates on the σ^- transition between the $2S_{1/2}, m_J=-1/2$ and $2P_{3/2}, m_J=-3/2$ levels, shown in red in Fig. 4.3. An advantage of choosing this transition is that it is a cycling transition even at moderate magnetic fields. This eliminates the need for using repumping light in the Zeeman slower. We use a detuning⁴ of 1540 MHz, and a magnetic field profile given by

$$B_z = B_0(1 - \sqrt{1 - z/L})$$

where $B_0 \approx 800$ G and $L = 34.5$ cm.

⁴This detuning is measured with respect to the $F=1/2$ state. Since the lock is referenced to the $F=3/2$ state, the reading on the frequency counter of the offset lock is $1540 - 228 = 1312$ MHz.

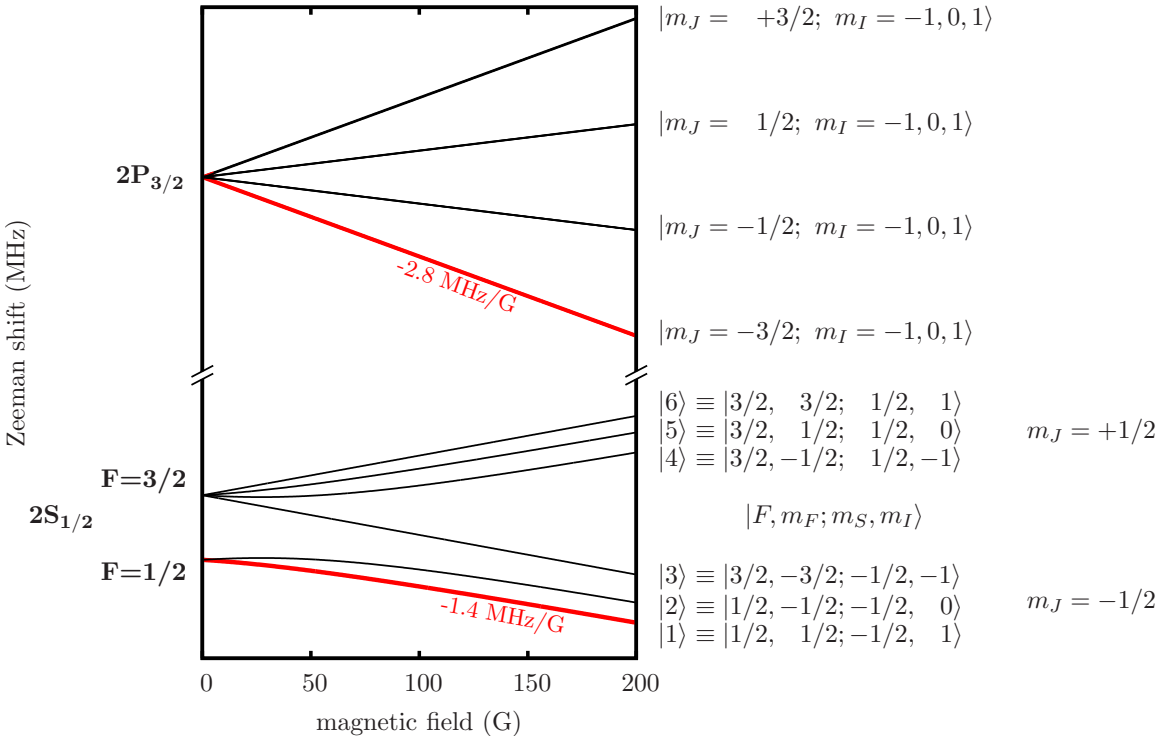


Figure 4.3: Energy level diagram of ${}^6\text{Li}$ in a magnetic field. The red lines show the levels used in the Zeeman slower.

4.2.3 2DMOT and MOT

The 671 nm MOT is loaded from a Zeeman slower plus a 2DMOT. The 2DMOT is at the output of the Zeeman slower and helps collimate the slow thermal beam of atoms before it reaches the MOT. The 2DMOT consists of a quadrupole field with two pairs of counter-propagating beams which lie on a plane almost normal to the direction of propagation of the atomic beam. In our setup, the atomic beam is offset from the center of the chamber by $\approx 1\text{ cm}$, and the angle of the 2DMOT is such that the slowed atoms from the Zeeman slower will be redirected towards the MOT, located at the center of the chamber (see Fig. 4.4).

In 5 s we load 1.4×10^9 atoms in the MOT at a temperature of $\approx 780\text{ }\mu\text{K}$. After loading, we shutter the Zeeman slower laser using a hard disk drive shutter [105]. At this point we proceed to cool and compress the 671 nm MOT by reducing the intensity and detuning of the cooling and repumping light, and increasing the magnetic field gradient to the

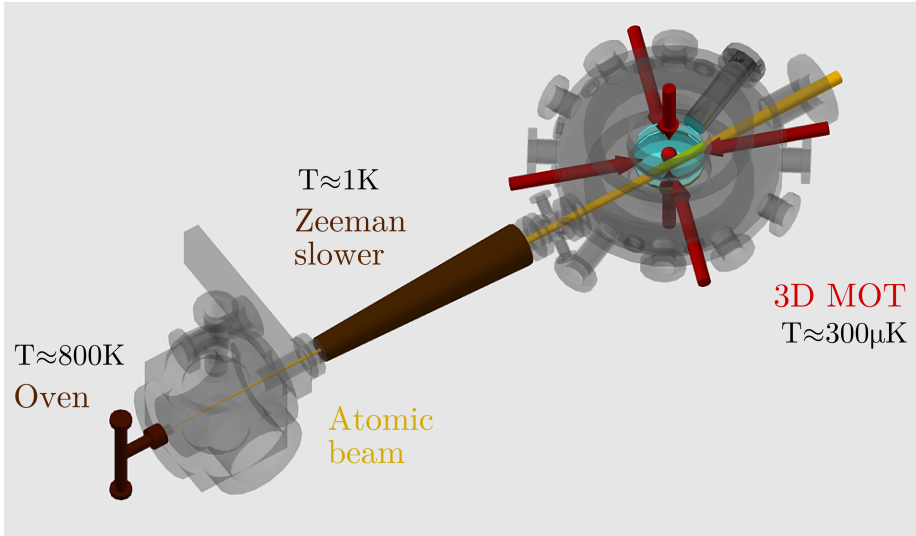


Figure 4.4: Schematic of apparatus showing the oven, Zeeman slower and 3DMOT. The 2DMOT beams (not shown) enter the setup on the small 4-way cross located between the slower and the main chamber. Notice that the atomic beam is slightly offset from the center of the chamber.

	MOT	CMOT	unit
Trap intensity per beam	1.26	0.034	I_{sat}^{2P}
Trap detuning	-33	-12	MHz
Repump intensity per beam	0.36	0.007	I_{sat}^{2P}
Repump detuning	-25.2	-17	MHz
dB_z/dz	22.6	26.1	G/cm
Number	1.5	1	10^9
$1/e$ radius	0.22	0.18	cm
Peak density	2.39	3.40	10^{10} cm^{-3}
Temperature	783	288	μK
Phase space density	3.9×10^{-7}	2.5×10^{-6}	-

Table 4.1: Comparison between the settings used for loading the 671 nm MOT and the settings after cooling and compressing (CMOT). $I_{\text{sat}}^{2P} = 5.1 \text{ mW/cm}^2$ is the saturation intensity of the 671 nm transition. For cooling and compressing, first the field gradient is increased in 40 ms, then after a wait of 40 ms the intensity and detuning of the beams are ramped linearly to their final values in 1 ms. The phase space density is defined as $n_0 \lambda_T^3$ where n_0 is the peak density and $\lambda_T = \frac{\hbar}{(2\pi m k_B T)^{1/2}}$ is the thermal de Broglie wavelength.

values shown as CMOT on Table. 4.1. We take time-of-flight images of the MOT and the CMOT, and infer their temperatures by fitting the cloud sizes to a ballistic expansion as shown in Fig. 4.5.

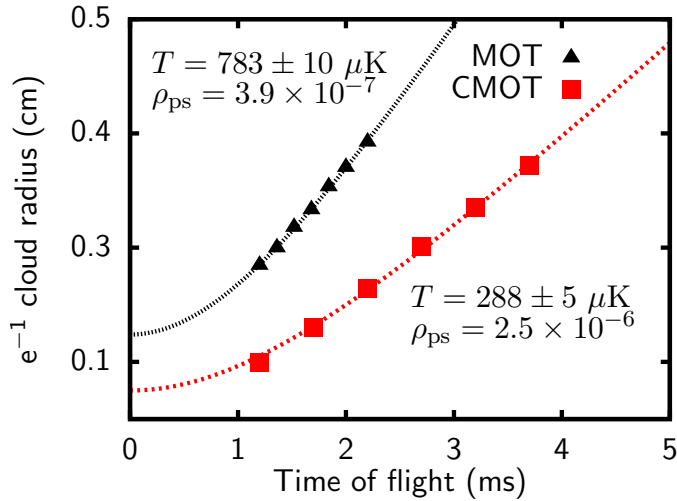


Figure 4.5: Time-of-flight expansion of atoms released from the 671 nm MOT right after loading (black triangles) and after cooling and compressing (red squares). The points represent the $1/e$ width of Gaussian fits to the spatial profile of the freely expanding clouds. The lines are fits to ballistic expansions. ρ_{ps} stands for phase-space density.

4.3 323 nm laser cooling system

Atoms from the 671 nm MOT are transferred to the 323 nm UVMOT, where owing to the smaller Doppler temperature limit, lower temperatures can be achieved (see Fig. 4.6). The Doppler temperature limit, T_D , of laser cooling is set by the linewidth of the excited state. The $2S_{1/2} \rightarrow 3P_{3/2}$ transition being narrower than the $2S_{1/2} \rightarrow 2P_{3/2}$ allows for a lower value of T_D . Furthermore the wavelength of the transition being smaller results in a smaller optical scattering cross section, which enables reaching larger densities in the UVMOT, a feature that is favorable when loading the atoms into an optical dipole trap [106].

4.3.1 Laser system

The 323 nm laser system is much simpler than the 671 nm system. We use a commercial second harmonic generation (SHG) system from Toptica Photonics to generate the UV light. The frequency is stabilized via saturated absorption spectroscopy, and trapping and repumping frequencies are derived via using acousto-optic modulators. The 323 nm system

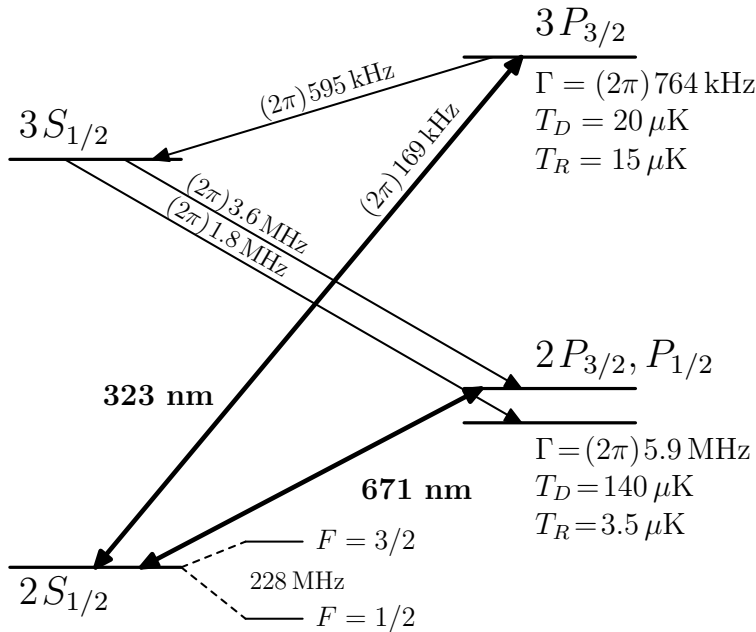


Figure 4.6: Lithium-6 energy level diagram. Lines in bold represent the transitions used to laser cool atoms. Lighter lines represent decay pathways from the excited $3P_{3/2}$ state; the decay rates are indicated along the associated paths. On the right side, beside each excited state we show its linewidth, the associated Doppler temperature limit (T_D), and the recoil temperature limit (T_R).

is on the same table as the vacuum system so we do not use optical fibers, the light is guided in free space using mirrors to the final UVMOT configuration. A schematic of the laser system is shown in Fig. 4.7.

4.3.2 UVMOT

To choose the waist of the UVMOT beams we had to take into consideration the available laser power and the transmission losses on the viewports of our apparatus, which are not anti-reflection coated at 323 nm. Figure 4.8 tabulates the losses at each viewport. We set up all the beams to have the same intensity at the atoms, thus carefully taking into account the losses at each window. This was accomplished by varying the angle of incidence on dielectric beamsplitters until the desired power ratios were achieved. Considering the losses at the windows and other UV optics, We set the beam waists of the UVMOT beams to 3.3 mm, which results in an intensity of $1.0I_{\text{sat}}^{3P}$ per beam at an SHG output power of

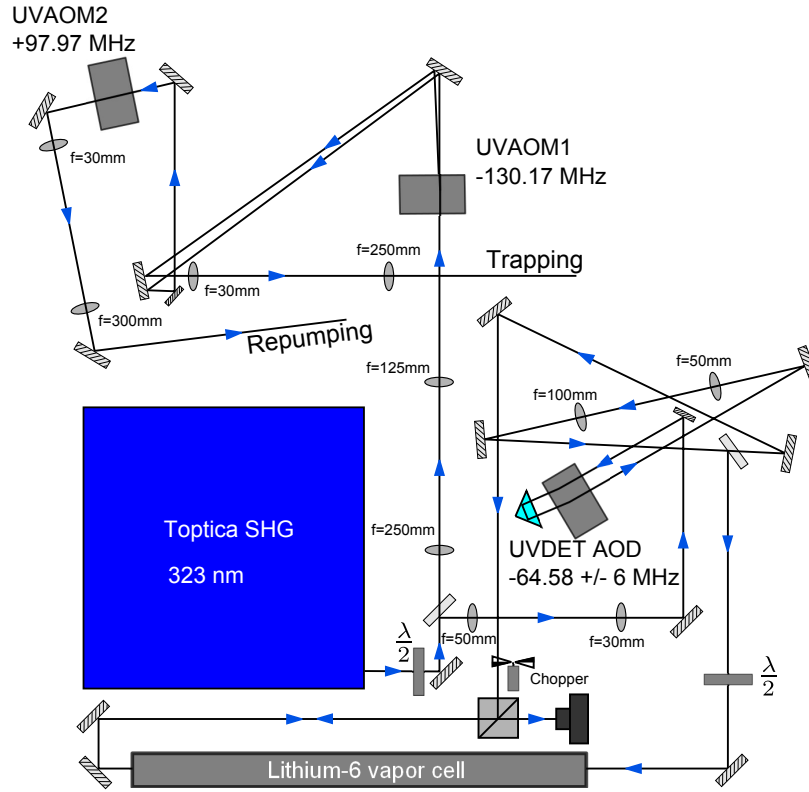


Figure 4.7: Schematic showing the optical setup for the 323 nm laser system. The frequency is stabilized using a saturated absorption spectroscopy setup [102]. The light that goes to the experiment is passed through an AOM (labeled UVAOM1), the first order is used for trapping and the zeroth order is sent to a second AOM (labeled UVAOM2) whose first order is used as the repump frequency. Trapping and repumping light are combined (not shown) and then split into six paths for the UVMOT.

27.4 mW. Here $I_{\text{sat}}^{3P} = 5.9\text{ mW/cm}^2$ is the saturation intensity of the 323 nm transition.

The UVMOT uses the same viewports as the 671 nm MOT. All six beams of both wavelengths are overlapped on dichroic mirrors that transmit 671 nm and reflect 323 nm. We were lucky to find a long-pass filter (Part Num. NT64-634) from Edmund Optics that, at very low cost per piece, provides > 99% reflection at 323 nm and > 99% transmission at 671 nm for both S and P polarizations at a 45° angle of incidence. The UVMOT and red MOT share an axis with the optical dipole trap (beams S and N on Fig. 4.8). After the 671 nm and 323 nm are combined, they are overlapped with the optical dipole trap (1070 nm) or optical lattice (1064 nm) light using a trichroic mirror (Custom made part from RMI Co.) that reflects IR and transmits 671 nm and 323 nm. The trichroic mirrors have a reflection

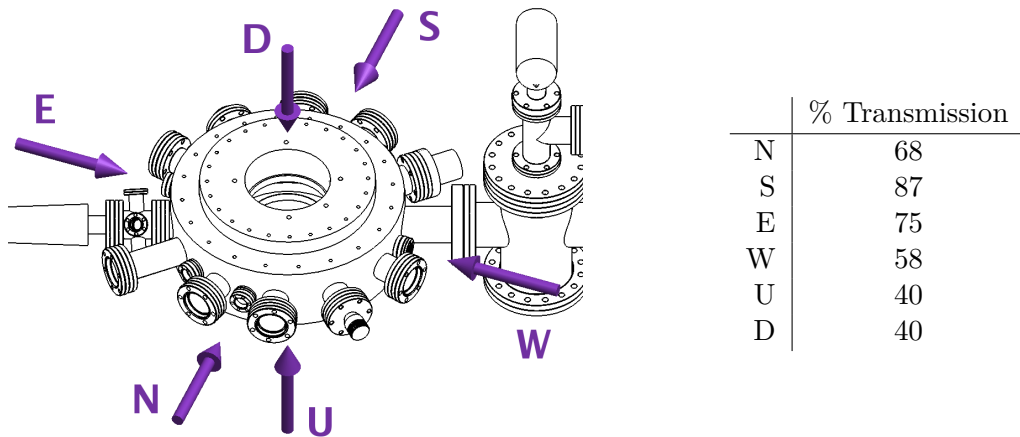


Figure 4.8: This figure shows the percentage transmission of the 323 nm light through the viewports on our vacuum chamber. For the side viewports the losses were accounted for by measuring the power reflected back by the window. For the top and bottom viewport it was harder to make this measurement due to restricted access, so the square root of the transmission through both windows is used.

coefficient $R > 99.5\%$ measured at 1064 nm and 1070 nm, and a transmission coefficient $T = 99\%$ at 671 nm and $T = 90\%$ at 323 nm, all measured at a 45° angle of incidence. Also the U and D beams of the UVMOT share an axis with the optical lattice (1064 nm and 532 nm). In this case a tetrachroic mirror (Lambda Research Optics) is used to overlap the wavelengths. This mirror satisfies $R_{532 \text{ nm}} \approx 0.92$, $R_{1064 \text{ nm}} \approx 0.99$, $T_{671 \text{ nm}} \approx 0.92$, and $T_{323 \text{ nm}} \approx 0.86$.

4.3.3 Transfer from MOT to UVMOT

The timing diagram for loading the UVMOT from the CMOT is shown in Fig. 4.9. The procedure consists of quickly reducing the magnetic field gradient and turning on the UV light at the same time as the 671 nm light is turned off. The magnetic field gradient is ramped back up slowly for compression. The UV detuning is constant throughout. The operating values of the UVMOT are shown in Table 4.2, and a measurement of the temperature is shown in Fig. 4.10.

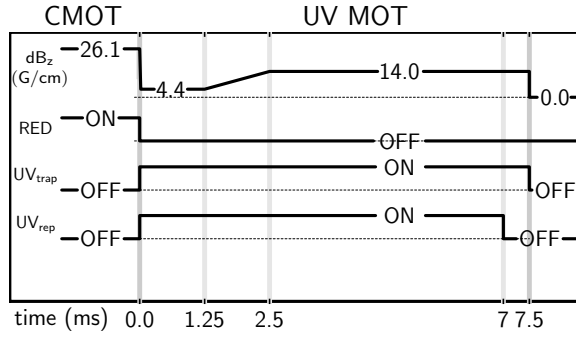


Figure 4.9: Timing diagram representing the transfer sequence from the CMOT to the UVMOT.

	UVMOT	unit
dB_z Final	14	G/cm
SHG Output power	25	mW
UV trap intensity per beam	1.0	I_{sat}^{3P}
UV repump intensity per beam	0.1	I_{sat}^{3P}
UV detuning (UVMOT only)	-1.6	MHz
UV detuning (loading to ODT)	-0.6	MHz
Number	5.3	10^8
$1/e$ radius	0.15	cm
Peak density	2.9	10^{10} cm^{-3}
Temperature	59	μK
Phase space density	2.3×10^{-5}	-

Table 4.2: UVMOT Settings. $I_{\text{sat}}^{3P} = 5.9 \text{ mW/cm}^2$ is the saturation intensity of the 323 nm transition. [106]. The two values shown for the detuning correspond to optimized number and temperature of the UVMOT (Fig. 4.10), and optimized number of atoms loaded into the ODT. More details on loading the ODT will be given on §4.6.

4.4 Optical dipole trap

We load the atoms from the UVMOT into the optical dipole trap (ODT), where we evaporatively cool them to degeneracy. The light for the ODT is provided by a broadband fiber laser operating at 1070 nm with an output power of 50 W. Two beams with orthogonal polarizations cross at an angle of 15° to form a crossed-beam trap. The resulting potential resembles an elongated ellipsoid, as shown in Fig. 4.11.

The ODT beams are cylindrically symmetric and focused to a $1/e^2$ radius of $\approx 70 \mu\text{m}$. For the purposes of tuning the potential to optimize the number of atoms loaded, the lens

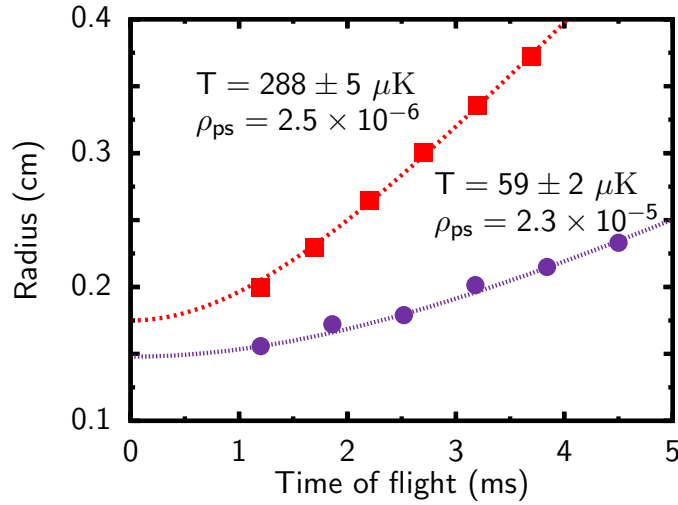


Figure 4.10: Time-of-flight expansion of the CMOT (red squares) and the UVMOT (violet circles). The points represent the $1/e$ width of Gaussian fits to the spatial profile of the freely expanding clouds. The lines are fit to ballistic expansions. ρ_{ps} stands for phase-space density.

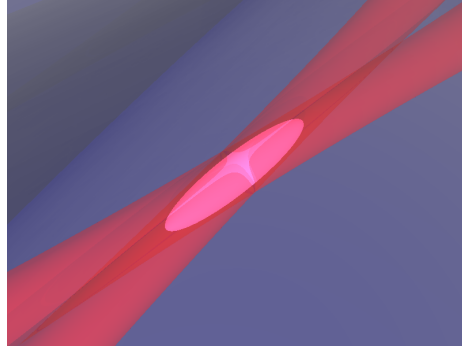


Figure 4.11: Illustration of the potential created by the crossed-beam optical dipole trap.

labeled F in Fig. 4.12 is positioned on a translation stage. Moving this lens along the beam path has a strong handle on the value of the $1/e^2$ beam radius of the ODT beams at their crossing, and thus affects the depth and volume of the trap strongly.

Trap depth and frequencies

The trapping potential produced by a light field of spatially varying intensity $I(\mathbf{r})$ is given by

$$U_{\text{dip}}(\mathbf{r}) = \frac{\hbar\Gamma^2}{4} \left(\frac{1}{\omega_0 + \omega} + \frac{1}{\omega_0 - \omega} \right) \frac{I(\mathbf{r})}{I_{\text{sat}}} \quad (4.1)$$

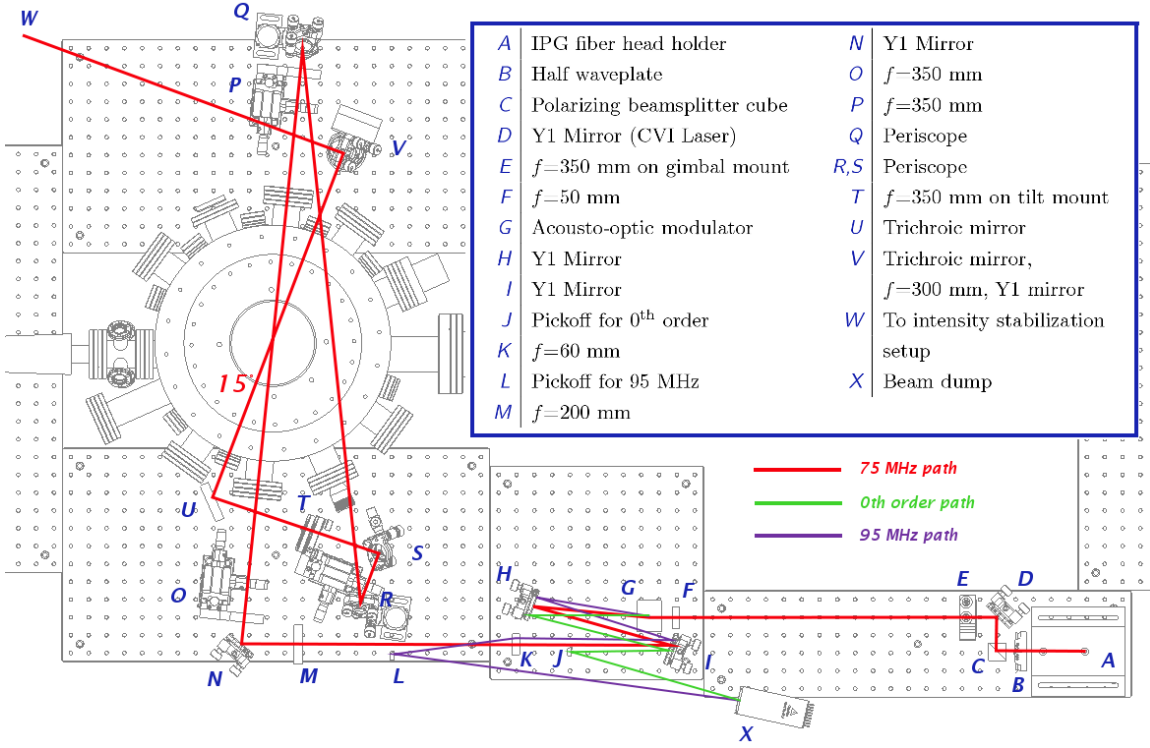


Figure 4.12: Optical dipole trap setup. The red lines show the path of the first order of the AOM labeled *G* when the AOM is operated at 75 MHz. Light can be dumped by driving the AOM at 95 MHZ (purple path) or by turning it off (green path). All mirrors in this setup are Part Num. Y1-1025-45-UNP from CVI Laser, which have a damage threshold of 10 MW/cm^2 . All the lens substrates are UV fused silica to reduce power dissipation and thermal lensing. The acousto-optic modulator is Part Num. 46080-2-1.06 from Neos Technologies.

For ${}^6\text{Li}$, a single Gaussian beam of power *P* and $1/e^2$ beam waist *w*, produces a trap depth

$$\frac{U_0}{k_B} = \frac{P}{w^2} \times 38.7 \times 10^3 \text{ K}^{-1} \text{ m}^2 \text{ W}^{-1} \quad (4.2)$$

The first pass through the atoms has 39 W of power and, after losses at subsequent optics and windows, there are 35 W for the second pass. The pass with lower power sets the trap depth, which is $U_0/k_B \approx 280 \mu\text{K}$. Atoms with an energy higher than U_0 can escape the intersection region of the two beams by drifting away along the 39 W beam.

The trap frequencies are calculated to be approximately 490 Hz and 3750 Hz along the axial and radial directions of the trap, respectively. We measured the radial trap frequency, ω_r , by turning the dipole trap off briefly ($40 \mu\text{s}$) and then turning it back on. The resulting breathing mode oscillates at twice the radial trap frequency and we obtain

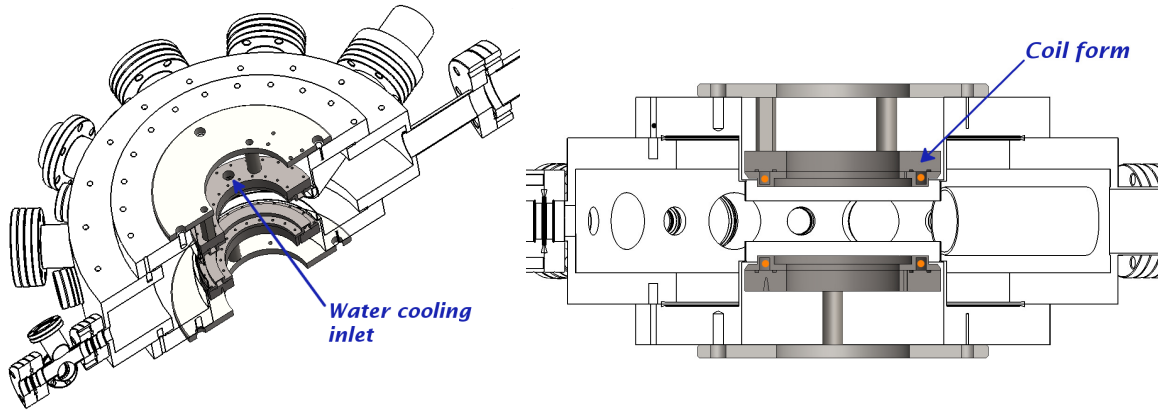


Figure 4.13: Cut-out view of vacuum chamber showing the location of the coils that create the magnetic field. The coil forms are close to the atoms inside the re-entrant top and bottom viewports. The forms themselves are attached to a mounting plate that bolts to the re-entrant viewport flange. The coils are water cooled. Only the water inlet is shown in this picture, the water outlet is on the half that is cut out.

$\omega_r = (2\pi)3.8$ kHz. The axial trap frequency, ω_a , was measured via parametric heating by sinusoidally modulating the trap depth, and determined to be $\omega_a = (2\pi)470$ Hz.

4.5 Magnetic field

The magnetic field in our experiment is created by a set of coils in Helmholtz configuration, which sit close to the atoms, inside the recessed top and bottom viewports of our vacuum chamber (see Fig. 4.13). The radius of the coils is 4.72 cm, and is equal to the separation between them. There are $n = 35$ turns on the top coil and $n - 1 = 34$ turns on the bottom coil. During the MOT stages of our experiment, the current through the coils is run such that they are in anti-Helmholtz configuration. For a current I , produce a quadrupole magnetic field with a gradient along z , given by

$$\frac{dB_z}{dz} = \left(\frac{4}{5}\right)^{5/2} \frac{3\mu_0(2n-1)I}{4r^2} \quad (4.3)$$

which for $n = 35$ and $r = 4.72$ cm amounts to 1.72 G/cm/A.

After the optical dipole trap is loaded from the UVMOT the direction of the current in

the top coil is reversed and they produce a bias field given by

$$B = \left(\frac{4}{5}\right)^{3/2} \frac{\mu_0(2n-1)I}{2r} \quad (4.4)$$

which amounts to 6.8 G/A. Due to the mismatch in the number of turns between the two coils, in bias configuration there is a residual gradient given by

$$\frac{dB_z}{dz} = \left(\frac{4}{5}\right)^{5/2} \frac{3\mu_0 I}{4r^2} \quad (4.5)$$

For a bias field of 500 – 650 G, where we perform most of our experiments, this field gradient produces a force on the atoms which is directed upwards and has about twice the magnitude of the gravitational force. We have setup circuitry to controllably shunt some current from the top coil, such that the atoms are levitated.

The diagram in Fig. 4.14 shows a schematic of the magnetic field system. The polarity of the current on the top coil is switched by using an H-bridge made with four field-effect transistors (FETs), labeled 1 to 4 in Fig. 4.14. FETs labeled 5 and 6 control the amount of current shunted from the top coil to levitate the atoms. FETs labeled 7 and 8 control the total amount of current in the system. The total current through the system is measured using a Danfisik Ultrastab 866 current transducer, which acts as the source of feedback for stabilization. For the current shunted for levitation, the transducer used is an LEM HTB-200. The power supply is a 15 kW Lambda Genesys (80 V, 187.5 A), operated in constant voltage mode. A feed forward scheme is implemented to set the voltage output of the power supply so that the control FETs do not have to dissipate too much power.

4.6 Loading the ODT

To load the atoms into the ODT one simply needs to turn the ODT light at maximum power a few milliseconds before the UVMOT is switched on ($t = 0$ in the timing diagram of Fig. 4.9). We currently turn on the ODT 70 ms before $t = 0$, so it overlaps in time with the 671 nm MOT. The operation of the 671 nm MOT is not harmed at all by the presence of the ODT, owing to a small differential polarizability between the ground $2S_{1/2}$

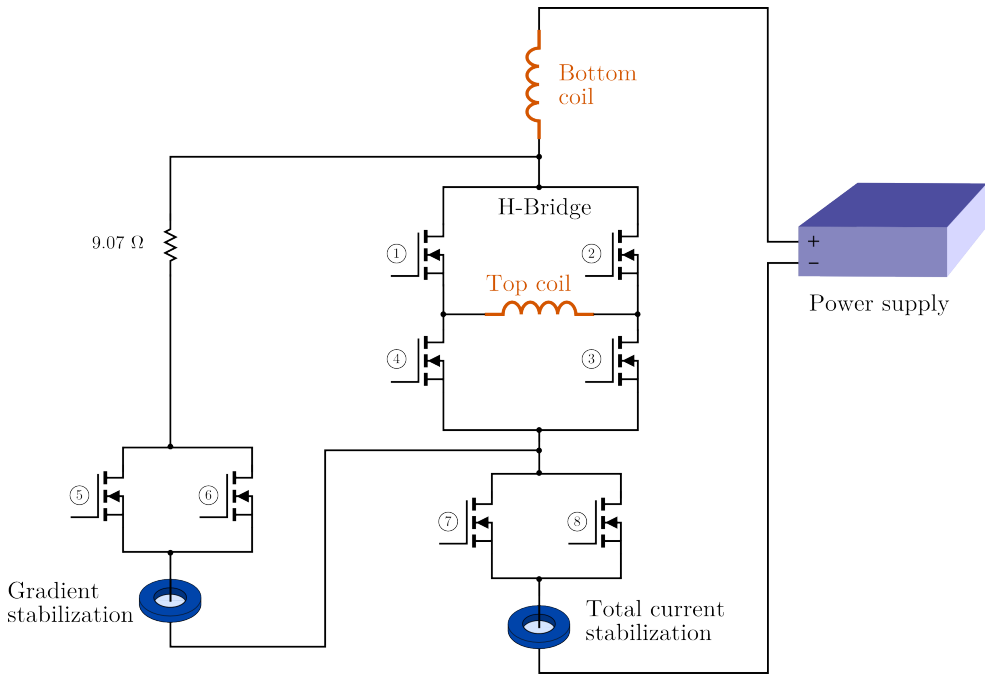


Figure 4.14: Schematic of the magnetic field stabilization circuit. An H-bridge is used to reverse the polarity of the current on the top coil. Current is shunted from the top coil to stabilize the residual gradient and levitate the atoms. Current transducers (blue rings) are used for feedback control of the total current in the system and the current shunted off the top coil. FETs in the H-bridge are Part Num. STE180NE10. All other FETs are Part Num. IXFN230N10. Transient voltage suppressors, Part Num. 15KW90CA, are used across all the FETs to reduce any voltage spikes and increase the turn-off speed of the coils.

and excited $2P_{3/2}$ states. In other words, both ground and excited states shift by an equal amount when in the presence of the 1070 nm ODT light, and thus the laser cooling process is not affected by the presence of the ODT.

A wavelength of light where the differential polarizability for a certain transition vanishes is referred to as a magic wavelength. Figure 4.15 shows the polarizabilities for the $2S$ and $2P$ states of ${}^6\text{Li}$ and gives exact values for the magic wavelengths of $2P_{3/2}$ states. There is small variability with wavelength around the wavelength of the ODT (1070 nm), and the differential polarizability is small. A calculation (Fig. 4.17) reveals that, for the maximum intensity of the ODT, a maximum shift of $\approx 1.5\Gamma$ is expected, where Γ is the linewidth of the 671 nm transition.

The situation is different for the $2S_{1/2} \rightarrow 3P_{3/2}$ transition, see Fig. 4.16. In that case,

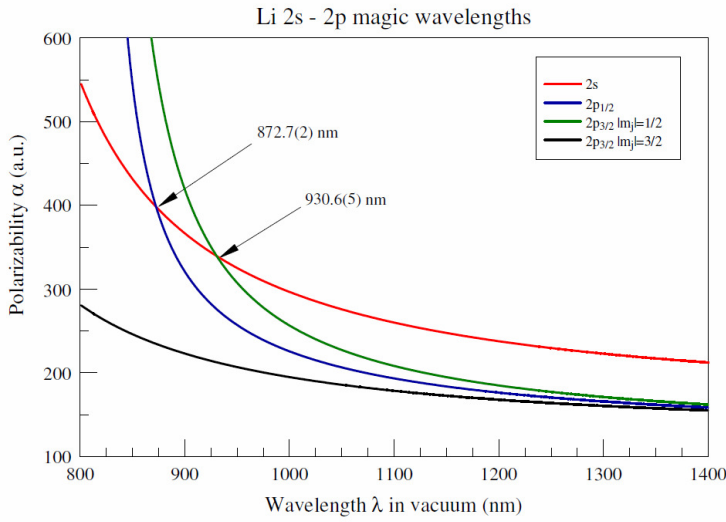


Figure 4.15: Polarizability in atomic units for the $2S$ and $2P$ states. Magic wavelengths are indicated by the arrows. The atomic units for polarizability (a.u.) can be converted to SI units ($\text{C m}^2 \text{ V}^{-1}$) by multiplying by 1.648×10^{-41} [107, 108].

if the wavelength differs much from a magic wavelength, the differential polarizability of the transition can become very large. A calculation for our trap (Fig. 4.17) reveals that for the ODT wavelength of 1070 nm a light shift of at most a few linewidths is expected at the deepest point in the trap. It was a great coincidence that the magic wavelength for the $2S_{1/2} \rightarrow 3P_{3/2}$ transition happened to be so close to the operating wavelength of our ODT laser. Being able to continue to laser cool atoms that are in the volume of the trap greatly enhances the number of atoms that can be loaded into the ODT, which can be as large as $\approx 1.4 \times 10^7$ atoms.

As was briefly mentioned in §4.3.3, we change the detuning of the 323 nm light in order to optimize the number of atoms loaded into the ODT. We find that shifting the frequency of the light to the blue by 1 MHz optimizes the number loaded. We also measured the light shift of the $2S_{1/2} \rightarrow 3P_{3/2}$ transition in our ODT and find that, in the presence of the full power ODT, the transition is shifted ≈ 800 kHz to the blue, see Fig. 4.18.

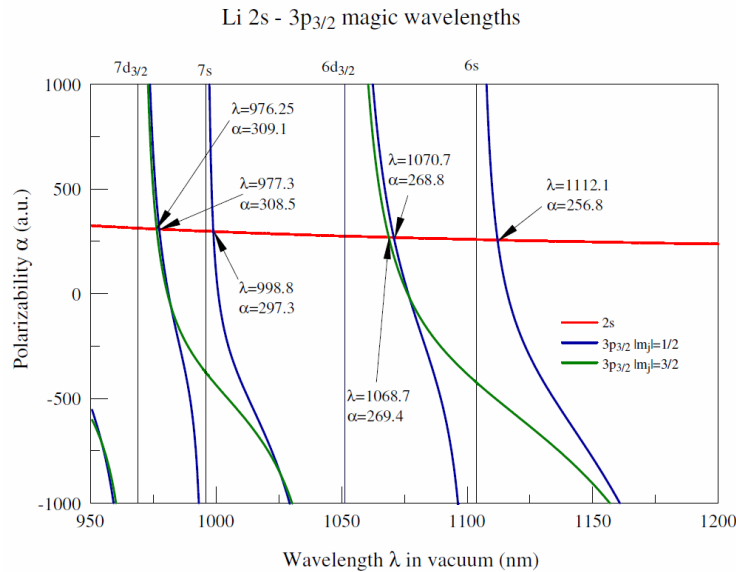


Figure 4.16: Polarizability in atomic units of the 2S and 3P states. The atomic units for polarizability can be converted to SI units ($\text{C}^2 \text{m}^{-3} \text{V}^{-1}$) by multiplying by 1.648×10^{-41} [107, 108].

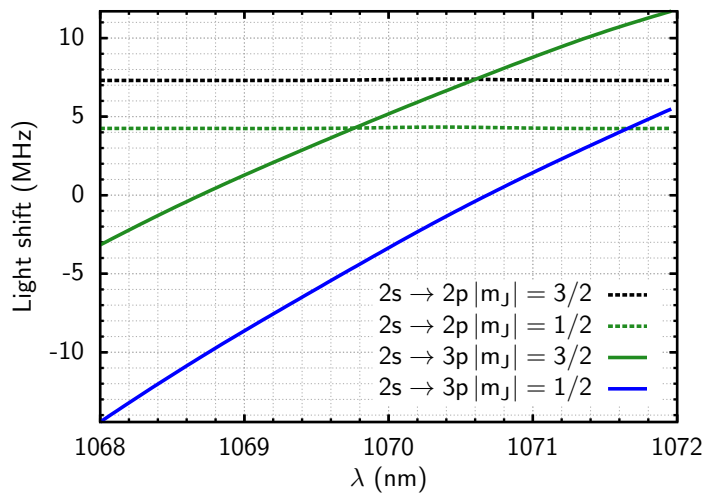


Figure 4.17: Differential AC Stark shift of the $2S_{1/2} \rightarrow 2P_{3/2}$ and $2S_{1/2} \rightarrow 3P_{3/2}$ transitions as a function of wavelength for an intensity of 910 kW/cm^2 (the maximum intensity the ODT can provide), calculation by M. Safronova (personal communication).

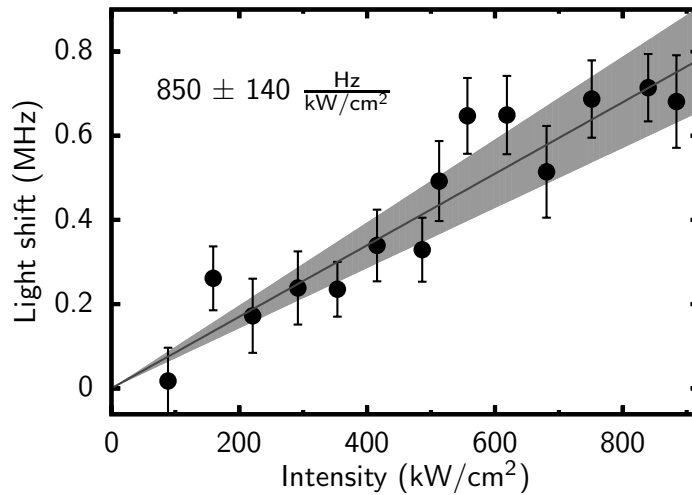


Figure 4.18: Differential AC Stark shift of the $2S_{1/2} \rightarrow 3P_{3/2}$ transition as a function of intensity of the optical trapping light at $\lambda = 1070$ nm. The circles represent the center of a Gaussian fit of a loss resonance, obtained by heating up atoms in the ODT with a single UV beam. The error bars are 1σ statistical error of the resonance fits. The solid line is a linear fit to the resonance position with a slope of 850 ± 140 Hz/(kW/cm 2), where the error (indicated in the plot by the gray shaded area) represents the statistical uncertainty of the fit and a systematic uncertainty of 10% on the value of the trap intensity.

Spin mixture

Our experiments are realized with a spin mixture of atoms in the two lowest hyperfine states, labeled $|1\rangle$ and $|2\rangle$ in Fig. 4.3. To create such a spin mixture, we simply turn off the UV repumping beam 0.5 ms before turning off the UV trapping beam, after the atoms have been loaded into the ODT. In that brief time the trapping light optically pumps all of the atoms into the $F = 1/2$ hyperfine state, creating a balanced mixture of the two hyperfine spin levels.

After shutting off the UV repumping beam, we turn off the UVMOT magnetic field gradient, switch the polarity of the top coil, and ramp up a bias field of 340 G, where the scattering length is $\approx -280a_0$. The scattering length is large enough that it leads to efficient evaporative cooling in the trap. From this point on, we perform forced evaporation by reducing the power of the ODT beams. As the ODT is evaporated away we ramp up a dimple potential, described in the next section, such that when the ODT is fully evaporated

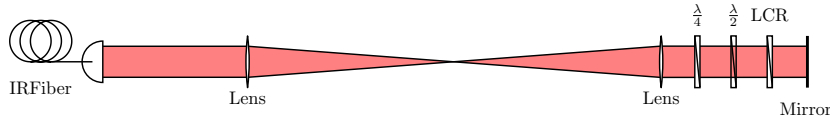


Figure 4.19: Simplified setup for a one-dimensional lattice. In our implementation we have included waveplates and a variable liquid crystal retarder (LCR). This allows us to control the polarization of the retroreflection.

away we are left with a degenerate spin mixture in the dimple at a temperature $T/T_F \approx 0.04$.

The details of the evaporation trajectory will be discussed later in Chapter 10.

4.7 Compensated optical lattice

The compensated optical lattice is the potential in which we realize the Hubbard model and carry out all our experiments. In Chapter 5 and Appendix A we give much more details about the compensated optical lattice. In this section we will give an overview of the setup used to create the potential.

4.7.1 Optical lattice and dimple

An optical lattice potential results due to the stationary interference pattern of two or more laser beams. The simplest configuration consists of a laser beam that is retroreflected upon itself. We have used this basic configuration and added a variable liquid crystal retarder LCR, along with a quarter waveplate and a half waveplate, in front of the retro-reflection mirror, as shown in the simplified schematic in Fig. 4.19. The LCR allows us to set the polarization of the retro-reflected beam. If the polarization of the retroreflected beam is equal to the polarization of the incident beam, and both are linear, then the potential will be a lattice potential. On the other hand, if the polarization of the retroreflected beam is perpendicular to that of the input, there will be no interference and the potential will be a regular trap.

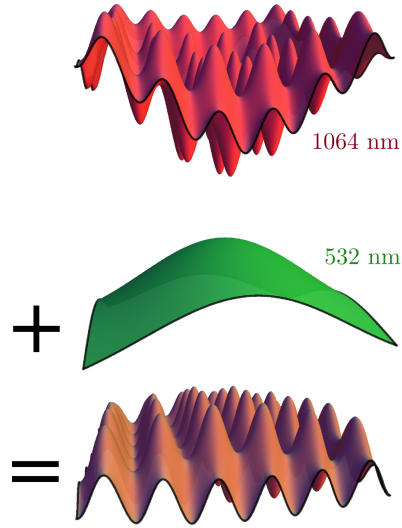


Figure 4.20: Illustration of the concept behind a compensated optical lattice.

We have setups like the one shown in Fig. 4.19 along three orthogonal axes in order to form a simple cubic lattice potential. The waist of each beam is $\approx 45\mu\text{m}$ and thus the intersection region of all three beams is quite small. When the polarization of the retro beams is set perpendicular to the input polarization, we refer to the trap formed at the intersection of all three axes as the **dimple trap**. The dimple trap provides an excellent starting point for our experiments. The large confinement strength resulting from the small volume of the trap leads to efficient evaporation. In the dimple we can routinely achieve temperatures as low as $T/T_F \approx 0.04$. By comparison, in the ODT one has to spend considerable effort optimizing the evaporation trajectory, alignment, and beam profile of the ODT beams to get below $T/T_F \approx 0.05$, and routinely the ODT can only get down to $T/T_F \approx 0.15$.

4.7.2 Compensation

The compensation is a repulsive potential used to tune the amount of confinement produced by the optical lattice. An illustration of this idea is shown in Fig. 4.20. Adjusting the density of the sample is critical when trying to access the different phases of the Hubbard

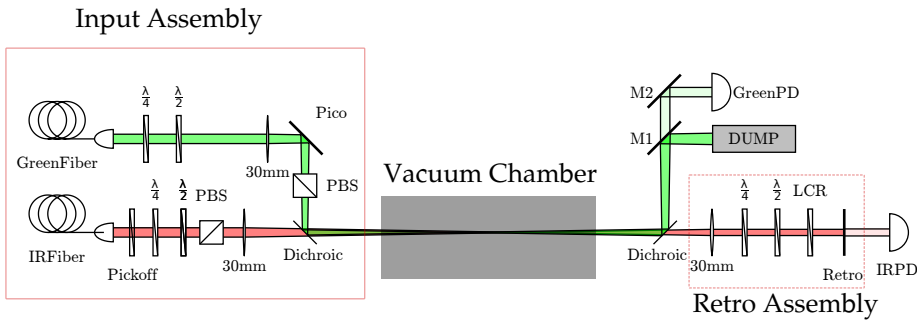


Figure 4.21: Compensated optical lattice setup along one of the three axes. More details regarding the construction of the setup can be found in Ernie Yang’s Master’s thesis [109]

model. Furthermore the compensation was designed such that it enables the possibility of continuing to evaporatively cool the atoms once they are in the lattice potential (this will be discussed in Chapter 5. Reaching lower temperatures in an optical lattice is a major goal for quantum simulation with ultracold atoms.

The compensating potential is formed by Gaussian beams that co-propagate with the incident lattice beams but are not retroreflected. A schematic of the compensation plus optical lattice setup is shown in Fig. 4.21. The details of this setup are described in detail in Ernie Yang’s Master’s thesis [109]. The light that is coming out of the fibers in Fig. 4.21 is prepared in a separate optical table. For the lattice we use 1064 nm light from a single mode IPG Photonics fiber laser. The optical layout is shown in Fig. 4.22. For the compensation we use 532 nm light from a Coherent Verdi. The optical layout is shown in Fig. 4.23.

4.8 Diagnostics

Having described all the systems that we use to manipulate the atoms, we will now describe very generally the systems used to measure their properties. For diagnostics we exploit again the strong interaction of the atoms with near resonant light. We can perform fluorescence, absorption and phase contrast imaging of the atoms. We have also built a setup to measure Bragg scattering of light, a probe of the crystalline and spin order of atoms in a lattice [58]. A detailed description of the Bragg scattering setup will be presented in

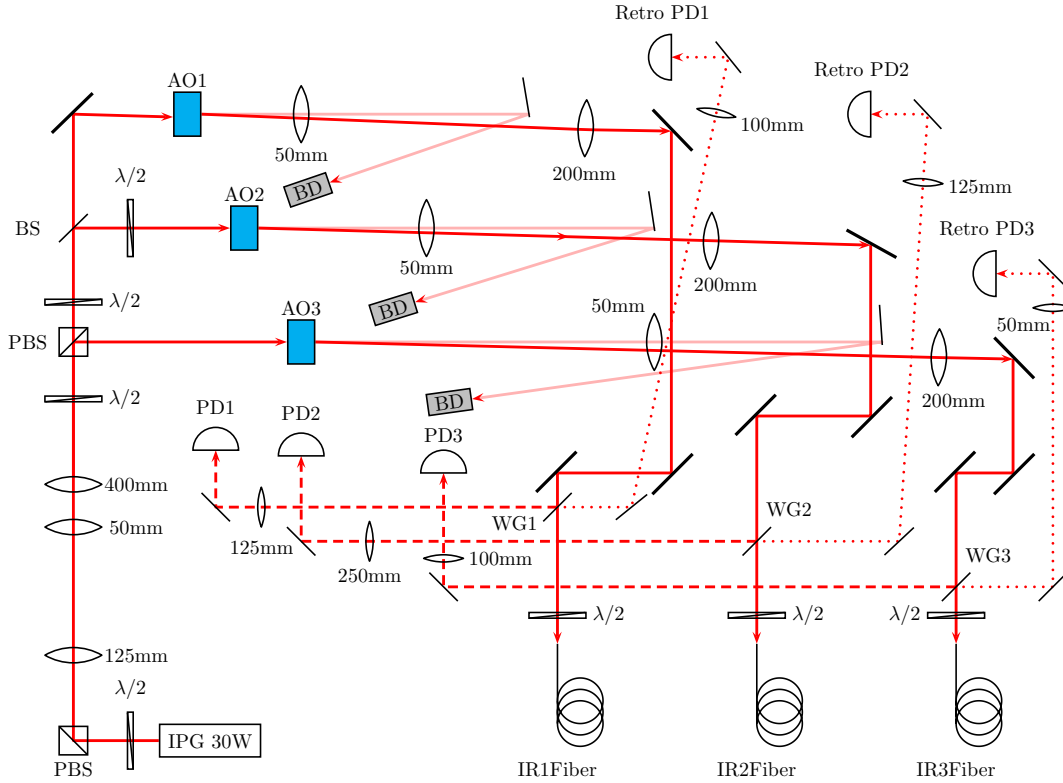


Figure 4.22: Optical setup showing how the 1064 nm light from the 30 W IPG laser is split up before coupling into the fibers for each of the three lattice axes. The acousto-optic modulators, labeled AO1-3, are used for intensity stabilization of the intensity. Feedback to these AOs comes from the photodetector labeled IRPD in Fig. 4.21. The driving frequencies of AOs 1-3 is 70, 80, and 90 MHz respectively, with the offset used to avoid interference between the different lattice axes.

Chapter 9.

For the purposes of imaging the MOT and UVMOT, which can reach a spatial extent of up to several millimeters after TOF expansion, we use fluorescence imaging using a surveillance CCD camera, see Fig. 4.24.

To image the smaller samples (tens of microns) in the ODT, the dimple, or the optical lattice, we use a nearly diffraction limited relay lens system (Fig. 4.25) which creates a real image of the atoms outside the vacuum chamber. The numerical aperture (NA=0.16) of the relay lens determines the resolution of the imaging system ($\sigma_{\text{res}} \approx 3 \mu\text{m}$)⁵. A commercial

⁵Here the resolution of the imaging system is defined as the $1/e$ radius of the point-spread function PSF

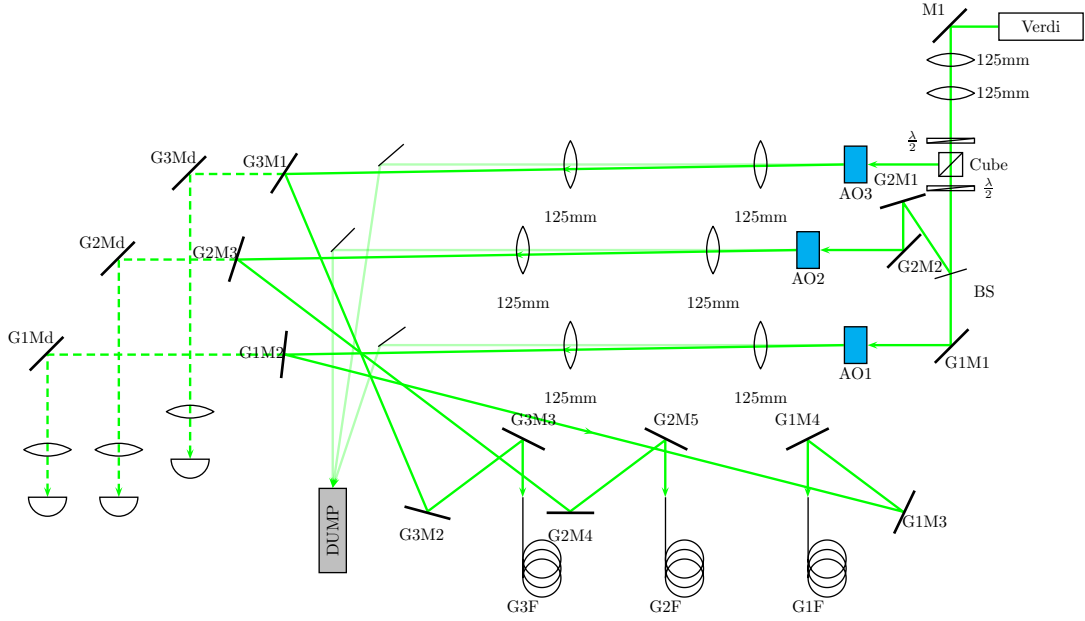


Figure 4.23: Optical setup showing how the 532 nm light from the Coherent Verdi is split up before coupling into the fibers for each of the three lattice axes. The acousto-optic modulators, labeled AO1-3, are used for intensity stabilization of the intensity. Feedback to these AO's comes from the photodetector labeled GreenPD in Fig. 4.21. The driving frequencies of AOs 1-3 is 80, 88, and 72 MHz respectively, with the offset used to avoid interference between the different compensation axes.

microscope objective is then used, in conjunction with a Nikon telephoto lens, to image the the relayed image of the atoms onto a CCD. The setup is shown in Fig. 4.24,

4.9 Control, automation, and data analysis

Finally, we describe the computer control system that orchestrates the behavior of all other systems in our experiment. The control system is based on the National Instruments PXI chassis NI-PXIe1062Q.

The chassis hosts three 6733 Analog Output cards and a 6259 Multifunction DAQ card.

of the imaging system, $\text{PSF}(x) \propto \exp\left[-\frac{x^2}{\sigma_{\text{res}}^2}\right]$. The size of the PSF was obtained by fitting images of a 1951 USAF test target.

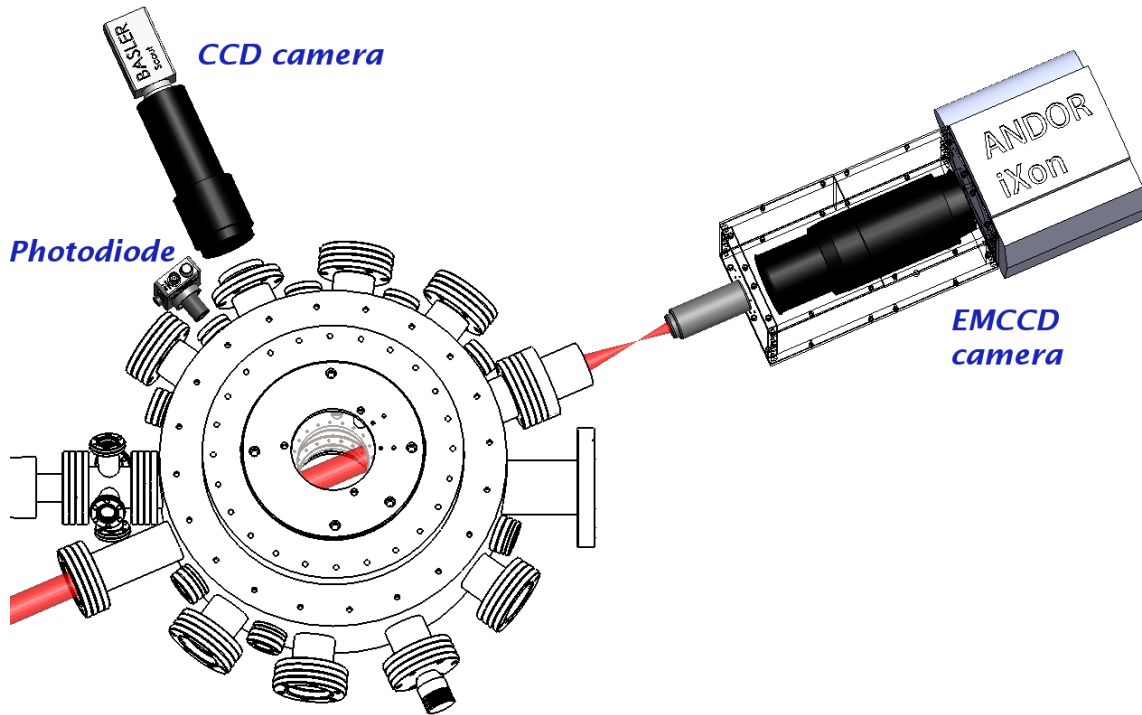


Figure 4.24: This figure shows instruments that we use for diagnostics. A photodiode can be used for basic monitoring of the MOT loading level. Fluorescence imaging with the Basler CCD camera is used to characterize the MOT and UVMOT. Smaller samples in the ODT and optical lattice are imaged using a relay lens (not shown). A microscope objective and Nikon telephoto lens, project the image of the atoms onto the Andor iXon EMCCD camera (DU-897-E).

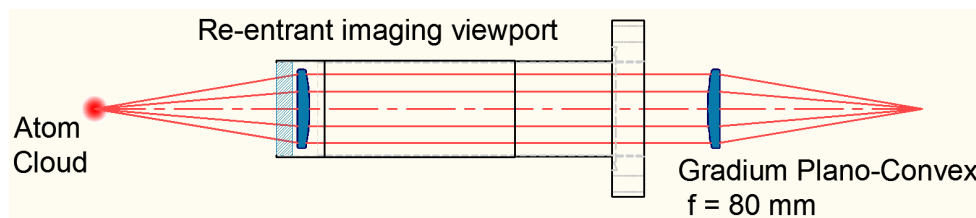


Figure 4.25: Relay lens system to form an image of the atoms outside the vacuum chamber. A re-entrant imaging viewport on the vacuum chamber allows placing a 1 inch diameter lens 80 mm away from the atom sample. The lenses are gradient index plano-convex lenses, Part Num. GPX-30-80 from LightPath Technologies.

An experimental sequence consists of a series of TTL pulses that control the timing of events related to instruments on the apparatus. The clock to which TTL pulses are synchronized is an 80 MHz oscillator on the 6259 Multifunction DAQ card. A digital sequence can have a maximum output rate of 10 MHz (resolution time step of $1 \mu\text{s}$) and at this output rate the buffer can hold sequences that last several tens of seconds. We use the analog output channels of the PXI system as one typically uses arbitrary waveform generators; waveform outputs can be triggered by TTL pulses at any given time during the experimental sequence. The timebase for arbitrary waveform outputs on analog output channels is the on-board oscillator of each card. For the 6259 it is a 80 MHz oscillator and for the 6733 it is a 20 MHz oscillator.

The experimental sequences, including all waveform outputs, are programmed in a format based on the Python programming language. This makes it very easy to program new sequences and recycle parts of old sequences. The Python based sequence code is interpreted by a program written also in Python which produces a raw sequence output file that contains all the TTL timings and the waveforms for a particular experiment. The raw sequence output is read by LabVIEW, which takes care of outputting the sequence on the TTL and analog output channels.

In an experimental cycle, the MOT is loaded until a certain fluorescence is reached. At that point a trigger synchronized with the 60 Hz mains starts the output of the experimental sequence.

5. Compensated optical lattice potential

One of the most important aspects of the work presented in this thesis has been the design and construction of the potential in which our experiments take place. In previous chapters we have referred to ultracold atoms in optical lattices as a nearly ideal realization of the Hubbard model. In fact, there are important differences between ultracold atoms in optical lattices and idealized models.

To start with, optical lattices are created with finite laser beams, and thus the value of the lattice depth is never constant throughout the sample. In addition, when using ultracold atoms one is forced to use an overall confining potential, to achieve large enough densities close to one particle per site (half-filling) such that the effects of correlations between particles become manifest. An illustration of these ideas is shown in Fig. 5.1. In recent years there has been significant work in trying to make “square-well” potentials, that are flat but have very steep walls [110, 111]. In such potentials one could reach densities near half-filling and have a homogeneous lattice depth at the same time. This approach, to our knowledge, has not yet been realized with optical lattices.

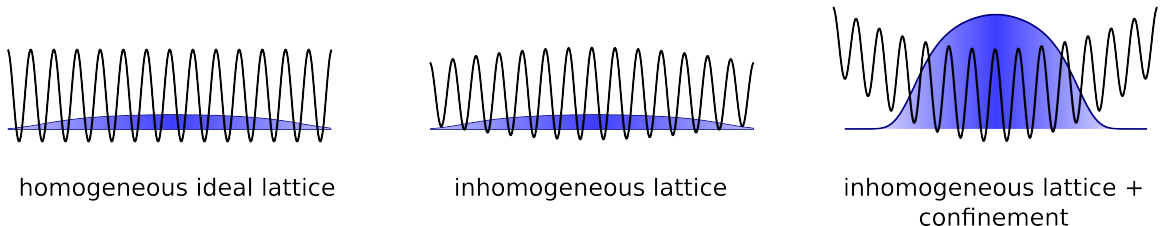


Figure 5.1: In an ideal system (left) a lattice is homogeneous and flat, extending to infinity. For a finite number of particles the density would go to zero, as the gas continues to expand in the lattice. For real Gaussian beams (center), the lattice is inhomogeneous. Notice that the inhomogeneity of the lattice beams results in a small amount of confinement (curvature of lower envelope of the potential), but not sufficient to increase the density significantly. Additional confinement (right) must be provided to achieve the necessary densities with a finite number of particles.

Experiments in lattices have traditionally dealt with at least one of the problems stated above: the inhomogeneity of the lattice depth. Typically, experiments use lattice beam waists that are large comparable to the size of the system. An additional Gaussian beam (or arrangement of beams) with smaller waists provides the external confinement and determines the size of the system. This approach has the advantage that the lattice depth, being nearly constant throughout the extent of the sample, results in Hubbard parameters t and U that are also nearly constant throughout the sample. In any case, the density distribution of the atoms still remains inhomogeneous due to the external confinement, and that presents a problem for the interpretation of bulk measurements. Furthermore, the traditional setup (large beam waist + additional confinement) has a disadvantage that has to do with the possibility of continuing to evaporatively cool the atoms once they are loaded into the lattice potential.

The field of ultracold atomic physics has built its success by exploiting the power of two very effective atom cooling techniques, laser cooling and evaporative cooling. The former makes use of dissipative forces imparted by light on atoms to decelerate their center of mass motion, and has helped bridge the gap from the Kelvin to the microKelvin regime. The latter takes over at the limit of laser cooling and is able to take the samples deep into quantum degeneracy. Evaporative cooling works on a simple principle: when a particle, with energy larger than the mean energy per particle of the system, escapes the potential, then mean energy per particle of the system decreases. After an elastic collision between a pair of atoms, there is a probability that one of them may have enough energy to escape the trap. But this probability becomes negligible if the trap is too deep, which renders evaporative cooling ineffective.

In our work we have chosen to trade-off the uniformity of the Hubbard parameters, t and U , in exchange for the possibility of continuing to evaporatively cool the atoms once they are loaded into the optical lattice. The goal of this experiment has been to create an antiferromagnetic (AFM) Mott insulator in the center of the trap, and continued evaporative cooling in the lattice is a promising path to that end. As we will see, our lattice setup uses

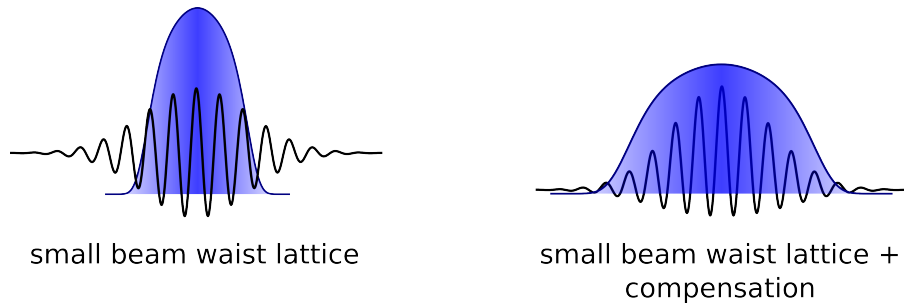


Figure 5.2: A lattice with beam waist comparable to the extent of the sample (left) produces excessive confinement, resulting in densities above half-filling at the center. Compensation is added (right) to reduce the confinement and tune the density. In this approach, the sample in the lattice has the possibility to undergo continued evaporative cooling.

lattice beam waists that are comparable to the size of the sample. The inhomogeneity of the lattice is thus very pronounced, and the lattice beams alone confine the atoms in excess, as shown in Fig. 5.2. The addition of a repulsive compensation potential allows tuning the peak density of the system to reasonable values in the vicinity of half-filling, and pushes up the chemical potential such that atoms have the possibility of escaping the trap and evaporative cooling becomes effective.

In this chapter we will use the local density approximation (LDA) in conjunction with the second order high-temperature series expansion (HTSE) to calculate the properties of various trapping potentials. We will compare our compensated lattice potential with a traditional optical lattice setup with large beam waists, and we will discuss ways in which further improvements to our setup can be realized. In doing this comparison we will keep in mind practical considerations such as the total atom number required to achieve a density near half-filling at the center of the trap. For more technical aspects of our potential, such as calculation and calibration of beam waists, and calculation of heating rates, refer to Appendix A.

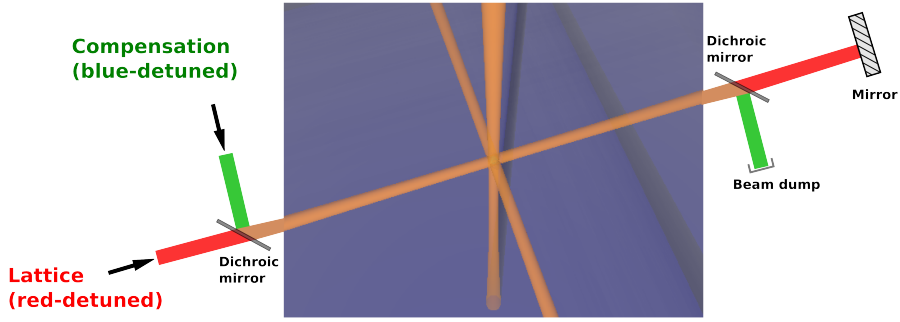


Figure 5.3: Simplified schematic of the compensated lattice setup along one of the axes.

5.1 Form of the potential

The compensated simple cubic optical lattice potential is formed at the intersection of three orthogonal axes, see Fig. 5.3. Along each axis, a 1D lattice potential is formed by retro-reflecting a red-detuned Gaussian beam. Overlapped onto each of the lattice beams there is a compensation beam, which is blue-detuned and thus produces a repulsive potential. The compensation beam is not retro-reflected, so it does not form a standing wave potential.

The lattice beam that propagates along the x axis produces a potential of the form

$$V_L(x; y, z) = -s_0 \exp \left[-2 \frac{y^2 + z^2}{w_L^2} \right] \cos^2(k_L x) \quad (5.1)$$

where s_0 is the lattice depth at the center of the potential, w_L is the lattice beam waist and $k_L = 2\pi/\lambda_L$ is the wavenumber of the lattice light. The compensation beam that propagates along x produces a potential

$$V_C(x; y, z) = g_0 \exp \left[-2 \frac{y^2 + z^2}{w_C^2} \right] \quad (5.2)$$

where g_0 is the depth (or rather height since it is repulsive) of the compensating potential, and w_C is the beam waist of the compensation beam.

The combined potential of lattice plus compensation for the beams propagating along x is

$$V_{1D}(x; y, z) = V_L(x; y, z) + V_C(x; y, z) \quad (5.3)$$

The total potential for our simple cubic lattice is given by

$$V_{3D}(x, y, z) = V_{1D}(x; y, z) + V_{1D}(y; z, x) + V_{1D}(z; x, y) \quad (5.4)$$

5.2 General aspects

Before we go ahead and deploy the full machinery of the LDA+HTSE we will discuss some general aspects of the potential using analytical approximations to its shape and considering a zero temperature sample. We will find that at a certain ratio of the lattice to compensation beam waist, $\alpha_w \equiv w_L/w_C$, one can create a potential optimal for evaporative cooling, which is also flat at the bottom, in a way reminiscent of the idealized square-well potential. We will also make an estimate of the atom number required to realize this setup.

One of the important things to note, is that at each point in space we will, in general, have three different lattice depths, associated with each of the x , y , and z lattice directions. We denote the lattice depths as s_x , s_y and s_z , all of which depend on position. To make things simpler, we can consider the potential along the 111 direction; along this direction we have equal lattice depths in x , y , and z :

$$s_x(r_{111}) = s_y(r_{111}) = s_z(r_{111}) = s_0 \exp\left[-\frac{4r_{111}^2}{3w_L^2}\right] \equiv s(r_{111}) \quad (5.5)$$

where r_{111} represents the distance along the 111 direction.

The bottom envelope of the lattice potential along 111 is given by

$$V_{L,\text{env}}(r_{111}) = -3s_0 \exp\left[-\frac{4r_{111}^2}{3w_L^2}\right] \quad (5.6)$$

At each point in space there is a local band structure determined by $V_{L,\text{env}}$, s_x , s_y , and s_z . The lowest energy of the band, which we will refer to as E_0 , can be approximated by the zero-point energy of the 3D harmonic oscillator obtained by Taylor expanding the potential at a lattice site. This approximation is only valid for deep lattices¹ (refer back to Fig. 2.1

¹Recall that the recoil energy, E_r , is defined as $\frac{\hbar^2}{8m\lambda^2}$, where m is the mass of an atom and λ is the wavelength of the lattice.

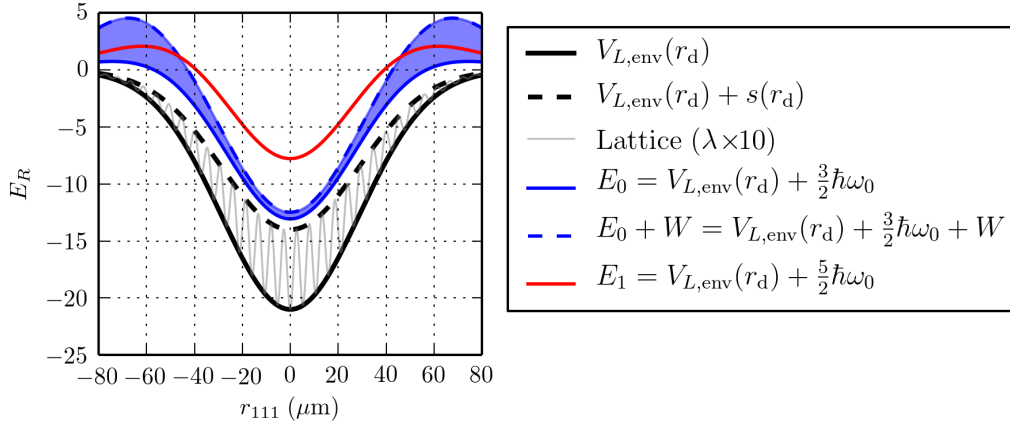


Figure 5.4: Profiles along r_{111} for a $7E_r$ lattice with $w_L = 47 \mu\text{m}$ and $\lambda = 1064 \text{ nm}$. The energy levels in the lowest band of the lattice correspond to the shaded blue region. The curvature of E_0 determines the confinement.

for reference) but we will use it here for its simplicity:

$$E_0 = V_{L,\text{env}} + \frac{3}{2} \hbar \omega_0 = V_{L,\text{env}} + 3E_r \sqrt{s/E_r}. \quad (5.7)$$

We can also obtain an expression for the bandwidth, W , of the lowest energy band valid in the limit of deep lattices (cf. Eq. 2.45 or Ref. [66]):

$$W = 12t = E_r \frac{48}{\sqrt{\pi}} (s/E_r)^{3/4} e^{-2\sqrt{s/E_r}}. \quad (5.8)$$

Notice that the quantities E_0 , W , ω_0 , s , and t are all position dependent, and thus functions of r_{111} . The profiles of these quantities (and also of the energy of the first excited band, E_1) are shown in Fig. 5.4 for a simple cubic lattice with lattice beam waist $w_L = 47 \mu\text{m}$.

Notice that the Gaussian profile of the lattice beams, being comparable to the size of typical samples $\approx 40 \mu\text{m}$, will provide a significant overall confinement for the atoms. This is in contrast with traditional setups, where the lattice beam waist is typically larger than $150 \mu\text{m}$ and in the length scale of typical samples the inhomogeneity of the lattice potential is not noticeable.

Compensation

If the lattice beam waist is comparable to the size of the system (as is the case in our setup), the confinement from the lattice itself will be too large, and it will result in a very large density². Repulsive compensation beams are then used to set the exact amount of confinement in the system and tune its density.

Beyond simply tuning the density, one can choose a ratio of lattice to compensation beam waist, defined as $\alpha_w = w_L/w_C$ [112], in order to affect the exact spatial dependence of the lowest band. A setup which flattens the profile of the lowest band at the center of the trap can enlarge the size of a local phase which may exist there, an idea suggested in Ref. [112], which is at the heart of our compensated lattice design. Ideally one would like to reach the square-well potential scenario, with a completely flat band and steep walls. In our implementation with Gaussian beams, the lowest band can be made quartic at best. Besides flattening the band, the use of compensation enables the possibility of evaporative cooling the sample in the lattice, as we will explain later on.

Power series expansion of the lowest band

With the addition of repulsive compensation beams (depth g_0 and beam waist w_C , as in Eq. 5.2) we can expand the lowest band profile of the lattice in a power series as

$$\begin{aligned} E_0(r_{111}) \approx & 3(g_0 + E_r \sqrt{s_0/E_r} - s_0) + \left[\frac{4s_0 - 2E_r \sqrt{s_0/E_r}}{w_L^2} - \frac{4g_0}{w_C^2} \right] r_{111}^2 \\ & + \left[\frac{-8s_0 + 2E_r \sqrt{s_0/E_r}}{3w_L^4} + \frac{8g_0}{3w_C^4} \right] r_{111}^4 + \mathcal{O}(r_{111}^6) \end{aligned} \quad (5.9)$$

If our interest is to maximally flatten the profile of the lowest band, the quadratic term in the series expansion can be nulled out if one chooses

$$g_0 = \frac{4s_0 - 2E_r \sqrt{s_0/E_r}}{4\alpha_w^2} \equiv g_{\text{quartic}}. \quad (5.10)$$

²Since we consider the single band Hubbard model, the density will be saturated at 2 particles per lattice site.

If an AFM phase forms at the center of the trap, this choice of g_0 will be the most favorable to enlarge the size of the AFM domain.

If $\alpha_w > 1$ and we use a compensation larger than g_{quartic} , the band profile will have a bump in the center. Experimentally we have observed that in that case it becomes hard to align the compensation beams such that the sample actually stays at the center of the trap.

In our current experiments we use $s_0 = 7 E_r$, and the beam waists in our setup are calibrated (see Appendix A for details about the calibration procedure) to be approximately $w_L = 47 \mu\text{m}$ and $w_C = 40 \mu\text{m}$, which gives $\alpha_w = 1.17$. The necessary compensation to flatten the band, according to this simplified analytical model, is then $g_{\text{quartic}} = 4.1 E_r$.

Evaporation

We want to consider the possibility of evaporative cooling in a sample that has $n = 1$ at the center (as is the case for an AFM Mott insulator). The density of the sample determines its Fermi energy and, if the Fermi energy is close to the energy required to escape the potential, evaporation will be effective. Here, we will consider a cloud with $n = 1$ and will set its Fermi energy to match the enenergy threshold for evaporation. This will determine the compensation g_0 required for optimal evaporation. We then equate this g_0 with g_{quartic} , obtained above, to find out the parameters for a trap that is optimal for evaporation and has a flattened bottom.

To impose $n = 1$ at the center we set the global chemical potential³ to

$$\mu_{\text{global}} \equiv \mu(r_{111} = 0) = E_0(r_{111} = 0) + U/2, \quad (5.11)$$

where U is the on-site interaction strength ⁴

At zero temperature, μ_{global} can be obtained as the value of E_0 at the edge of a cloud

³At zero temperature the global chemical potential is equal to the Fermi energy.

⁴For a discussion of the thermodynamic properties of the Hubbard model refer to Chapter 3

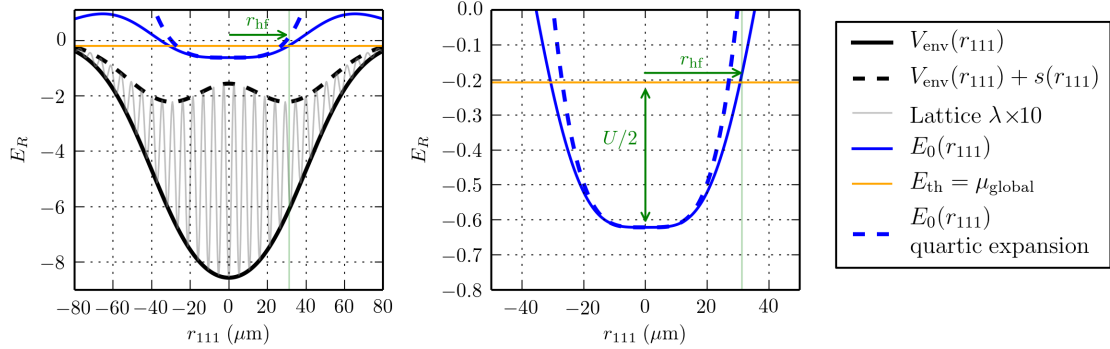


Figure 5.5: Profiles along r_{111} for a $7E_r$ lattice with $w_L = 47\mu\text{m}$. The chemical potential is set to match the threshold for evaporation, and the compensation is set to $g_0 = g_{\text{quartic}}$. This conditions determine the waist ratio $\alpha_{w,\text{evap}}$ (see text). The panel on the right shows the energy of the band close up, and the panel of the left is zoomed out to reveal the small scale of the band energies compared to the energies of the optical dipole potential.

that has a density $n = 1$ throughout. If the radius of this this half-filled cloud is defined as r_{hf} , the $n = 1$ condition can be written as

$$\mu_{\text{global}} = E_0(r_{\text{hf}}) = U/2 + E_0(0) \quad (5.12)$$

This situation is illustrated in Fig. 5.5 (see right panel).

For optimal evaporation in the trap we need μ_{global} to come as close as possible to the evaporation threshold energy, E_{th} . In our setup, E_{th} is the energy required to escape along one of the lattice beams⁵:

$$E_{\text{th}} = -s_0 + E_r \sqrt{s_0/E_r} + g_0 \equiv E_0(0)/3 \quad (5.13)$$

Setting $\mu_{\text{global}} = E_{\text{th}}$. This condition, along with Eq. 5.12, results in

$$U/2 + E_0(0) = E_0(0)/3 \quad \Rightarrow \quad \frac{U}{2} = -\frac{2}{3}E_0(0) \quad \Rightarrow \quad g_0 = -U/4 + s_0 - E_r \sqrt{s_0/E_r} \quad (5.14)$$

We recall that $g_{\text{quartic}} = \frac{4s_0 - 2E_r \sqrt{s_0/E_r}}{4\alpha_w^2}$. From Eq. 5.14 we obtain the equation that defines $\alpha_{w,\text{evap}}$, the beam waist ratio that optimizes evaporation while flattening the bottom

⁵Since we have set the zero of energy at infinity (where no dipole potentials exist), the energy threshold to escape along a beam is negative.

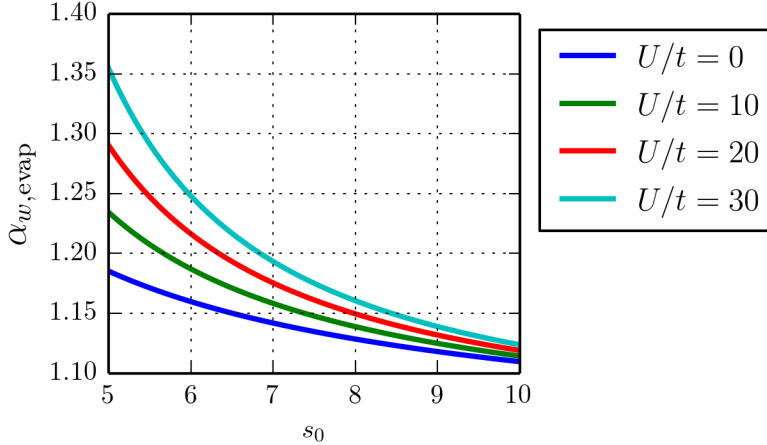


Figure 5.6: Optimal beam waist ratio for enlarging the central flat portion on the band and maximizing the rate of evaporative cooling.

of the band:

$$\frac{4s_0 - 2E_r \sqrt{s_0/E_r}}{4\alpha_w^2} = -U/4 + s_0 - E_r \sqrt{s_0/E_r} \quad (5.15)$$

Solving we obtain:

$$\alpha_{w,\text{evap}}^2 = \frac{4s_0 - 2E_r \sqrt{s_0/E_r}}{4s_0 - 4E_r \sqrt{s_0/E_r} - U} \quad (5.16)$$

In Fig. 5.6 we show plots of $\alpha_{w,\text{evap}}$ for various values of U/t as a function of lattice depth. For a $7 E_r$ lattice $\alpha_{w,\text{evap}}$ is between 1.14 and 1.20, depending on the interaction strength.

We conclude from the analytical considerations presented in this section that, for a $7 E_r$ compensated lattice, a beam waist ratio $\alpha_w \approx 1.17$ and compensation $g_0 = g_{\text{quartic}}$ will offer the best scenario for evaporation while flattening the bottom of the band.

Atom number

We now turn to examine the number of atoms required to realize the setup described above. We need to solve for the half-filling radius, r_{hf} , which is defined by Eq. 5.12 (and also graphically on the right panel of Fig. 5.5). Using $n = 1/a^3$, where a is the lattice spacing, we obtain the atom number from the radius, as $N_{\text{hf}} = \frac{4}{3}\pi(r_{\text{hf}}/a)^3$.

To solve for r_{hf} we can use the power series expansion of the band energy (Eq. 5.9), which for $g_0 = g_{\text{quartic}}$ is

$$E_0(r_{\text{hf}}) - E_0(0) = \left[\frac{2E_r\sqrt{s_0/E_r} - 8s_0 + 4(2s_0 - E_r\sqrt{s_0/E_r})\alpha_w^4}{3w_L^4} \right] r_{\text{hf}}^4 = \frac{U}{2} \quad (5.17)$$

The solution for r_{hf} is then

$$r_{\text{hf}} = \frac{w_L}{\alpha_w} \left[\frac{3(1 - 2\alpha_w^4 + 2\sqrt{s_0/E_r}(\alpha_w^4 - 1))}{2(1 - 2\alpha_w^4 + 4\sqrt{s_0/E_r}(\alpha_w^4 - 1))} \right]^{1/4} \quad (5.18)$$

For $s_0 = 7$, E_r and $\alpha_w = 1.17$, $r_{\text{hf}} \approx 0.7w_L$. For a lattice beam waist $w_L = 47 \mu\text{m}$ this amounts to $N_{\text{hf}} = 990,000$ atoms.

Current setup

In our current setup we use a lattice depth $s_0 = 7E_r$, and we have approximately $w_L = 47 \mu\text{m}$ and $w_C = 40 \mu\text{m}$, which corresponds to $\alpha_w = 1.175$. As we have seen above, we should compensate this sample with $g_{\text{quartic}} = 4.11 E_r$ and populate it with $N \approx 990,000$ atoms. This would yield a half-filled sample with optimal conditions for evaporative cooling in the lattice.

Empirically, we have found that with $N = 200,000$ atoms we obtain the largest amount of AFM correlations as measured by Bragg scattering of light (see Chapter 12). With this number of atoms, the compensation has to be reduced down to $3.6 E_r$ to obtain a density $n = 1$ at the center (see Appendix A for more details on the calibration of the compensation). Reducing the atom number and the compensation moves us away from the optimal scenario for evaporative cooling in the lattice.

There are two other important factors that play a role in our ability to detect AFM correlations. The first one has to do with the stability of our setup and the ability to make a reproducible potential. It turns out that when the optimal value of compensation is used the potential is near an unstable point, such that if the alignment of one of the lattice or compensation beams drifts slightly, the point at the center of the trap becomes a local maxima of the potential and the atoms are pushed away from the it.

The second factor has to do with our measurement procedure. We measure AFM correlations by using Bragg scattering of light. Before probing the system we project its state onto a product state where each lattice site is isolated from the rest and has a well defined occupation. This is done by quickly ramping up the power of the lattice beams to change the lattice depth from $7 E_r$ to $20 E_r$. This achieves the desired projection and freezes any tunneling between neighboring sites. If the atoms occupy a large fraction of the lattice beam waist (the optimal setup described above requires $r_{\text{hf}} = 0.7w_L$), the lattice lock to $20 E_r$ can have a negative effect on the sample, preventing us from observing the AFM correlations. We will elaborate more on this point in § 5.4.2.

5.3 Local density approximation

In what follows we will investigate in more detail the properties of the compensated lattice setup using the LDA+HTSE. In the local density approximation (LDA), we consider each point in the potential as a homogeneous system and we set the condition that all of these local homogeneous systems are in thermal equilibrium with each other at some temperature T . At each point in space we can obtain a local value of the lattice depth, which along with the scattering length, determines the local values of the Hubbard parameters t and U . With these in hand, we can use a known solution to the homogeneous Hubbard model (the HTSE) and obtain local values for the thermodynamic quantities, such as density, double occupancy, entropy, etc. We can then plot the local thermodynamic quantities as a function of trap position to obtain trap profiles.

5.3.1 Format for presentation of LDA results

An example of the results that are obtained within the LDA is shown in Fig. 5.7 for a (nearly) uniform lattice potential plus harmonic confinement, i.e. a traditional lattice setup. Notice that to obtain the uniform lattice plus confinement we use the geometry of our current setup (parameters are s_0, g_0, w_L, w_C), but we set large values of the beam

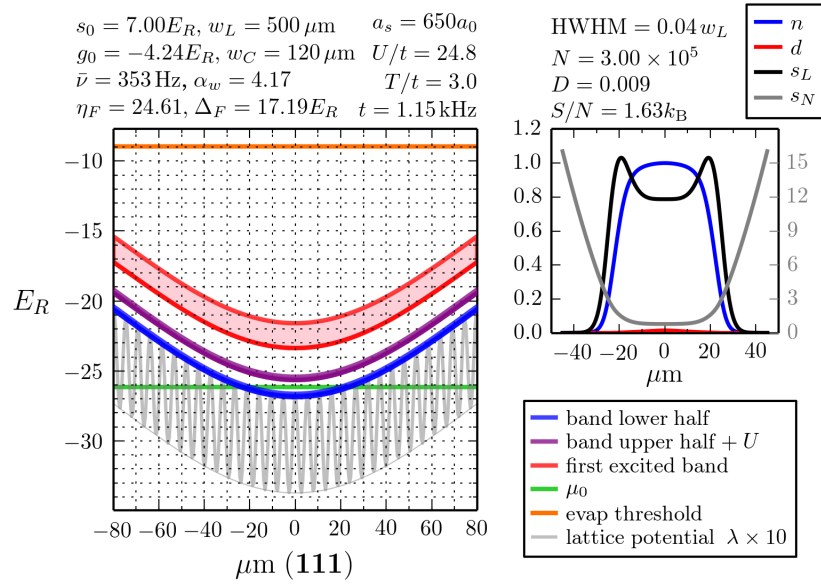


Figure 5.7: Red detuned uniform lattice with additional harmonic confinement. The confinement is adjusted so that the density is one per site at the center with $N = 300,000$ atoms. The temperature is set to $T = 0.12 E_r$, which results in an overall entropy per particle $S/N = 1.63 k_B$. See the text for a detailed explanation of the information in this plot.

waists for the lattice and compensation beams, and set a negative depth ($g_0 < 0$) for the compensation.

In Fig. 5.7 the large panel shows the relevant energies as a function of distance (in μm) along the 111 body diagonal of the lattice. The small panel shows the corresponding profiles of the thermodynamic quantities calculated with the LDA+HTSE. We now give detailed information about each of the labels and regions displayed in Fig. 5.7.

Energies and figures of merit for evaporation

- **Parameters of the potential.** The labels on the top left indicate the depth of the lattice and compensating potentials in recoils, and also the waists used for the lattice and compensating beams. Also shown are the beam waist ratio, α_w and the confinement frequency $\bar{\nu}$, which is calculated from the curvature of the bottom of the lowest band at the center. At the top left we also show values for η_F and Δ_F . The meaning of these quantities will be explained below.

- **Hubbard parameters.** The labels on the top right of the main plot indicate the scattering length and the resulting Hubbard parameters for the given lattice depth. The values of U/t , T/t , and t given are for the center of the sample. As one moves away from the center, t increases and U/t and T/t decrease.
- **Lattice potential** (gray line). This line shows a representation of the modulation produced by the lattice potential. The period of the modulations shown is arbitrary and for illustration purposes only. A thin line is also plotted showing the envelope of the lattice potential.
- **Band lower half** (blue shaded region). This is the blue shaded region on the large panel. The bottom line corresponds to the lowest energy level accessible to a single particle in the local Hubbard Hamiltonian. The top line corresponds to the energy at the center of the lowest band.

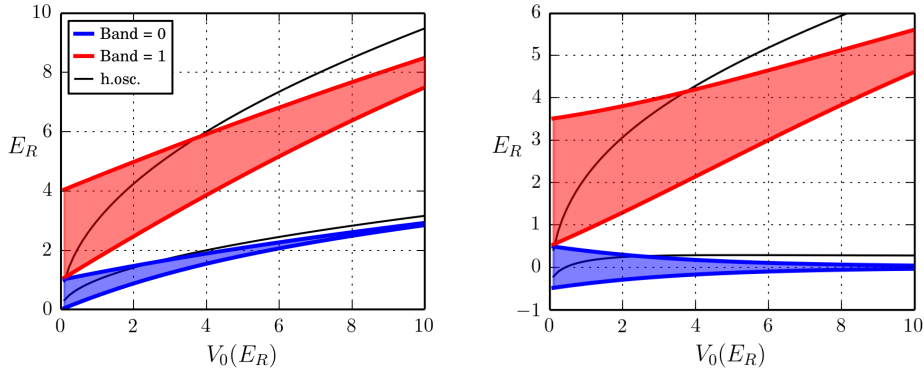
The central energy of the lowest band is an important reference in the Hubbard model, as we saw in Chapter 2. The Hamiltonian for a single particle in a lattice is

$$H = -\frac{\hbar^2}{2m} \frac{\partial}{\partial x^2} + V_0 \sin^2(kx) \quad (5.19)$$

where the zero of energy is at the bottom of a lattice site. The energy level structure as a function of lattice depth is as shown in Fig 5.8a. In second quantized form this single particle Hamiltonian is usually written as

$$H = -t \sum_{\langle ij \rangle, \sigma} a_{i\sigma}^\dagger a_{j\sigma} \quad (5.20)$$

What is typically not mentioned is that writing the Hamiltonian as in Eq. 5.20 implies a lattice-depth-dependent shift of the energy zero, such that the band structure looks like in Fig. 5.8b (see also the discussion after Eq. 2.42). In Chapter 3, when solving the Hubbard model using the HTSE, we used the second quantized form of the Hamiltonian, so the chemical potential is referenced from the center of the lowest band.



(a) Band structure when the zero of energy is at the bottom of the lattice sites. The zero of energy does not change with lattice depth, and the band energies go up almost like the harmonic oscillator state in an individual lattice site.

(b) Band structure when the zero of energy is at the center of the lowest band. This shift is implicit when the Hamiltonian is written in second quantized form as in Eq. 5.20.

Figure 5.8: Band structure in the Hubbard model.

Most importantly, the center of the lowest band is a ubiquitous energy in the Hubbard model because states below that energy will be almost unperturbed by interactions, whereas states above that energy will be affected significantly by interactions (cf. the exact diagonalization eigenvalues for a double-well and a plaquette show in Figs. 3.2 and 3.3).

- **Band upper half + U** (purple shaded region) This region represents the energy levels in the upper half of the lowest band shifted up by the interaction, U . This simple picture is not correct in the interacting many-body system but it provides a good representation of what is going on. The separation U between the band lower half and the band upper half represents the Mott-Hubbard gap.
- **First excited band** (red region). This region is simply bounded by the lowest and highest energies in the first excited band. For this band we do not apply shifts due to interactions. This band is shown so that, at a glance, one can assess whether or not the system satisfies the single band Hubbard regime (see Fig. 2.10).
- **Global chemical potential** (green line). A fixed global chemical potential is set

across the cloud. The local chemical potential is obtained by looking at the separation between μ_0 and the local zero of energy. We remind the reader that the local zero of energy is the point at the center of the lowest band, i.e. the upper boundary of the blue shaded region.

- **Evaporation threshold** (orange line). This is the energy required to escape along one of the lattice beams. It is calculated by looking at the profile of the lowest energy level along the 100 direction and finding its maximum. In most cases the maximum will be at infinity, but for $\alpha_w < 1$ the lowest band profile along 100 can have a local maximum. In such cases the local maximum is used as the evaporation threshold, since an atom has to exceed that energy to escape the trap.
- **Figures of merit for evaporative cooling in the lattice (η_F , Δ_F)**.

When evaporative cooling a thermal gas of atoms, one considers the parameter $\eta = U_{\text{trap}}/k_B T$, where T is the temperature of the gas, and U_{trap} is the energy threshold required for a particle to leave the trap measured with respect to the lowest single-particle energy state. The evaporation rate is suppressed by a factor $\exp(-\eta)$ where typically $\eta \sim 10$ for efficient evaporation, and, as the gas cools down, the trap depth is reduced to force further evaporation [113].

For a deeply degenerate Fermi gas ($T \ll T_F$, where T_F is the Fermi temperature) the evaporation rate is given by [113].

$$\Gamma_{\text{evap}} \propto \gamma_{\text{coll}} \frac{T}{T_F} \exp \left[-\frac{U_{\text{trap}} - k_B T_F}{k_B T} \right] \quad (5.21)$$

where γ_{coll} is the classical collision rate evaluated at the Fermi surface and the exponential factor corresponds to the tail of the Fermi-Dirac distribution. At fixed temperature, the evaporation rate Γ_{evap} will depend only on $U_{\text{trap}} - k_B T_F$, which can be approximated as $\Delta_F = U_{\text{trap}} - \mu_0$. If we consider fixed entropy⁶ rather than fixed temperature, we can write

$$\Gamma_{\text{evap}} \propto \gamma_{\text{coll}} \frac{T}{T_F} \exp \left[\frac{1}{T/T_F} \right] \exp \left[-\frac{1}{T/T_F} \left(\frac{U_{\text{trap}}}{k_B T_F} \right) \right] \quad (5.22)$$

⁶The entropy of a Fermi gas in a harmonic trap is given by $S = N\pi^2 T/T_F$ [114]

We define $\eta_F \equiv U_{\text{trap}}/k_B T_F$ and observe that

$$\Gamma_{\text{evap}} \propto \gamma_{\text{coll}} \frac{T}{T_F} \exp \left[-\frac{\eta_F - 1}{T/T_F} \right] \quad (5.23)$$

For a given value of the entropy (T/T_F), the rate depends only on η_F , and thus the parameter η_F can serve as a figure of merit for evaporation.

In terms of Δ_F or η_F , the effective factor, η_{eff} , which determines the exponential suppression of evaporation due to the trap depth is given by

$$\exp(-\eta_{\text{eff}}) = \frac{T}{T_F} \exp \left[-\frac{\Delta_F}{k_B T} \right] = \frac{T}{T_F} \exp \left[-\frac{\eta_F - 1}{T/T_F} \right] \quad (5.24)$$

Besides the Boltzmann exponential suppression, the evaporation rate is additionally suppressed by a factor T/T_F due to Pauli blocking of one of the final states of a collision, which occurs for $T \ll T_F$ [113].

Thermodynamic quantities

- **Trap profiles of thermodynamic quantities.** The smaller panel on the top left corner on Fig. 5.7 shows the trap profiles of the thermodynamic quantities. It includes the density (n), double occupancy (d), entropy per lattice site (s_L) and entropy per particle (s_N). The entropy per particle is plotted on the right side axis.
- **Overall values of the thermodynamic quantities.** The labels above the smaller panel in Fig. 5.7 indicate the overall trap values of the thermodynamic quantities: number (N), double occupancy (D) and entropy per particle (S/N). These are obtained by integrating the local values across the volume of the trap. Also shown is the half-width at half-max (HWHM) of the density distribution in units of the lattice beam waist.

The LDA results for a given trap, as exemplified by Fig. 5.7, will serve as the point of comparison for different trap parameters. To assess the ability to evaporatively cool in a given setup we will look at η_F and Δ_F . Beyond that, the atom number is important

for practical considerations, and as we will now explain, the resulting overall entropy per particle is an important metric as well.

5.3.2 Entropy redistribution

When considering the possibility of accessing the ground state of the Hubbard Hamiltonian, the overall entropy per particle, $S/(Nk_B)$, is an important quantity. It determines the number of quantum states that are accessible to each atom. At half-filling there is an average of one-particle per site; if the temperature of the system is high, $T \gg U$, there is an equal probability for a site to be empty ($|0\rangle$), singly ($|\uparrow\rangle$ or $|\downarrow\rangle$) or doubly ($|\uparrow\downarrow\rangle$) occupied. With four equally probable states at each lattice site, the entropy per particle⁷ is $\ln 4 = 1.38$.

When the temperature is $T \ll U$, double occupancies and vacancies are suppressed and the system enters the Mott insulating state. At each site, a particle can still be spin-up or spin-down with equal probability, so the entropy per particle becomes $\ln 2 = 0.69$.

If the temperature of the system goes below the Néel temperature, the atoms start to order antiferromagnetically. At zero temperature each site has only one possible quantum state (spin-up or spin-down depending on the lattice site) and the entropy per particle goes to zero⁸.

Numerical studies calculate the highest value of the Néel temperature for a homogeneous simple cubic lattice to be $T_N \approx 0.33t - 0.36t$, occurring at $U/t = 8$ [55, 54, 115]. As we have explained, real systems with a finite number of atoms and external confinement have an inhomogeneous density profile that decays as a function of distance to the center. If one creates an AFM domain at the core of the sample, it will be surrounded by a shell where $n < 1$. We saw in Chapter 3 that the metallic phase at $n < 1$ has an enhanced entropy

⁷Notice that at half-filling any quantity per particle is the same as per lattice site, since $n = 1$

⁸Strictly speaking, at $T = 0$ the entire system can be in only one of two quantum states corresponding to the two possible orientations of the antiferromagnet. The entropy per particle is $\ln 2/N$ which goes to zero for very large N .

capacity which grows as $n \rightarrow 0$. This leads to the concept of entropy redistribution in the inhomogeneous trap: the shell will carry the largest fraction of S/N , and this will result in a lower local value of the entropy at the core, enhancing the possibility of accessing an ordered phase. In Ref. [54] it is shown that the Néel entropy per particle necessary to achieve an ordered phase, which is $S/(Nk_B) \approx 0.36$ for a homogeneous sample, can be as large as $S/(Nk_B) \approx 0.6$ in a harmonically trapped sample.

This shows that the presence of the trap, although a deviation from the ideal model, serves as means to facilitate the realization of ordered phases. When considering a particular implementation of the potential, there is a trade-off between entropy redistribution and flatness of the band. In the limit of a square-well confinement there is no entropy redistribution at all, but if the AFM phase is realized it will occupy the entire trap. On the other hand for a harmonic trap entropy redistribution enables the creation of an AFM core at slightly larger entropies than in the homogeneous case, but the AFM domain will occupy a small fraction of the sample.

When comparing different trapping potentials, there are two ways to quantify the amount of entropy redistribution. One can calculate the trap properties at a fixed value of S/N and compare the resulting temperature for the different trap parameters; the one with the lowest T will be better at entropy redistribution. Alternatively, one can do the calculation at fixed T/t and compare the resulting values of S/N . At fixed T a larger value of S/N is indicative of better entropy redistribution.

5.4 Results

After explaining the results that the LDA calculation can offer for a given trap, and introducing the figures of merit for evaporation and entropy redistribution, we will now show results for different values of the beam waist ratio, α_w .

We start by considering the evaporation figure of merit. We set the global chemical

potential such that $n = 1$ at the center of the sample and we find the largest compensation that the setup will tolerate based on the following constraints:

Constraint 1: The lowest band is required to have positive curvature at the origin (avoid Mexican hat type band profile). Also, the resulting density profile is required to decrease monotonically as a function of distance from the center.

Constraint 2: The thermal tail of the Fermi distribution is required to be negligible below the asymptotic energy of an atom along one of the lattice axes (avoid spilling atoms into the lattice beams). This condition can be written as

$$\mu + T < E_{100}(\infty),$$

where $E_{100}(\infty)$ is the asymptotic bottom of the band along the 100 lattice beam.

Constraint 3: The thermal tail of the Fermi distribution is required to be negligible below the threshold energy for evaporation:

$$\mu + T < E_{\text{th}}$$

Depending on the value of α_w one of these three constraints will determine the largest compensation. Below we explain the possible scenarios:

Scenario 1, $\alpha_w = \alpha_{w,\text{evap}}$

This is the optimal scenario for both band flattening and evaporation. In this case the curvature of the lowest band at the origin is zero (optimal flattening), and $\mu + T = E_{\text{th}}$ (optimal evaporation). Back in Eq. 5.16 we used a zero temperature analytical model to derive an expression for $\alpha_{w,\text{evap}}$, which we found to be $\alpha_{w,\text{evap}} \approx 1.15$ for $7 E_r$ and $U/t = 24.8$ ($a_s = 650 a_0$).

Scenario 2, $1 < \alpha_w < \alpha_{w,\text{evap}}$

Constraint 3 determines g_0 , evaporation is optimal but band is not optimally flattened.

Scenario 3, $\alpha_w > \alpha_{w,\text{evap}}$

Constraint 1 determines g_0 , band is optimally flattened but evaporation is not optimal.

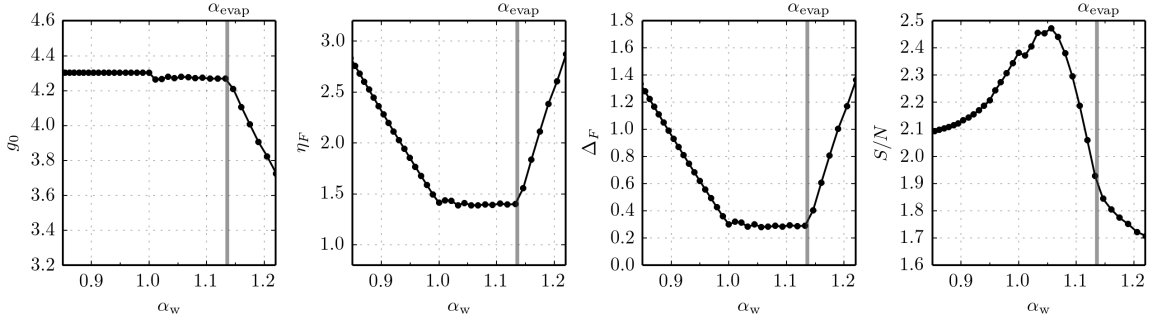


Figure 5.9: Evaporation optimization results for a $7 E_r$ lattice with $a_s = 650 a_0$, obtained at $T = 0.2 E_r$ (equivalent to $T = 5.1t$) at the center. The vertical line on the plots shows the value of $\alpha_{w,\text{evap}}$, where evaporation is optimized and the curvature of the lowest band is zero. For the parameters here $\alpha_{w,\text{evap}}$ is determined by the LDA to $\alpha_{w,\text{evap}} \approx 1.12$

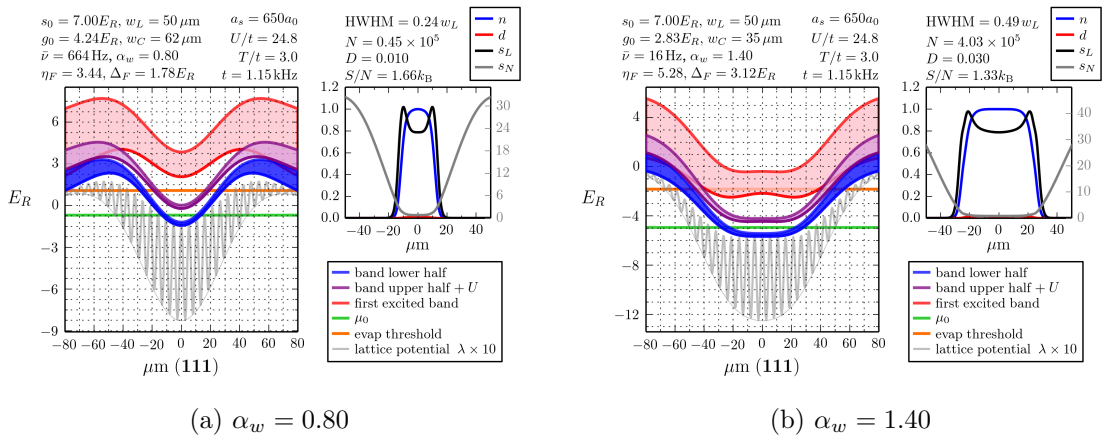


Figure 5.10: Density profiles for $\alpha_w < 1$ and $\alpha_w > \alpha_{w,\text{evap}}$. In both cases evaporation is not optimal. In panel (a) the value of $E_{100}(\infty)$ restricts the chemical potential to a very low value. In panel (b) the bottom of the band is flattened, but a higher compensation (to raise the chemical potential for evaporation) would result in a negative curvature of the band.

Scenario 4, $\alpha_w < 1$

In this case the band cannot be flattened. Evaporation will be optimal only if $E_{\text{th}} = E_{100}(\infty)$.

We run the numerical calculation for various values of α_w , at each point finding the largest possible compensation (to optimize evaporation) allowed by the constraints outlined above. The results for g_0 , η_F , Δ_F , and S/N are shown in Fig. 5.9. Below we make some remarks:

- The figures of merit for evaporation, η_F and Δ_F , are optimized for $1 < \alpha < \alpha_{w,\text{evap}}$
- For $\alpha < 1$ the band cannot be flattened and also evaporation cannot be optimal due to Constraint 2. See Fig. 5.10a.
- For $\alpha > \alpha_{w,\text{evap}}$ the band can be flattened, but using a value of the compensation that does not result in optimal evaporation. See Fig. 5.10b.
- The fourth panel in Fig. 5.9 shows the overall entropy per particle, S/N . This quantity can be used to assess the entropy redistribution at different α_w . We observe that flattening plus optimal evaporation ($\alpha_w = \alpha_{w,\text{evap}}$) does not occur at the same value of α as optimal entropy redistribution (larger S/N at fixed T/t). This is reasonable, because a flattened trap goes towards the limiting case of a square-well potential, where entropy cannot be redistributed at all. Experimentally, having a value of α that is easily tunable, such that one can explore the different possibilities, is a very desirable feature for a future setup.

5.4.1 Atom number

We have seen that the above results depend only on the ratio $\alpha_w = w_L/w_G$ and are thus independent of length scale. For practical purposes it is necessary to consider the length scale because it determines the total atom number required to realize a certain configuration. In Fig. 5.11, we show the results for the atom number for different values of w_L . We see in the figure that as one approaches $\alpha_{w,\text{evap}}$, the sample starts to occupy a much larger fraction of the lattice beam waist. This in turn leads to a much larger atom number required to realize the setup. Beyond the practical issue of cooling down the necessary number of atoms, there are other reasons to try to avoid a large value of HWHM/ w_L . These have to do with the fact that the local value of the lattice depth goes down with radius and, at the edge, the system will not be described by a single band Hubbard model. Additionally, for lower lattice depths the lattice locking protocol may excite atoms to higher bands, complicating the interpretation of experimental measurements.

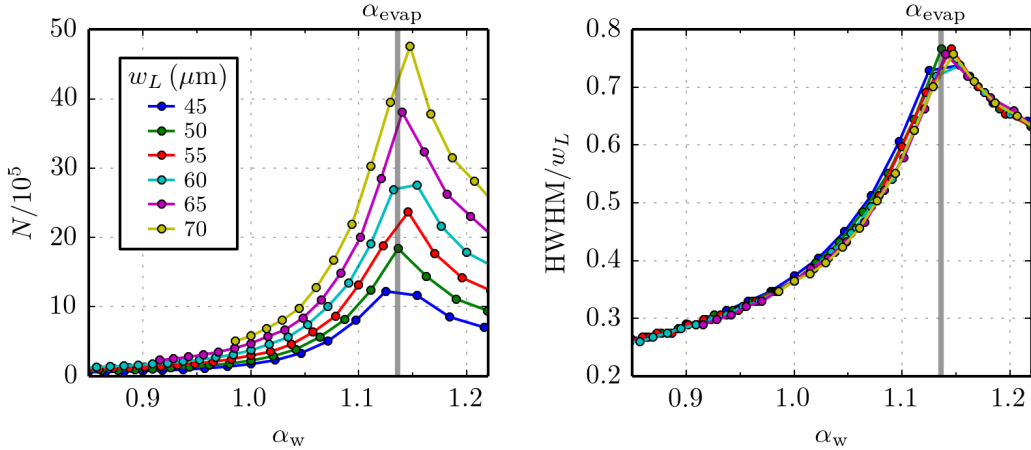


Figure 5.11: Atom number vs. α_w (left), and half-width at half max (HWHM) in units of the lattice beam waist w_L (right). The right panel shows that as the value of $\alpha_{w,\text{evap}}$ is approached, the density distribution occupies a much larger fraction of the lattice beam waist.

5.4.2 Timescales for locking the lattice

In order to freeze the density distribution, for instance prior to taking a Bragg scattering measurement, the lattice locking timescale must be much faster than the tunneling rate t . However, if the ramp rate is too fast, transitions can be excited to higher bands of the lattice. The relevant energy scales are the band gap, Δ , and the bandwidth $W = 12t$.

The ratio Δ/W depends only on the lattice depth and is given analytically (in the limit of a deep lattice) by

$$\Delta/W = \frac{2\sqrt{s}}{(48/\sqrt{\pi})s^{3/4}e^{-2\sqrt{s}}} \quad (5.25)$$

In Fig. 5.12 (right panel) we show the ratio Δ/W as function of r_{111}/w_L , using the analytical model of the trap introduced in §5.2. We see in the figure that, for a $7 E_r$ lattice, the cloud radius must be kept below $\approx 0.63w_L$ to maintain a reasonable ratio of at least $\Delta/W > 2$ throughout the sample.

Optimally flattened samples with $\alpha_w \approx 1.10 - 1.15$ can result in sample radii as large as $r = 0.7 w_L$. For a $7 E_r$ this poses a problem with the edge of the cloud when interpreting measurements that have to be performed after locking the lattice. To avoid lattice locking complications one can select $\alpha_w < \alpha_{w,\text{evap}}$.

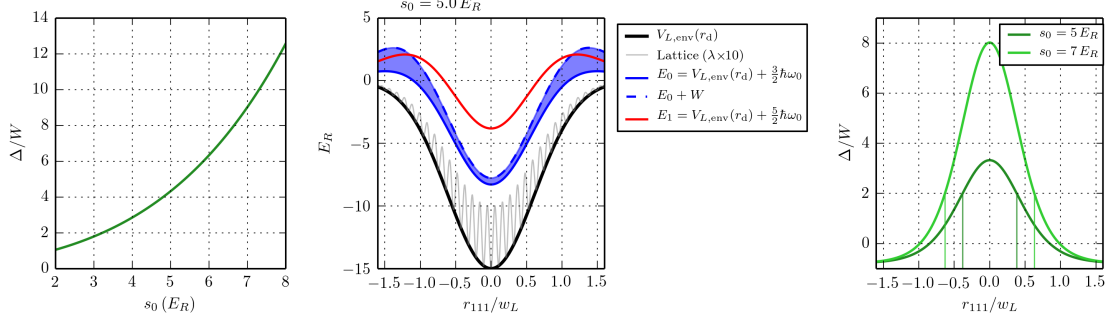


Figure 5.12: Lattice locking considerations. To avoid issues when locking the lattice, a large ratio Δ/W should be maintained across the extent of the cloud. The left panel shows the general dependence of Δ/W on lattice depth (deep lattice limit), the central panel shows energy profiles for a $5 E_R$ lattice, and the right panel shows the spatial dependence of Δ/W for a $5 E_R$ and a $7 E_R$ lattice.

In our current setup $\alpha_w \approx \alpha_{w,\text{evap}}$ and we have undercompensated the setup slightly, for a $7 E_r$ deep lattice we use $g_0 \approx 3.6 - 3.8 E_r$ rather than the optimal $4.3 E_r$. This allows us to realize half-filling with the atom number that we have available ($N \approx 2 \times 10^5$ atoms) and avoid significant issues when locking the lattice ($r \approx 0.4w_L$). In a future implementation it will be desirable to have the possibility of changing α_w and try to realize setups with $\alpha_w \approx 1.05$ where evaporation will still be optimal, entropy redistribution will be best, and there won't be issues locking the lattice.

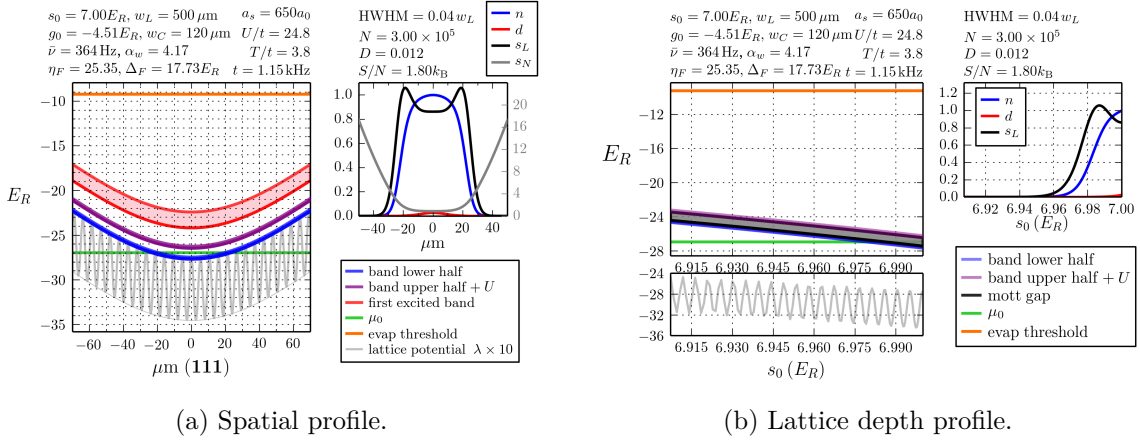
5.5 Comparison between different kinds of traps

We now consider different setups and look closely at the possibilities for evaporative cooling in the lattice and entropy redistribution. We take into account the atom number as a practical consideration, and do the comparisons at constant entropy (rather than at constant temperature). The parameters for the comparison are as follows:

1. $N = 300,000$ atoms

2. $S/N = 1.8 k_B$

3. $n = 1$ at the center



(a) Spatial profile.

(b) Lattice depth profile.

Figure 5.13: Uniform lattice with harmonic confinement

4. $a_s = 650 a_0$

The setups that we consider are:

Harmonic confinement

This is the traditional lattice setup with a nearly uniform lattice depth throughout and external harmonic confinement. See profiles in Fig. 5.13.

Optimal compensated

This is a compensated lattice setup with $\alpha_w = \alpha_{w,\text{evap}}$, where evaporation is optimized and the bottom of the band is flattened. See profiles in Fig. 5.14.

Current setup

This is our current setup with $\alpha_w = \alpha_{w,\text{evap}}$, but undercompensated. See profiles in Fig. 5.15.

Proposed setup

This is a proposed setup for future implementation with $\alpha_w = 1.05$ and optimal evaporation but not optimal band flattening. See profiles in Fig. 5.16.

The reader can examine in detail the profiles obtained for each setup. The ranking according to the evaporation figures of merit is shown in Table 5.1, and a ranking according to the entropy redistribution capacity is shown in Table 5.2.

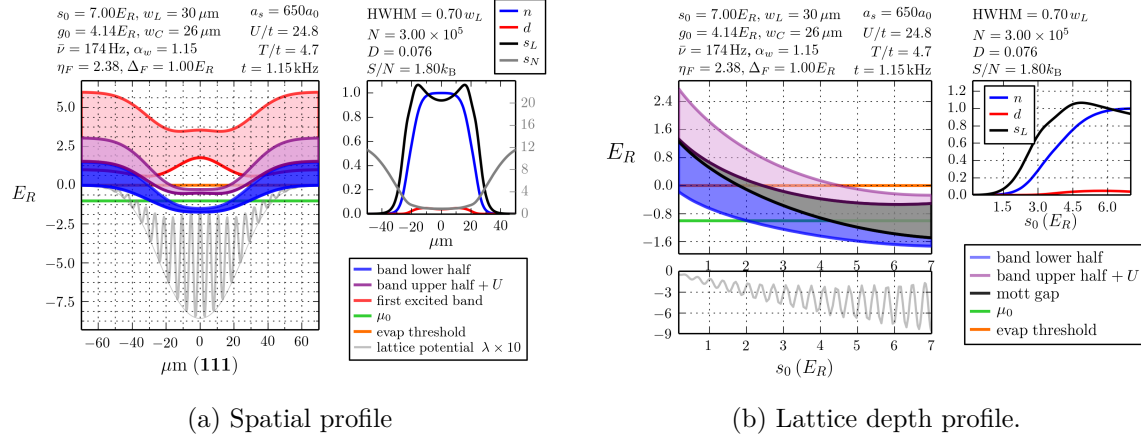


Figure 5.14: **Optimal compensated trap**, $\alpha_w = 1.15$ In this case we have to use very small beam waists to meet the atom number requirement.

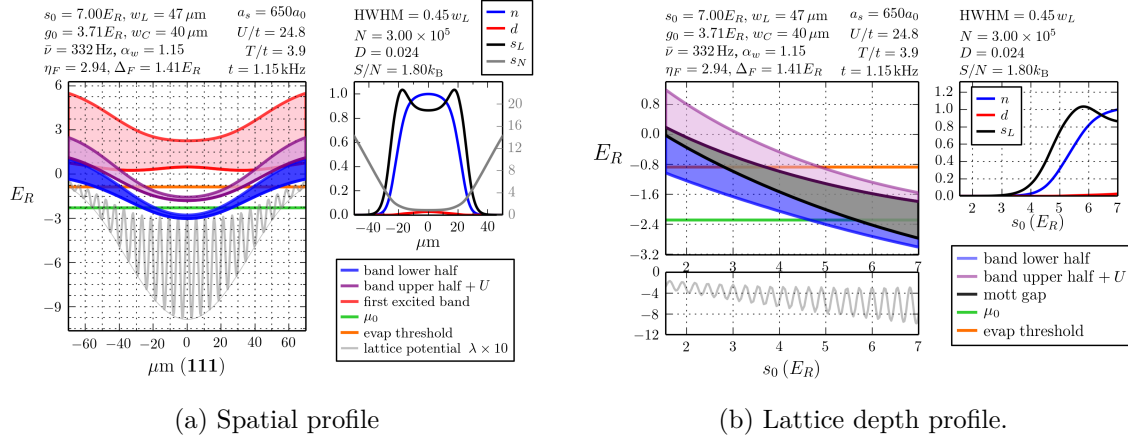
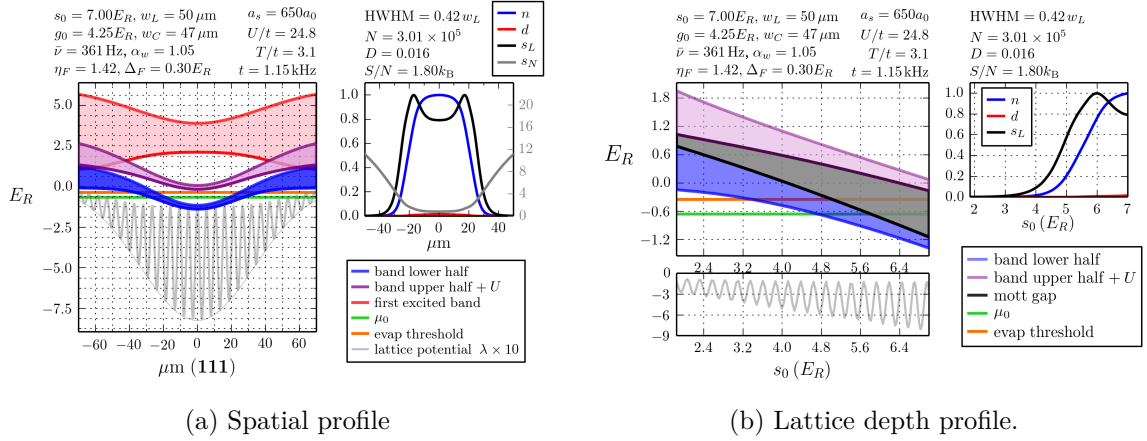


Figure 5.15: **Current setup.** In this case we have to reduce the green compensation so even though the value of α_w is correct for optimal flattening, we use less compensation in order to have $n = 1$ at the center with a lower number of atoms.

rank	η_F	$\Delta_F(E_r)$	
1	1.42	0.30	Proposed setup
2	2.38	1.00	Optimal flattening
3	2.94	1.41	Current setup
4	25.4	17.8	Uniform lattice with harmonic confinement

Table 5.1: Ranking of the different traps according to the evaporation figures of merit, η_F and Δ_F .

Figure 5.16: **Proposed setup**, $\alpha_w = 1.05$, $w_L = 50 \mu\text{m}$

rank	T/t	scenario
1	2.4	Proposed setup
2	2.9	Uniform lattice with harmonic confinement
3	3.0	Current setup
4	3.6	Optimal flattening

Table 5.2: Ranking of the different traps according to the entropy redistribution capacity. Since the simulation was done at constant entropy, a lower value of T/t indicates a better redistribution of the entropy.

We can see that our current setup, due to the fact that it is slightly undercompensated, does not reach its potential for evaporative cooling. As a trade-off, undercompensation results in better entropy redistribution. The proposed setup would be better for evaporation and also for redistribution of the entropy. A traditional setup, with a nearly uniform lattice and harmonic confinement, offers no possibility for evaporative cooling at all. In that case the energy levels are buried deep by the optical potentials, which results in very large values of η_F and Δ_F .

To summarize, in this chapter we have given details about the design of the compensated optical lattice potential and the practical aspects that limit our current setup. We introduced the figures of merit for evaporation, and the entropy redistribution as metrics with which to characterize a given trap. Our studies have indicated the direction in which we want to go when designing a future setup. Having an easily tunable value of the beam

waist ratio α_w will allow optimizing the performance of the trap.

The code written to realize the LDA simulations with the HTSE solutions of the Hubbard model and produce all of the results in this chapter is available for download at [116].

More technical details about the current implementation of the lattice potential were relegated to Appendix A.

6. Diagnostic tools I: Polarization phase-contrast imaging

Experiments with ultracold atoms rely on a variety of very well established measurement and diagnostic techniques [117, 118]. Most measurement techniques are based on the possibility of imaging the column density distribution of the sample *in-situ* or after releasing it in time-of-flight (TOF). These include absorption imaging, fluorescence imaging, and phase-contrast imaging. More complicated techniques change the state of the gas prior to imaging in order to gain access to other physical quantities. These include, for example, Stern-Gerlach separation in a magnetic field gradient, association of free atoms into molecules using a Feshbach resonance, or band-mapping of atoms in an optical lattice, just to name a few.

From the raw images obtained after a measurement one has to implement analysis and diagnostic tools, which extract the relevant physical quantities. For instance, the shape or size of the column density distribution (*in-situ* or after TOF) of a Fermi gas in a harmonic trap can be used to obtain its temperature.

Over the course of this thesis we have elaborated and improved some of the already established measurement and diagnostic techniques in the lab (polarization phase-contrast imaging and Fermi gas thermometry). We have also developed new techniques not previously available in the lab (measurement of double occupancies in an optical lattice using molecular association), and pioneered a new technique (spin sensitive Bragg scattering of light) to probe the spin-ordering of atoms in lattices. The following chapters are devoted to the detailed explanation of those techniques that were improved or newly developed for the work in this thesis.

6.1 Polarization phase-contrast imaging

Polarization phase-contrast imaging (PPCI) has been a workhorse at the Hulet lab since the early days [119, 120]. It is used at various stages of our experiment to measure the *in-situ* column density of the dilute gas. The general goal of imaging is to obtain a quantitative measure of the density distribution of the sample by analyzing the intensity, phase and polarization profiles of light that has gone through it. The widely used absorption imaging technique looks at the intensity attenuation profile for a resonant, or nearly resonant laser beam. On the other hand, light with a larger detuning is used for PPCI. Rather than looking for attenuation of the intensity, the information about the density of the gas can be extracted from the phase profile of the transmitted beam. Techniques that rely on phase change are referred to as dispersive, in contrast to absorptive techniques which measure intensity changes.

Traditionally, a two-level model of the atom has been used in our lab in order to relate the measured phase profile to an atomic density. In an optical lattice with site spacing $a = 532 \text{ nm}$, a density of one atom per site corresponds to $6.64 \times 10^{12} \text{ cm}^{-3}$. At these densities the detuning from the atomic transition must be increased in order to avoid non-linearities in the phase to density conversion, which can occur if the phase change of the electric field after going through the atom cloud is $> \pi/5$. Typically, a detuning $< 100 \text{ MHz}$ is used for PPCI in our lab for samples of moderate densities and the two-level model is sufficient to obtain the atomic density. However, for some of our samples in the optical lattice and the optical dipole trap (see Chapter 4 for a description of the experimental setup) we have had to increase it to several hundred MHz. When the detuning becomes comparable to the energy spacing between the excited state and other fine-structure levels in the excited manifold, the contributions to the phase change from these other states becomes non-negligible and must be taken into account when calculating the atomic density distribution from the measured phase profile.

Here we derive the formulas that are used to convert phase-contrast to atomic density

including the effects from other fine-structure levels in the excited state. The treatment is separated into five parts:

1. We calculate how the light is affected by the polarized atomic cloud. This is done classically, using Maxwell's equations and assuming that we know the polarization of the medium.
2. We calculate the polarization of the atomic cloud, which results from the oscillating electric field of the imaging light acting as a perturbation on the atoms. We derive the form of the electric susceptibility tensor, which determines the polarization response of the gas to the oscillating field.
3. We evaluate the elements of the susceptibility tensor for the atomic structure relevant to us, namely a spin-mixture of ${}^6\text{Li}$ atoms at high magnetic field.
4. We then proceed to derive expressions that relate the phase profile of the transmitted beam to the column density of the cloud.
5. We examine the general experimental setup which allows one to convert the phase profile into an intensity profile that can be recorded on a CCD camera.

To start out with some context, Fig. 6.1 shows the energy level structure relevant for our experiment. We typically use a spin mixture of hyperfine states $|1\rangle$ and $|2\rangle$ in the $F = 1/2$ manifold of the $2S_{1/2}$ ground state. The magnetic field where we carry out our experiments is usually > 300 G, where the energy dependence of states is linear with field. The red lines in Fig. 6.1 indicate state $|1\rangle$ and the excited state involved in the imaging process. For a large red detuning, the spacing between the $m_J = -1/2$ and $m_J = -3/2$ excited states can be comparable to the detuning. If blue-detuned light is used the contributions from states other than $m_J = -3/2$ will be even more significant.

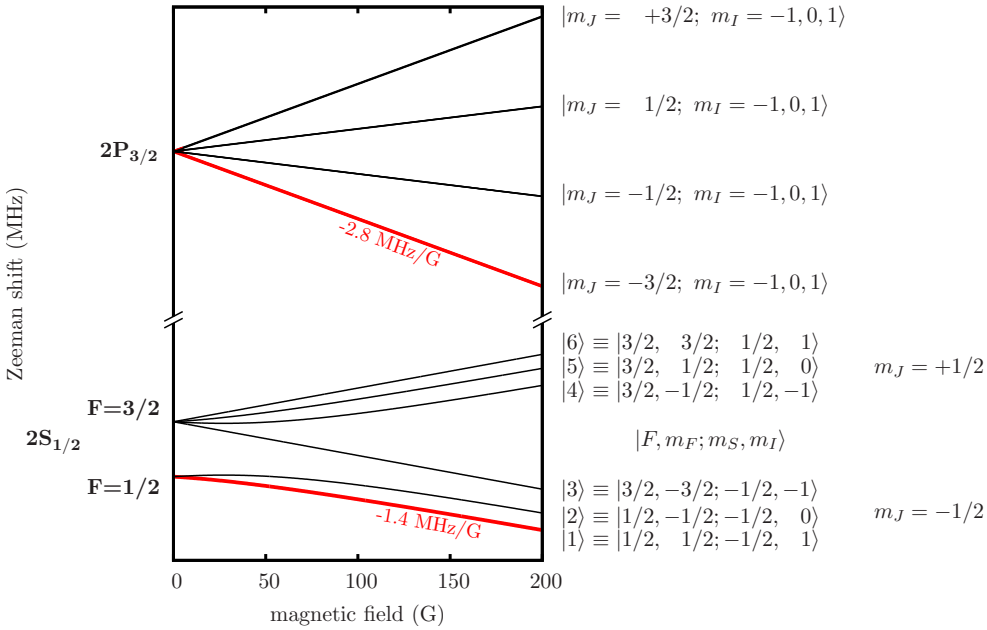


Figure 6.1: Level diagram relevant for imaging transitions. The levels relevant for imaging are highlighted in red.

6.1.1 Transmission of light through a polarized gas

The electric field of the light that traverses the atomic cloud can be written in general form (see Sec. 6.1 of [121]) as

$$\mathcal{E}(\mathbf{r}, t) = \text{Re}\{\mathcal{E}_0 e^{i(\mathbf{k} \cdot \mathbf{r} - \omega t + \varphi)} [\cos \zeta \hat{\mathbf{e}}_1 + \sin \zeta e^{i\phi} \hat{\mathbf{e}}_2]\} \quad (6.1)$$

where $\hat{\mathbf{e}}_{1,2}$ are two orthogonal unit vectors perpendicular to the wave vector \mathbf{k} and perpendicular to each other, ϕ is the relative phase between the two polarization components, \mathcal{E}_0 is the electric field amplitude, φ is an overall phase, and ζ is related to the angle of the polarization ellipse with respect to $\hat{\mathbf{e}}_1$ and $\hat{\mathbf{e}}_2$.

The wave equation in a dielectric medium can be obtained from Maxwell's equations¹, and is given by

$$\nabla^2 \mathcal{E} - \frac{1}{c^2} \frac{\partial^2 \mathcal{E}}{\partial t^2} = \frac{4\pi}{c^2} \frac{\partial^2 \mathbf{P}}{\partial t^2}. \quad (6.2)$$

¹Note that Gaussian units are used in this section, following the treatment in [121]

Here, the medium polarization \mathbf{P} (which is induced by the imaging light) corresponds to the dipole moment per unit volume. If we know the dipole moment of a single atom $\langle d \rangle$ then

$$\mathbf{P} = n\langle d \rangle \quad (6.3)$$

where n is the density of the gas.

Just as the electric field was parameterized in Eq. 6.1, the polarization can be written in terms of the four real parameters P_i as

$$\mathbf{P} = \text{Re}\{e^{i(\mathbf{k} \cdot \mathbf{r} - \omega t + \varphi)}[(P_1 - iP_2)\hat{\mathbf{e}}_1 + (P_3 - iP_4)\hat{\mathbf{e}}_2]\} \quad (6.4)$$

Using the oscillatory time dependence of \mathcal{E} and \mathbf{P} the wave equation is reduced to

$$\frac{\partial^2 \mathcal{E}}{\partial \ell^2} + k^2 \mathcal{E} = -4\pi k^2 \mathbf{P} \quad (6.5)$$

where ℓ is the distance along the light propagation direction.

The parameterized electric field and polarization are plugged into the wave equation, and one proceeds to neglect terms that are of second order in the derivatives of the electric field parameters. This is justifiable, as long as the fractional change of the parameters is small over distances of the order of the imaging light wavelength, which is certainly the case for our dilute atom cloud. The resulting expressions for the change of the field parameters per unit distance are:

$$\begin{aligned} \frac{1}{\mathcal{E}_0} \frac{d\mathcal{E}_0}{d\ell} &= \frac{2\pi\omega}{\mathcal{E}_0 c} (P_2 \cos \zeta + P_4 \sin \zeta) \\ \frac{d\varphi}{d\ell} &= \frac{2\pi\omega}{\mathcal{E}_0 c} \left(\frac{P_1}{\cos \zeta} \right) \\ \frac{d\zeta}{d\ell} &= \frac{2\pi\omega}{\mathcal{E}_0 c} (-P_2 \sin \zeta + P_4 \cos \zeta) \\ \frac{d\phi}{d\ell} &= \frac{2\pi\omega}{\mathcal{E}_0 c} \left(\frac{P_1 \sin \zeta - P_3 \cos \zeta}{\sin \zeta \cos \zeta} \right) \end{aligned} \quad (6.6)$$

6.1.2 Polarization of the cloud

If we can calculate the electric dipole moment induced on one atom, $\langle \mathbf{d} \rangle$, and if we know the density of the cloud, $n(\vec{r})$, then we can simply write the induced polarization as

$$\mathbf{P}(\mathbf{r}) = \langle \mathbf{d} \rangle n(\mathbf{r}) \quad (6.7)$$

An ensemble of atoms (in which each atom may be in a different quantum state) is best described using the density matrix, which is defined as

$$\rho = \frac{1}{N} \sum_{i=1}^N |\psi_i\rangle\langle\psi_i| \quad (6.8)$$

where the i^{th} atom in the ensemble is in state $|\psi_i\rangle$. The expectation value of the electric dipole moment is then given by

$$\begin{aligned} \langle \mathbf{d} \rangle &= \text{Tr}(\rho \mathbf{d}) \\ &= \sum_{mn} \rho_{mn} \langle n | \mathbf{d} | m \rangle \end{aligned} \quad (6.9)$$

Since the dipole operator only couples states of different parity, the terms that contribute to this sum correspond to the pair m, n being a ground and excited state pair.

The equation of motion for the density matrix (Liouville equation) follows from the Schrodinger equation for the $|\psi_i\rangle$, and including the spontaneous decay of the excited state [121] can be written as

$$i\hbar\dot{\rho} = [H, \rho] - \frac{i\hbar}{2}\{\hat{\Gamma}, \rho\} + i\hbar\text{Tr}(F\rho) \quad (6.10)$$

where $\hat{\Gamma}$ is the relaxation matrix, a diagonal matrix with the decay rate of each state on the diagonal (see Sec. 5.5 in [121]), and F is the spontaneous emission operator (see Sec. 12.1 in [121]). The Hamiltonian H can be split into a diagonal part, H_0 , which includes the level structure of the atom in the presence of a magnetic field, and the time dependent perturbation from the electric field $\hbar V$:

$$H = H_0 + \hbar V \quad (6.11)$$

The matrix element ρ_{ge} , where g, e represent a ground and an excited state respectively, can be plugged into the Liouville equation to obtain

$$\begin{aligned}\dot{\rho}_{ge} &= \frac{1}{i\hbar} \langle g | [H_0, \rho] | e \rangle - i \langle g | [\hbar V, \rho] | e \rangle - \frac{1}{2} \langle g | \{\hat{\Gamma}, \rho\} | e \rangle + \langle g | \text{Tr}(F\rho) | e \rangle \\ &= -i\tilde{\omega}_{ge}\rho_{ge} - i \sum_p (V_{gp}\rho_{pe} - \rho_{gp}V_{pe}) + \sum_{rs} F_{ge}^{sr}\rho_{rs}\end{aligned}\quad (6.12)$$

where

$$\tilde{\omega}_{ge} = (E_g - E_e)/\hbar - i\Gamma_e/2 \quad (6.13)$$

We notice that $F_{ge}^{sr} = 0$, since F is only nonzero if the lower indices are both ground states and the upper indices are both excited states. So we are left with

$$\dot{\rho}_{ge} = -i\tilde{\omega}_{ge}\rho_{ge} - i \sum_p (V_{gp}\rho_{pe} - \rho_{gp}V_{pe}) \quad (6.14)$$

At this point we switch to the rotating frame (see Sec. 10.2.2 in [121]), in which the density matrix $\tilde{\rho}$ can be obtained from

$$\tilde{\rho} = U^\dagger \rho U \quad (6.15)$$

where U is a unitary diagonal matrix with entries given by

$$U_{mm} = \begin{cases} 1 & \text{if } m \text{ is a ground state} \\ e^{i(\mathbf{k} \cdot \mathbf{r} - \omega t)} & \text{if } m \text{ is an excited state} \end{cases} \quad (6.16)$$

We thus have $\tilde{\rho}_{ge} = \rho_{ge}e^{i(\mathbf{k} \cdot \mathbf{r} - \omega t)}$, and the equation of motion for the ρ_{ge} matrix element in the rotating frame is

$$\begin{aligned}\dot{\tilde{\rho}}_{ge} &= -i\omega\tilde{\rho}_{ge} + \dot{\rho}_{ge}e^{i(\mathbf{k} \cdot \mathbf{r} - \omega t)} \\ &= -i\omega\tilde{\rho}_{ge} + \left[-i\tilde{\omega}_{ge}\rho_{ge} - i \sum_p (V_{gp}\rho_{pe} - \rho_{gp}V_{pe}) \right] e^{i(\mathbf{k} \cdot \mathbf{r} - \omega t)} \\ &= -i\tilde{\rho}_{ge}\tilde{\omega}'_{ge} - i \sum_p (V_{gp}\rho_{pe} - \rho_{gp}V_{pe}) e^{i(\mathbf{k} \cdot \mathbf{r} - \omega t)}\end{aligned}\quad (6.17)$$

where

$$\tilde{\omega}'_{ge} = \omega + (E_g - E_e)/\hbar - i\Gamma_e/2 \equiv \Delta_{ge} - i\Gamma_e/2 \quad (6.18)$$

We recall that the interaction term is of the electric dipole type:

$$\hbar V = -\mathbf{d} \cdot \mathcal{E} = -\mathbf{d} \cdot \mathcal{E}_0 \text{Re}[\hat{\boldsymbol{\varepsilon}} e^{i(\mathbf{k} \cdot \mathbf{r} - \omega t)}] = -\mathbf{d} \cdot \frac{\mathcal{E}_0 (\hat{\boldsymbol{\varepsilon}} e^{i(\mathbf{k} \cdot \mathbf{r} - \omega t)} + \hat{\boldsymbol{\varepsilon}}^* e^{-i(\mathbf{k} \cdot \mathbf{r} - \omega t)})}{2}. \quad (6.19)$$

Introducing this in the equation of motion for $\tilde{\rho}_{ge}$, neglecting the rapidly oscillating terms, and making use of the fact that the wavelength of the light is much larger than the extent of the atom (so that the spatially dependent exponential can be taken outside of matrix elements) one gets to

$$\dot{\tilde{\rho}}_{ge} = -i\tilde{\rho}_{ge}\tilde{\omega}'_{ge} + \frac{i}{2\hbar} \sum_p [\mathbf{d}_{gp}\rho_{pe} - \rho_{gp}\mathbf{d}_{pe}] \cdot \mathcal{E}_0 \hat{\boldsymbol{\varepsilon}}^* \quad (6.20)$$

which has a steady-state solution given by

$$\tilde{\rho}_{ge} = \frac{1}{2\hbar\tilde{\omega}'_{ge}} \sum_p [\mathbf{d}_{gp}\rho_{pe} - \rho_{gp}\mathbf{d}_{pe}] \cdot \mathcal{E}_0 \hat{\boldsymbol{\varepsilon}}^* \quad (6.21)$$

Finally, we neglect coherences and populations in the excited states ($\rho_{ee'} = 0$) and coherences in the ground states ($\rho_{gg'} = 0$ if $g \neq g'$). This can be justified since the perturbation is weak and is not expected to modify the initial excited state populations (which are zero). Furthermore, coherences between ground states $g \neq g'$ can only be expected if there is population in the excited state: these coherences can only develop if there is excitation from one ground state and then spontaneous or stimulated emission to a different ground state, so they can be neglected in the weak perturbation limit. The final result is

$$\tilde{\rho}_{ge} = -\frac{\mathbf{d}_{ge} \cdot \mathcal{E}_0 \hat{\boldsymbol{\varepsilon}}^*}{\hbar(2\Delta_{ge} - i\Gamma)} \rho_{gg} \quad (6.22)$$

which after plugging back into the equation for the expectation value of the dipole moment gives

$$\begin{aligned} \langle \mathbf{d} \rangle &= \sum_{ge} 2\text{Re}[\rho_{ge}\mathbf{d}_{eg}] \\ &= \sum_{ge} 2\text{Re}[\tilde{\rho}_{ge}e^{-i(\mathbf{k} \cdot \mathbf{r} - \omega t)}\mathbf{d}_{eg}] \\ &= \sum_{ge} \rho_{gg} \text{Re}[-\frac{\mathbf{d}_{ge} \cdot \mathcal{E}_0 \hat{\boldsymbol{\varepsilon}}^*}{\hbar(\Delta_{ge} + i\Gamma/2)} e^{-i(\mathbf{k} \cdot \mathbf{r} - \omega t)} \mathbf{d}_{eg}] \\ &\equiv \sum_{ge} \rho_{gg} \text{Re}[-\frac{\mathbf{d}_{eg} \cdot \mathcal{E}_0 \hat{\boldsymbol{\varepsilon}}}{\hbar(\Delta_{ge} - i\Gamma/2)} e^{i(\mathbf{k} \cdot \mathbf{r} - \omega t)} \mathbf{d}_{ge}] \\ &= \sum_{ge} \rho_{gg} \text{Re}[-\frac{\mathbf{d}_{eg} \cdot \tilde{\mathcal{E}}}{\hbar(\Delta_{ge} - i\Gamma/2)} \mathbf{d}_{ge}] \end{aligned} \quad (6.23)$$

where in the last line $\tilde{\mathcal{E}} = \mathcal{E}_0 \hat{\epsilon} e^{i(\mathbf{k} \cdot \mathbf{r} - \omega t)}$ is the complex electric field vector (not to be confused with the actual electric field vector which is a real quantity).

Labeling the cartesian components of \mathbf{d} with Greek upper indices and implying sums over repeated Greek indices (Einstein notation), we have

$$\begin{aligned}\langle d^\mu \rangle &= \sum_{ge} \rho_{gg} \operatorname{Re} \left[-\frac{d_{eg}^\nu \tilde{\mathcal{E}}^\nu d_{ge}^\mu}{\hbar(\Delta_{ge} - i\Gamma/2)} \right] \\ &= \operatorname{Re} \left[\left(\sum_{ge} -\rho_{gg} \frac{d_{eg}^\nu d_{ge}^\mu}{\hbar(\Delta_{ge} - i\Gamma/2)} \right) \tilde{\mathcal{E}}^\nu \right]\end{aligned}\quad (6.24)$$

and from here we can write

$$\mathbf{P} = \operatorname{Re} [\boldsymbol{\chi} \tilde{\mathcal{E}}] \quad (6.25)$$

where we have defined the electric susceptibility tensor as

$$\begin{aligned}\chi_{\mu\nu} &= -\frac{n}{\hbar} \sum_{ge} \rho_{gg} \frac{d_{eg}^\nu d_{ge}^\mu}{\Delta_{ge} - i\Gamma/2} \\ &= -\frac{n}{\hbar} \sum_{ge} \rho_{gg} \frac{\langle e | d^\nu | g \rangle \langle g | d^\mu | e \rangle}{\Delta_{ge} - i\Gamma/2}\end{aligned}\quad (6.26)$$

6.1.3 Susceptibility for ${}^6\text{Li}$ atoms at high magnetic field

Going back to the parameterization scheme for the electric field and the medium polarization, introduced in Eqs. 6.1,6.4, we can identify²:

$$(P_1 - iP_2)\hat{e}_1 + (P_3 - iP_4)\hat{e}_2 = \mathcal{E}_0 \boldsymbol{\chi} [\cos \zeta \hat{e}_1 + \sin \zeta e^{i\phi} \hat{e}_2] \quad (6.27)$$

Using $\hat{e}_1 = [1 0]$ and $\hat{e}_2 = [0 1]$ this can be written in matrix form as

$$\begin{bmatrix} P_1 - iP_2 \\ P_3 - iP_4 \end{bmatrix} = \mathcal{E}_0 \begin{bmatrix} \chi_{11} & \chi_{12} \\ \chi_{21} & \chi_{22} \end{bmatrix} \begin{bmatrix} \cos \zeta \\ \sin \zeta e^{i\phi} \end{bmatrix} \quad (6.28)$$

At this point we have to make a choice for the real space orientation of the vectors $\hat{e}_{1,2}$. In our imaging setup the magnetic field is oriented along the z axis, and the probe beam

² The reader is reminded that $\boldsymbol{\chi}$ is a tensor and, for instance, the product $\boldsymbol{\chi} \hat{e}_1$ may have components along both \hat{e}_1 and \hat{e}_2 .

propagates along y , perpendicular to the magnetic field. The polarization of the light lies on the xz plane, so we will assign $\hat{e}_1 = \hat{x}$ and $\hat{e}_2 = \hat{z}$, and we will evaluate the corresponding components of the electric susceptibility tensor: χ_{xx} , χ_{xz} , χ_{zx} , and χ_{zz} .

The first thing to notice is that the off-diagonal components of the susceptibility vanish. This is because the x and z components of the dipole cannot couple to the same excited state (due to the dipole transition angular momentum projection selection rules). For the diagonal components we will need to evaluate the matrix elements $|\langle e|d_i|g\rangle|^2$ for $i = x, z$, which can be expressed in terms of the spherical basis components of the dipole moment, d_q , as

$$|\langle e|d_i|g\rangle|^2 = \sum_q |\hat{e}_i \cdot \hat{e}_q|^2 |\langle e|d_q|g\rangle|^2 \quad (6.29)$$

The relevant quantum numbers for the ground and excited states are ³

$$|g\rangle = |R_g L_g S_g J_g m_g\rangle \quad (6.30)$$

$$|e\rangle = |R_e L_e S_e J_e m_e\rangle \quad (6.31)$$

where the labels R, L, S, J, m refer to the radial quantum number, orbital angular momentum, spin, total angular momentum, and projection on z -axis of total angular momentum, respectively. At the field of interest, the nuclear spin and its projection are decoupled from the angular momentum of the electron, so they do not play any role in imaging, which is an electric dipole process. In our experiment, we typically have atoms in an incoherent spin mixture of states $|1\rangle$ and $|2\rangle$. Looking back at the energy level diagram in Fig. 6.1, both of those states have $m_J = -1/2$, so one can drive transitions from either of them to excited states with $m_J = -3/2, -1/2, +1/2$. In what follows we refer to those excited states $|e\rangle$ as $|-\rangle$, $|\pi\rangle$, and $|+\rangle$ respectively.

To evaluate $|\langle e|d_q|g\rangle|^2$, we use the Wigner-Eckart theorem(see Sec. 5.4.1 of [122]) to

³We omit the J subscript in $m_J \equiv m$ for simplicity.

make the J, m_J selection rules explicit in a $3j$ -symbol. This results in

$$|\langle e|d_q|g\rangle|^2 = \begin{pmatrix} J_e & 1 & J_g \\ -m_e & q & m_g \end{pmatrix}^2 |\langle R_e L_e S_e J_e | d | R_g L_g S_g J_g \rangle|^2 \quad (6.32)$$

which defines the reduced matrix element $\langle R_e L_e S_e J_e | d | R_g L_g S_g J_g \rangle$.

The rate of spontaneous decay from the excited to the ground state is given by [123]

$$\begin{aligned} \Gamma &= \frac{4\omega_0^3}{3\hbar c^3} \sum_{J_g, m_g} \begin{pmatrix} J_e & 1 & J_g \\ -m_e & q & m_g \end{pmatrix}^2 |\langle R_e L_e S_e J_e | d | R_g L_g S_g J_g \rangle|^2 \\ &= \frac{4\omega_0^3}{3\hbar c^3} \frac{|\langle R_e L_e S_e J_e | d | R_g L_g S_g J_g \rangle|^2}{2J_e + 1} \end{aligned} \quad (6.33)$$

and since $J_e = 3/2$

$$\Rightarrow |\langle R_e L_e S_e J_e | d | R_g L_g S_g J_g \rangle|^2 = \Gamma \frac{3\hbar c^3}{\omega_0^3} = \Gamma \frac{3\hbar\lambda^3}{8\pi^3} \quad (6.34)$$

We thus have

$$|\langle e|d_q|g\rangle|^2 = \begin{pmatrix} J_e & 1 & J_g \\ -m_e & q & m_g \end{pmatrix}^2 \frac{3\hbar\Gamma\lambda^3}{8\pi^3} \quad (6.35)$$

and for the cartesian component of the dipole moment

$$|\langle e|d_i|g\rangle|^2 = \sum_q |\hat{\mathbf{e}}_i \cdot \hat{\mathbf{e}}_q|^2 \begin{pmatrix} J_e & 1 & J_g \\ -m_{Je} & q & m_{Jg} \end{pmatrix}^2 \frac{3\hbar\Gamma\lambda^3}{8\pi^3} \quad (6.36)$$

Going back to the x and z components of the dipole moment we have

$$\begin{aligned} \chi_{xx} &= -\frac{n}{\hbar} \sum_{ge} \rho_{gg} \frac{|\langle g|d_x|e\rangle|^2}{\Delta_{ge} - i\Gamma/2} \\ &= -\frac{n}{\hbar} \sum_g \rho_{gg} \frac{3\hbar\Gamma\lambda^3}{8\pi^3} \left(\frac{1}{\Delta_- - i\Gamma/2} |\hat{\mathbf{e}}_x \cdot \hat{\mathbf{e}}_-|^2 \begin{pmatrix} 3/2 & 1 & 1/2 \\ 3/2 & -1 & -1/2 \end{pmatrix}^2 \right. \\ &\quad \left. + \frac{1}{\Delta_+ - i\Gamma/2} |\hat{\mathbf{e}}_x \cdot \hat{\mathbf{e}}_+|^2 \begin{pmatrix} 3/2 & 1 & 1/2 \\ -1/2 & +1 & -1/2 \end{pmatrix}^2 \right) \quad (6.37) \\ &= -\frac{n}{\hbar} \sum_g \rho_{gg} \frac{3\hbar\Gamma\lambda^3}{8\pi^3} \left(\frac{1/8}{\Delta_- - i\Gamma/2} + \frac{1/24}{\Delta_+ - i\Gamma/2} \right) \end{aligned}$$

$$\begin{aligned}
\chi_{zz} &= -\frac{n}{\hbar} \sum_{ge} \rho_{gg} \frac{|\langle g | d_z | e \rangle|^2}{\Delta_{ge} - i\Gamma/2} \\
&= -\frac{n}{\hbar} \sum_g \rho_{gg} \frac{3\hbar\Gamma\lambda^3}{8\pi^3} \frac{1}{\Delta_\pi - i\Gamma/2} |\hat{\mathbf{e}}_z \cdot \hat{\mathbf{e}}_0|^2 \begin{pmatrix} 3/2 & 1 & 1/2 \\ 1/2 & 0 & -1/2 \end{pmatrix}^2 \\
&= -\frac{n}{\hbar} \sum_g \rho_{gg} \frac{3\hbar\Gamma\lambda^3}{8\pi^3} \frac{1/6}{\Delta_\pi - i\Gamma/2}
\end{aligned} \tag{6.38}$$

In our experiment we have a balanced spin mixture of atoms in the ground states $|1\rangle$ and $|2\rangle$, so the sum over ρ_{gg} can be carried out to give

$$\begin{aligned}
\chi_{xx} &= -n \frac{3\Gamma\lambda^3}{8\pi^3} \left(\frac{1/8}{\Delta_- - i\Gamma/2} + \frac{1/24}{\Delta_+ - i\Gamma/2} \right) \\
\chi_{zz} &= -n \frac{3\Gamma\lambda^3}{8\pi^3} \frac{1/6}{\Delta_\pi - i\Gamma/2}
\end{aligned} \tag{6.39}$$

If we express the detunings in units of the linewidth we have

$$\begin{aligned}
\frac{2\pi\omega}{c} \chi_{xx} &= -n \frac{3\lambda^2}{2\pi} \left(\frac{1/4}{2\Delta_- - i} + \frac{1/12}{2\Delta_+ - i} \right) \equiv -n\xi_{xx} \\
\frac{2\pi\omega}{c} \chi_{zz} &= -n \frac{3\lambda^2}{2\pi} \frac{1/3}{2\Delta_\pi - i} \equiv -n\xi_{zz}
\end{aligned} \tag{6.40}$$

Here we also have defined ξ_{xx} and ξ_{zz} which will be useful to simplify the notation later on.

From the matrix equation for the polarization parameters, Eq. 6.28, we see the correspondence

$$\begin{aligned}
P_1 - iP_2 &= \mathcal{E}_0 \chi_{xx} \cos \zeta \\
P_3 - iP_4 &= \mathcal{E}_0 \chi_{zz} \sin \zeta e^{i\phi} = \mathcal{E}_0 \sin \zeta [(\text{Re}\chi_{zz} \cos \phi - \text{Im}\chi_{zz} \sin \phi) \\
&\quad + i(\text{Re}\chi_{zz} \sin \phi + \text{Im}\chi_{zz} \cos \phi)]
\end{aligned} \tag{6.41}$$

which results in

$$\begin{aligned}
P_1 &= \mathcal{E}_0 \text{Re}\chi_{xx} \cos \zeta \\
P_2 &= -\mathcal{E}_0 \text{Im}\chi_{xx} \cos \zeta \\
P_3 &= \mathcal{E}_0 \sin \zeta (\text{Re}\chi_{zz} \cos \phi - \text{Im}\chi_{zz} \sin \phi) \\
P_4 &= -\mathcal{E}_0 \sin \zeta (\text{Re}\chi_{zz} \sin \phi + \text{Im}\chi_{zz} \cos \phi)
\end{aligned} \tag{6.42}$$

6.1.4 Change in field parameters due to atomic column density

In terms of ξ_{xx} and ξ_{zz} , the differential equations for the electric field parameters, which were obtained in Eq. 6.6, become

$$\begin{aligned}\frac{1}{\mathcal{E}_0} \frac{d\mathcal{E}_0}{d\ell} &= -[\text{Im}\xi_{xx} \cos^2 \zeta + (\text{Re}\xi_{zz} \sin \phi + \text{Im}\xi_{zz} \cos \phi) \sin^2 \zeta] n(\ell) \\ \frac{d\varphi}{d\ell} &= -\text{Re}\xi_{xx} n(\ell) \\ \frac{d\zeta}{d\ell} &= -\sin \zeta \cos \zeta (\text{Im}\xi_{xx} - \text{Re}\xi_{zz} \sin \phi - \text{Im}\xi_{zz} \cos \phi) n(\ell) \\ \frac{d\phi}{d\ell} &= -[\text{Re}\xi_{xx} - \cos \phi \text{Re}\xi_{zz} + \sin \phi \text{Im}\xi_{zz}] n(\ell)\end{aligned}\tag{6.43}$$

If we knew the exact form of the density distribution of the gas $n(\ell)$ we could solve these differential equations exactly, but in fact, the goal of this treatment is to do the converse. We want to find an expression for the column density of the gas

$$n_{\text{col}} = \int n(\ell) d\ell\tag{6.44}$$

In general, the field parameters change from an initial value before the atoms to a final value after the atoms. To solve the differential equations for the field parameters in terms of the column density, we will make the following approximation

$$\int f(\zeta, \phi) n(\ell) d\ell \approx f(\zeta_i, \phi_i) \int n(\ell) d\ell,\tag{6.45}$$

where the subscript i denotes the value of the respective field parameter before the light encounters the atom cloud. This approximation assumes that the field parameters ζ and ϕ will not change too much across the extent of the cloud, and it leads to the following expressions for the change in the field parameters:

$$\begin{aligned}\delta(\ln \mathcal{E}_0) &= -[\text{Im}\xi_{xx} \cos^2 \zeta_i + (\text{Re}\xi_{zz} \sin \phi_i + \text{Im}\xi_{zz} \cos \phi_i) \sin^2 \zeta_i] n_{\text{col}} \\ \delta\varphi &= -\text{Re}\xi_{xx} n_{\text{col}} \\ \delta\zeta &= -\sin \zeta_i \cos \zeta_i (\text{Im}\xi_{xx} - \text{Re}\xi_{zz} \sin \phi_i - \text{Im}\xi_{zz} \cos \phi_i) n_{\text{col}} \\ \delta\phi &= -(\text{Re}\xi_{xx} - \cos \phi_i \text{Re}\xi_{zz} + \sin \phi_i \text{Im}\xi_{zz}) n_{\text{col}}\end{aligned}\tag{6.46}$$

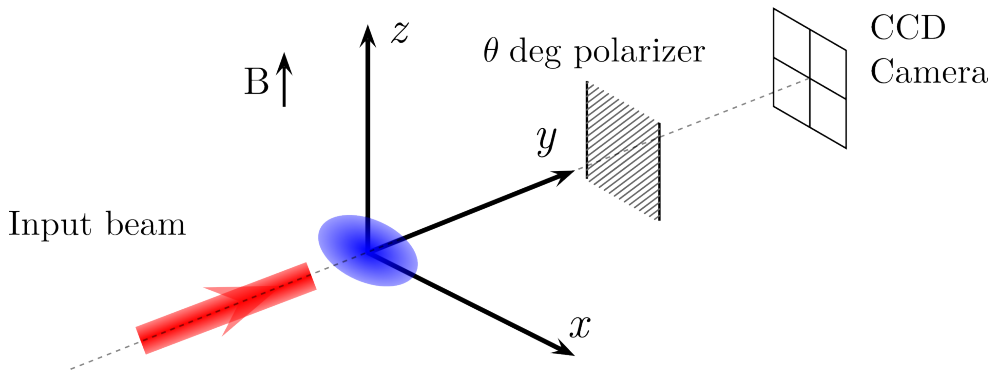


Figure 6.2: Simple schematic showing the setup for PPCI. For simplicity we do not show any of the imaging optics (lenses and microscope objective) and just include the parts which affect the polarization of the light. The atom cloud is represented by the blue ellipsoid sitting at the origin.

We point out that, for the approximation in Eq. 6.45 to be valid, one must be careful to keep the change in field parameters small when performing phase-contrast imaging. It is recommended to keep the phase shift $\delta\phi < \pi/5$ to guarantee the applicability of this analysis.

6.1.5 Experimental setup for PPCI

In the above section we have obtained equations that relate the change in the field parameters to the column density of the gas. In this section we describe the setup used to measure that change. We also motivate the choice of initial field parameters which results in the largest phase-contrast signal. To get started, in Fig. 6.2 we show a simple schematic of the setup for PPCI.

We use the subscript f to denote the electric field parameters after the light has interacted with the atom cloud:

$$\tilde{\mathcal{E}}_f = \mathcal{E}_0 e^{i(\mathbf{k} \cdot \mathbf{r} - \omega t + \varphi_f)} [\cos \zeta_f \hat{\mathbf{e}}_1 + \sin \zeta_f e^{i\phi_f} \hat{\mathbf{e}}_2] \quad (6.47)$$

As shown in Fig. 6.2, after passing through the atom cloud, the light is passed through a polarizer with transmission axis at an angle θ , measured with respect to the magnetic

field axis. The resulting field after the polarizer is

$$\tilde{\mathcal{E}}_{\text{pol}} = \mathcal{E}_{0f} e^{i(\mathbf{k} \cdot \mathbf{r} - \omega t + \varphi_f)} (\cos \zeta_f \sin \theta + \sin \zeta_f e^{i\phi_f} \cos \theta) \hat{e}_\theta \quad (6.48)$$

The polarizer thus sums (interferes) the two complex amplitudes corresponding to $\hat{e}_{1,2}$. The light is then imaged onto a CCD, which is sensitive only to intensity. The intensity at the CCD is given by

$$\begin{aligned} I_A &= |\tilde{\mathcal{E}}_{\text{pol}}|^2 \\ &= \mathcal{E}_{0f}^2 (\cos \zeta_f \sin \theta + \sin \zeta_f \cos \theta \cos \phi_f)^2 + \mathcal{E}_{0f}^2 (\sin \zeta_f \cos \theta \sin \phi_f)^2 \\ &= \mathcal{E}_{0f}^2 (\cos(\zeta_i + \delta\zeta) \sin \theta + \sin(\zeta_i + \delta\zeta) \cos \theta \cos(\phi_i + \delta\phi))^2 \\ &\quad + \mathcal{E}_{0f}^2 (\sin(\zeta_i + \delta\zeta) \cos \theta \sin(\phi_i + \delta\phi))^2 \end{aligned} \quad (6.49)$$

If one repeats the analysis, but without atoms, only considering the effect of the polarizer, one obtains at the CCD:

$$\begin{aligned} I_N &= |\tilde{\mathcal{E}}_i|^2 \\ &= \mathcal{E}_0^2 (\cos \zeta_i \sin \theta + \sin \zeta_i \cos \theta \cos \phi_i)^2 + \mathcal{E}_0^2 (\sin \zeta_i \cos \theta \sin \phi_i)^2 \end{aligned} \quad (6.50)$$

In practice one takes a picture with atoms and another picture without atoms, and defines the contrast as:

$$\frac{I_A - I_N}{I_N} \quad (6.51)$$

We would like to maximize the contrast $(I_A - I_N)/I_N$ for a given change in the field parameters.

Expanding the expression for $I_A - I_N$ in the small parameter $\delta\phi$ (and for the moment assuming that $\delta\zeta = 0$, and $\mathcal{E}_{0f} = \mathcal{E}_0$) yields⁴.

$$I_A - I_N \approx -\frac{1}{2} \sin(2\zeta) \sin(2\theta) \sin(\phi) \delta\phi \quad (6.52)$$

Looking at expression 6.52 for small $\delta\phi$ points at the choice for maximizing the contrast: $\zeta = \theta = \pi/4$ and $\phi = \pi/2$. This corresponds to having circularly polarized light at the input and placing the transmission axis of the polarizer at 45° from the magnetic field axis.

⁴ Assuming no change in $\delta\zeta$ and \mathcal{E}_0 is justifiable, since both $\delta\zeta$ and $\delta(\ln \mathcal{E}_0)$ are $\propto \xi_{zz} \sim 1/\Delta_\pi$, whereas $\delta\phi$ is proportional to $\xi_{xx} \sim 1/\Delta_-$, and therefore we expect $\delta\phi > \delta(\ln \mathcal{E}_0), \delta\zeta$.

Having made this choice we go back to the equations for I_A and I_N and obtain for the contrast

$$\begin{aligned}\frac{I_A - I_N}{I_N} &= -1 + \left(\frac{\mathcal{E}_{0f}}{\mathcal{E}_0}\right)^2 [1 - \cos(2\delta\zeta) \sin(\delta\phi)] \\ &= -1 + e^{2\delta(\ln \mathcal{E}_0)} [1 - \cos(2\delta\zeta) \sin(\delta\phi)]\end{aligned}\quad (6.53)$$

Since the parameter changes $\delta(\ln \mathcal{E}_0)$, $\delta\zeta$, and $\delta\phi$ are all small, we have to first order

$$\frac{I_A - I_N}{I_N} \approx \delta\phi \quad (6.54)$$

Plugging in the initial values for the field parameters ($\zeta_i = \pi/4$ and $\phi_i = \pi/2$) into Eqs. 6.46 we obtain

$$\begin{aligned}\delta(\ln \mathcal{E}_0) &= -\frac{1}{2}[\text{Im}\xi_{xx} + \text{Re}\xi_{zz}]n_{\text{col}} \\ \delta\varphi &= -\text{Re}\xi_{xx}n_{\text{col}} \\ \delta\zeta &= -\frac{1}{2}[\text{Im}\xi_{xx} - \text{Re}\xi_{zz}]n_{\text{col}} \\ \delta\phi &= -[\text{Re}\xi_{xx} + \text{Im}\xi_{zz}]n_{\text{col}},\end{aligned}\quad (6.55)$$

and finally the expression that relates the measured contrast with the column density:

$$\frac{I_A - I_N}{I_N} = -1 + e^{-[\text{Im}\xi_{xx} + \text{Re}\xi_{zz}]n_{\text{col}}} [1 + \cos([\text{Im}\xi_{xx} - \text{Re}\xi_{zz}]n_{\text{col}}) \sin([\text{Re}\xi_{xx} + \text{Im}\xi_{zz}]n_{\text{col}})] \quad (6.56)$$

where ξ_{xx} and ξ_{zz} were defined in Eq. 6.40 as

$$\begin{aligned}\xi_{xx} &= \frac{3\Gamma\lambda^2}{2\pi} \left(\frac{1/4}{2\Delta_- - i\Gamma} + \frac{1/12}{2\Delta_+ - i\Gamma} \right) \\ \xi_{zz} &= \frac{3\Gamma\lambda^2}{2\pi} \frac{1/3}{2\Delta_\pi - i\Gamma}\end{aligned}\quad (6.57)$$

Equation 6.56 can be inverted numerically to recover the column density from a measured value of the contrast.

6.1.6 Results

To conclude the chapter on phase-contrast imaging, we show how the consideration of other excited states affects a measurement of the total atom number. We prepare a sample in

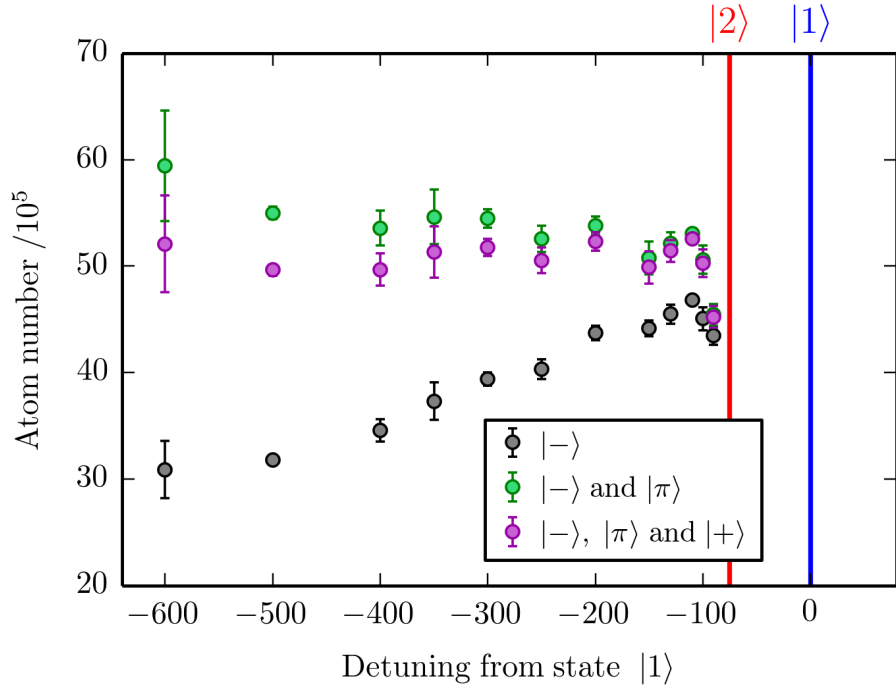


Figure 6.3: Total atom number obtained from polarization phase-contrast imaging. The different points show analyses of the contrast signal using contributions from one (black), two (green), and three (purple) of the excited states. Only if we include all three contributions we obtain, as expected, a measurement which is independent of the imaging light detuning.

our optical dipole trap, and image it *in-situ* using different values of the imaging detuning. Figure 6.3 shows that we get the same atom number (as expected) only if the analysis includes the contribution from all the excited states. We also verified that the absolute scale of the atom number was correct by independently determining the atom number using strong saturation absorption imaging [124]. For detunings close to resonance with state $|2\rangle$, the phase-contrast analysis breaks down because the detuning and the linewidth become comparable and the interaction of the light can no longer be described as purely dispersive.

7. Diagnostic tools II: Fermi gas thermometry

The starting point for all of our experiments is a deeply degenerate Fermi gas at a temperature $T \approx 0.04T_F$, where T_F is the Fermi temperature. This degenerate sample is created in a harmonic trapping potential, and from there we slowly ramp up the optical lattice potential, where final measurements take place. Measuring the T/T_F ratio in a harmonic trap is an important part of our experiment. Most of the time in the lab is spent optimizing the performance of the apparatus, so that the lowest temperatures can be reached in the dimple trap and we can proceed with experiments in the optical lattice. To obtain T/T_F , we image the column density distribution of the atomic gas and fit its shape to a Thomas-Fermi distribution. This procedure is well documented in the literature [118], and pretty much every PhD thesis on ultracold Fermi gases has something to say about it. This one is no exception.

The main contribution from this work to the process of Fermi thermometry in our lab has been in the creation of high-performance fitting routines to enable feedback to the experimenter on a time scale faster than the repetition rate of the experimental cycle. The performance bottleneck in the fitting algorithm is the evaluation of the Fermi-Dirac integral (or polylogarithm), a special function that describes the shape of the density distribution at low temperatures (as we will see below). The imaging process produces a two-dimensional (2D) column density distribution, however, previous experiments in the lab fitted cuts over the distribution, or sums over it in order to have the fitting routine handle the easier one-dimensional (1D) fitting problem.

In our work, we started by exploring 2D surface fits of the column density in order to gain advantage of all of the information contained in the measurement. We first implemented

fitting routines in Python but found that it would take up to several minutes to fit a single image. We then developed fitting routines using C++ , the GNU Scientific Library¹, and a simple for-loop parallelization using OpenMP. This cut down the fitting time to single digit seconds. The duty cycle in our experiment is $\sim 20 - 30$ s, so the new fitting routines allowed us to gain immediate feedback on the temperature of the sample.

The substance of our contribution is of course in the code itself, which is archived on the web and available for download at [125]. In this section we outline the derivation of the fitting functions that are implemented in the code.

7.0.7 Density distributions of a trapped Fermi gas

In the Thomas-Fermi approximation one considers the number density of the gas in phase space, $w(\vec{r}, \vec{p})$:

$$w(\vec{r}, \vec{p}) = \frac{1}{(2\pi\hbar)^3} \frac{1}{\exp[\beta(\vec{p}^2/2m + V(\vec{r}) - \mu)] + 1} \quad (7.1)$$

The density distribution of the trapped gas can be obtained by integrating the phase space density over momentum space [126]. For example, at zero temperature, where the energy dependence of the number density is the usual Fermi step function, the profile takes the shape of the trapping potential elevated to the 3/2 power:

$$n(\vec{r}) = \int w(\vec{r}, \vec{p}) d\vec{p} \xrightarrow{T \rightarrow 0} \int_{|\vec{p}| < \sqrt{2m(\mu - V(\vec{r}))}} i \frac{d\vec{p}}{(2\pi\hbar)^3} = \frac{1}{6\pi^2} \left(\frac{2m}{\hbar^2} \right)^{3/2} (\mu - V(\vec{r}))^{3/2} \quad (7.2)$$

In a harmonic trap at zero temperature the density distribution is

$$n(\vec{r}) = \frac{8}{\pi^2} \frac{N}{R_{F_x} R_{F_y} R_{F_z}} \left[\max \left(1 - \sum_i \frac{x_i^2}{R_{F_i}^2}, 0 \right) \right]^{3/2}, \quad (7.3)$$

where the Fermi radius is defined as $R_{F_i} = \sqrt{\frac{2E_F}{m\omega_i^2}}$.

¹<http://www.gnu.org/software/gsl/>

At a finite temperature, one can carry out the integral by first changing to dimensionless momentum $\vec{q} = \sqrt{\frac{\beta}{2m}}\vec{p}$ and then changing variables to replace the magnitude of \vec{q} as $w = q^2$:

$$\begin{aligned} n(\vec{r}) &= \int w(\vec{r}, \vec{p}) d\vec{p} = \frac{(2m/\beta)^{3/2}}{(2\pi\hbar)^3} \int \frac{d\vec{q}}{\exp[q^2 - (\mu - V(\vec{r}))\beta] + 1} \\ &= \frac{1}{\lambda_{\text{th}}^3} \frac{1}{\Gamma(3/2)} \int_0^\infty \frac{w^{1/2}}{\exp[w - (\mu - V(\vec{r}))\beta] + 1} dw. \end{aligned} \quad (7.4)$$

Here we have introduced the thermal de Broglie wavelength, $\lambda_{\text{th}} = \frac{\hbar}{\sqrt{2\pi m k_B T}}$, and used the Gamma function (rather than the usual 4π) to represent the surface area of the sphere.² This allows us to readily identify the integral on the right as a Fermi-Dirac integral or a polylogarithm. These two special functions are defined as follows:

$$n^{\text{th}} - \text{order Polylogarithm} \quad \text{Li}_n(z) = \frac{1}{\Gamma(n)} \int_0^\infty dq \frac{q^{n-1}}{e^q/z - 1} \quad (7.5)$$

$$j^{\text{th}} - \text{order Fermi - Dirac Integral} \quad F_j(z) = \frac{1}{\Gamma(j+1)} \int_0^\infty dt \frac{t^j}{e^{t-z} + 1} \quad (7.6)$$

(7.7)

Different authors pick the polylogarithm or the Fermi-Dirac function, they are equivalent to each other in the following way:

$$F_n(z) = -\text{Li}_{n+1}(-e^z) \quad (7.8)$$

Here we use the Fermi-Dirac integral notation, for the simple reason that this function is readily available in the GNU Scientific Library. The reader can use the equivalence relation to go back to the polylog notation when necessary. The density of the thermal gas in Eq. 7.4 can then be simply written as

$$n(\vec{r}) = \lambda_{\text{th}}^{-3} F_{1/2}(\beta[\mu - V(\vec{r})]) \quad (7.9)$$

²The surface area of an n -shell with radius R and thickness dR is given by $\frac{2\pi^{n/2}}{\Gamma(n/2)} R^{n-1} dR$

7.0.8 Time-of-flight

If the cloud is suddenly released from the trapping potential, the density distribution at time t after the release can be written as

$$n(\vec{r}, t) = \int w(\vec{r} - \vec{p}_0 t/m, \vec{p}_0) d\vec{p}_0 \quad (7.10)$$

Here we neglected the interactions between the particles. Experimentally, we use a magnetic Feshbach resonance which allows us to control the scattering length between ${}^6\text{Li}$ atoms in two different hyperfine states [101]. The Feshbach resonance allows us to set the scattering length to zero, such that the collision cross section vanishes and the the cloud expands ballistically.

The integration over momentum, which we performed easily in Eq. 7.4 could be complicated because the momentum now appears inside the potential energy as $V(\vec{r} - \vec{p}_0 t/m)$. A harmonic trapping potential has a quadratic dependence on position, and one finds that the integral is easy to carry out with a change of variables. If the potential has trapping frequencies ω_i such that

$$V(\vec{r}) = \sum_i \frac{1}{2} m \omega_i^2 r_i^2 \quad (7.11)$$

then one finds for the density after time-of-flight (TOF)

$$n(\vec{r}, t) = \lambda_{\text{th}}^{-3} \left(\prod_i (1 + \omega_i^2 t^2)^{-1/2} \right) F_{1/2} \left(\beta \left[\mu - \sum_i \frac{1}{2} m \frac{\omega_i^2}{1 + \omega_i^2 t^2} x_i^2 \right] \right) \quad (7.12)$$

For the harmonic potential this is the same functional form as in Eq. 7.9, except the lengths are rescaled as

$$x_i^2 \rightarrow \frac{x_i^2}{1 + \omega_i^2 t^2} \quad (7.13)$$

In this case the expansion is said to be self-similar, because the shape of the density distribution never changes as the cloud expands. Since we determine the ratio T/T_F from fitting the shape of the cloud, for a harmonic potential this can be done *in-situ* or after TOF.

Practically there are two advantages from performing thermometry after TOF. As we saw in the previous section, having a very large optical density requires large detunings to

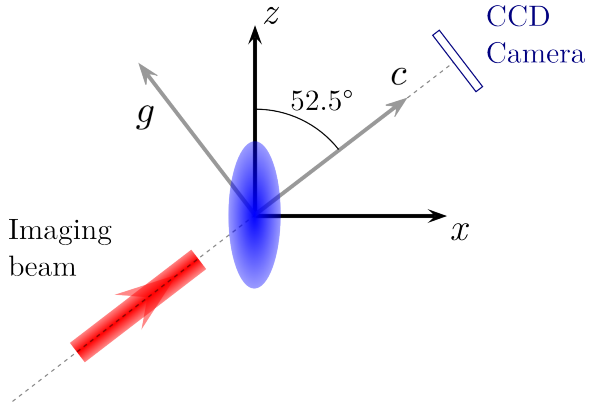


Figure 7.1: Camera axis is at 52.5° from z . New axes c and g are defined, y remains the same. The shorthand notation $\alpha = \cos(52.5^\circ)$ and $\gamma = \sin(52.5^\circ)$ is used.

stay within the dispersive requirements for phase-contrast imaging. As the atoms expand their density is reduced and eases those requirements. The second reason, is that the features of the shape of the distribution, which will reveal the temperature of the gas, now occupy a larger number of pixels in the image. In other words, the expansion provides more resolution at no cost.

7.0.9 Column density and imaging geometry

In our experiment we take phase-contrast images in one of three traps: the crossed-beam optical dipole trap (ODT), the dimple trap or the optical lattice. The dimple and optical lattice are nearly spherically symmetric, but the ODT is highly elongated. Using the principal axes of the ODT we define a coordinate system, as shown in Fig. 7.1. The direction of propagation of the imaging light is not along any of the principal axes, so we define the directions c and g which go along the imaging direction and perpendicular to it, respectively.

The column density that we record when imaging the cloud corresponds to the integral along c :

$$\int n(\vec{r}, t) \, dc \quad (7.14)$$

Since we wish to keep the information regarding the trap frequencies, which are measured

along the principal axes of the ODT we derive here formulas for the column density of the cloud when imaging along the c direction. We define the following notation:

$$\alpha = \cos(52.5^\circ) \quad \gamma = \sin(52.5^\circ) \quad (7.15)$$

$$J_i = \frac{\omega_i^2}{1 + \omega_i^2 t^2} \quad M = \sqrt{\gamma^2 J_x + \alpha^2 J_z} \quad (7.16)$$

$$N = \frac{\alpha\gamma(J_z - J_x)}{M} \quad J_g = \alpha^2 J_x + \gamma^2 J_z - N^2 \quad (7.17)$$

We can write down the phase-space density as

$$w(p, c, g, y) = \frac{1}{\exp\left[\frac{\beta p^2}{2m} - \beta\mu + \frac{m\beta}{2}((Mc + Ng)^2 + J_g g^2 + J_y y^2)\right] + 1} \quad (7.18)$$

and the column density becomes

$$n_{\text{col}}(g, y, t) = \frac{1}{(2\pi\hbar)^3} \left(\prod_i (1 + \omega_i^2 t^2)^{-1/2} \right) \int w(p, c, g, y) \, d\vec{p} \, dc \quad (7.19)$$

The following change of variables: $s = \sqrt{\beta/2}(Mc + Ng)$ and $\vec{p}' = \sqrt{\beta/(2m)}\vec{p}$, allows us to carry out the integral, by exploiting the four-dimensional symmetry in (\vec{p}', s) -space and using

$$\int d\vec{p}' \, dc = \left(\frac{2}{\beta}\right)^2 \frac{m}{M} \int d\vec{p}' \, ds = \left(\frac{2}{\beta}\right)^2 \frac{m}{M} \int \frac{2\pi^2}{\Gamma(2)} R^3 \, dR \quad (7.20)$$

where R is the radius of the 4D sphere defined by $p'^2 + s^2 = R^2$. We obtain

$$n_{\text{col}}(g, y, t) = \frac{1}{(2\pi\hbar)^3} \left(\prod_i (1 + \omega_i^2 t^2)^{-1/2} \right) \left(\frac{2}{\beta}\right)^2 \frac{m}{M} \times \int \frac{R^3}{\exp\left[R^2 - \beta\mu + \frac{m\beta}{2}(J_g g^2 + J_y y^2)\right] + 1} \frac{2\pi^2 \, dR}{\Gamma(2)} \quad (7.21)$$

A final change of variables to $q = \sqrt{R}$ gives

$$n_{\text{col}}(g, y, t) = \frac{1}{(2\pi\hbar)^3} \left(\prod_i (1 + \omega_i^2 t^2)^{-1/2} \right) \left(\frac{2}{\beta}\right)^2 \frac{\pi^2 m}{M} \times \int \frac{q}{\exp\left[q - \beta\mu + \frac{m\beta}{2}(J_g g^2 + J_y y^2)\right] + 1} \frac{dq}{\Gamma(2)} \quad (7.22)$$

where the Fermi-Dirac integral can be spotted again (this time of order 1 rather than 1/2) to yield

$$n_{\text{col}}(g, y, t) = \frac{1}{(2\pi\hbar)^3} \left(\prod_i (1 + \omega_i^2 t^2)^{-1/2} \right) \left(\frac{2}{\beta}\right)^2 \frac{\pi^2 m}{M} F_1 \left(\beta\mu - \frac{m\beta}{2}(J_g g^2 + J_y y^2) \right) \quad (7.23)$$

At zero temperature this becomes:

$$n_{\text{col},T=0}(g, y, t) = \frac{1}{(2\pi\hbar)^3} \left(\prod_i (1 + \omega_i^2 t^2)^{-1/2} \right) \frac{m}{M} \frac{2\pi^2}{\Gamma(2)} \left[\max \left(\mu - \frac{m}{2} (J_g g^2 + J_y y^2), 0 \right) \right]^2 \quad (7.24)$$

7.0.10 Fitting functions

For the actual fitting routine, we absorb all of the prefactors in front of the Fermi-Dirac function in Eq. 7.23 into a fit parameter, $n_{\text{col},0}$, and also define the cloud radii as

$$R_g^2 = \frac{F_0(\beta\mu)}{F_{-1}(\beta\mu)} \frac{2}{m\beta J_g} \quad (7.25)$$

$$R_y^2 = \frac{F_0(\beta\mu)}{F_{-1}(\beta\mu)} \frac{2}{m\beta J_y} \quad (7.26)$$

$$(7.27)$$

to obtain

$$n_{\text{col}}(g, y, t) = \frac{n_{\text{col},0}}{F_1(\beta\mu)} F_1 \left(\beta\mu - \frac{F_0(\beta\mu)}{F_{-1}(\beta\mu)} \left(\frac{g^2}{R_g^2} + \frac{y^2}{R_y^2} \right) \right) \quad (7.28)$$

The fit parameters are then: $n_{\text{col},0}$, $\beta\mu$, R_g and R_y . One can obtain the reduced temperature of the cloud as

$$T/T_F = (6F_2(\beta\mu))^{-1/3} \quad (7.29)$$

Also, if the trap frequencies are known one can obtain the absolute temperature of the cloud from the sizes long the g and y directions as:

$$k_B T_g = m \frac{\alpha^2 J_x + \gamma^2 J_z - N^2}{2} \frac{R_g^2}{F_0(\beta\mu)/F_{-1}(\beta\mu)} \quad (7.30)$$

$$k_B T_y = m \frac{J_y}{2} \frac{R_y^2}{F_0(\beta\mu)/F_{-1}(\beta\mu)} \quad (7.31)$$

In Fig. 7.2 we show the dependence of T/T_F and $\frac{F_0(\beta\mu)}{F_{-1}(\beta\mu)}$ on $\beta\mu$. We see that when the gas is not degenerate ($\beta\mu < 0$) the radius prefactor, $\frac{F_0(\beta\mu)}{F_{-1}(\beta\mu)}$, goes to 1. This reflects the fact that in that case the size of the cloud squared is proportional to the temperature. On the other hand, for a degenerate gas ($\beta\mu > 0$) the radius prefactor goes to $\beta\mu$, which reflects

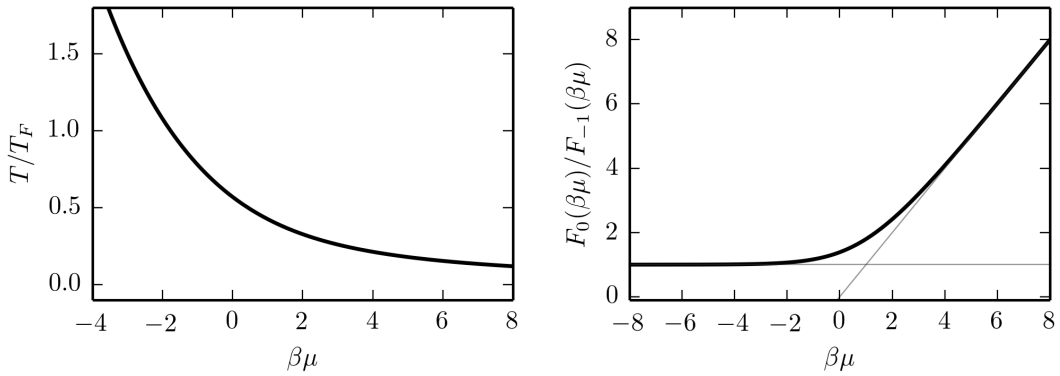


Figure 7.2: Dependence of T/T_F and $\frac{F_0(\beta\mu)}{F_{-1}(\beta\mu)}$ on $\beta\mu$. For a thermal gas $\beta\mu < 0$ and for a highly degenerate gas $\beta\mu \gg 1$.

the fact that the size of the cloud squared is proportional to the Fermi temperature. More details on this choice for the fitting function can be found in [118].

8. Diagnostic tools III: Double occupancy

As we saw in Chapter 3, an important thermodynamic quantity in the Hubbard model is the double occupancy. Detailed studies of this quantity have been used to demonstrate the achievement of a Mott insulating regime [34, 35], to extract the compressibility of Fermions in a lattice [127], and to measure temperature and entropy via comparison with theoretical calculations [128]. Measurements of the double occupancy in an optical lattice have been achieved mainly by two methods: using Feshbach resonances to spectroscopically differentiate the singly and doubly occupied sites [100], or using one-color photoassociation, which selectively expels atoms in doubly occupied sites from the trap [129] (and then measuring the remaining atom number).

Measurements of the double occupancy using one-color photoassociation to an excited molecular state were first performed on bosonic atoms [129, 130], but have also been realized for fermionic ^{173}Yb [131]. This technique requires a dedicated laser tuned to the excited molecular state (which can be several hundred GHz away from the excited state of free atoms). In our experiment we did not have the required frequency readily available, so we implemented double occupancy measurements using the Feshbach resonance technique.

The presence of more than one Feshbach resonance for a pair of hyperfine states, or Feshbach resonances at different magnetic fields for spin mixtures in different hyperfine states, can be exploited in a variety of ways to measure double occupancies in an optical lattice. The possibilities depend on the scattering properties of the atom used. Previous experiments with ^{40}K atoms [70, 132] have used Feshbach resonances to measure the double occupancy. In ^{40}K , repulsive interactions are realized with a spin mixture of atoms in the $m_F = -5/2$ and $m_F = -9/2$ hyperfine states, with total angular momentum $F = 9/2$. A

Feshbach resonance between the $m_F = -9/2$ and $m_F = -7/2$ spin states can be used to shift the energy required to flip the spin of an $m_F = -5/2$ atom. If such an atom is in a singly occupied state it can be flipped to $m_F = -7/2$ by driving a π -pulse at a frequency f_{single} . If it is in a doubly occupied site, flipping the spin to $m_F = -7/2$ will create a bound state, so the RF spin flip resonance is shifted by the binding energy: $f_{\text{double}} = f_{\text{single}} + E_{\text{binding}}/h$. In such a way, one can selectively change the spin of $m_F = -5/2$ atoms only if they are in a doubly occupied site [133]. After doing this, the atoms are released in TOF, applying a strong magnetic field gradient to effect a Stern-Gerlach separation of the populations in the different spin states. Once separated the different populations can be imaged and counted, giving the double occupancy in the lattice.

The same procedure will not work in ${}^6\text{Li}$ for two reasons. The first one has to do with the scattering properties of ${}^6\text{Li}$, which we will review in a moment. The second one is simply because lithium is a light atom, and it expands quickly in TOF. It is then challenging to resolve the different spin states in a Stern-Gerlach separation measurement.

8.1 ${}^6\text{Li}$ Feshbach resonances

Figure 8.1 shows the scattering length between ${}^6\text{Li}$ atoms in states $|1\rangle$ and $|2\rangle$ (see the energy level diagram in Fig. 4.3 for reference) as a function of magnetic field. Most of our experiments take place in the range between 550 G and 650 G, to the right of the narrow Feshbach resonance (little bump in the plot) present at 543.3 G [72, 134]. Within this range, the scattering length is $< 800 a_0$, avoiding larger values where significant collisional losses are observed.

To give rise to a virtual molecular bound state that can be used to selectively flip the spins of atoms in singly and doubly occupied sites, one needs to approach a Feshbach resonance between a different pair of hyperfine states ($|1\rangle, |3\rangle$ or $|2\rangle, |3\rangle$ in our case) from the attractive to the repulsive side. The broad resonances between $|1\rangle, |3\rangle$, and $|2\rangle, |3\rangle$ occur at 690 G and 811 G, respectively, so within our operating field range we cannot cross any of

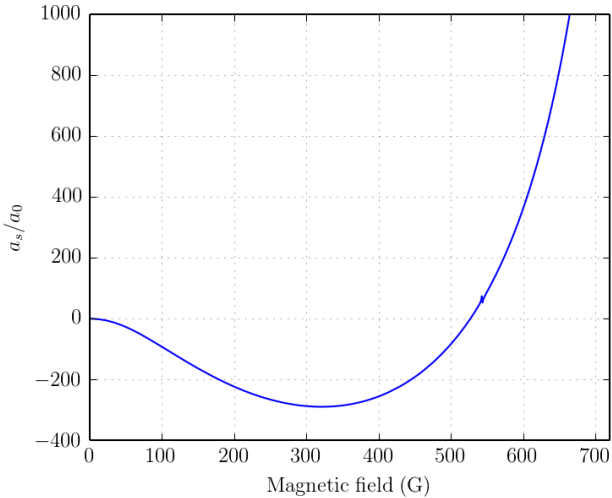


Figure 8.1: Scattering length between ${}^6\text{Li}$ atoms in states $|1\rangle$ and $|2\rangle$ vs. magnetic field in Gauss. A broad Feshbach resonance is centered at 832 G and a narrow Feshbach resonance is centered at 543.3 G [134]. The data for this plot was obtained from Ref. [73].

these resonances to exploit the binding energy of the virtual molecular state. Nevertheless, as can be seen in Fig. 8.1, we have at our disposal the narrow Feshbach resonance between states $|1\rangle$ and $|2\rangle$, which occurs at 543.3 G.

In a narrow resonance, the molecular state that exists on the repulsive side of the resonance becomes deeply bound for fields even a few Gauss away from the resonance [134]. In this case, the narrowness of the resonance places a significant constraint on the stability of the magnetic field if one is to exploit RF transitions in close proximity to the resonance. However, the binding energy of the molecular state away from the resonance is so large, that atoms and molecules can be resolved spectroscopically with the $2S_{1/2} \rightarrow 2P_{3/2}$ optical transition. In addition, since the resonance is between states $|1\rangle$ and $|2\rangle$ (the states we use in the experiment), the molecular state is not virtual. If the field is ramped slowly across the resonance in the direction of decreasing field, then atoms in doubly occupied sites will be associated to form molecules with a probability very close to 1 due to the strong confinement of a lattice site [135].

8.2 Measurement procedure

The sequence to measure the double occupancy using molecular association across the Feshbach resonance proceeds as indicated in Fig. 8.2. Below we list all the steps that are shown in the figure:

- The experiment starts out (in this example) at a field of 595 G ($a_s = 326 a_0$) and a lattice depth of $7 E_r$. At $t = 0$ ms, the lattice depth is suddenly (in 1 ms) increased to $50 E_r$ (this lattice depth ramp is not shown in the figure). One could take an image at this time (labeled as [1] in the figure) to measure the total atom number¹
- During the lock ramp to $50 E_r$ each site is projected into a number state, so singly and doubly occupied sites are well defined. Additionally, in the locked lattice the atoms are prevented from continuing to tunnel during the duration of the double occupancy measurement. The minimum duration of the measurement determines the lattice depth requirements. A few values of the tunneling rate as a function of lattice depth are given in the table below. We will refer back to these in a moment, after explaining the entire measurement procedure.

V_0	t (Hz)	$1/t$ (ms)
$7 E_r$	1153	0.867
$20 E_r$	73	13.7
$50 E_r$	0.7	1412

- After locking the lattice, the scattering length is quickly ramped down to $80 a_0$ (547 G) in 8 ms. The narrow resonance is then crossed using a slow ramp that goes from 80 to $61 a_0$ in 24 ms. A slow ramp is required to achieve nearly 100% conversion efficiency of atoms in doubly occupied sites to Feshbach molecules. Notice that ramps are linear in scattering length (we use a calibration for the scattering length that ignores the

¹Equivalently, the total atom number can also be measured before locking the lattice.

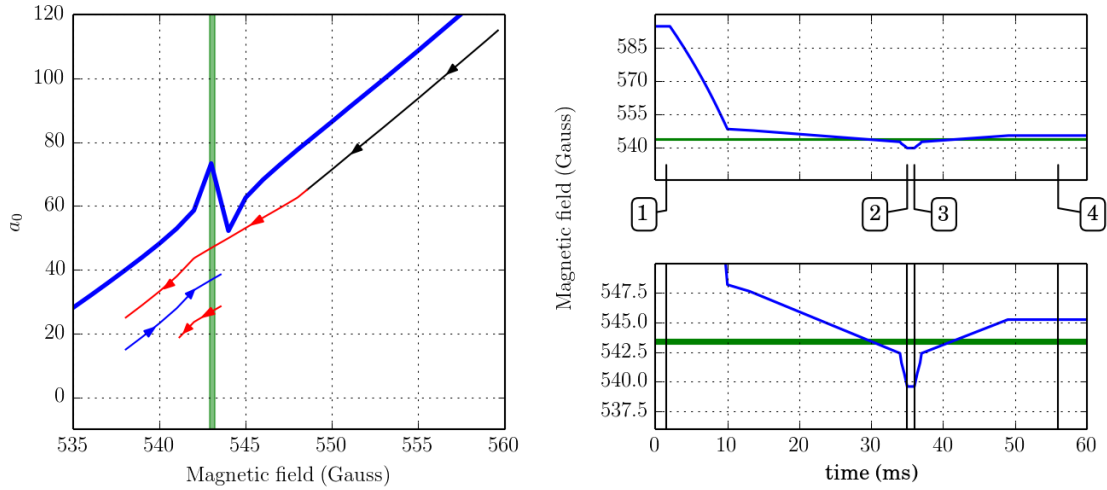


Figure 8.2: Experimental sequence for measuring double occupancy in an optical lattice. The steps are explained in the text. The direction of the magnetic field sweeps is shown by the colored lines with arrows on the left plot. The change in color represents a different slope in the field ramps.

narrow resonance) and so the ramps are not exactly straight lines when showed in units of the magnetic field, as in Fig. 8.2.

- After the field crosses the resonance, a 1 ms ramp takes the scattering length down to $48 a_0$, a field of ≈ 537.9 G, where the molecules are dark. At this point, labeled as [2] in the figure, one could take an image of atoms in singly occupied sites.
- In the short time that is spent below the resonance (time between points [2] and [3]) we proceed to blow away with resonant light any atoms in singly occupied sites. Two frequencies of light are needed in the pulse, targeting atoms in spin states $|1\rangle$ and $|2\rangle$.
- After getting rid of atoms in singly occupied sites, the ramp across the narrow resonance is reversed. At a scattering length of $70 a_0$ (≈ 545.1 G), where the Feshbach molecules are dissociated, we can go ahead and take a picture of atoms that were initially in doubly occupied sites. That point is labeled as [4] in Fig. 8.2.

As one can see from the explanations above, several experiments are possible depending on the time along these field ramps where one decides to image the atoms. For a direct

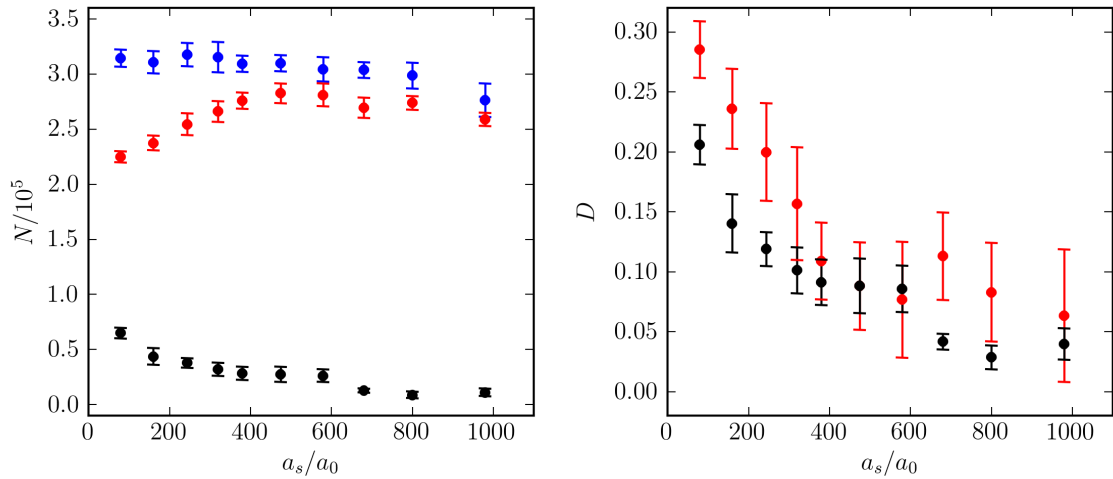


Figure 8.3: Measurement of the double occupancy for different scattering lengths in a compensated lattice. The atom number (left panel) measured at $\boxed{1}$ (blue), $\boxed{2}$ (red), and $\boxed{4}$ (black). The double occupancy, D (right panel), can be determined from $D = \boxed{4}/\boxed{1}$ (black) or $D = 1 - \boxed{2}/\boxed{1}$ (red).

image of the double occupancies, taken at point $\boxed{4}$, at least 50 ms are required for the field ramps involved in the measurement. A locked lattice depth $V_0 = 43 E_r$ is required to set a limit of less than one tenth of a tunneling event during that time.

8.3 Measurements in a compensated lattice

In Fig. 8.3 we show an example of the different measurements explained above. The sample is in the compensated lattice, with lattice depth set at $5.5 E_r$ and the compensation set at $3 E_r$. The atom number is $\approx 300,000$ atoms. The figure shows that the double occupancy decreases with scattering length, as expected in the single-band Hubbard model. A measurement of the density, shown in Fig. 8.4, reveals that this system enters the Mott insulating regime for scattering lengths $> 300 a_0$. At scattering lengths $> 500 a_0$ the atom number is insufficient to form a Mott insulating core, and for scattering lengths larger than $800 a_0$ the onset of collisional losses is (presumably) accompanied by heating of the cloud.

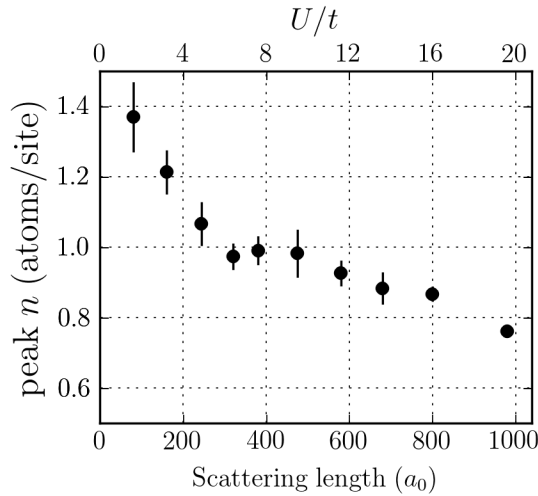


Figure 8.4: Measurement of the peak density of the cloud as a function of scattering length in a compensated lattice. The preparation of the sample is the same as for Fig. 8.3. For scattering lengths between $300 a_0$ and $500 a_0$, the peak density is clamped at $n = 1$ as the interaction strength is increased. This behavior is indicative of the system entering the Mott insulating regime.

8.4 *In-situ* measurement of double occupancies

Measurements taken at point [4] address directly the double occupancies. In that case, *in-situ* imaging would reveal the double occupancy profile of the cloud. It was not further investigated in this work, but it is clear that important information can be extracted from the *in-situ* double occupancy profile, in the same way as can be extracted from the *in-situ* density profile (as showed in Chapter 11). As an example we show a measurement in an uncompensated lattice, with $N = 75,000$ atoms in Fig. 8.5.

8.5 Measurement systematics

When measuring the double occupancies directly (point [4] in Fig. 8.2) one faces the issue that the molecules do not have a long lifetime in the lattice. Any amount of time that passes between the molecular association and the image will result in a systematic error of this measurement.

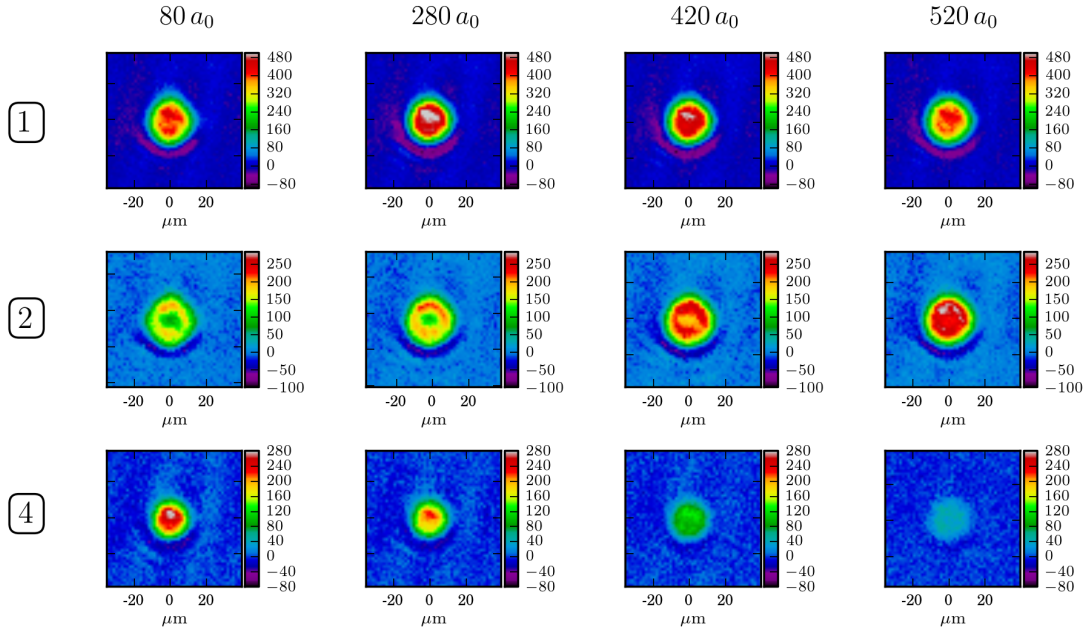


Figure 8.5: *In-situ* measurement of the double occupancy. Images at points $\boxed{1}$, $\boxed{2}$, and $\boxed{4}$ (as labeled in Fig. 8.2) are taken for various scattering lengths. One can see that the double occupancies are suppressed for large scattering length, and that they reside at the center of the sample, as expected. We point out that, even though we used a low number of atoms ($N = 75,000$), a sample in the uncompensated lattice does not satisfy the criteria for the single-band Hubbard model (due to the large confinement). At the large resulting densities, significant dispersive distortions are noticeable in the images (half-circle on the bottom part of the cloud).

In the descriptions above we also omitted an important fact. We found that the lifetime of the molecules is shortened dramatically in the presence of 532 nm light (we use 532 nm for the compensation). It is unclear what is the exact decay mechanism for the molecules both in the presence or absence of 532 nm light. For measurements on a compensated lattice, like the one in Fig. 8.3, all of the 532 nm light was turned off after locking the lattice and before starting the Feshbach association ramps to avoid the extremely fast losses observed in the presence of 532 nm light.

In the absence of 532 nm light, we measured the lifetime of the molecules by varying the time between points $\boxed{2}$ and $\boxed{3}$ in the field ramps, and observing the final number of dissociated atoms at point $\boxed{4}$. The details of the measurement are presented in Fig. 8.6. The observed lifetime was $\approx 100\text{-}200$ ms, which is of the order of magnitude of the time it

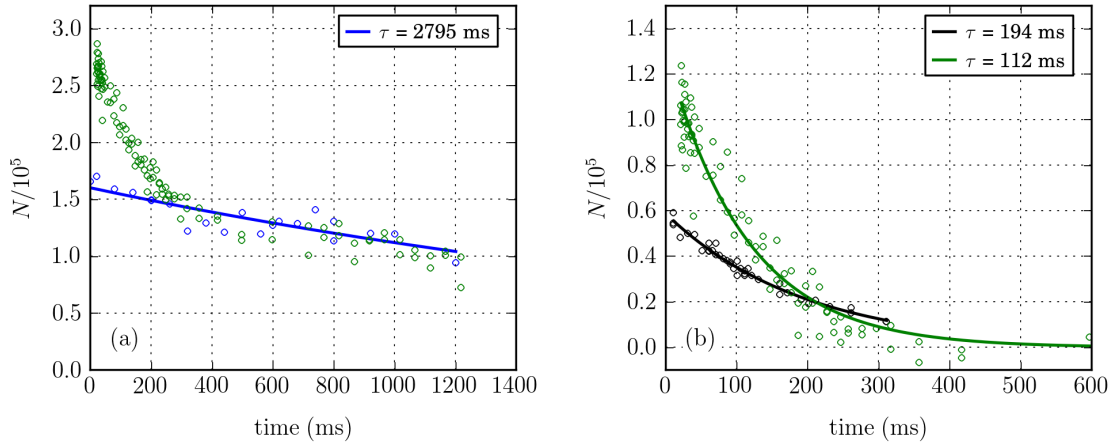


Figure 8.6: Measurement of the lifetime of Feshbach molecules in the uncompensated optical lattice.

(a) The blue points show a loss curve of the sample in the lattice (including singly and doubly occupied sites). The green points show a measurement taken at point [4], in which the atoms in singly occupied sites are not blown away. The time is the hold time between association and dissociation ramps. One can see that the decay has a short time scale (lifetime of the molecules) and a longer time scale which matches the blue points.

(b) Green points are the same data in panel (a), with the long time scale decay subtracted out. Black points are a measurement taken at point [4], in which the atoms in singly occupied sites were blown away at point [2]. In essence, the green shows the lifetime of molecules in the presence of singly occupied sites and the black shows the lifetime of a sample made only of molecules.

takes to make a direct measurement of the double occupancy.

In addition to possible systematic due to molecule lifetime, we have found that the sample gets affected when locking the lattice depth up to $50 E_r$. Measurements of AFM correlations using Bragg scattering show that the correlations effectively wash out for lock depths larger than $20 E_r$. It is unclear why this happens; in any case, according to the results of AFM correlations we cannot do a deep lattice lock without affecting the system. This casts another shadow of doubt on the results of our double occupancy measurements shown here, which use a lock depth of $50 E_r$. If we were to reduce the lock depth to $20 E_r$, then the duration of the double occupancy measurement would be comparable to the tunneling rate. We speculate that in a system with a large lattice beam waist, and with a beam waist ratio, α_w , closer to 1, the issues with the lock depth would be mitigated. A

future setup, currently under construction, will help us get the answer to this question.

9. Diagnostic tools IV: Bragg scattering of light

The most important contribution in this thesis has been the development of Bragg scattering thermometry for ultracold atoms in optical lattices. This kind of thermometry exploits the long range spin order that develops in the system below the Néel transition temperature, T_N . The idea behind Bragg scattering is very simple: a wave scattered coherently from a periodic ensemble of particles will show enhanced scattering at a certain direction, depending on the angle of the incoming light and the periodic pattern of the ensemble. In the case of ultracold atoms the wave used is light, which is near resonant to an atomic transition in order to have a significant cross section. In materials science and crystallography, Bragg scattering of X-rays and neutrons is routinely used to characterize samples. Besides probing the periodic pattern of the ensemble of particles, the structure of the scatterers also affects the angular distribution of the scattered light. As a notable example, X-ray scattering was used to infer the double-helix structure of DNA. In the case of ultracold atoms, Bragg scattering can be used to measure the spatial extent of atomic wavefunctions [136].

It is clear that below T_N , long range spin ordering will give rise to a large Bragg signal, proportional to the square of the number of atoms in a hypothetical AFM domain. Above T_N , antiferromagnetic (AFM) correlations start to develop as the system approaches the transition. It was unclear whether it would be possible to experimentally detect the weak AFM correlations, however in the end we find the signal to be detectable, if one has enough statistics from repeating the experiment many times.

Modeling the Bragg scattering experiment with ultracold atoms is very simple if one considers the far-detuned or weak intensity limit, where all of the light is scattered coherently by the atoms. In fact there were some studies of Bragg scattering in the early BEC

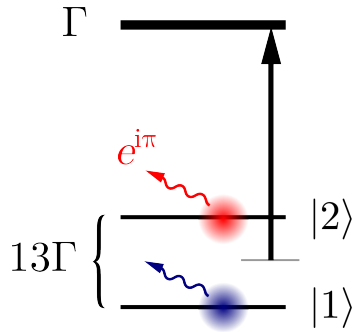


Figure 9.1: Illustration of spin-sensitive light scattering.

days that realized such a scenario [137, 138]. More recent experimental studies, which have used Bragg scattering to study many-body states of bosons in optical lattices [136], also operate on that regime. There has also been theoretical work which suggests ways to exploit the characteristics of the scattered light to probe the many body states that form in an optical lattice [139]. However this work is also in the context of a very weak probe and does not consider the effects of saturation of the atomic transition.

When performing Bragg scattering to detect the spin ordering of atoms in a lattice, one must have a spin-sensitive probe, i.e. light that scatters differently from atoms in states $|1\rangle$ and $|2\rangle$. The phase shift, δ , of the scattered light is related to the detuning Δ (in units of the linewidth) from the atomic transition as $e^{i\delta} \propto \Delta^{-1}$. If one sets the light detuning right in between the two states, light scattered from one state will have a π phase shift with respect to light scattered from the other one (see Fig. 9.1). We find experimentally that, to obtain a measurable scattering signal, we must use probe parameters that are not in the far-detuned or weak intensity ideal scenarios. The detuning is fixed by the requirement to have a spin-sensitive measurement, the power of the probe is determined by the signal to noise ratio of our detection setup, and the duration is constrained by the effects of inelastic scattering modifying the center of mass state of the atoms.

This chapter starts out with a detailed derivation of the equations for light scattering by an array of atoms, including saturation effects of the transition via the optical Bloch equations. We will then introduce the experimental setup that was constructed for Bragg

scattering. Finally we will show results for a measurement of the crystalline structure of the optical lattice using Bragg scattering. These results will serve as an illustration of the power of this technique. Details of the measurement of AFM correlations using spin-sensitive light scattering will be deferred until Chapter 12.

9.1 Coherent light scattering by an array of atoms.

For a collection of two-level atoms, the steady-state scattered intensity measured at a detector can be obtained by coherently adding up the field emitted by all the atoms and squaring it to find the intensity.

When illuminated with probe light with wavevector \mathbf{k} (magnitude $k = |\mathbf{k}|$) and angular frequency ω_{in} , the n^{th} atom emits a field proportional to its dipole moment [140, 141]:

$$\mathbf{E}_n^+ = \frac{1}{\sqrt{2\epsilon_0 c}} \left[\frac{3}{8\pi} \frac{\hbar ck\Gamma}{r_D^2} \right]^{1/2} \boldsymbol{\Lambda} e^{i(\mathbf{k}' - \mathbf{k}) \cdot \hat{\mathbf{r}}_n} \varsigma_{n-} \quad (9.1)$$

where

- c is the speed of light, ϵ_0 is the vacuum permittivity, \hbar is Planck's constant divided by 2π .
- Γ is the linewidth of the transition
- \mathbf{E}_n^+ is the positive frequency component of the electric field amplitude at a point in space that is a distance r_D from the sample in the direction of the wavevector of the scattered light
- \mathbf{k}' is the wave vector of the scattered light
- $\hat{\mathbf{r}}_n$ is the position operator of the n^{th} atom $\boldsymbol{\Lambda} = \mathbf{k}' \times (\mathbf{k}' \times \mathbf{d}_{ge})/(k'^2|\mathbf{d}_{ge}|)$ is the polarization vector of the field (dipole radiation pattern)
- $\mathbf{d}_{ge} = \langle g | \mathbf{d} | e \rangle$ is the transition matrix element between the ground $|g\rangle$ and excited $|e\rangle$ electronic states

- $\varsigma_{n-} = e^{i\omega_{\text{int}}t}|g\rangle\langle e|$ is the off-diagonal matrix element of the atomic density matrix in the rotating frame

The two atomic states, $|\uparrow\rangle$ and $|\downarrow\rangle$, only differ in the projection of the nuclear spin, so \mathbf{d}_{ge} is the same for either state. For this reason, we make no distinction of the spin part of the wavefunction in states $|e\rangle$ and $|g\rangle$. Both states $|\uparrow\rangle$, $|\downarrow\rangle$ have an electronic angular momentum projection $m_J = -1/2$ and the respective excited states are $m_J = -3/2$. The matrix element can then be written as $\mathbf{d}_{ge} = \mathbf{d}_{ge} = |\mathbf{d}_{ge}|\hat{\mathbf{e}}_{-1}$ (as for any $\Delta m_J = -1$ transition).

The intensity at the detector, for a momentum transfer $\mathbf{Q} = \mathbf{k}' - \mathbf{k}$, can be obtained by summing the field contributions from the individual atoms and squaring the total field:

$$I_{\mathbf{Q}} = 2\epsilon_0 c \langle \Psi | \left(\sum_m \mathbf{E}_m^- \right) \cdot \left(\sum_n \mathbf{E}_n^+ \right) | \Psi \rangle. \quad (9.2)$$

Here $|\Psi\rangle$ is the product state of the array of atoms: $|\Psi\rangle = \prod_n |u\rangle_n |\sigma\rangle_n$ where u and σ represent the center of mass and electronic states of the atom respectively. The wavefunction for the system of atoms in the lattice (which in general can be a highly entangled many-body state) must be projected into a product state (like $|\Psi\rangle$) before performing the measurement. This is achieved by quickly ramping the lattice depth up to $20 E_r$, which projects the state of the system into a state with a well defined atom number in each site, and prevents further tunneling during the measurement.

Using Eq. 9.1 inside Eq. 9.2 and separating the sum into off-diagonal and diagonal terms yields

$$I_{\mathbf{Q}} = A \left[\sum_{\substack{m,n \\ m \neq n}} \langle \varsigma_{n+} \rangle \langle \varsigma_{m-} \rangle \langle u | e^{-i(\mathbf{k}' - \mathbf{k}) \cdot \hat{\mathbf{r}}_m} | u \rangle_m \langle u | e^{i(\mathbf{k}' - \mathbf{k}) \cdot \hat{\mathbf{r}}_n} | u \rangle_n + \sum_n \langle \varsigma_{n+} \varsigma_{n-} \rangle \right] \quad (9.3)$$

where $A = \frac{3}{8\pi} \frac{\hbar ck\Gamma}{r_D^2} |\mathbf{A}|^2$.

We assume that the center of mass state for all atoms is the harmonic oscillator ground state of a single site

$$|u\rangle_m = |0\rangle_m \quad (9.4)$$

We also neglect the possibility of an atom recoiling to a different center of mass state. The center of mass expectation value that appears inside the sum in Eq. 9.3 is evaluated by using the identity $\langle e^{\hat{A}} \rangle = e^{\frac{1}{2}\langle \hat{A}^2 \rangle}$, which is valid for a simple harmonic oscillator eigenstate if \hat{A} is a linear combination of displacement and momentum operators of the oscillator.

$$\begin{aligned}
\langle u | e^{-i(\mathbf{k}' - \mathbf{k}) \cdot \hat{\mathbf{r}}_m} | u \rangle_m &= \langle 0 | e^{-i(\mathbf{k}' - \mathbf{k}) \cdot \hat{\mathbf{r}}_m} | 0 \rangle_m \\
&= e^{-i(\mathbf{k}' - \mathbf{k}) \cdot \mathbf{R}_m} e^{-\frac{1}{2}\langle [(\mathbf{k}' - \mathbf{k}) \cdot \hat{\mathbf{r}}_m]^2 \rangle} \\
&= e^{-i\mathbf{Q} \cdot \mathbf{R}_m} e^{-\frac{1}{2}\langle [\mathbf{Q} \cdot \hat{\mathbf{r}}_m]^2 \rangle} \\
&= e^{-i\mathbf{Q} \cdot \mathbf{R}_m} \prod_{i=x,y,z} e^{-\frac{1}{2}Q_i^2 \langle r_{mi}^2 \rangle} \\
&= e^{-i\mathbf{Q} \cdot \mathbf{R}_m} e^{-W}
\end{aligned} \tag{9.5}$$

Plugging the center of mass expectation value back into Eq. 9.3 we obtain

$$I_Q/A = e^{-2W} \sum_{\substack{m,n \\ m \neq n}} \langle \varsigma_{n+} \rangle \langle \varsigma_{m-} \rangle e^{i\mathbf{Q} \cdot (\mathbf{R}_n - \mathbf{R}_m)} + \sum_n \langle \varsigma_{n+} \varsigma_{n-} \rangle. \tag{9.6}$$

Here e^{-2W} is the Debye-Waller factor defined as

$$e^{-2W} = \prod_{i=x,y,z} e^{-Q_i \langle \hat{r}_i^2 \rangle} \tag{9.7}$$

where $\langle r_i^2 \rangle$ is the variance in the i^{th} coordinate of an atom, assumed to be the same for all atoms in the array.

The resulting intensity in Eq. 9.6 is seen to be the result of two contributions. The first one is the coherent scattering by all the atoms in the ensemble. The magnitude of this contribution is multiplied by the Debye-Waller factor, which is related to the spatial extent of an atomic wavefunction. The second part corresponds to the incoherently scattered light, which has an intensity at the detector proportional to the number of atoms in the system.

The steady-state solutions to the optical Bloch equations can be used to obtain expressions for the expectation values of ς that remain in Eq. 9.6:

$$\langle \varsigma_{m+} \rangle \langle \varsigma_{n-} \rangle = 2 \frac{\rho_m^{ee} \rho_n^{ee}}{s_0} (2\Delta_n - i)(2\Delta_m + i) \tag{9.8}$$

$$\langle \varsigma_{n+} \varsigma_{n-} \rangle = \rho_n^{ee} \tag{9.9}$$

where the steady-state population of the excited state is

$$\rho_n^{ee} = \frac{s_0/2}{1 + 4\Delta_n^2 + s_0}, \quad (9.10)$$

and Δ_n is the detuning expressed in units of the linewidth Γ . The on-resonance saturation parameter of the transition is

$$s_0 = I_{\text{in}} |\hat{\mathbf{e}}_{\text{in}} \cdot \hat{\mathbf{e}}_{-1}|^2 / \left(\frac{\pi \hbar c \Gamma}{3 \lambda_0^3} \right) \quad (9.11)$$

where I_{in} is the intensity of the incident light with polarization $\hat{\mathbf{e}}_{\text{in}}$, and $\lambda_0 = 671$ nm is the wavelength of the transition. The polarization of the incident light in our experiment (for both of the directions at which Bragg scattering was measured) is linear and perpendicular to the quantization axis, so $|\hat{\mathbf{e}}_{\text{in}} \cdot \hat{\mathbf{e}}_{-1}|^2 = 1/2$.

9.1.1 Incoherent scattering

The word “incoherent” is used here to define any light that is scattered by the atoms with a random phase. A random phase arises due to quantum fluctuations of the electric dipole moment, which occur if the atom is driven with large enough intensity (see for instance §V.D.2b in [140]). The Bloch equation solutions capture this, as they incorporate the effects of saturation of the atomic transition. In the limit of purely incoherent scattering (large s_0 or small Δ) the off-diagonal components of the density matrix $\langle \varsigma_{n\pm} \rangle \rightarrow 0$, and the intensity at a detector in Eq. 9.6 reduces to

$$I_Q = \frac{3}{8\pi} \frac{\hbar c k \Gamma}{r_D^2} |\mathbf{A}|^2 \sum_n \rho_n^{ee} \quad (9.12)$$

One can see that the same limit would be found for an uncorrelated sample. For instance, a sample where the wavefunctions of neighboring atoms overlap significantly and $e^{-2W} \rightarrow 0$. In either case, uncorrelated or incoherent, the total photon scattering rate can be evaluated by integrating I_Q along all directions:

$$\Gamma_{\text{scatt}} = \frac{1}{\hbar c k} \int I_Q r_D^2 d\Omega, \quad (9.13)$$

and using $\int |\mathbf{A}|^2 d\Omega = \frac{8\pi}{3}$ we find

$$\Gamma_{\text{scatt}} = \Gamma \sum_n \rho_n^{ee} \quad (9.14)$$

just as we expect for a collection of uncorrelated atoms or in the limit of a strong probe.

9.1.2 Coherent scattering

The coherent part of the scattering intensity is

$$\begin{aligned} I_{\mathbf{Q}}/A &= e^{-2W} \sum_{\substack{m,n \\ m \neq n}} e^{i\mathbf{Q} \cdot (\mathbf{R}_n - \mathbf{R}_m)} 2 \frac{\rho_m^{ee} \rho_n^{ee}}{s_0} (2\Delta_n - i)(2\Delta_m + i) \\ &= e^{-2W} \sum_{\substack{m,n \\ m \neq n}} e^{i\mathbf{Q} \cdot (\mathbf{R}_n - \mathbf{R}_m)} \frac{\rho_m^{ee} \rho_n^{ee}}{s_0} (8\Delta_n \Delta_m + 4i\Delta_n - 4i\Delta_m + 2) \end{aligned} \quad (9.15)$$

To get an idea of the contributions of the four different terms inside the last parenthesis we split up the double sum over m and n explicitly for each of them:

$$8 \sum_m e^{i\mathbf{Q} \cdot \mathbf{R}_n} \rho_n^{ee} \Delta_n \sum_{n \neq m} e^{-i\mathbf{Q} \cdot \mathbf{R}_m} \rho_m^{ee} \Delta_m \quad (9.16)$$

$$4i \sum_m e^{i\mathbf{Q} \cdot \mathbf{R}_n} \rho_n^{ee} \Delta_n \sum_{n \neq m} e^{-i\mathbf{Q} \cdot \mathbf{R}_m} \rho_m^{ee} \quad (9.17)$$

$$-4i \sum_m e^{i\mathbf{Q} \cdot \mathbf{R}_n} \rho_n^{ee} \sum_{n \neq m} e^{-i\mathbf{Q} \cdot \mathbf{R}_m} \rho_m^{ee} \Delta_m \quad (9.18)$$

$$2 \sum_m e^{i\mathbf{Q} \cdot \mathbf{R}_n} \rho_n^{ee} \sum_{n \neq m} e^{-i\mathbf{Q} \cdot \mathbf{R}_m} \rho_m^{ee} \quad (9.19)$$

9.1.3 Crystal structure

For a large detuning with respect to both states, such that $\Delta_m \approx \Delta$ (independent of the spin of the atom in question) the terms in 9.17 and 9.18 cancel each other out, and the one in 9.19 can be neglected in comparison to the first¹. We then have the following result, including the coherent and incoherent part of the intensity:

¹ For Δ_m to be the same for atoms in either spin, one must necessarily have $\Delta \gg 1$

$$\begin{aligned}
I_{\mathbf{Q}}^{\text{crystal}}/A &= e^{-2W} \frac{8(\rho^{ee})^2 \Delta^2}{s_0} \sum_{\substack{m,n \\ m \neq n}} e^{i\mathbf{Q} \cdot (\mathbf{R}_n - \mathbf{R}_m)} + \sum_n \rho^{ee} \\
&= e^{-2W} \frac{2s_0 \Delta^2}{(4\Delta^2 + s_0)^2} \sum_{\substack{m,n \\ m \neq n}} e^{i\mathbf{Q} \cdot (\mathbf{R}_n - \mathbf{R}_m)} + N \frac{s_0/2}{4\Delta^2 + s_0}
\end{aligned} \tag{9.20}$$

If \mathbf{Q} is a reciprocal lattice vector, then coherent scattering from all atoms will interfere constructively at the detector. The off-diagonal sum becomes

$$\sum_{\substack{m,n \\ m \neq n}} e^{i\mathbf{Q} \cdot (\mathbf{R}_n - \mathbf{R}_m)} = N(N-1) \tag{9.21}$$

and $I_{\mathbf{Q}}^{\text{crystal}}/A \sim N^2$

The crystal structure factor, a measure of the spatial ordering of the ensemble of atoms, is defined as

$$S_{\mathbf{Q}}^{\text{crystal}} = \frac{1}{N} \sum_{m,n} e^{i\mathbf{Q} \cdot (\mathbf{R}_n - \mathbf{R}_m)} \tag{9.22}$$

and we find that it can be related to the scattered intensity as

$$I_{\mathbf{Q}}^{\text{crystal}}/A = e^{-2W} \frac{2s_0 \Delta^2}{(4\Delta^2 + s_0)^2} N(S_{\mathbf{Q}}^{\text{crystal}} - 1) + N \frac{s_0/2}{4\Delta^2 + s_0} \tag{9.23}$$

9.1.4 Magnetic structure

As was mentioned before, to have sensitivity to the magnetic ordering of spins in the lattice the light must be detuned in between the two spin states. We then have $\Delta_{\uparrow} = -\Delta_{\downarrow}$, and $\Delta_n^2 \equiv \Delta^2$. We can replace the detuning for the n^{th} atom with the projection of its spin along z as

$$\Delta_n = 2\langle \sigma_z \rangle \Delta \tag{9.24}$$

The intensity at the detector (including coherent and incoherent components) then becomes:

$$I_{\mathbf{Q}}^{\text{spin}}/A = e^{-2W} \frac{2s_0 \Delta^2}{(4\Delta^2 + s_0)^2} \sum_{\substack{m,n \\ m \neq n}} 4\langle \sigma_z \rangle_m \langle \sigma_z \rangle_n e^{i\mathbf{Q} \cdot (\mathbf{R}_n - \mathbf{R}_m)} + N \frac{s_0/2}{4\Delta^2 + s_0} \tag{9.25}$$

For arbitrary \mathbf{Q} , the terms in Eqs. 9.17-9.19 can be neglected on the basis that $|\Delta| = 6.5 \gg 1$. When the spins are antiferromagnetically ordered, a magnetic face-centered cubic

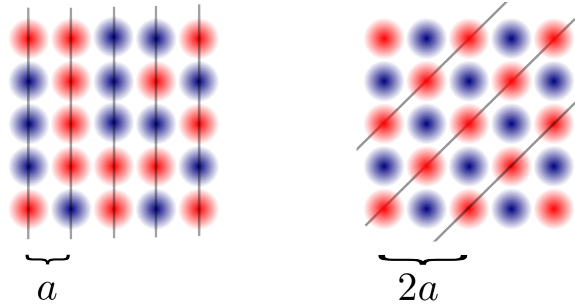


Figure 9.2: Illustration of disordered spins in a square optical lattice (left). When the spins order antiferromagnetically, a face-centered square lattice (right) is formed, which has twice the lattice spacing as the underlying optical lattice. Planes relevant for Bragg scattering are indicated by the gray lines. The situation is analogous in three dimensions.

sublattice is formed, which has twice the lattice spacing of the crystal lattice. This situation is illustrated in Fig. 9.2.

If \mathbf{Q} is a reciprocal lattice vector of the magnetic sublattice, then the sum

$$\sum_{\substack{m,n \\ m \neq n}} 4\langle \sigma_z \rangle_m \langle \sigma_z \rangle_n e^{i\mathbf{Q} \cdot (\mathbf{R}_n - \mathbf{R}_m)} = N(N-1) \quad (9.26)$$

and $I_Q^{\text{spin}}/A \sim N^2$. In that case, the terms in Eqs. 9.17-9.19 become negligible, since at least one of the sums in the product does not add constructively.

In an analogous way to the crystal structure factor we define the spin structure factor, which is a measure of the spin order of the ensemble, as

$$S_Q = \sum_{m,n} 4\langle \sigma_z \rangle_m \langle \sigma_z \rangle_n e^{i\mathbf{Q} \cdot (\mathbf{R}_n - \mathbf{R}_m)} = N(N-1) \quad (9.27)$$

and we can relate it to the measured intensity as

$$I_Q^{\text{spin}}/A = e^{-2W} \frac{2s_0\Delta^2}{(4\Delta^2 + s_0)^2} N(S_Q - 1) + N \frac{s_0/2}{4\Delta^2 + s_0} \quad (9.28)$$

9.1.5 Time-of-flight

We have seen that the Debye-Waller factor, e^{-2W} depends on the spatial extent of the atomic wavefunctions. It appears in front of the coherent term for both I_Q^{crystal} and I_Q^{spin} .

If the atoms confined to the locked lattice have a position variance given by $\langle r_i^2 \rangle$, then after releasing them in time-of-flight (TOF) the variance will evolve according to

$$\begin{aligned}\langle r_i^2 \rangle_t &= \langle r_i^2 \rangle_0 + \frac{t^2}{m^2} \langle p_i^2 \rangle_0 \\ &= \langle r_i^2 \rangle_0 + \frac{t^2}{m^2} \frac{\hbar^2}{4\langle r_i^2 \rangle_0}\end{aligned}\tag{9.29}$$

In a harmonic oscillator potential

$$\langle r^2 \rangle = \frac{\hbar}{2m\omega}\tag{9.30}$$

and for a lattice with spacing a and depth v_0 ,

$$\langle r^2 \rangle = \frac{a^2}{2\pi^2 \sqrt{v_0/E_r}}\tag{9.31}$$

After some time-of-flight, t , the Debye-Waller factor will be

$$[e^{-2W}]_t = [e^{-2W}]_0 \exp \left[-\frac{\sqrt{v_0/E_r}}{2} \left(\frac{|\mathbf{Q}|h}{2ma} \right)^2 t^2 \right]\tag{9.32}$$

For a sufficiently long TOF, which we indicate with the subscript ∞ , the Debye-Waller factor goes to zero:

$$[e^{-2W}]_\infty \rightarrow 0\tag{9.33}$$

and the intensity at the detector will consist only of the incoherent part:

$$I_{Q\infty} = A \frac{Ns_0/2}{4\Delta^2 + s_0}\tag{9.34}$$

Using the above expression for the intensity after long TOF, we can rewrite the expressions for the crystal and structure factors in the simple form:

$$\frac{I_Q^{\text{crystal}}}{I_{Q\infty}^{\text{crystal}}} = C_Q^{-1}(S_Q^{\text{crystal}} - 1) + 1$$

crystal structure
(9.35)

$$\frac{I_Q}{I_{Q\infty}} = C_Q^{-1}(S_Q - 1) + 1$$

spin structure
(9.36)

where we have defined the correction factor $C_{\mathbf{Q}}$ as

$$C_{\mathbf{Q}} = e^{2W} \left(1 + \frac{s_0}{4\Delta^2} \right) \quad (9.37)$$

This correction factor allows one to obtain the crystal and spin structure factors from the ratio of *in-situ* and TOF measurements of the intensity at \mathbf{Q} . The correction takes care of accounting for the finite spatial extent of the wavefunctions in the locked lattice, and also accounts for saturation of the atomic transition due to the intensity and detuning of the probe light.

9.2 Experimental setup

One of the limitations when doing Bragg scattering in an ultracold atom experiment is the lack of sufficient optical access to setup the vectors \mathbf{k} and \mathbf{k}' of the input and output light such that the momentum transfer, \mathbf{Q} , matches a vector or the reciprocal crystal lattice or the reciprocal magnetic sublattice. The orientation of the lattice in the vacuum chamber, the lattice spacing, and the wavelength of the light define the possible angles at which the Bragg condition will be satisfied.

We have implemented setups to guarantee access to two values of the momentum transfer. One of them corresponds to scattering from the $(0\ 1\ 0)$ lattice planes, and the other one corresponds to scattering from the $(-\frac{1}{2}\ -\frac{1}{2}\ +\frac{1}{2})$ magnetic sublattice planes. Both cases are illustrated in Fig. 9.3. The situation for the $(-\frac{1}{2}\ -\frac{1}{2}\ +\frac{1}{2})$ scattering with respect to our vacuum chamber is shown in Fig. 9.4. In the figure, the lattice beams propagate along x , y and z . To facilitate the alignment of the $(-\frac{1}{2}\ -\frac{1}{2}\ +\frac{1}{2})$ input beam we planned for it to lie on the yz -plane. To satisfy the Bragg condition, the direction of propagation of the Bragg input beam makes an angle of 3.06° with the positive y -axis. The input beam for the $(0\ 1\ 0)$ scattering direction (not shown in the Fig. 9.4) is also selected to lie on the yz -plane. It propagates along a line that makes an angle of 50.9° with the negative y -axis.

The illustration in Fig. 9.4 has the top viewport of the vacuum system removed. The

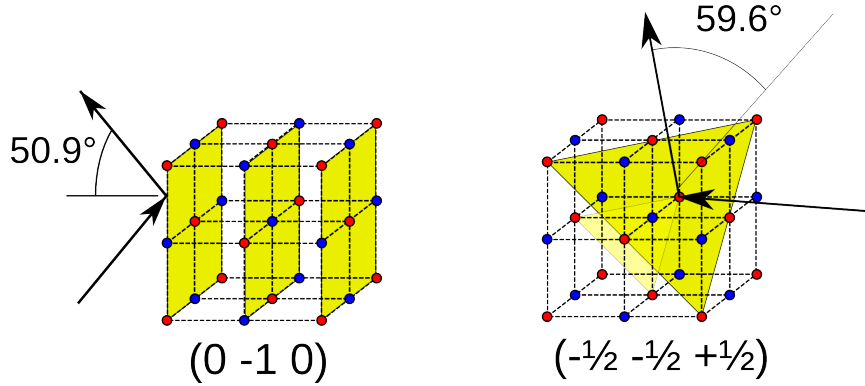


Figure 9.3: Illustration of the angles involved in Bragg scattering. The crystal structure factor is addressed by scattering off of the $(0 1 0)$ lattice planes, and the spin structure factor is addressed by scattering off of the $(-1/2 -1/2 +1/2)$ magnetic sublattice planes.

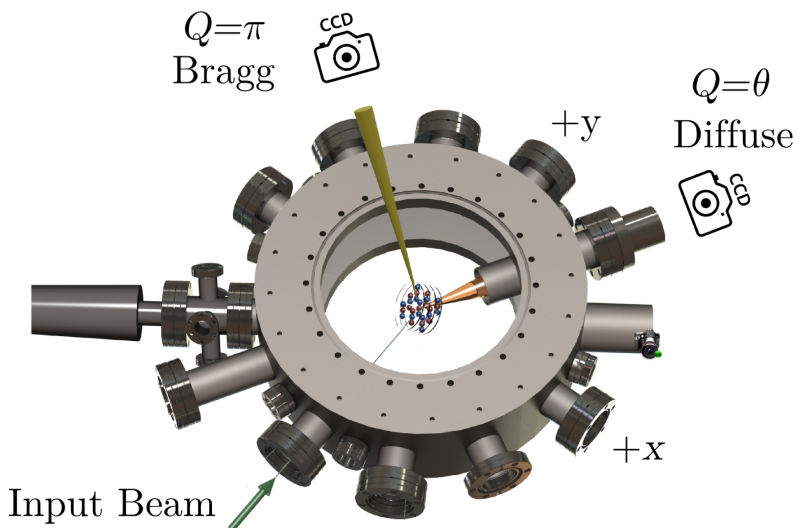


Figure 9.4: Experimental setup for the $(-1/2 -1/2 +1/2)$ Bragg scattering direction, showing the vacuum chamber. The momentum transfer \mathbf{Q} for Bragg scattering off of the $(-1/2 -1/2 +1/2)$ magnetic sublattice is denoted as π . An additional imaging viewport allows us to measure the light scattered in a direction that does not satisfy the Bragg condition, labeled as $\mathbf{Q} = \theta$.

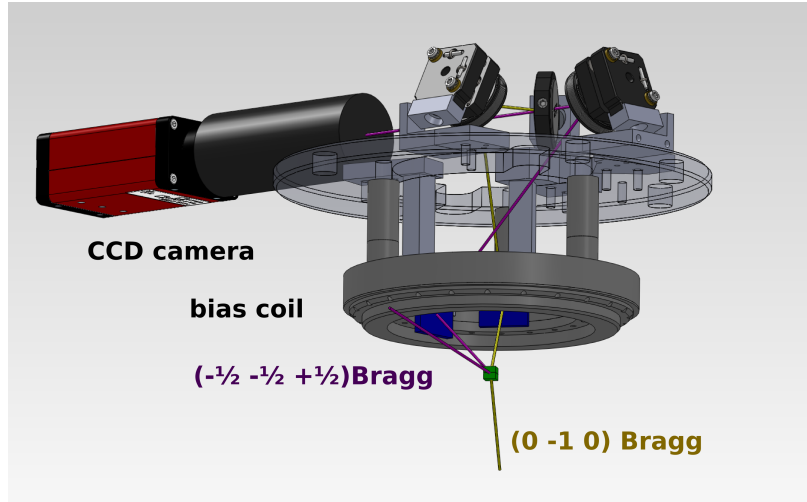


Figure 9.5: Optical setup to guide the output Bragg light to the CCD for detection. Two dropdown mirrors are positioned inside the re-entrant viewport to reflect the Bragg output light for the $(0 1 0)$ and $(-\frac{1}{2} -\frac{1}{2} +\frac{1}{2})$ setups. In both cases the light is reflected by a second mirror positioned on the rim of the re-entrant viewport. A removable mirror allows to select whether the $(0 1 0)$ or the $(-\frac{1}{2} -\frac{1}{2} +\frac{1}{2})$ output light goes to the imaging setup.

reader may remember that we have a re-entrant viewport on the top, and that the magnetic coils sit inside the re-entrant viewport to be close to the atoms (see Fig. 4.13). In Fig. 9.5 we show the optical setup used to guide the output Bragg light from the atoms to an imaging system and CCD camera, where the light is collected.

9.2.1 Diffuse background

In addition to the CCD camera used for dedicated imaging of either the crystal or spin structure factor, we have at our disposal the camera that is regularly used to image the atom cloud. Keeping the same direction of the Bragg input beam, and measuring the scattered light at a direction that does not satisfy the Bragg condition provides an alternative background for the Bragg scattering measurement, in addition to the normalization done with an uncorrelated sample after long TOF. Figure 9.4 illustrates this additional imaging direction, which we refer to as “diffuse”.

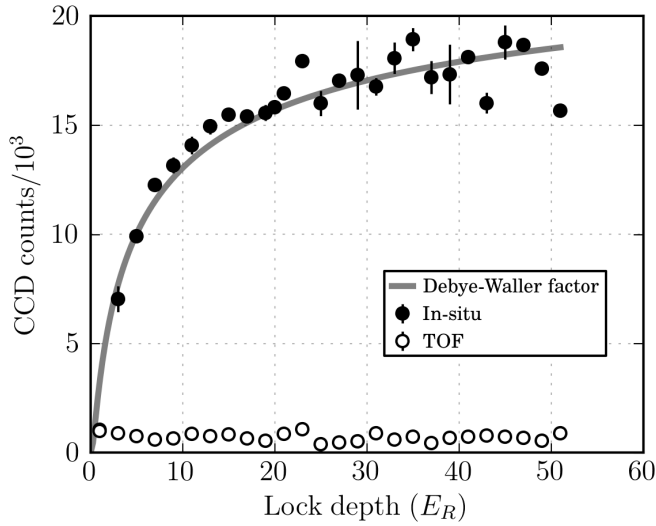


Figure 9.6: Measurement of Bragg scattering signal vs. lock depth. The Bragg probe used had a waist of $500 \mu\text{m}$ and a $200 \mu\text{W}$ of power, for a saturation parameter $s_0 = 12.4$. The detuning used was $-28 \text{ MHz} (-4.7\Gamma)$ from state $|2\rangle$. The exposure time was $1.7 \mu\text{s}$. A measurement taken after a long TOF ($6 \mu\text{s}$) shows the incoherent scattering background.

9.3 Measurement of the crystal structure factor

As a test of our ability to do Bragg scattering, and also to find out the practical limits of sensitivity for this technique, we set out to measure the crystal structure factor along the $(0 1 0)$ scattering direction. We used a sample in an uncompensated lattice, for the simple reason that we do not have to guarantee the proper alignment of the compensation beams to perform the experiment. We also used a surveillance CCD camera, which does not have the best noise characteristics. As we will explain later on, when we went on to measure Bragg scattering in the $(-\frac{1}{2} -\frac{1}{2} +\frac{1}{2})$ direction we had to make use of a low noise cooled CCD camera.

Figure 9.6 shows a measurement of the Bragg scattered light versus the lock depth of the lattice. For larger lock depth, v_0 , the Debye-Waller factor increases as

$$[e^{-2W}]_0 = e^{-2\sqrt{v_0/E_r}} \quad (9.38)$$

Releasing the atoms in time of flight reveals the expansion of the atomic wavefunction, causing a decay of the Bragg scattering signal in a very short time of only a few micro

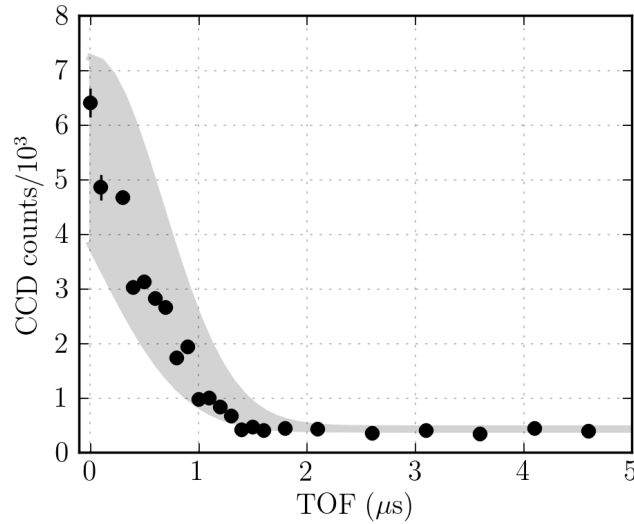


Figure 9.7: Measurement of Bragg scattering signal vs. TOF. The lattice depth was locked to $20 E_r$. For this measurement the power, waist and exposure of the probe are the same as in Fig. 9.6. The detuning is -53 MHz (-9.0Γ) from state $|2\rangle$, resulting in a lower overall signal than is seen in Fig. 9.6 at a lock depth of $20 E_r$.

seconds, as shown in Fig. 9.7

9.3.1 Angular dependence of the scattering

We also measured the variation of the Bragg scattering signal with respect to the angle of the input beam. For this measurement we kept the $(0\ 1\ 0)$ input Bragg beam in the yz -plane and varied the angle it makes with the xz -plane. The results are shown in Fig. 9.8. From a measurement of the $1/e$ radius of the angular distribution one can obtain the correlation length of the sample. In this case every atom is localized at a lattice site, and all of the them contribute constructively to the Bragg scattered signal in the detector. The correlation length must then be indicative of the size of the entire sample.

In order to relate the width of the angular distribution to the correlation length, one must assume some functional form for a correlation function. For example, if correlations are starting to form on the approach to a phase transition, the correlation function may be

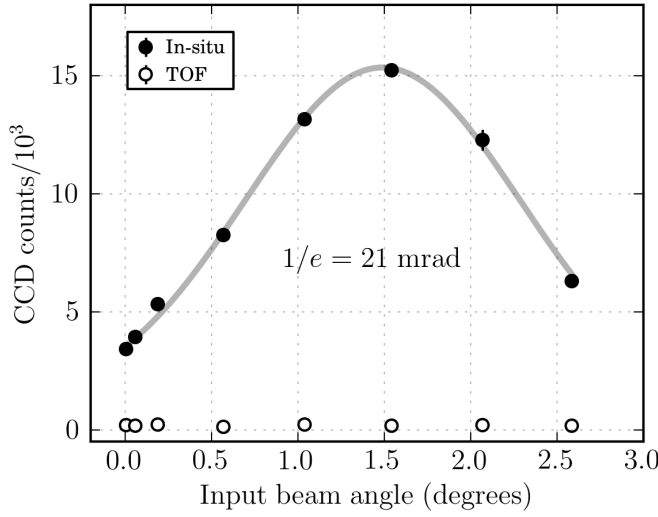


Figure 9.8: Measurement of Bragg scattering signal vs. input angle of the Bragg probe. The label shows the $1/e$ radius of the Gaussian fit, determined to be 21 mrad.

an exponential:

$$f_c(|\mathbf{R}_m - \mathbf{R}_n|) = e^{-|\mathbf{R}_m - \mathbf{R}_n|/L_c} \quad (9.39)$$

In terms of the correlation function, a generic structure factor can be written as

$$F_{\mathbf{Q}} = \frac{1}{N} \sum_{m,n} e^{i\mathbf{Q} \cdot (\mathbf{R}_m - \mathbf{R}_n)} f_c(|\mathbf{R}_m - \mathbf{R}_n|) \quad (9.40)$$

If the Bragg condition is fulfilled at $\mathbf{Q} = \mathbf{Q}_0$ ², one can define the small vector $\mathbf{p} = \mathbf{Q} - \mathbf{Q}_0$.

In terms of the small vector \mathbf{p} , and splitting the sum into $m = n$ and $m \neq n$ parts:

$$\begin{aligned} F(\mathbf{p}) &= \frac{1}{N} \left(\sum_{m=n} + \sum_{m \neq n} \right) e^{i\mathbf{p} \cdot (\mathbf{R}_m - \mathbf{R}_n)} f_c(|\mathbf{R}_m - \mathbf{R}_n|) \\ &\approx 1 + \sum_k e^{i\mathbf{p} \cdot \mathbf{R}_k} e^{-|\mathbf{R}_k|/L_c} \end{aligned} \quad (9.41)$$

where in the last line we have changed variables according to $\mathbf{R}_m = \mathbf{R}_n + \mathbf{R}_k$, and neglected edge effects by assuming that the correlation function vanishes at a length smaller than the size of the crystal³. The sum in the last term can be approximated as an integral as

$$F(\mathbf{p}) \approx 1 + \frac{1}{a^3} \int_{\mathbb{R}^3} d\mathbf{R}_k e^{i\mathbf{p} \cdot \mathbf{R}_k} e^{-|\mathbf{R}_k|/L_c} \quad (9.42)$$

²Which implies $e^{i\mathbf{Q}_0 \cdot (\mathbf{R}_m - \mathbf{R}_n)} = 1$ for all m, n .

³This assumption does not apply in the present case (crystal structure factor), but will be true for the spin structure factor, where at the lowest achievable temperatures the correlations are still short ranged

where a is the lattice spacing. The Fourier transform of a spherically symmetric function in three dimensions is equivalent to the Fourier-Bessel transform of the radial function:

$$F(\mathbf{p}) \approx 1 + 4\pi \int_0^\infty f(R) \frac{\sin(pR)}{pR} R^2 dR \quad (9.43)$$

which can be integrated analytically to obtain

$$F(\mathbf{p}) \approx 1 + \frac{8\pi}{a^3} \frac{L_c^3}{[1 + (L_c|\mathbf{p}|)^2]^2} \quad (9.44)$$

If one changes the angle of the input vector by a small amount $\delta\alpha$ (measured in radians) then, to first order, the magnitude of \mathbf{p} changes as $\delta p = \frac{2\pi}{\lambda_0} \delta\alpha$, where λ_0 is the wavelength of the Bragg probe.

The final result for the angular distribution of the scattered light is

$$\frac{F(\delta\alpha) - 1}{F(0)} \approx \frac{1}{\left[1 + \left(\frac{2\pi L_c}{\lambda_B} \delta\alpha\right)^2\right]^2} \approx \exp\left[-2\left(\frac{2\pi}{\lambda_B} L_c \delta\alpha\right)^2\right] \quad (9.45)$$

and the $1/e$ radius of the angular distribution is given by

$$\delta\alpha_{1/e} \approx \frac{\lambda_B}{2\pi\sqrt{2}} \frac{1}{L_c} = \frac{\lambda_B/a}{2\pi\sqrt{2}} \frac{1}{L_c/a} = \frac{0.14}{L_c/a} \quad (9.46)$$

For the $(0\ 1\ 0)$ Bragg scattering results shown in Fig. 9.8, if one assumes an exponential correlation function, the correlation length would be $L_c = 7a$. The $1/e$ radius of the cloud in the uncompensated lattice is measured to be $13\ \mu\text{m}$ ($24a$). According to the analysis presented, the measured angular distribution should have been narrower. The discrepancy is, most likely, due to the fact that the correlation function in the crystal structure case is not exponential, but rather has a sharp cutoff at some radius. Nevertheless, the disagreement points at a possible error on the measurement, or maybe hints at the fact the the assumption of a certain correlation function can systematically affect an estimate of the correlation length obtained from the width of the angular distribution.

Summary To summarize, in this chapter we have derived a way to relate measured intensities to structure factors using Bragg scattering. The measurement relies on the ability to realize an uncorrelated sample by simply releasing the atoms in time of flight. Corrections due to the finite extent of the atomic wavefunctions in the lattice (Debye-Waller factor) and due to the saturation of the atomic transition have been derived. Taking into account saturation effects is not necessary for the $(0\ 1\ 0)$ Bragg scattering, because the light can be far detuned, but it will be mandatory for spin sensitive Bragg scattering on the $(-1/2\ -1/2\ +1/2)$ direction, where the detuning is determined by the spacing between levels $|1\rangle$ and $|2\rangle$.

In Chapter 12 we will show the results for a measurement of the spin structure factor, S_Q , in a sample which has developed short range correlations on the approach to the Néel transition. There we will see that the measurement of S_Q , can be compared to theoretical calculations in order to establish precise thermometry of the atoms in the lattice.

10. Experimental procedures

Back in Chapter 4 we gave an overview of the experimental setup and gave some details of the experimental procedure up to loading the atoms into the optical dipole trap (ODT). From this point, the atoms are evaporated down to degeneracy, which leaves them in the dimple trap. Then we proceed to load the optical lattice where we carry out our experiments. The operation of the experiment up to the UVMOT step is very robust and very rarely needs adjustments, other than performing maintenance on the 323 nm laser system to ensure it has enough output power. On the other hand, loading enough atoms into the ODT and making sure that evaporation proceeds properly to ensure the lowest final temperatures is a critical step which requires much more attention. The alignment of the lattice and compensation beams is extremely sensitive, and is something that needs to be checked every day, and right before we start taking data. In fact, we find that our most sensitive signal (antiferromagnetic (AFM) correlations) only persists for a few hours after the alignment process, as the beams slightly drift away and get misaligned. The process of ramping up the lattice, by slowly rotating the polarization of the lattice retro beams, is also something that we find critical for the experiment. As the polarization is rotated, the power in the compensation beams is adjusted to ensure that the density distribution of the atoms does not change much in going from the dimple to the final compensated lattice. In this chapter, I will give more details about the procedures outlined above.

10.1 Production of a deeply degenerate ${}^6\text{Li}$ spin mixture in a dimple potential

Before we started using the dimple potential as the default starting point of most of our experiments, we spent significant time optimizing the evaporation trajectory in the ODT itself. In the ODT, it is very difficult to consistently get temperatures below $T/T_F \approx 0.10$. The final temperature is very sensitive to the final depth of the ODT, which can change slightly on a daily basis. Drifts in the calibration of the intensity control loop, the exact shape of the potential (and therefore the trapping frequencies which determine the collision rate), or minor changes in alignment and mode quality of the beams are the principal factors that affect evaporation in the ODT.

Despite the sensitivity of the performance of the ODT itself, we found that adding the dimple potential makes the system much more robust. We keep the evaporation trajectory of the ODT the same, and simply ramp up the dimple potential to a certain depth at the beginning of evaporation, while the ODT is still deep. At that point, the dimple ($\sim 1.4 \mu\text{K}$) is a minor perturbation on the ODT potential ($\sim 300 \mu\text{K}$). As the ODT is evaporated away, the atoms collect in the dimple, where the trapping frequencies are larger, the collision rate is increased and evaporation proceeds more efficiently. We find that after the ODT is evaporated away, the atoms in the dimple reach the coldest temperatures that we record, as low as $T/T_F = 0.04$. Depending on the depth of the dimple, which is set at the beginning, the final number of atoms can be varied and low temperatures still achieved. We have verified this to be the case for atom numbers as high as $N \approx 500,000$ atoms.

10.1.1 Optimized trajectory for evaporation in the ODT

After loading the atoms from the UVMOT into the ODT the magnetic field is set to 340 G, where the scattering is $\sim -300a_0$. We keep the depth of the ODT constant for 1 s, letting the atoms undergo unforced evaporation, and then we start ramping down the

power of the ODT.

The trajectory for evaporation of the ODT is based on the work by the group of John Thomas [113, 142]. It is defined by the following equations:

$$\text{evap}(t) = \begin{cases} (1 - u_0)(p_0 - p_1) \frac{\tanh\left[\frac{\beta}{\tau} \frac{p_1}{p_0 - p_1}(t - t_1)\right]}{\tanh\left[\frac{\beta}{\tau} \frac{p_1}{p_0 - p_1}(-t_1)\right]} + p_1 + u_0 & \text{if } t \leq t_1 \\ (1 - u_0)p_1(1^\beta) \frac{1}{\left(1 + \frac{(t - t_1)}{\tau}\right)^\beta} + u_0 & \text{if } t_1 < t \leq t_2 \\ \left((1 - u_0)p_1(1^\beta) \frac{1}{\left(1 + \frac{(t_2 - t_1)}{\tau}\right)^\beta} + u_0 \right) \frac{1}{1 + \frac{(t - t_2)}{\tau_2}} & \text{if } t_2 < t \end{cases} \quad (10.1)$$

The first portion is a smoothing “knee”, to avoid an abrupt start of the ramps. The second and third parts use a power law decay with time constants τ and τ_2 . The initial time constant is appropriate above degeneracy, and as the gas becomes degenerate ($t \approx t_2$) the trajectory is slowed down ($\tau_2 > \tau$). The trajectory as defined in Eq. 10.1 has a kink (discontinuous derivative) at t_2 . In addition to the definition above we define a time δt , and for times $t_2 - \delta t/2 < t \leq t_2 + \delta t/2$ we patch the second and third parts of the piece-wise function with a third order polynomial that makes sure the derivative of the trajectory stays continuous. The values of the parameters that we currently use are as follows:

p_0	p_1	t_1	τ	β	u_0	t_2	τ_2	δt
10.25	6.5	780.0	1400.0	1.55	-0.157	3000.	1000.	200.

A plot of the trajectory is shown in Fig. 10.1. The reader may have noticed that the equation that defined the trajectory has no physical units. We define the maximum stabilized intensity of the ODT as 10, and the ODT being maximally attenuated as 0. According to our parameters there is a small part of the trajectory in which we overdrive the intensity stabilization circuitry ($p_0 > 10$), thus getting the maximum power available from the ODT.

Along the evaporation trajectory we can measure the temperature of the atoms in four different ways, which are listed below:

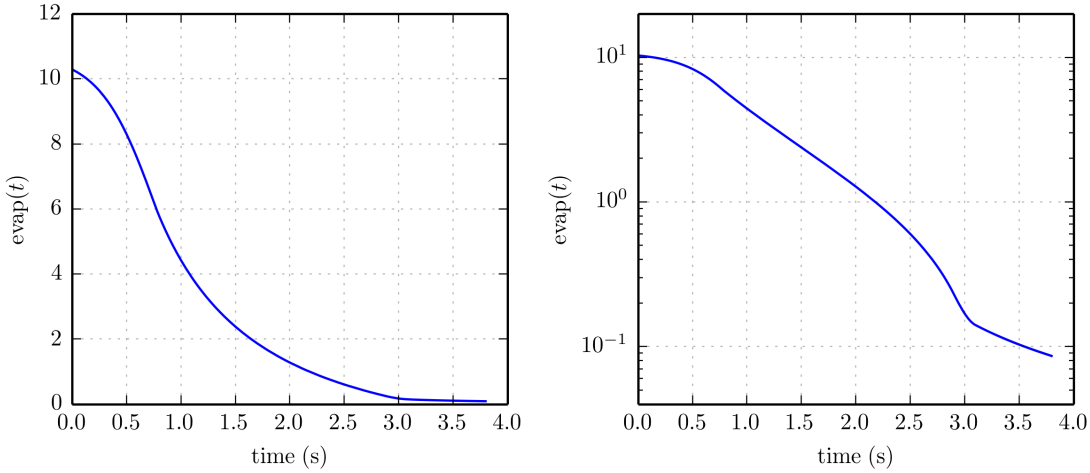


Figure 10.1: Evaporation trajectory define in Eq. 10.1. The parameters used to generate this curve are tabulated in the text. The evaporation trajectory is shown here up to 3.8 seconds.

1. From a 2D fit of the cloud to a Thomas-Fermi distribution one can extract T/T_F from the fixity, $e^{\beta\mu}$. This only works for degenerate clouds, $T/T_F \lesssim 0.5$.
2. From a fit to the azimuth ally averaged density distribution, one can extract T/T_F from the fixity. This only works for degenerate cloud, $T/T_F \lesssim 0.5$
3. From a fit to the azimuth ally averaged density distribution, T can be extracted from the size of the fit. If the trap frequencies are well known, this can be done using *in-situ* images. Otherwise a long time-of-flight (larger than the inverse of the trap frequencies) can be used to address the momentum distribution directly. This method works well above and below degeneracy.
4. A ballistic expansion measurement can be done, where the size of the cloud is measured as a function of time-of-flight. This method only works for non-degenerate samples with a negative fixity, $\beta\mu < 0$. For degenerate clouds this method can be used as a measure of the Fermi energy.

Figure 10.2 shows measurements of the temperature using the four methods outlined above, as a function of time along the evaporation trajectory.

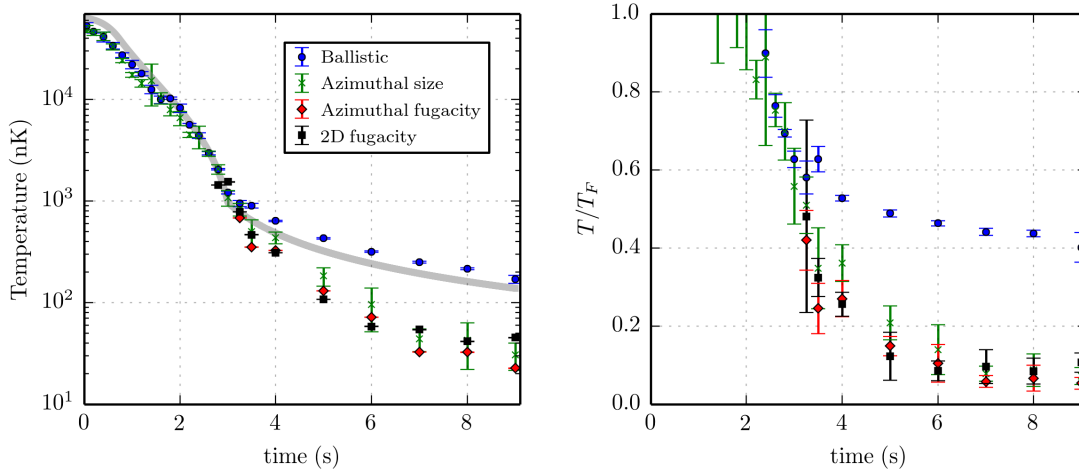


Figure 10.2: Temperature measured along the evaporation trajectory defined in Eq.10.1. The trap depth divided by a factor of 5 is shown as a thick gray line. The gas becomes degenerate when the temperature determined from ballistic expansion deviates from the other methods. The Fermi temperature (used to obtain T from measured values of T/T_F) is calculated using the calibrated trap frequencies. The coldest values are obtained after at least 7 seconds of evaporation and can reach $T/T_F < 0.1$.

Maintenance tips

Troubleshooting evaporation in the ODT is something we have to do routinely, below we mention a few points to which one has to pay attention.

- The stabilization circuitry for the ODT uses a dual photodiode scheme in which the feedback transfer function changes abruptly at a point during the evaporation ramp. This is discussed in detail in Ernie Yang's Master's thesis [109]. The circuit is prone to developing noise if the parameters to control the gain in the crossover region are not set appropriately. One must check the power measured by the stabilization circuit on the oscilloscope, and make sure that no noise is added on the intensity in the vicinity of the transfer function kink.
- The maximum trap depth of the ODT determines the number of atoms loaded, which ultimately affects the efficiency of the evaporation trajectory. To measure the trap depth, we take the temperature of the atoms after 1 s of unforced evaporation in

the ODT, using a ballistic expansion method. The idea is that the scattering length (which is fixed) determines the ratio between the trap depth and the final temperature after enough time of unforced evaporation. We usually observe a temperature between 30 and 40 μK , anything less indicates that the ODT may not be deep enough.

- If the ODT is not deep enough there are a few usual suspects. Number one is accumulation of dust on the ODT optics. The prime optic where this happens is lens labeled F in Fig. 4.12. Try cleaning that lens first and then go after any optic that faces upwards. The proper crossing of the two ODT passes is also critical, as is the efficiency of the AOM that controls the ODT intensity.

10.1.2 Modifications to the trajectory for evaporating into the dimple

When evaporating the atoms from the ODT into the dimple trap we make a few simple changes to the evaporation trajectory. The magnetic field is changed 3 seconds into the evaporation, going from 340 G ($-300a_0$) to 595 G ($+326a_0$). This is done so that we finish up preparing the sample in the vicinity of the magnetic field necessary to realize a Hubbard model with repulsive interactions. During the 1 s of unforced evaporation, right after loading the atoms from the ODT, the dimple trap is slowly ramped up to the desired depth. This depth is varied to control the number of atoms in the sample. Finally, after evaporating the ODT (with the usual trajectory) for 5.5 s, we turn it completely off using a smooth (hyperbolic tangent) turn-off ramp with a time constant of 80 ms. The ramps used for this procedure are shown in Fig. 10.3

T/T_F measurement

After evaporation into the dimple trap we measure T/T_F by imaging the atoms after 0.5 ms of time-of-flight. The distribution is allowed to expand so that we effectively gain some resolution, necessary to capture the details of the tail of the distribution, to which

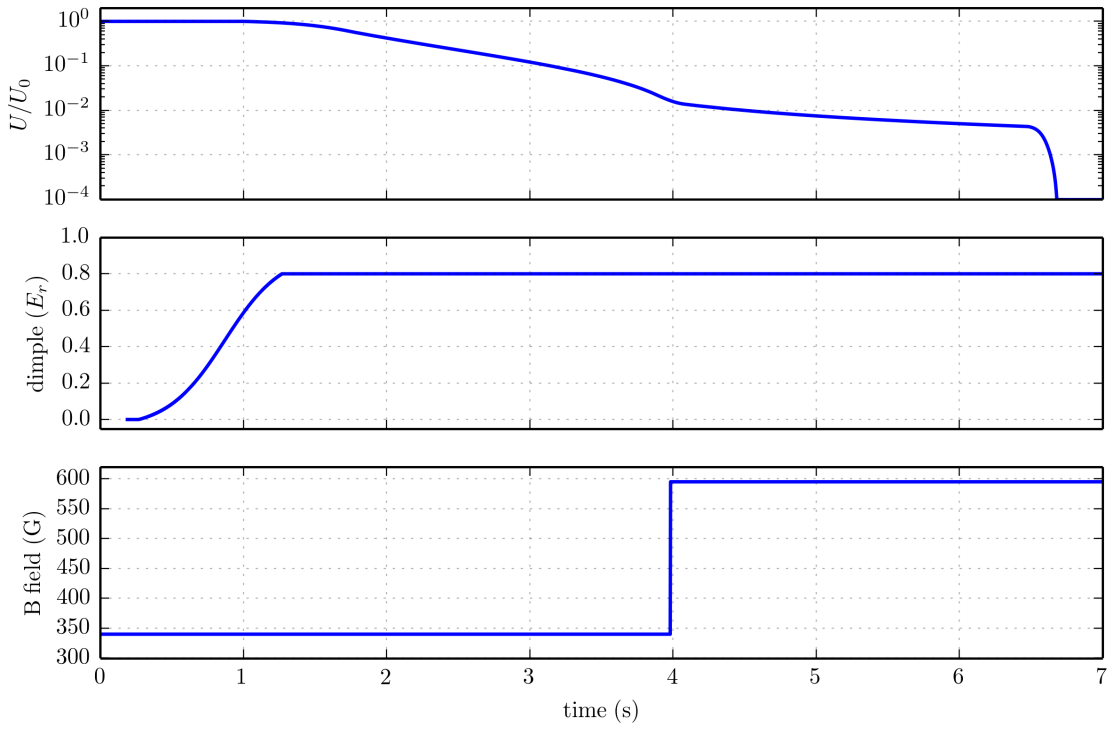


Figure 10.3: Ramps for evaporating atoms into the dimple trap. The top plot shows the relative depth of the ODT. There is 1 s of unforced evaporation, and then the ramps presented in the previous section take over. The central plot shows the dimple trap depth per beam, which is turned on at the very beginning during the unforced evaporation. The bottom plot shows the magnetic field. At $t = 7$ s a degenerate cloud at $T/T_F \approx 0.04$ is produced in the dimple trap.

the temperature fit is most sensitive. An example of a cold cloud released from the dimple is shown in Fig. 10.4. We determine the temperature from 2D fits to the column density distribution and also fits to the Azimuthal average of the density distribution. The $1-\sigma$ confidence interval for a given fit typically spans the range from $T/T_F = 0.01$ to $T/T_F = 0.10$, as the Thomas-Fermi function loses its sensitivity at such low temperatures. Nevertheless, the variance of the fitted value for a set of shots is low. In Fig. 10.4, we quote the standard deviation of the fitted value (for a set of eight realizations) as the error in T/T_F .

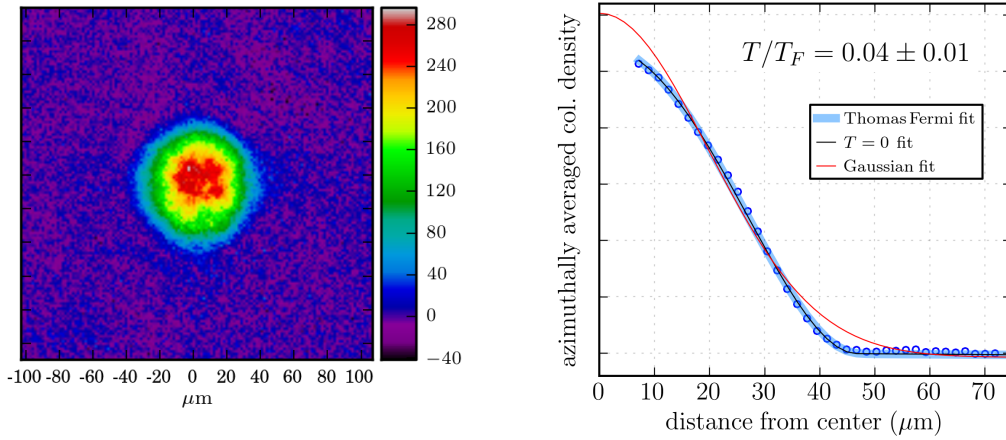


Figure 10.4: (Left) Average of the column density for 6 shots. Images taken after 0.5 ms TOF. (Right) Azimuthal average of the column density for a single shot, along with curves showing different fits to the distribution. The azimuthal average at small radii tends to have larger noise, so we exclude the first few data points from the fit.

10.2 Lattice alignment procedure

The alignment of the beams that make up the final compensated lattice potential is critical for producing AFM correlations in the final sample. The lattice loading ramps and the final compensation parameters are tailored specifically to a certain shape of the potential, so if that changes slightly, the final density distribution and the density distribution during loading will be affected.

The alignment procedure starts out by aligning the ODT to make sure it is centered on the lattice. The three lattice beams are then fine tuned, and the compensation beams are positioned such that they overlap the lattice beams. Below we outline the procedure for aligning the system.

- The lattice axes propagating along x , y , and z , are labeled 1 2 and 3 respectively.
The input pass of beam 3 is never moved and serves as an anchor point for the entire system.
- First we align the first pass of the ODT (refer to Fig. 4.12) with beam 3 of the lattice.

The polarization of the beam 3 retro is set in lattice configuration (parallel to that of the input beam), and a cross beam trap is formed with the first pass of the ODT. The second pass of the ODT is blocked with a beam dump, placed between mirrors Q and R in Fig. 4.12. The translation stage labeled O is used to maximize the number of atoms that remain, after evaporation, in the crossing between beam 3 and the first pass of the ODT.

- The second pass of the ODT is aligned (using translation stage labeled T in Fig. 4.12) such that images of the full ODT and the crossing of beam 3 and the ODT first pass appear at the same spot in *in-situ* phase-contrast images. At this point, beam 3 and the ODT are centered with respect to each other.
- A cross beam trap is formed between beams 1 and 3 of the lattice (both in dimple configuration). *In-situ* imaging is used to adjust the vertical position of beam 1 such that the crossing of beams 1 and 3 appears in the images at the same height as the ODT. The same method is used to adjust the height of beam 2 of the lattice.
- The horizontal adjustment of beam 1 is done by maximizing the number of atoms that can be evaporated from the ODT into a cross beam trap formed by beams 1 and 3 (both beams in dimple configuration). The same method is used to adjust the horizontal positioning of beam 2 of the lattice. After this step, all of the lattice axes are in place and only the compensation beams are left.
- **Remark.** Please note that the entire input assembly for the lattice plus compensation beams is mounted on a translator stage, see Fig. 10.5. The vertical and horizontal adjustments mentioned in the two steps above for beams 1 and 2 refer to motions of that stage. The entire retro assembly for the lattice beams is also in a single translation stage, as shown in the figure. Every time the input assembly is moved, the retro assembly must be aligned to maximize the light that is back coupled through the lattice optical fiber. The retro assembly positioning is controlled with stepper

motors. Feedback from a photodiode, which measures the light back coupled through the fiber, is used to automatically set the retro assembly position.

- To align the compensation beams we have two degrees of freedom, given by the two knobs of the final mirror before the lattice and compensation beams are overlapped (refer to Fig. 4.21). The two knobs are controlled by PicoMotor actuators (Newport Corporation), which allow changing the pointing of the beam by steps of $0.7 \mu\text{rad}$. An illustration of the positioning accuracy of the PicoMotor, recorded with a CCD while moving the compensation beam waist with respect to the lattice beam waist, can be seen in video at <http://bit.ly/moving-picomotor>.
- The horizontal and vertical positioning of the compensation beams is performed by an automated procedure which takes images of the evaporated cloud and feeds back to the PicoMotor stepper. For example, to adjust the vertical positioning of the compensation along axis 1, we form a cross beam trap with lattice beams 1 and 3 (both in dimple configuration). If the compensation is totally misaligned this dimple trap is unperturbed. As the compensation is brought into alignment, the confinement of beam 1 is modified, causing the position of the crossing to move along beam 3, and the size of the resulting samples to start increasing along beam 3. When the compensation is aligned, the position of the sample in the crossed beam trap is the same as without compensation, and the size of the sample along beam 3 is increased noticeably. We show an illustration of this behavior in Fig. 10.6.
- The automated procedure in the last step is iterated a few times until the horizontal and vertical adjustments on the compensation converge. The same process is then repeated for the other compensation beams.
- **Remark.** Even though most of the procedure is automated, it is not always successful. Sometimes the alignment of one of the lattice beams can drift and the procedure to align the compensation has to be started all over. There is a chance of approximately 9 out of 10 to succeed in the alignment of the entire system on a given day.

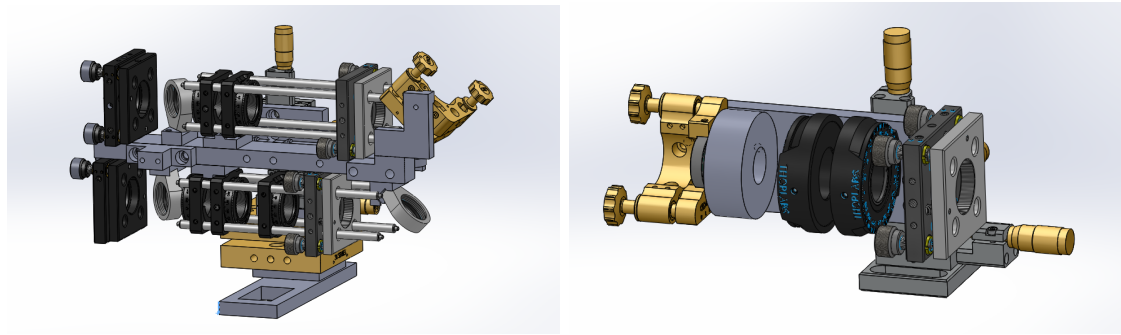


Figure 10.5: Input assembly for the compensated lattice (left). Retro assembly for the compensated lattice (right). Refer to Fig. 4.21 for a schematic of the optical setup in each assembly.

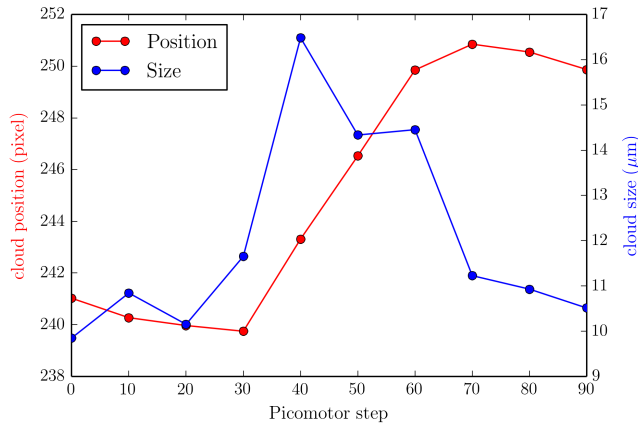


Figure 10.6: Positioning of the compensation beam with PicoMotor stepper. The position and size of the cloud in a cross beam trap of beams 1 and 3 is plotted versus the PicoMotor actuator step.

10.3 Lattice loading ramps

Once we have a cold sample in the dimple, we proceed to load it into the optical lattice and to set the on-site interactions, U/t , to the desired value for the experiment. The ramps we have chosen to do that are piece-wise linear in the power of the beams and in the scattering length. Different segments can be easily added from the control interface to tailor the ramps. Figure 10.7 shows the present version of the ramps, used for the data presented in the next two chapters.

The first thing we do, is abruptly switch the control voltage to the liquid crystal retarders (LCRs) that set the polarization of the lattice retro beams. The response time scale (\sim

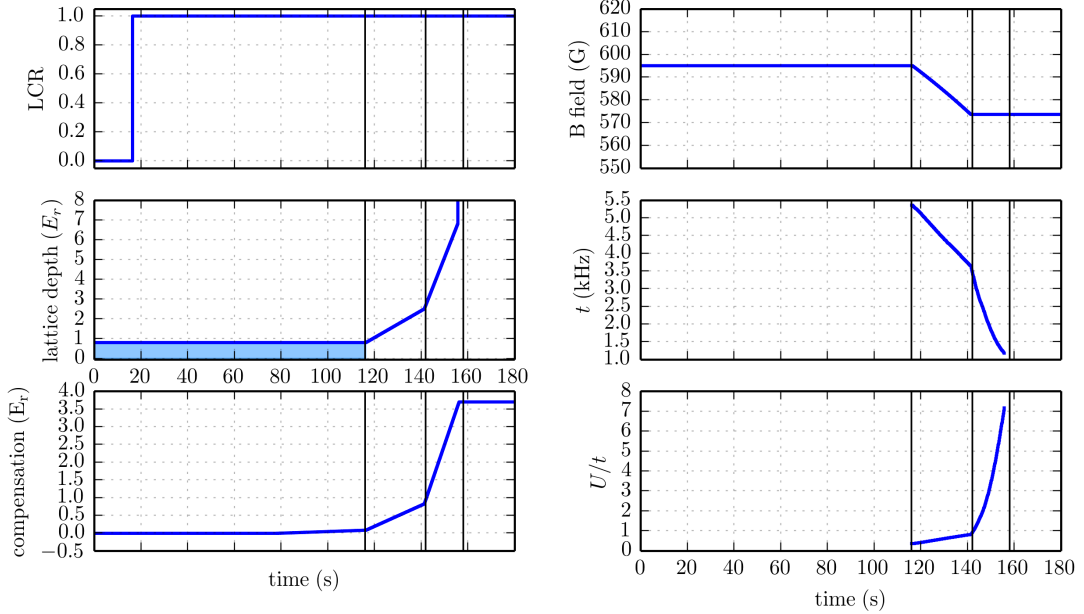


Figure 10.7: Lattice loading ramps. The LCR is switched from dimple (0) to lattice (1) mode. The polarization is fully rotated at $t = 116$ ms in the figure. The plot labeled dimple/lattice is proportional to the power of the lattice beams. In dimple configuration the y -axis is the depth per beam, and in lattice configuration the y -axis is the lattice depth. The shaded region in this plot indicates times where the retro polarization is not fully in dimple or lattice mode. The tunneling rate, t , and Hubbard interaction U/t are shown only for times where the potential is in full lattice mode.

100 ms) of the LCRs sets the time scale for the rotation of the polarization. We have observed that perhaps the ramps could proceed a little faster, but we are ultimately limited by the response time of the LCRs.

As the polarization is rotated, the sample tends to increase in density due to the larger confinement of the lattice as compared to the dimple. The power of the compensation beams is increased very slightly, to keep the peak density of the sample constant. From $t = 80$ to 116 ms, $0.06 E_r$ of compensation is added.

After the polarization is fully rotated, the lattice depth is increased from $0.8 E_r$ to $2.5 E_r$ in 25 ms. This part of the lattice ramp is done slowly because, for lattice depths below $2.4 E_r$ the lowest and first bands in the 3D lattice have not fully separated yet (refer to Fig. 2.6). During the same 25 ms the compensation is increased to $0.65 E_r$, and also the

scattering length is set (by adjusting the magnetic field) to the value that will be used in the experiment.

Once the 3D bands are separated, the ramps proceed more quickly and in 15 ms we go from $2.5 E_r$ to $7 E_r$. The compensation is adjusted to minimize the variation of the density distribution as the ramps proceed. At $t = 156$ ms in the figure, the lattice depth is locked to $20 E_r$ where we proceed to measure Bragg scattering on the $(-1/2 \ -1/2 \ +1/2)$ direction. For experiments where images of the *in-situ* density distributions are recorded we do not effect the lattice lock.

11. Mott insulating state in a simple cubic lattice

The contents of this chapter are based on a paper currently being prepared for submission, titled “Compressibility of a fermionic Mott insulator of ultracold atoms”.

We realize the repulsive Hubbard model in a $7E_r$ lattice. The scattering length is adjusted in the range of $80 - 470 a_0$, which results in interaction strengths U_0/t_0 in the range 3.1 to 18.0. The number of atoms for this study was varied between 1 and 2.5×10^5 . As was mentioned in Chapter 5, in our realization the Hubbard parameters are not constant throughout the extent of the cloud, so we use the subscript $_0$ to indicate the value of the Hubbard parameters at the center of the sample.

We perform measurements of the *in-situ* column density of the atom cloud and analyze them to extract quantities that reveal the Mott insulating regime in a simple cubic lattice with repulsive interactions. An example of the measured column density distributions is shown in Fig. 11.1. A fit to a Gaussian distribution (red line in the figure) clearly does

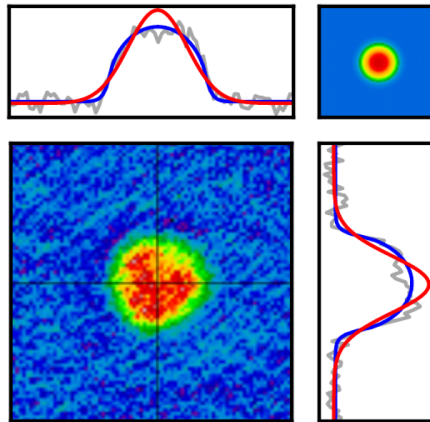


Figure 11.1: Column density distribution taken in a $7 E_r$ lattice at a scattering length $a_s = 380 a_0$. The on-site interactions are $U/t_0=14.5$. The lines are fits to the column density distribution which are explained in the text.

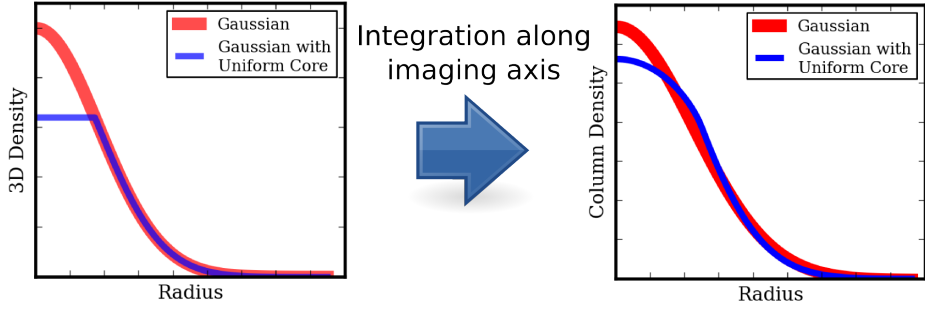


Figure 11.2: Illustration of the Mott fit function which was implemented to extract the central density from an in-situ measurement of the column density.

not properly describe the column density profile of the cloud. As was shown in Chapter 5, density profiles calculated in the local density approximation (LDA) for large interaction strengths (as the system enters the Mott insulating regime), are expected to have an $n = 1$ Mott insulating plateau at the center. Guided by the results of the LDA, we implemented a fit function that can interpolate between a Gaussian fit and what we call a Mott fit. The Mott fit function is the column integral¹ of a flat-topped density distribution function given by

$$\tilde{n}(\rho, z) = \begin{cases} \tilde{n}_0 & \text{if } \rho^2 + z^2 < r_0^2 \\ \tilde{n}_0 \exp\left[\frac{r_0^2 - \rho^2 - z^2}{\sigma^2}\right] & \text{otherwise} \end{cases}, \quad (11.2)$$

where the fit parameters are the peak density, \tilde{n}_0 , flat-top radius, r_0 , and Gaussian $1/e$ radius of the cloud's wings, σ .

Figure 11.2, illustrates the idea behind the Mott fit function, which assumes an underlying flat-topped density distribution. In Fig. 11.1, a Gaussian fit to the column density is shown as a red line, and the Mott fit is shown as a blue line. It is clear that the Mott fit is a much better representation of the observed profiles.

We used the Mott fits to extract the central density of the cloud, \tilde{n}_0 for various atom

¹ The column integral is defined as

$$\tilde{n}_{\text{col}}(\rho) = \int \tilde{n}(\rho, z) dz, \quad (11.1)$$

numbers and interaction strengths. Armed with our knowledge of the trap parameters we used the LDA to calculate theoretical profiles that could be compared to the measurements. The reader is reminded that, to realize the LDA, one must have a solution for the homogeneous Hubbard model at a grid of values for the Hubbard Hamiltonian parameters U/t , T/T and μ/t . In Chapter 5 the solution used was provided by the HTSE. We found however, that to reproduce the measured data we had to realize the calculations at a much lower temperature. The validity of the HTSE breaks down at around $T/t \approx 2.4$, so we turned to a set of solutions using NLCE and DQMC which were provided by our theoretical collaborators. At the end of Chapter 3, we have briefly described the NLCE and DQMC techniques.

In Fig. 11.3 we show the comparison of the experimental data and the LDA at two different values of the central temperature T/t_0 . For the calculations, it is assumed that the entire sample is in equilibrium at a temperature T . The local value of T/t then varies according to the variation of t in our lattice. Figure 11.3 is very revealing, first of all it shows dramatically the Mott insulating behavior obtained at large interaction strengths, where the central density of the cloud does not depend much at all on atom number. Secondly, a clear Mott insulating behavior can be observed down to $U_0/t_0 = 11.1$. This is in contrast with previous observations of the Mott insulating regime [34, 35] which required significantly larger values of U/t to obtain evidence for an incompressible state.

The low values of U_0/t_0 at which we can detect Mott insulating behavior are revealing of the temperature of the sample, which by comparison with the LDA calculations shown in Fig. 11.3 can be established to be around $T/t_0 \approx 0.6$. This value is consistent with the value that was obtained using light-scattering thermometry, as will be explained in the following chapter.

In addition to the results obtained from global fits to the column density distribution, we also went ahead and analyzed the spatial dependency of the column density profiles. One of the advantages of realizing the Hubbard model with an external confinement potential

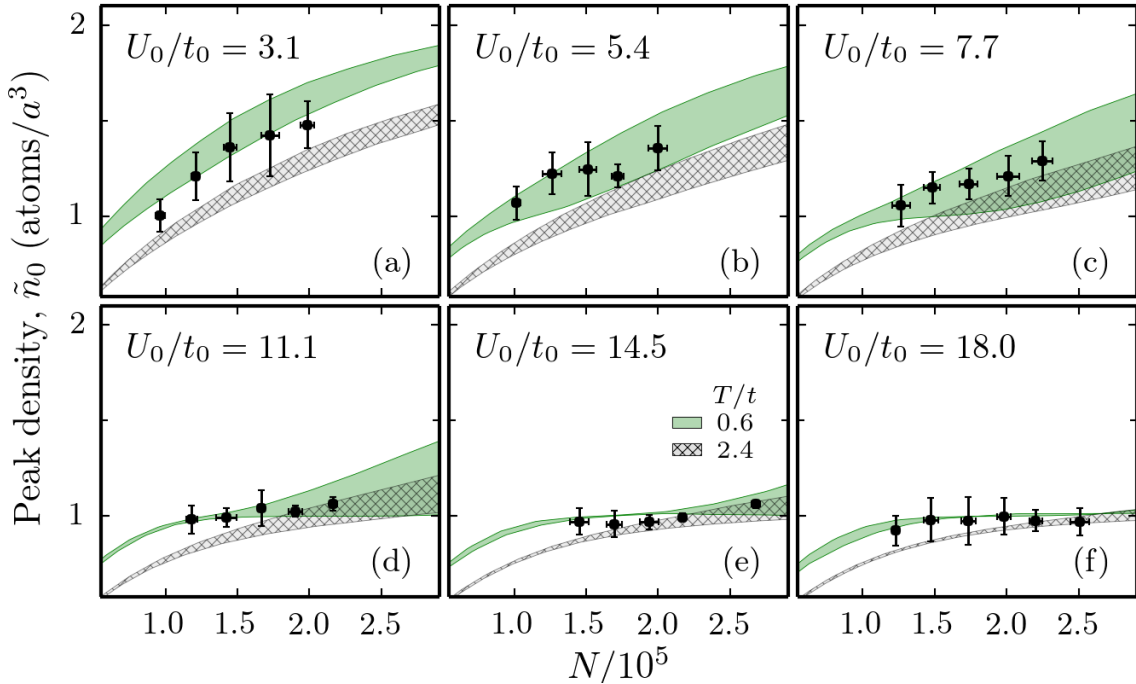


Figure 11.3: Peak density, \tilde{n}_0 vs. atom number for various interaction strengths. A fit to the column density of the cloud is used to obtain \tilde{n}_0 . The symbols show the average for a set of 5 to 10 independent realizations, with error bars indicating the standard deviation. The shaded regions are numerical calculations for our trap at $T/t_0 = 0.6$ and 2.4, with the width of the region indicating a 25% uncertainty in the value of U_0/t_0 .

is that the chemical potential varies spatially and gives the opportunity to characterize multiple regimes within a single cloud [21].

The compressibility as a function of density is an important indicator for the formation of a Mott insulating state. A Mott insulating state is incompressible, and it occurs at a density $\tilde{n} = 1$. If one can measure a compressibility as a function of density then one can provide direct proof of having accessed the Mott insulating regime.

The isothermal compressibility of a gas is defined as

$$\kappa = \frac{1}{n^2} \frac{\partial n}{\partial \mu}. \quad (11.3)$$

For atoms in a 3D lattice we consider the unitless quantity $(t/a^3)\kappa$, where a is the lattice spacing. In the limit of zero lattice depth, $t \rightarrow -\frac{a}{2\pi} \int_{-\pi/a}^{\pi/a} \frac{\hbar^2 q^2}{2m} \exp[iqa] dq = (2/\pi^2)E_r$, where q is the quasimomentum, $E_r = \frac{\hbar^2 \pi^2}{2ma^2}$ is the recoil energy, and m is the mass of the particles.

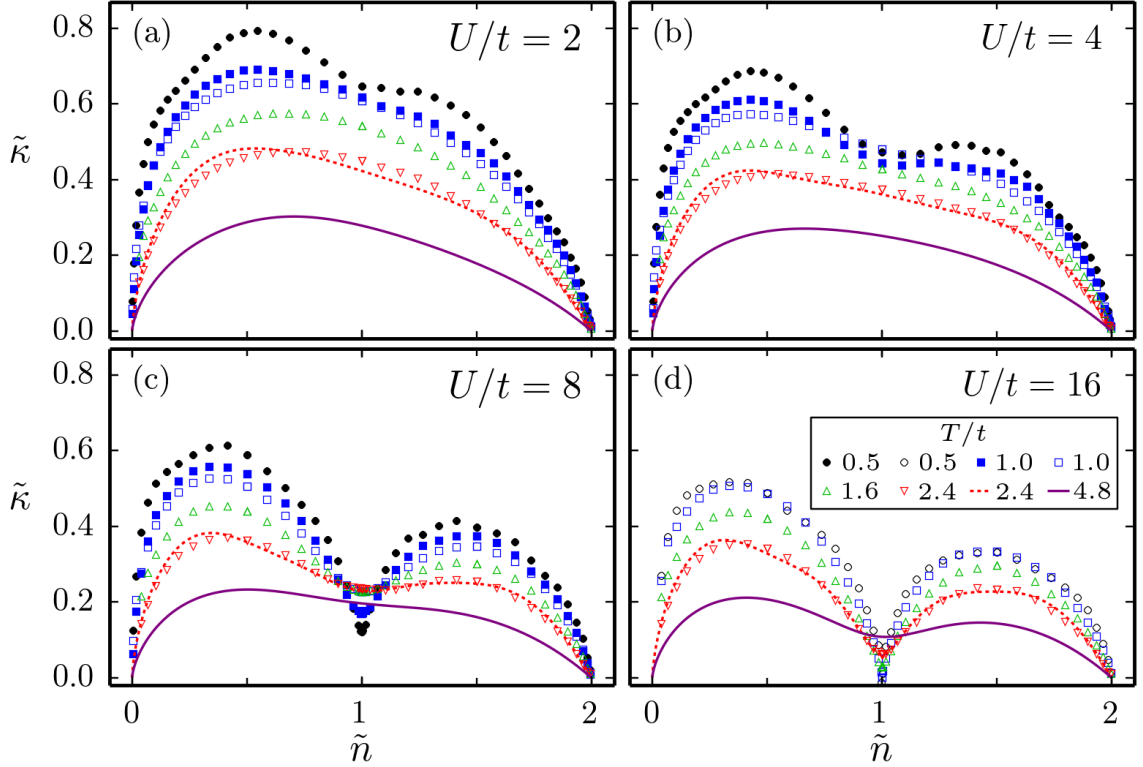


Figure 11.4: (Color online) Normalized compressibility versus density for the homogeneous Hubbard model in three dimensions, shown for various interaction strengths and temperatures. The different curves were obtained using DQMC (closed symbols) NLCE (open symbols) and the second order HTSE (lines). At half-filling, $\tilde{n} = 1$, the compressibility vanishes for strong interactions and low temperatures as the system enters the Mott insulating regime.

For a free gas with no interactions, the compressibility at zero temperature is given by $\kappa_0 = \frac{3}{2nE_F}$, where E_F is the Fermi energy for each spin component. Here we consider the ratio $\tilde{\kappa}$, defined as

$$\tilde{\kappa} \equiv \frac{(t/a^3)\kappa}{(2E_r/(\pi^2a^3))\kappa_0} = \frac{(3\pi^2)^{2/3}}{2} \frac{\partial \tilde{n}^{2/3}}{\partial(\mu/t)}, \quad (11.4)$$

where $\tilde{n} = a^3 n$.

In Fig. 11.4 we show theoretical results for $\tilde{\kappa}$ at various values of T/t and U/t , obtained using determinantal quantum Monte Carlo (DQMC) [94, 143], a numerical linked-cluster expansion (NLCE) [59, 96] up to the eighth order in the site expansion, and a high temperature series expansion (HTSE) up to second order in T/t [89]. These three methods complement each other, and provide results over a wide range of interactions and temper-

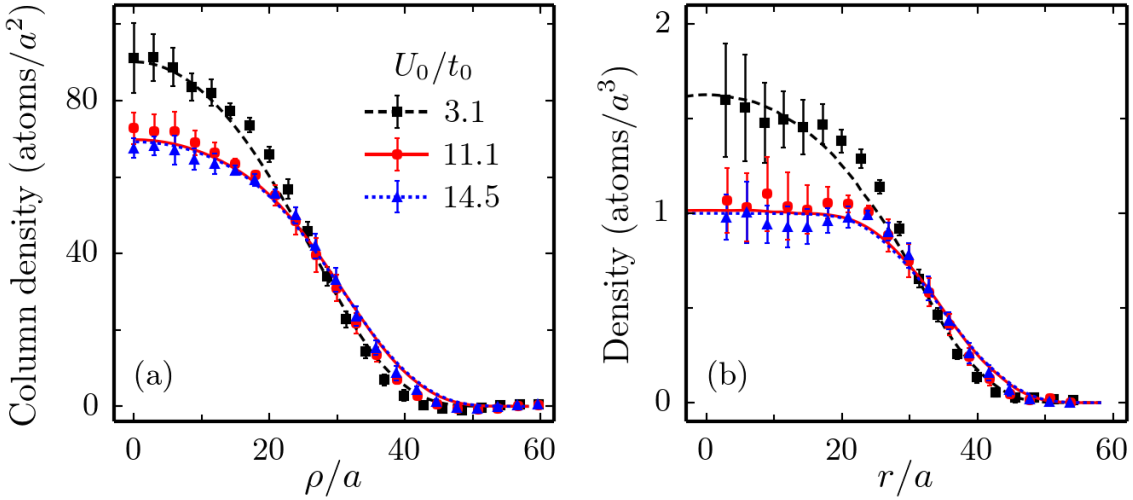


Figure 11.5: (Color online) (a) Azimuthally averaged column density (includes both spin states) profiles for different values of U_0/t_0 . Closed symbols represent the average of eight individual realizations, with error bars corresponding to the standard deviation. The lines are calculated for our trap with $N = 2 \times 10^5$ atoms at $T/t_0 = 0.6$ (the density does not change appreciably for $T/t \lesssim 1$). (b) Density profiles calculated along a body diagonal of the lattice (lines), and density profiles extracted from the column densities (data points).

atures. Figure 11.4 shows that the theoretical compressibility diminishes at half-filling, as the system enters the Mott insulating regime, and at $\tilde{n} = 2$, where a band insulator forms.

The *in-situ* column density measured in the experiment is azimuthally averaged, and the inverse Abel transform² is used to obtain the density profile of the cloud. Figure 11.5 shows the column density and density profiles for three different values of U_0/t_0 , compared with profiles obtained for our trap potential using the LDA. For the LDA we set T and the global chemical potential, μ_0 ; local values of U/t , T/t , and μ/t are then calculated using the known trap potential. As was explained above, the local value of the density is obtained from linear interpolation between NLCE and DQMC results for a homogeneous system calculated in a $(U/t, T/t, \mu/t)$ grid.

We obtain $\tilde{\kappa}$ from the measured and calculated density profiles as

$$\tilde{\kappa} = \frac{(3\pi^2)^{2/3}}{2} \frac{\partial \tilde{n}^{2/3}}{\partial r} \left(\frac{\partial(\mu/t)}{\partial r} \right)^{-1}, \quad (11.5)$$

²The inverse Abel transform is a way to obtain the density profile from the column density profile, assuming spherical symmetry of the sample.

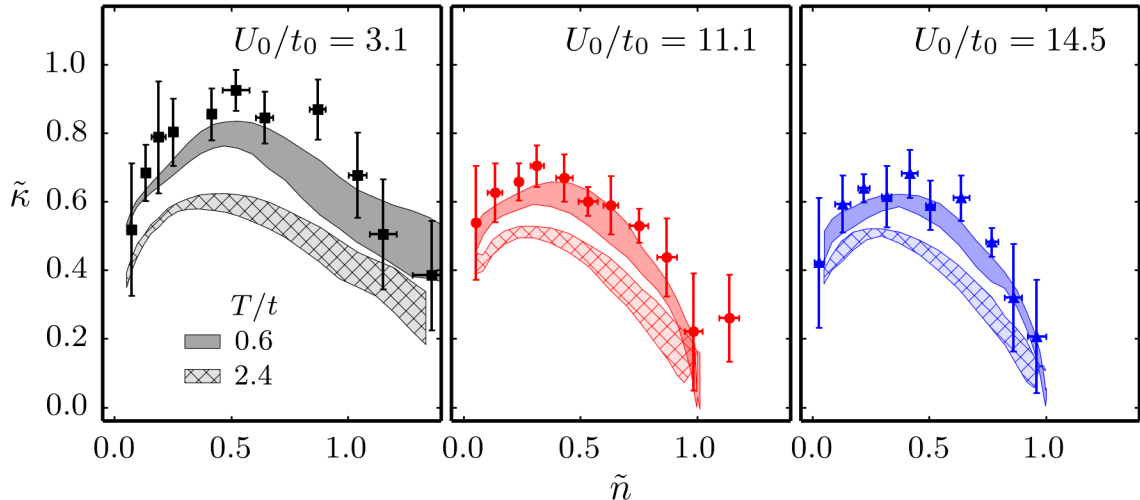


Figure 11.6: (Color online) Normalized compressibility, $\tilde{\kappa}$ versus density for different values of U_0/t_0 . Closed symbols show the average of eight individual realizations with error bars indicating the standard deviation. The shaded regions are numerical calculations at $T/t = 0.6$ and $T/t = 2.4$. The shaded region reflects a 10% systematic uncertainty in the lattice depth, which results in a 25% uncertainty in the value of U_0/t_0 .

where the derivative of the local chemical potential is determined from the trap parameters and the global chemical potential. For the data, the azimuthal average of the column density, and the inverse Abel transform are noisy at small radii, so, to avoid excessive noise in the determination of the radial derivative of $\tilde{n}^{2/3}$, we restrict our analysis to $r/a > 12$. Figure 11.6 shows $\tilde{\kappa}$ vs \tilde{n} for the experimental data and for the calculated density profile. The decrease of the compressibility near \tilde{n} , for $U_0/t_0 = 11.1$ and 14.5 , is consistent with the system entering the Mott insulating regime.

11.1 Summary

The compressibility, shown in Fig. 11.6, and the central density, shown in Fig. 11.3 are both consistent with the system entering the Mott insulating regime for values of $U_0/t_0 \geq 11.1$. Qualitatively, we observe that in both cases the data is consistent with $T/t = 0.6$. Below $T/t \approx 1$, the density and the compressibility are insensitive to temperature, since all of the entropy in the system resides in the spin degree of freedom.

We have found in this analysis, that the systematic uncertainty in the trap parameters prevents us from using the compressibility for a more precise quantitative determination of temperature. In the same system, a measurement of AFM correlations using Bragg scattering of light showed $T/t_0 = 0.62^{+0.05}_{-0.03}$ as will be explained in the next chapter.

12. Antiferromagnetic correlations in the Hubbard model

The contents of this chapter are based on a paper that has been submitted to Nature, titled “Observation of antiferromagnetic correlations in the Hubbard model with ultracold atoms”.

For this experiment we realize the Hubbard model in a $7 E_r$ lattice with repulsive interactions. We varied the interaction strength U_0/t_0 in the range $3.1 < U_0/t_0 < 21.4$. For each value of the interaction strength we measured the spin structure factor of the system S_Q as a function of atom number (in the range of 1 to 2.5×10^5 atoms). We found that, for a momentum transfer $\mathbf{Q} = \pi$ satisfying the $(^{-1/2} \ ^{-1/2} \ ^{+1/2})$ Bragg condition, S_π is sharply peaked with respect to atom number. A plot of the maximal S_π (obtained at each value of U_0/t_0) versus U_0/t_0 is plotted alongside theoretical calculations at different temperatures. From the comparison we can quantitatively extract a temperature for our system in a previously unexplored regime, where the entropy is mostly contained in the spin degree of freedom.

12.1 Technical details

A schematic of the setup for Bragg scattering is shown in Fig. 12.1. As was mentioned in Chapter 9, we obtain spin sensitivity, in analogy to neutron scattering used to characterize magnetism in solid-state materials, by setting the Bragg laser frequency between the optical transition frequencies for states $|1\rangle$ and $|2\rangle$. The spin structure factor, S_Q , defined in Eq. 9.27 is obtained by measuring the ratio of *in-situ* and TOF intensities scattered with momentum transfer \mathbf{Q} . Measurements of the scattered intensities are taken after locking the lattice to a depth of $20 E_r$.

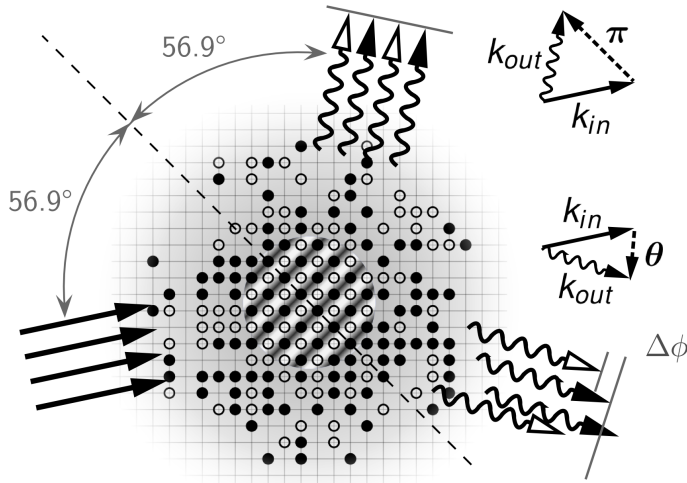


Figure 12.1: Two-dimensional (2D) schematic of the 3D scattering experiment. The two spin states (open and filled circles) show an increasing degree of AFM ordering, resulting in a magnetic sublattice, as T approaches T_N with $n \simeq 1$. AFM correlations are suppressed outside the central region where $n < 1$. Bragg scattering requires the input and output wavevectors, \mathbf{k}_{in} and \mathbf{k}_{out} , respectively, to satisfy the Bragg condition $\mathbf{k}_{out} - \mathbf{k}_{in} = \boldsymbol{\pi}$, with $\boldsymbol{\pi}$ a reciprocal lattice vector of the magnetic sublattice. The black and white arrowheads denote light scattered from one spin state, or the other. For a different momentum transfer $\mathbf{k}_{out} - \mathbf{k}_{in} = \boldsymbol{\theta}$, scattering is insensitive to spin ordering or AFM correlations due to the lack of constructive interference between the scattered photons resulting from a random phase shift $\Delta\phi$.

We realize the spin structure factor measurement for two values of the momentum transferred which are labeled $\boldsymbol{\pi}$ and $\boldsymbol{\theta}$. The Bragg condition is satisfied for $\mathbf{Q} = \boldsymbol{\pi}$ but not for $\mathbf{Q} = \boldsymbol{\theta}$, so the results at $\boldsymbol{\theta}$ serve as a control for the experiment. Figure 12.2 shows these angles with respect to the vacuum chamber and provides values for the components of \mathbf{Q} along the lattice axes, the Debye-Waller factor, the overall correction factor C_Q (defined in Eq. 9.37), and the numerical aperture of the imaging setup along each of the measured directions.

As was mentioned in Chapter 9, it is important to include the effects of saturation of the atomic transition when extracting the spin structure factor from the measured intensities. Here, the Bragg probe beam is a collimated Gaussian beam, with a $1/e^2$ radius of $450 \mu\text{m}$ and power of $250 \mu\text{W}$. The saturation parameter is $s_0 = 15.5$ and the detuning is $|\Delta| = 6.4$,

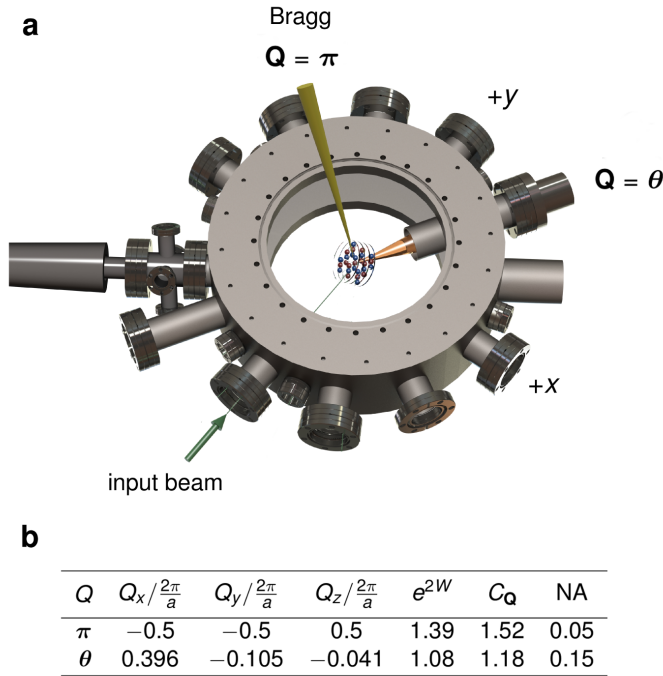


Figure 12.2: **Experimental setup for measuring the spin structure factor.** Lattice beams propagate along the x , y and z directions (the coordinate system is right handed). A magnetic field pointing along $+z$ defines the quantization axis and is tuned near the Feshbach resonance to set the scattering length and thus U . The input Bragg beam lies in the yz plane. Its wavevector makes an angle of 3.0° with the positive y axis and it is linearly polarized along x . The table shows the vector components, Debye-Waller factor, correction factor, and numerical aperture (NA) for the π and θ momentum transfers.

which results in a correction due to saturation effects

$$1 + \frac{s_0}{4\Delta^2} = 1.09, \quad (12.1)$$

a 9% effect of the measured value of S_Q .

There are additional considerations that must be taken into account for this measurement. We comment on them in the sections below.

12.1.1 Momentum transferred from the probe to the atoms.

In the derivation of the relationship between the intensity and the structure factor, showed in Chapter 9, we assumed that the center of mass state of the atom remains un-

changed after scattering a photon. For this assumption to be valid, the Lamb-Dicke parameter, η^2 , which relates the energy of the photon to the harmonic oscillator spacing in a lattice site¹, needs to be $\eta^2 \ll 1$. In the locked $20 E_r$ lattice, $\eta^2 = 0.27$, meaning that approximately one out of every 4 photons scattered will excite an atom to the second band of the lattice. An atom in the second band has larger position variance and therefore a smaller Debye-Waller factor, so it contributes less to the Bragg scattering signal.

The total number of photons scattered is given by $t_{\text{exp}} \Gamma \frac{s_0/2}{s_0 + 4\Delta^2}$, where the duration of the probe is $t_{\text{exp}} = 1.7 \mu\text{s}$ and the linewidth of the excited state is $1/27 \text{ ns}^{-1}$. For $s_0 = 15.5$ and $\Delta = 6.4 \Gamma$ this corresponds to 2.7 photons scattered per atom during the probe pulse. In a $20 E_r$ lattice it is then justifiable to assume the atoms remain in the lowest band during the pulse.

For the Bragg scattering measurements performed after time-of-flight, the momentum transferred from the probe to the atoms plays a more significant role, since the atoms are not trapped and will recoil after every photon scatter. As we will show in the measurements below (Fig 12.3), we still see good agreement between the observed decay of the Bragg scattering signal in time-of-flight and the decay expected for a Heisenberg limited wavepacket (Eq. 9.32). A similar consideration arises for Bragg scattering off of the (0 1 0) lattice planes, where in Chapter 9 we saw that there was good agreement with Eq. 9.32.

12.1.2 Optical density.

A low optical density of the sample is important so that the probe light goes unattenuated through the atom cloud, and multiple scattering events of the Bragg scattered photons are limited [58]. The optical density of the sample can be approximated as

$$\text{OD} \simeq \frac{\sigma_0 |\hat{e}_{\text{in}} \cdot \hat{e}_{-1}|^2}{4\Delta^2 + s_0} \frac{1}{a^2} \left(\frac{3N}{4\pi} \right)^{1/3} \quad (12.3)$$

¹

$$\eta^2 = \hbar\omega_{\text{in}}/(2E_r \sqrt{v_0/E_r}) \quad (12.2)$$

where ω_{in} is the angular frequency of the incident light, and v_0 is the lattice depth.

where $\sigma_0 = 3\lambda_0^2/2\pi$ and λ_0 is the wavelength of the optical transition. With $s_0 = 15.5$, $\Delta = 6.4\Gamma$ and $N = 180,000$ atoms we have $\text{OD} \simeq 0.072$. At this value of the optical density we do not expect significant corrections to the spin structure factor measurement due to the attenuation of the probe. We have not included any corrections in our measurement due to finite optical density effects, although it can be done by numerically solving the Lippmann-Schwinger equation [58] to account for multiple scattering of photons.

12.1.3 Light collection.

We collect Bragg scattered light in the π direction over a full angular width of 110 mrad, given by a 2.5 cm diameter collection lens that is placed 23 cm away from the atoms (Fig 9.5). In the θ direction, light is collected by a 2.5 cm diameter lens placed 8 cm away from the atoms, corresponding to a full angular width of 318 mrad (Fig. 4.25). For $N = 180,000$, $s_0 = 15.5$, $\Delta = 6.4\Gamma$ and a $1.7\mu\text{s}$ pulse, the detector in the the π direction collects approximately 1300 photons, whereas the detector in the θ direction collects approximately 10^4 photons. The noise floor from readout, dark current and background light per shot on both cameras has a variance equivalent to approximately 250 photons in the π direction and 1000 photons in the θ direction.

12.1.4 Data averaging.

The signals we detect are small enough that an uncorrelated sample may, in a single shot, produce a scattering signal as large as the ones produced by samples with AFM correlations. To obtain a reliable measurement of S_π we average approximately 60 *in-situ* shots to obtain I_{Q0} and 60 TOF shots to obtain $I_{Q\infty}$.

We estimate the expected variance on S_π by considering a randomly ordered sample in which $e^{i\boldsymbol{\pi}\cdot\mathbf{R}_n}2\langle\sigma_z\rangle_n$ is equal to +1 or -1 with equal probability. S_π can be written as

$$S_\pi = \left| \sum_n e^{i\boldsymbol{\pi}\cdot\mathbf{R}_n} \frac{2\langle\sigma_z\rangle_n}{\sqrt{N}} \right|^2, \quad (12.4)$$

which is equivalent to the square of the distance traveled on an unbiased random walk with step size $1/\sqrt{N}$. The mean and standard deviation can then be readily calculated: $\overline{S_\pi} = 1$ and $\sqrt{\text{Var}(S_\pi)} = \sqrt{2}$, where $\text{Var}(S_\pi)$ denotes the variance of the random variable S_π . With a standard deviation that is larger than the mean value, a considerable number of shots needs to be taken in order to obtain an acceptable error in the mean. The standard error of the mean for 60 shots will be $\sqrt{2/60} = 0.18$, consistent with what we obtain in the experiment (cf. vertical error bars in Fig. 12.7).

12.2 Time-of-flight

One of the first observations that we performed to verify that the signal we obtained was consistent with Bragg scattering was a measurement of the decay of the signal in time-of-flight (TOF). Figure 12.3 shows the results for the scattered intensity at $\mathbf{Q} = \pi$ and $\mathbf{Q} = \theta$ as a function of TOF. The expansion matches the expected decay from the Debye-Waller factor of the wavefunctions expanding from the locked $20 E_r$ lattice. For $\mathbf{Q} = \pi$, we see enhanced scattering at $\tau = 0$ relative to the uncorrelated cloud ($\tau = 9 \mu\text{s}$), whereas for $\mathbf{Q} = \theta$, scattering at $\tau = 0$ is reduced. Double occupancies, present in the many-body wavefunction even at low temperatures [55], reduce coherent scattering in all directions, since each spin state scatters with opposite phase and their fields cancel out. Along $\mathbf{Q} = \pi$ the coherent enhancement from AFM spin correlations exceeds the reduction due to double-occupancies, whereas at $\mathbf{Q} = \theta$ a reduced intensity is observed *in-situ*.

12.3 Number variation

One of the important technical aspects that we encountered with the Bragg signal was the sensitivity to the number of atoms in the trap. The number of atoms determines the profile of the chemical potential across the trap, and consequently (in the local density approximation) the profiles of the different thermodynamic quantities. Bragg scattering is

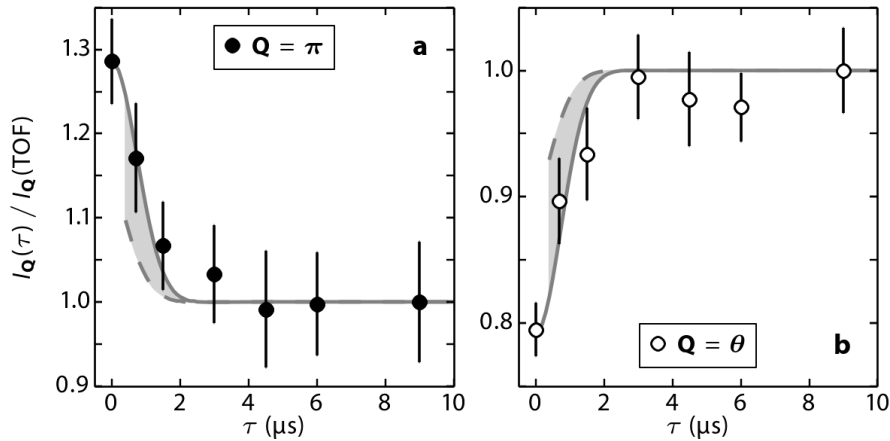


Figure 12.3: **Time-of-flight measurement of scattered intensity from a sample with AFM correlations.** **a**, Intensity of Bragg scattered light (π direction) as a function of time-of-flight, τ , after suddenly switching off the lattice. The Bragg signal at $\tau = 0$ disappears after a long TOF as the spins become uncorrelated. **b**, In the θ direction the *in situ* ($\tau = 0$) sample shows a reduction of scattering as compared to long TOF due to the presence of double occupancies and to the presence of AFM spin correlations. Each data point and error bar is the mean and standard error of the mean of at least 17 measurements of the scattered intensity. The gray solid line is the intensity calculated using the value of the Debye-Waller factor at τ , whereas the dashed gray line uses the average value of the Debye-Waller factor during the $1.7\ \mu\text{s}$ exposure of the Bragg probe.

a measurement of the spin structure factor, S_π , which is a bulk property of the system. In the LDA one can interpret S_π as an integral over the local value of the spin structure factor over the atom cloud. This can be expressed as

$$S_\pi = a^{-3} N^{-1} \int s_\pi(\mu/t, T/t, U/t) d^3 \quad (12.5)$$

where s_π is the local spin structure factor per lattice site, which depends on the local Hubbard parameters.

The results for the Bragg scattering signal as a function of atom number are shown in Fig. 12.4 for various values of U_0/t_0 . This figure shows how the Bragg signal from AFM correlations can be very sensitive to the atom number. We speculate that this sensitivity may be related with equilibration or adiabaticity of the loading ramps, which can be different for samples with different atom numbers. Calculations of S_π using the LDA for a sample in equilibrium at a constant temperature T , do not show such a pronounced sensitivity on

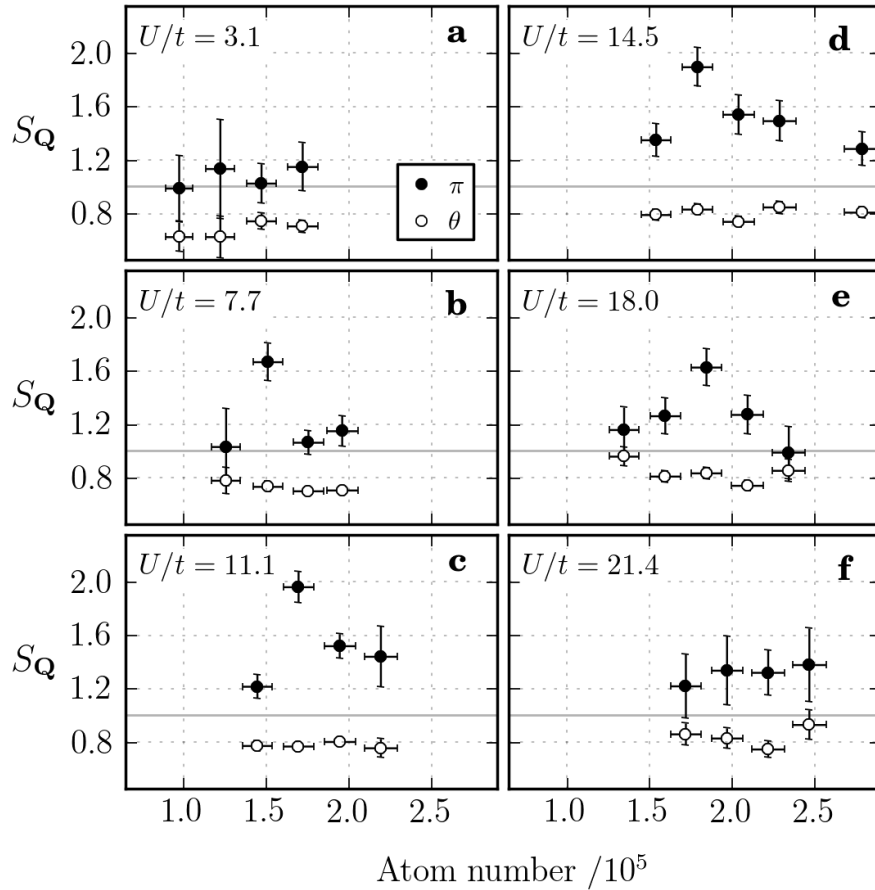


Figure 12.4: Spin structure factor as a function of N . **a-f**, For each U/t we vary the atom number N loaded into the lattice and measure S_π and S_θ , (closed and open circles, respectively). We find that S_π depends sensitively on N for all but the lowest and highest values of U/t , where S_π is near 1. This sensitivity is consistent with the assumption that only a small volume with $n \simeq 1$ mainly contributes to S_π . The peak in S_π shifts to higher N with increasing U/t since the global chemical potential to realize $n = 1$ at the center is proportional to U/t . S_θ shows no systematic dependence on N . Vertical error bars represent the standard error of the mean of at least 15 and up to 60 measurements; more measurements were taken at the peak of S_π . Horizontal error bars represent the standard error of the mean of at least 20 measurements of N .

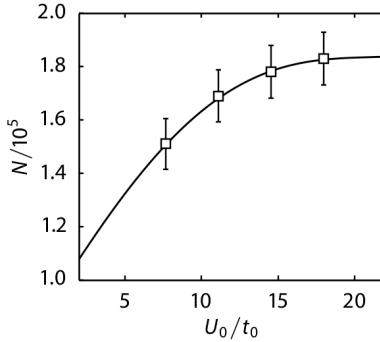


Figure 12.5: **Atom number that maximizes S_π .** For various U_0/t_0 , N which maximizes S_π (open squares) and third order polynomial fit (line). The value of N determined by this polynomial fit is used in LDA calculations to calculate S_π (see Fig. 12.6 for examples of the LDA calculations).

the atom number. The calculations are also robust with respect to uncertainties in the parameters of the trap.

From Fig. 12.4 one can extract the atom number at which AFM correlations are maximized, for the values of U_0/t_0 that show a peak in S_π . This is shown in Fig. 12.5.

12.4 Calculations using the LDA

In a similar way as was done in Chapter 11 for the density, profiles of other thermodynamic quantities at low temperatures can be obtained using the LDA along with DQMC and NLCE results for the homogeneous Hubbard model. Here we use the LDA to calculate the local spin structure factor, which can be integrated over the trap to obtain the measured S_π . Figure 12.6 shows an example of DQMC results for a homogeneous system, and also LDA calculations for our trap. In the figure we can see that the maximum of the local spin structure factor does not occur at the center of the trap. This happens because of the increase in t as one moves away from the center; this results in a decreasing T/t which in turn results in a larger spin structure factor as calculated in the homogeneous system (as long as the density stays close to $n = 1$).

We compare the experimental results with theoretical calculations at each value of U_0/t_0

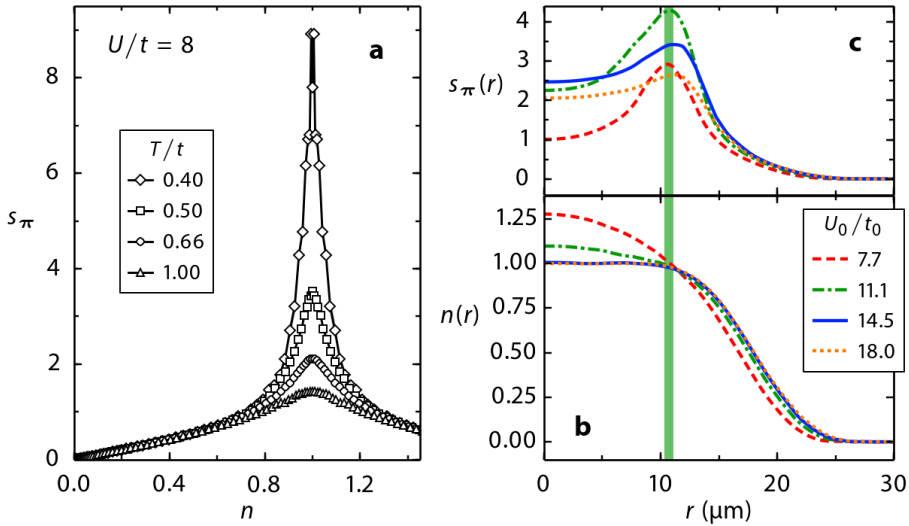


Figure 12.6: Spin structure factor for a homogeneous lattice and LDA for the inhomogeneous sample. **a**, DQMC calculation of the spin structure factor per lattice site as a function of density for a homogeneous lattice. s_π is sharply peaked near $n = 1$ and diverges as T approaches T_N . **b**, Density profiles calculated using the local density approximation (LDA), for different U_0/t_0 at $T/t_0 = 0.89$. The atom number used to obtain each profile maximizes S_π , as measured in the experiment (see Fig. 12.3). **c**, $s_\pi(r)$ profiles calculated in the LDA at $T/t_0 = 0.53$. Although $n = 1$ at the center for larger U_0/t_0 , s_π has a maximum at larger radius due to the decrease of T/t with increasing r . The vertical green line in panels **b** and **c** denotes, for $U_0/t_0 = 11.1$, the radius at which $s_\pi(r)$ is maximized.

realized in the experiment. For the comparison we use the largest value of S_π measured at a given U_0/t_0 . Our assumption is that when S_π is maximize, the experiment realizes the best conditions for equilibration in the lattice and adiabaticity of the loading ramps.

12.4.1 Extraction of the temperature

Fig. 12.7a shows the maximum S_π for various values of U_0/t_0 , along with the corresponding S_θ . We find that S_π is peaked for $10 < U_0/t_0 < 15$, whereas S_θ decreases slightly for weaker interactions as a consequence of the increase in double occupancies. For values of $U/t > 10$ our system is not expected to be completely described by a single-band Hubbard model and corrections involving higher bands may become non-negligible [69, 144].

Also in Fig. 12.7a, we plot results obtained from theoretical calculations for various

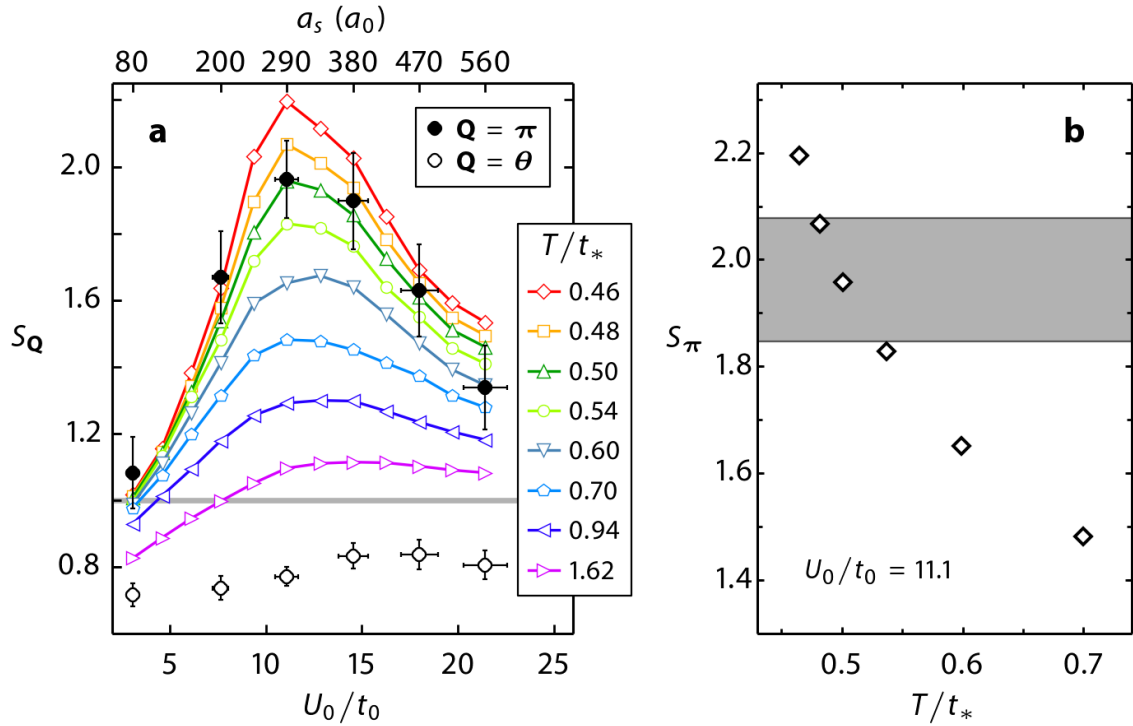


Figure 12.7: Spin structure factor variation with U_0/t_0 and determination of T . **a**, S_π (filled circles) at optimized N (see text) for various U_0/t_0 . LDA calculations (open symbols) for various values of T/t_* (lines are guides to the eye). The corresponding range of the s -wave scattering length a_s , in units of the Bohr radius a_0 , is shown along the top axis. S_θ (open circles) decreases slightly for weakly interacting systems where the fraction of double occupancies increases. The points are the mean of at least 40 measurements and the error bars are the standard error of the mean. Horizontal error bars represent a 5% systematic uncertainty in lattice depth. **b**, Comparison between measured S_π at $U_0/t_0 = 11.1$ (gray shaded area corresponds to the error bar in Fig. 4a) and LDA results (open diamonds) as a function of T/t_* . Comparison with theory establishes thermometry which becomes increasingly precise as T approaches T_N .

temperatures. Comparison of the measured S_π with the theoretical calculations provides precise thermometry as is shown for $U_0/t_0 = 11.1$ in Fig. 12.7b. We define t_* as the local value of the tunneling where the local spin structure factor, s_π , is maximized (see Fig. 12.6c). As shown in Fig. 12.7b, we can determine $T/t_* = 0.50^{+0.04}_{-0.02}$ for $U_0/t_0 = 11.1$, and a similar temperature agrees well with the data at different values of U_0/t_0 (Fig. 12.7a). Uncertainties in the measured T/t_* represent the statistical error in the measured S_π .

We studied the systematic variation of the determined temperature as a function of the trap parameters and found that the spin structure factor, being a bulk quantity, is not very

sensitive to the particular shape of the trap. A systematic uncertainty of ~ 0.05 in T/t^* is obtained from these estimates.

Remarks

- We observe that the largest measured S_π occurs at $U_0/t_0 = 11.1$, where the dominant contribution comes from an $n = 1$ shell where the local value of U/t is $U_*/t_* = 9.1$. This is consistent with DQMC calculations [145, 54, 146] which place the maximum of the Néel temperature, T_N/t , at U/t between 8 and 9 and with value $T_N = 0.36t$ for the homogeneous lattice.
- In units of the tunneling rate at the center of the trap, the temperature of the system is $T/t_0 = 0.62^{+0.05}_{-0.03}$, consistent with the results obtained from analysis of *in-situ* density distributions in Chapter 11.
- For $U_0/t_0 = 11.1$, $t_* = 1.3 \text{ kHz}$, and we can infer the absolute temperature of the system to be $T \approx 31 \text{ nK}$.
- In units of the maximal local T_N the observed temperature is $T/T_N = 1.39^{+0.11}_{-0.06}$, corresponds to an overall entropy per particle $S/(Nk_B) = 0.42 \pm 0.02$, where k_B is the Boltzmann constant (see Extended Data Fig. 4). This entropy range is consistent with $T/T_F \simeq 0.04$ measured in the harmonic dimple trap before loading the atoms into the lattice [114].
- It is possible for the AFM order to develop along a different axis than the z axis probed by the Bragg scattering [147, 148]. We checked for this possibility by applying a $\pi/2$ radiofrequency pulse to rotate the spin of the atoms prior to Bragg scattering. No change in S_π was detected to within our uncertainty, which is consistent with the spin correlations in the system being isotropic (i.e. the ordered spins can be linear combinations of the states $|1\rangle$ and $|2\rangle$).

12.5 Summary

We have observed AFM correlations in the Hubbard model using ultracold atoms in an optical lattice via spin-sensitive Bragg scattering of light. Because magnetic order is extremely sensitive to T in the vicinity of T_N , Bragg scattering provides precise thermometry in regimes previously inaccessible to quantitative temperature measurements.

In future studies our experimental setup can be configured to study the 2D Hubbard model in an array of planes. Given the temperature achieved here in a 3D lattice, we may be in a position to answer questions about competing pairing mechanisms in 2D, and ultimately resolve the long standing question of *d*-wave superconductivity in the Hubbard model.

13. Conclusion

I feel very proud to be the first student that will receive a Ph.D. for work done in this apparatus. We started out in 2007 and have always battled more than what would seem necessary to get the experiment up and running. Luckily, we were able to change some problems into opportunities, and now the results of our efforts have paid off.

The low atom numbers that we would achieve in the ODT when loading it directly from the red MOT, led us to focus our efforts on the UVMOT, which was the subject of my Master's thesis. The UVMOT is basically what gives this experiments its edge; it works much better than anybody ever expected (except perhaps Randy). The 323 nm power necessary to operate it is not too high, and it barely needs any repump light. The UVMOT allows us to load a significant number of atoms (10^7) into an ODT with a very moderate depth ($300 \mu\text{K}$) which is sufficient for the experiments that we carry out.

It was only until my fifth year in grad school (Fall 2011) that we started building up the compensated lattice. We first observed Bragg scattering from the (0 1 0) planes in the summer of 2012. That moment was an important turning point, from then on most of our time was no longer spent building something new for the apparatus but actually running experiments.

The last two years have been almost fully dedicated to achieving our goal of measuring the spin structure factor in the lattice using Bragg scattering of light. Somehow everybody thought that the Bragg signal would be like a beacon, but we soon realized that we were looking for a needle in a haystack. We were forced to rely heavily on statistics to bring the AFM correlations signal out of the background. The complications with the signal to noise ratio led to my efforts in understanding the Bragg scattering measurement in the

limit where the signal is just above the incoherent scattering background. Furthermore, in order to consolidate our results, we saw the need to collaborate closely with theorists. I quickly realized how little I new about the Hubbard model which I had been trying to realize experimentally, but I saw here another opportunity to serve as the bridge between the theoretical results and our experimental measurements.

Understanding the theoretical results available for the Hubbard model, and implementing the local density approximation has led to the possibility of using Bragg scattering as a thermometer for atoms in a lattice. This is a technique that we hope will be useful for other groups. In our apparatus we hope to continue perfecting the measurement of AFM correlations and use it as a guiding light to find ways of squeezing more entropy out of the system and bring it closer to realizing the full potential of quantum simulation. Studying pairing may not be so far after all, given that some entropy can be squeezed out of the system by increasing the lattice depth along one of the axis, which would create a set of uncorrelated two-dimensional (2D) planes, each one an independent realization of the 2D Hubbard model. As was already shown for 1D chains [45], when you have a fixed amount of entropy in the total system you can “divide and conquer”. The big challenge then would be figuring out how to obtain information about the 2D systems in our setup, given that Bragg scattering as presented here, would not work between the uncorrelated planes. Nevertheless, the 3D system can be used in that case solely for the purpose of thermometry.

In the near future our experiment will undergo a significant upgrade to a new compensated optical lattice setup. The setup has been carefully designed to implement the ideas that were presented in Chapter 5 of this thesis. It also boasts superior mechanical stability, which we hope will eliminate the need to realign the compensated lattice every day.

In the near future there are also plans to explore physics in one dimension (1D) using our apparatus. This geometry can be created in our system by simply turning off one of the lattice beams, giving rise to an array of one-dimensional (1D) tubes. The physics of 1D systems provides an interesting test-bed for quantum simulation, since exact solutions

exist for the many-body problem in 1D.

I believe that it is a good idea for the apparatus to diversify and try to study systems for which the temperature requirements are not as low as in the strongly correlated regime of the 3D Hubbard model. The 1D systems mentioned above are one example, but also there are a lot of interesting possibilities such as studying the Hubbard model with attractive interactions or also trying to develop techniques to study the dynamics of systems out of equilibrium.

The apparatus has finally reached maturity. It is a versatile machine, capable of producing some the coldest degenerate Fermi gases of ultracold atoms ever recorded. I hope that the new generations of graduate students that come to it have as much fun as I did trying to figure it out.

A. Compensated optical lattice potential

Experiments with ultracold atoms rely on the forces that can be applied on an atom using light. When the light is near resonant with an atomic transition the force is dissipative, and can be used to dramatically slow down the motion of atoms and bring their temperatures into the μK regime. If the light is far detuned, a conservative force referred to as the dipole force arises. An electric field induces an electric dipole moment on an atom, which then can have a spatially dependent potential energy if the electric field is itself inhomogeneous. The dipole potential is an important part of nearly all experiments with ultracold atoms at the present time. The ability to shape the transverse profile of a laser beam and to create interference patterns between multiple beams, gives the experimenter a wide range of possibilities [149].

As part of this work we have used a potential that we referred to as a compensated lattice. In this appendix we go into more detail regarding the technical aspects of the compensated lattice potential.

A.1 Dipole potential and scattering rate

The dipole potential [149] produced by far-detuned light of frequency ω_L on a two-level atom is given by

$$U_{\text{dip}}(\mathbf{r}) = -\frac{3\pi c^2}{2\omega_0^3} \Gamma \left(\frac{1}{\omega_0 - \omega_L} + \frac{1}{\omega_0 + \omega_L} \right) I(\mathbf{r}) \quad (\text{A.1})$$

The associated photon scattering rate is

$$\Gamma_{\text{sc}} = \frac{3\pi c^2}{2\hbar\omega_0^3} \Gamma^2 \left(\frac{\omega_L}{\omega_0} \right)^3 \left(\frac{1}{\omega_0 - \omega_L} + \frac{1}{\omega_0 + \omega_L} \right)^2 I(\mathbf{r}) \quad (\text{A.2})$$

The beams that we use in our lattice have a Gaussian cross section such that the intensity (of a single beam) is given by

$$I(\mathbf{r}) = \frac{2P}{\pi w^2} \exp \left[-2 \frac{r_\perp^2}{w^2} \right] \quad (\text{A.3})$$

where r_\perp is the perpendicular distance from the beam axis and we neglect the small variation of the intensity along the beam axis.

We will calculate the heating rate due to spontaneous emission at the center of the potential, where the intensity of all the beams is the largest. We define the constants u_L and h_L according to

$$\begin{aligned} k_B u_L &= \frac{3\pi c^2}{2\omega_0^3} \Gamma \left(\frac{1}{\omega_0 - \omega_L} + \frac{1}{\omega_0 + \omega_L} \right) \\ h_L &= \frac{3\pi c^2}{2\hbar\omega_0^3} \Gamma^2 \left(\frac{\omega_L}{\omega_0} \right)^3 \left(\frac{1}{\omega_0 - \omega_L} + \frac{1}{\omega_0 + \omega_L} \right)^2 \end{aligned} \quad (\text{A.4})$$

Which allows writing the dipole potential and the scattering rate simply as

$$\begin{aligned} U_0/k_B &= u_L I_0 \\ \Gamma_{sc0} &= h_L I_0 \end{aligned} \quad (\text{A.5})$$

In our experiments we use lasers at 1064 nm and 532 nm, the values of u_L and h_L for this two wavelengths are given in Table A.1 towards the end of this document.

A.2 Compensated lattice potential: definitions and simplified expressions

An optical lattice potential results due to the stationary interference pattern of two or more laser beams. The most common configuration, and the one relevant to our work, consists on a laser beam that is retroreflected upon itself, which produces a standing wave with nodes separated by half the wavelength of the light. Ideally the retroreflected path would have the same power and beam waist (at the position of the atoms) as the input path, however in practice this is not the case. The light for the lattice is brought to the apparatus using an optical fiber; the retro beam alignment process consists of maximizing

the light that goes back through this fiber. The alignment process guarantees that (within ~5%) the input and retro beam waists will be the same. In this treatment we will initially consider different input and retro waists, but in the end we will set them to be equal. On the other hand, the retro reflected power can be significantly lower due to losses on the retro path, so we do consider a different power for the input and retro beams throughout.

We define a factor, R , which characterizes the losses of the retro path, such that the power of the retro beam is $P_r = P_i R$, where r,i stand for retro and input respectively. Below we tabulate the beam waists and retro factors for the three axes of our simple cubic lattice potential:

	LATTICE	BEAM 1	BEAM 2	BEAM 3
w	beam waist	48.3	45.9	41.3
R	retro factor	0.93	0.77	0.68

The calibration method used to obtain these values will be presented in a later section.

In our setup we have the possibility of changing the polarization of the retro beam. We use a liquid crystal retarder, which allows us to accurately set the polarization of the retro beam parallel or perpendicular to that of the input beam. In between these two values we can continuously set the fraction of retro power that has the same polarization of the input beam, and this allows us to smoothly change the potential from a dimple (minimize retro power at input polarization) to a lattice (maximize retro power at input polarization). We will use the letter α to refer to the fraction of power in the retro beam that has the same polarization as the input beam, and thus can interfere with it to form the lattice.

A.2.1 Electric field

The electric field on the axis of our lattice (input propagating along $+z$) can be determined as a sum of the input and retro electric fields. We independently treat the interfering

(\parallel) and non-interfering (\perp) fields.

$$\begin{aligned}\sqrt{\frac{2}{\epsilon_0 c}} E_{1D\parallel}(x, y, z) &= A e^{ikz} + B e^{-ikz+\phi_{\parallel}(\alpha)} \\ \sqrt{\frac{2}{\epsilon_0 c}} E_{1D\perp}(x, y, z) &= C e^{-ikz+\phi_{\perp}(\alpha)}\end{aligned}$$

where

$$\begin{aligned}A &= \sqrt{\frac{2P_i}{\pi w_r^2}} \exp\left[-\frac{x^2+y^2}{w_r^2}\right] \\ B &= \sqrt{\frac{2P_i R \alpha}{\pi w_r^2}} \exp\left[-\frac{x^2+y^2}{w_r^2}\right] \\ C &= \sqrt{\frac{2P_i R(1-\alpha)}{\pi w_r^2}} \exp\left[-\frac{x^2+y^2}{w_r^2}\right]\end{aligned}\tag{A.6}$$

Notice that the field can have phase shifts that depend on α . We have not characterized those phase shift for our retarder setup. We will focus only on situations where $\alpha = 0$ or 1 , so that we can neglect them.

A.2.2 Lattice depth

To obtain the lattice depth we need to set $\alpha = 1$ and look at the oscillatory part of the interfering intensity $(\epsilon_0 c/2)|E_{1D\parallel}|^2$. The lattice depth will have a gaussian transverse profile as a function of x, y . To get the lattice depth at the axis of the beam we set $x = 0, y = 0$ and obtain

$$(\epsilon_0 c/2)|E_{1D\parallel}|^2 = I_{1D\parallel}(z) = \frac{8}{\pi} \sqrt{\frac{P_i^2 R}{w_{in}^2 w_r^2}} \cos^2(kz) - \frac{4}{\pi} \sqrt{\frac{P_i^2 R}{w_{in}^2 w_r^2}} + \frac{2P_i}{\pi w_{in}^2} + \frac{2P_i R}{\pi w_r^2}\tag{A.7}$$

The lattice depth is the dipole potential produced by the oscillatory part of $I_{1D\parallel}$

$$s = \frac{V_{latt}}{E_{R,ir}} = \frac{k_B |u_{ir}|}{E_{R,ir}} \frac{8}{\pi} \frac{P_i \sqrt{R}}{w_{in} w_r}\tag{A.8}$$

Assuming equal beam waists for input and retro this becomes

$$s = \frac{k_B |u_{ir}|}{E_{R,ir}} \frac{8}{\pi} \frac{P_i \sqrt{R}}{w^2}\tag{A.9}$$

A.2.3 Lattice and dimple radial frequencies

To find the lattice and dimple radial frequencies we have to look at the full intensity

$$I_{1D}(r) = (\epsilon_0 c / 2)(|E_{1D\parallel}|^2 + |E_{1D\perp}|^2)$$

and set $z = 0$ and $x^2 + y^2 = r^2$.

Lattice $\alpha = 1$

$$I_{1D}(r) = \frac{4}{\pi} \frac{P_i \sqrt{R}}{w_{in} w_r} \exp \left[-\frac{r^2}{w_{in}^2} - \frac{r^2}{w_r^2} \right] + \frac{2P_i}{\pi w_{in}^2} \exp \left[-2 \frac{r^2}{w_{in}^2} \right] + \frac{2P_i R}{\pi w_r^2} \exp \left[-2 \frac{r^2}{w_r^2} \right] \quad (\text{A.10})$$

Expanding the exponentials around $r = 0$ gives

$$I_{1D}(r) \approx I_{1D}(0) - \frac{1}{2} \left[\frac{8}{\pi} \frac{P_i \sqrt{R}}{w_{in} w_r} \left(\frac{1}{w_{in}^2} + \frac{1}{w_r^2} \right) + \frac{2P_i}{\pi w_{in}^2} \frac{4}{w_{in}^2} + \frac{2P_i R}{\pi w_r^2} \frac{4}{w_r^2} \right] r^2 \quad (\text{A.11})$$

Recall that $U(\mathbf{r}) = u_L k_B I(\mathbf{r})$. The radial frequency is

$$\nu_{latt}^2 = \frac{|u_{ir}| k_B}{m \pi^2} P_i \left[\frac{2}{\pi} \frac{\sqrt{R}}{w_{in} w_r} \left(\frac{1}{w_{in}^2} + \frac{1}{w_r^2} \right) + \frac{2}{\pi w_{in}^4} + \frac{2R}{\pi w_r^4} \right] \quad (\text{A.12})$$

which for equal beam waists becomes

$$\nu_{latt}^2 = \frac{|u_{ir}| k_B}{m \pi^2} P_i \left[\frac{2 + 4\sqrt{R} + 2R}{\pi w^4} \right] \quad (\text{A.13})$$

Dimple $\alpha = 0$

$$I_{1D}(r) = \frac{2P_i}{\pi w_{in}^2} \exp \left[-2 \frac{r^2}{w_{in}^2} \right] + \frac{2P_i R}{\pi w_r^2} \exp \left[-2 \frac{r^2}{w_r^2} \right] \quad (\text{A.14})$$

$$I_{1D}(r) \approx I_{1D}(0) - \frac{1}{2} \left[\frac{2P_i}{\pi w_{in}^2} \frac{4}{w_{in}^2} + \frac{2P_i R}{\pi w_r^2} \frac{4}{w_r^2} \right] r^2 \quad (\text{A.15})$$

$$\nu_{dimp}^2 = \frac{|u_{ir}| k_B}{m \pi^2} P_i \left[\frac{2}{\pi w_{in}^4} + \frac{2R}{\pi w_r^4} \right] \quad (\text{A.16})$$

For equal beam waists

$$\nu_{\text{dimp}}^2 = \frac{|u_{\text{ir}}|k_{\text{B}}}{m\pi^2} P_{\text{i}} \left[\frac{2 + 2R}{\pi w^4} \right] \quad (\text{A.17})$$

Lithium mass. For the mass of lithium which appears in the expressions for the radial frequency we use the convenient expression

$$\frac{m}{k_{\text{B}}} = 6 \frac{\text{AMU}}{k_{\text{B}}} = 6 \frac{h/k_{\text{B}}}{0.4 \mu\text{m}^2 \text{MHz}} = \frac{6(48 \mu\text{K}/\text{MHz})}{0.4 \mu\text{m}^2 \text{MHz}} = 7.2 \text{e-4} \frac{\mu\text{K}}{\mu\text{m}^2 \text{kHz}^2} \quad (\text{A.18})$$

A numerical value for $\frac{|u_L|k_{\text{B}}}{m\pi^2}$ is listed in Table A.1.

A.2.4 Compensation beams

Overlapped on each of our lattice axes we have a repulsive compensation beam at a wavelength of 532 nm. This is a single gaussian beam with a potential given by

$$U_{\text{c1D}}(x, y) = u_{\text{gr}} k_{\text{B}} \frac{2P_{\text{gr}}}{\pi w_{\text{gr}}^2} \exp \left[-2 \frac{r^2}{w_{\text{gr}}^2} \right] \quad (\text{A.19})$$

and radial frequency

$$\nu_{\text{gr}}^2 = \frac{|u_{\text{gr}}|k_{\text{B}}}{m\pi^2} \frac{2P_{\text{gr}}}{\pi w_{\text{gr}}^4} \quad (\text{A.20})$$

The beam waist for each of the three beams is shown below

	COMPENSATION	BEAM 1	BEAM 2	BEAM 3
w	beam waist	42.9	41.4	40.4

At the moment we use the following compensations for each of the three axes:

axis	1	2	3
$g_0 (E_R)$	3.65	3.90	2.9

With these values we have found empirically that we can obtain the same confinement frequencies in all three directions (which produces spherically symmetric samples) and we can achieve $n = 1$ at the center.

A.3 Fermi temperature for a compensated dimple

In our experiment we specify the powers of the IR beams by the lattice depth that they would generate if α were equal to 1, that is

$$P_i = s \frac{E_{R,ir}}{k_B |u_{ir}|} \frac{\pi w_{ir}^2}{8\sqrt{R}} \quad (\text{A.21})$$

$$\nu_{ir,dimp}^2 = s \frac{E_{R,ir}}{m\pi^2} \frac{1+R}{4w_{ir}^2 \sqrt{R}} \quad (\text{A.22})$$

$$\nu_{ir,latt}^2 = s \frac{E_{R,ir}}{m\pi^2} \frac{1+R+\sqrt{R}}{2w_{ir}^2 \sqrt{R}} \quad (\text{A.23})$$

A value for $\frac{E_{R,ir}}{m\pi^2}$ can be found in Table A.1.

For the green beams we specify the depth of the potential produced by each beam in units of the IR recoil, we call this quantity g .

$$P_{gr} = g \frac{E_{R,ir}}{k_B |u_{gr}|} \frac{\pi w_{gr}^2}{2} \quad (\text{A.24})$$

$$\nu_{gr}^2 = g \frac{E_{R,ir}}{m\pi^2} \frac{1}{w_{gr}^2} \quad (\text{A.25})$$

Along each axis we have that the radial frequency of the compensated dimple potential is

$$\begin{aligned} \nu_{comp}^2 &= \nu_{ir}^2 - \nu_{gr}^2 \\ &= \frac{E_{R,L}}{m\pi^2} (s\varphi_{dimp} - g\varphi_{gr}) \end{aligned} \quad (\text{A.26})$$

where we have defined

$$\varphi_{latt} = \frac{1+R+\sqrt{R}}{2w_{ir}^2 \sqrt{R}} \quad \varphi_{dimp} = \frac{1+R}{4w_{ir}^2 \sqrt{R}} \quad \varphi_{gr} = \frac{1}{w_{gr}^2} \quad (\text{A.27})$$

For each of the three axes we have

	AXIS 1	AXIS 2	AXIS 3	units
φ_{dimp}	2.14e-4	2.39e-4	2.99e-4	μm^{-2}
φ_{latt}	6.433e-4	7.160e-4	8.903e-4	μm^{-2}
φ_{gr}	5.434e-4	5.834 e-4	6.127 e-4	μm^{-2}

In order to produce spherically symmetric samples we set s for all three beams to the same (such that if α were equal to 1 the lattice depths would be the same along all three directions) and we adjust the green powers of beams 1 and 2 to match the compensated radial frequency of beam 3. To calculate the Fermi temperature we will set the radial frequencies for beams 1 and 2 equal to that of beam 3, which is given by

$$\nu_{\text{comp},3}^2 = \frac{E_{R,\text{ir}}}{m\pi^2} (s\varphi_{\text{dimp},3} - g\varphi_{\text{gr},3}) \quad (\text{A.28})$$

When the dimple beams in all three axis are turned on at the same time, the squares of the trap frequencies add up. Beams 1, 2, 3 propagate along x , y , and z respectively. And so we have

$$\begin{aligned} \nu_{\text{comp},x}^2 &= \nu_{\text{comp},2}^2 + \nu_{\text{comp},3}^2 \\ \nu_{\text{comp},y}^2 &= \nu_{\text{comp},3}^2 + \nu_{\text{comp},1}^2 \\ \nu_{\text{comp},z}^2 &= \nu_{\text{comp},1}^2 + \nu_{\text{comp},2}^2 \end{aligned} \quad (\text{A.29})$$

The Fermi temperature for a spin mixture of N total atoms is

$$k_B T_F = h(3N)^{1/3} \left[\prod_i \nu_{x_i} \right]^{1/3} \quad (\text{A.30})$$

$$\begin{aligned} T_F &= \frac{h}{k_B} (3N)^{1/3} (2\nu_{\text{comp},3}) \\ &= \frac{h}{k_B} 2(3N)^{1/3} \left(\frac{E_{R,L}}{m\pi^2} \right)^{1/2} (s\varphi_{\text{dimp},3} - g\varphi_{\text{gr},3})^{1/2} \\ &= [48e-3 \mu\text{K kHz}^{-1}] 2(3N)^{1/3} [14.1 \mu\text{m kHz}] (2.99 s - 6.13 g)^{1/2} [0.01 \mu\text{m}^{-1}] \\ &= [13.5 \text{nK}] \times (3N)^{1/3} \sqrt{2.99 s - 6.13 g} \end{aligned} \quad (\text{A.31})$$

A.4 Heating

A detailed treatment of heating as a diffusion of momentum has been carried out by Gordon and Ashkin [150] and also more recently in [151–153]. These references stay within

the rotating wave approximation, so here we have adapted their formulas to include the counter-rotating term as well as a factor of $(\omega_L/\omega_0)^3$ that corrects the decay rate for the different density of states at ω_L . From [150] the rate of momentum diffusion in the low saturation regime is given by

$$D_p = \frac{\hbar^2 k^2}{2} \frac{3\pi c^2}{2\hbar\omega_0^3} \frac{\Gamma^2}{\Delta^2} I(\mathbf{r}) \left(1 + \frac{1}{k^2} \left| \frac{\nabla(\langle g|\mathbf{d}|e\rangle \cdot \mathbf{E}(\mathbf{r}))}{\langle g|\mathbf{d}|e\rangle \cdot \mathbf{E}(\mathbf{r})} \right|^2 \right) \quad (\text{A.32})$$

where $\mathbf{E}(\mathbf{r})e^{-i\omega t}$ is the complex classical field and $I(\mathbf{r})$ is the intensity. If the polarization of the field is $\boldsymbol{\varepsilon}$ such that $\mathbf{E}(\mathbf{r}) = \boldsymbol{\varepsilon} E(\mathbf{r})$, we have

$$\begin{aligned} D_p &= \frac{\hbar^2 k^2}{2} \frac{3\pi c^2}{2\hbar\omega_0^3} \frac{\Gamma^2}{\Delta^2} I(\mathbf{r}) \left(1 + \frac{1}{k^2} \left| \frac{\langle g|\mathbf{d} \cdot \boldsymbol{\varepsilon}|e\rangle \nabla E(\mathbf{r})}{\langle g|\mathbf{d} \cdot \boldsymbol{\varepsilon}|e\rangle E(\mathbf{r})} \right|^2 \right) \\ &= \frac{\hbar^2 k^2}{2} \frac{3\pi c^2}{2\hbar\omega_0^3} \frac{\Gamma^2}{\Delta^2} I(\mathbf{r}) \left(1 + \frac{1}{k^2} \left| \frac{\nabla E(\mathbf{r})}{E(\mathbf{r})} \right|^2 \right) \end{aligned} \quad (\text{A.33})$$

At this point we generalize the result of Gordon and Ashkin to far detuned light by doing the replacement

$$\frac{1}{\Delta^2} \rightarrow \left(\frac{\omega_L}{\omega_0} \right)^3 \left(\frac{1}{\omega_0 - \omega_L} + \frac{1}{\omega_0 + \omega_L} \right)^2 \quad (\text{A.34})$$

which results in

$$D_p = \frac{\hbar^2 k^2}{2} \frac{3\pi c^2}{2\hbar\omega_0^3} \Gamma^2 \left(\frac{\omega_L}{\omega_0} \right)^3 \left(\frac{1}{\omega_0 - \omega_L} + \frac{1}{\omega_0 + \omega_L} \right)^2 I(\mathbf{r}) \left(1 + \frac{1}{k^2} \left| \frac{\nabla E(\mathbf{r})}{E(\mathbf{r})} \right|^2 \right) \quad (\text{A.35})$$

The momentum diffusion term is defined as

$$D_p = \frac{1}{2} \left(\langle p^2 \rangle - \langle \mathbf{p} \rangle \cdot \langle \mathbf{p} \rangle \right) \quad (\text{A.36})$$

so for an atom that starts at rest the energy deposited per unit time is $\dot{E} = D_p/m$.

For a plane wave propagating along x , $E(\mathbf{r})$ as defined above is $E_0 e^{ikx}$, so this gives a heating rate

$$\begin{aligned} \dot{E} &= E_{R,L} \frac{3\pi c^2}{2\hbar\omega_0^3} \Gamma^2 \left(\frac{\omega_L}{\omega_0} \right)^3 \left(\frac{1}{\omega_0 - \omega_L} + \frac{1}{\omega_0 + \omega_L} \right)^2 2I_0 \\ &= 2E_{R,L} \Gamma_{sc,0} \\ &= 2E_{R,L} \frac{\hbar_L}{k_B |u_L|} U_0 \end{aligned} \quad (\text{A.37})$$

For a standing wave, such as that produced in a optical lattice $E(\mathbf{r}) = E_0 \cos(kx)$ and $I(\mathbf{r}) = I_{\max} \cos^2(kx)$ which results in a heating rate

$$\begin{aligned}\dot{E} &= E_{R,L} \frac{3\pi c^2}{2\hbar\omega_0^3} \Gamma^2 \left(\frac{\omega_L}{\omega_0} \right)^3 \left(\frac{1}{\omega_0 - \omega_L} + \frac{1}{\omega_0 + \omega_L} \right)^2 I_{\max} \cos^2(kx) \left(1 + \frac{\sin^2(kx)}{\cos^2(kx)} \right) \\ &= E_{R,L} \Gamma_{sc,\max}\end{aligned}\quad (\text{A.38})$$

We see that the heating rate is independent of x and so it is the same for a red or blue detuned lattice.

A.5 Heating due to optical lattice beams

As we saw in §A.2, our lattice potential suffers from losses on the retro path. The intensity for one of the axis with the light propagating along the x direction (neglecting the transverse profile $\exp[-2r_\perp^2/w^2]$) is given by

$$I_{1D}(x) = \frac{2P_i}{\pi w^2} \left(4\sqrt{R} \cos^2(kz) - 2\sqrt{R} + R + 1 \right) \quad (\text{A.39})$$

The corresponding electric field is

$$\begin{aligned}E_{1D}(x) &\propto \sqrt{\frac{2P_i}{\pi w^2}} e^{ikx} + \sqrt{\frac{2P_i R}{\pi w^2}} e^{-ikx} \\ &\propto \sqrt{\frac{2P_i}{\pi w^2}} 2\sqrt{R} \cos(kx) + \sqrt{\frac{2P_i}{\pi w^2}} (1 - \sqrt{R}) e^{ikx}\end{aligned}\quad (\text{A.40})$$

such that

$$\begin{aligned}\left| \frac{\nabla E(\mathbf{r})}{E(\mathbf{r})} \right|^2 &= \frac{\left| -2k\sqrt{R} \sin(kx) + ik(1 - \sqrt{R}) e^{ikx} \right|^2}{\left| 2\sqrt{R} \cos(kx) + (1 - \sqrt{R}) e^{ikx} \right|^2} \\ &= k^2 \frac{4R \sin^2(kx) + (1 - \sqrt{R})^2 + 2\sqrt{R} \sin(kx)(1 - \sqrt{R})(2 \sin(kx))}{4R \cos^2(kx) + (1 - \sqrt{R})^2 + 2\sqrt{R} \cos(kx)(1 - \sqrt{R})(2 \cos(kx))} \\ &= k^2 \frac{4\sqrt{R} \sin^2(kx) + (1 - \sqrt{R})^2}{4\sqrt{R} \cos^2(kx) + 2\sqrt{R} + R + 1}\end{aligned}\quad (\text{A.41})$$

The spatially dependent factor that appears in Gordon and Ashkin's formula is

$$\begin{aligned} I(\mathbf{r}) \left(1 + \frac{1}{k^2} \left| \frac{\nabla E(\mathbf{r})}{E(\mathbf{r})} \right|^2 \right) &= \frac{2P_i}{\pi w^2} \left(4\sqrt{R} \cos^2(kz) - 2\sqrt{R} + R + 1 + 4\sqrt{R} \sin^2(kx) + (1 - \sqrt{R})^2 \right) \\ &= \frac{2P_i}{\pi w^2} 2(1 + R) \end{aligned} \quad (\text{A.42})$$

The heating rate for the 1D lattice is then

$$\begin{aligned} \dot{E}_{1D} &= E_{R,L} \frac{3\pi c^2}{2\hbar\omega_0^3} \Gamma^2 \left(\frac{\omega_L}{\omega_0} \right)^3 \left(\frac{1}{\omega_L - \omega_0} + \frac{1}{\omega_0 + \omega_L} \right)^2 \frac{2P_i}{\pi w^2} 2(1 + R) \\ &= E_{R,L} h_L \frac{2P_i}{\pi w^2} 2(1 + R) \end{aligned} \quad (\text{A.43})$$

where h_L is defined in Eq. A.5, and its value for 1064 nm and 532 nm appears in Table A.1.

The lattice depth in our retroreflected setup is given by the \cos^2 modulation of I_{1D} . This can be read off of Eq. A.39:

$$I_{\text{lattice}} = \frac{8P_i}{\pi w^2} \sqrt{R} \quad (\text{A.44})$$

Using the factor u_λ defined above, this produces a lattice depth

$$V_{\text{lattice}} = k_B |u_\lambda| \frac{8P_i \sqrt{R}}{\pi w^2} \quad (\text{A.45})$$

The lattice depth in units of E_R is usually represented by $s = V_{\text{lattice}}/E_R$.

$$s = \frac{k_B |u_\lambda|}{E_{R,\lambda}} \frac{8P_i \sqrt{R}}{\pi w^2} \quad (\text{A.46})$$

This result can be incorporated into the heating rate obtained above

$$\dot{E}_{1D} = s E_{R,L} \frac{h_L E_{R,L}}{k_B |u_\lambda|} \frac{(1 + R)}{2\sqrt{R}}$$

(A.47)

Numerical values for $\frac{h_L E_{R,L}}{k_B |u_\lambda|}$ are given in Table A.1. We can also write down the expression for it:

$$\frac{h_L E_{R,L}}{k_B |u_\lambda|} = E_{R,L} \frac{\Gamma}{\hbar} \left(\frac{\omega_L}{\omega_0} \right)^3 \left| \frac{1}{\omega_0 - \omega_L} + \frac{1}{\omega_0 + \omega_L} \right| \approx \frac{E_{R,L}}{\hbar |\Delta|} \Gamma \quad (\text{A.48})$$

where on the far right we have neglected the counter-rotating term and the different density of states, as it is customarily done in the rotating wave approximation (RWA). Within RWA the heating rate is

$$\dot{E}_{1D} = V_{\text{latt}} \frac{E_{R,L}}{\hbar |\Delta|} \Gamma \frac{(1 + R)}{2\sqrt{R}} \quad (\text{A.49})$$

	1064 nm	532 nm	units
u_λ	-60.81	+61.99	$\mu\text{K} \frac{\mu\text{m}^2}{\text{mW}_2}$
h_λ	0.0876	0.728	$\text{s}^{-1} \frac{\mu\text{m}^2}{\text{mW}}$
$\frac{E_{R,\lambda}}{k_B}$	1.41	5.64	μK
$\frac{h_\lambda E_{R,\lambda}}{k_B u_\lambda }$	2.03e-3	6.62e-2	s^{-1}
$\frac{ u_\lambda k_B}{m \pi^2}$	8.55e3	8.72e3	$\frac{\mu\text{m}^4 \text{kHz}^2}{\text{mW}}$
$\frac{E_{R,L}}{m \pi^2}$	198.4	793.68	$\mu\text{m}^2 \text{kHz}^2$

Table A.1: Helpful constants to calculate dipole potentials, trapping frequencies and heating rates.

A.6 Heating due to green compensation beams

Our green compensation beams are simply gaussian beams for which the heating rate was derived in Eq. A.37. Since we use this beams to compensate a lattice formed by the 1064 nm IR beams we specify the repulsive compensation at the center in units of the IR recoil, $E_{R,\text{ir}}$:

$$g = \frac{U_{0,g}}{E_{R,\text{ir}}} \quad (\text{A.50})$$

The heating rate due to each of the compensation beams is then

$$\dot{E}_g = 2E_{R,\text{ir}} \frac{h_g E_{R,g}}{k_B |u_g|} g$$

(A.51)

A.7 Total heating rate in the compensated lattice

We can then add up the contributions of the IR and green to obtain

$$\begin{aligned} \frac{\dot{E}_{1D,\text{tot}}}{E_{R,\text{ir}}} &= \frac{h_{ir} E_{R,\text{ir}}}{k_B |u_{ir}|} \left(s \frac{1+R}{2\sqrt{R}} + 2g \frac{h_g E_{R,g}}{k_B |u_g|} \right) \Big/ \frac{h_{ir} E_{R,\text{ir}}}{k_B |u_{ir}|} \\ &= \frac{h_{ir} E_{R,\text{ir}}}{k_B |u_{ir}|} \left(s \frac{1+R}{2\sqrt{R}} + \kappa g \right) \end{aligned} \quad (\text{A.52})$$

where we have defined $\kappa = \frac{h_g E_{R,\text{g}}}{k_B |u_g|} / \frac{h_{\text{ir}} E_{R,\text{ir}}}{k_B |u_{\text{ir}}|}$ (For reference $\kappa = 65.22$). Including the contribution from the three orthogonal axes that form our lattice we obtain

$$\frac{\dot{E}_{\text{tot}}}{E_{R,\text{ir}}} = \frac{h_{\text{ir}} E_{R,\text{ir}}}{k_B |u_{\text{ir}}|} \sum_{i=1,2,3} \left(s_i \frac{1+R_i}{2\sqrt{R_i}} + \kappa g_i \right) \quad (\text{A.53})$$

If we assume that the energy increase due to heating is redistributed equally in all three dimensions we have for the rate of increase in temperature

$$\dot{T} = \frac{\dot{E}_{\text{tot}}}{3k_B} = \frac{E_{R,\text{ir}}}{3k_B} \frac{h_{\text{ir}} E_{R,\text{ir}}}{k_B |u_{\text{ir}}|} \sum_{i=1,2,3} \left(s_i \frac{1+R_i}{2\sqrt{R_i}} + \kappa g_i \right)$$

(A.54)

Since $\bar{R} = 0.8$ and we typically use the same depth for all ir beams and nearly the same depth for all green beams this can be approximated by

$$\begin{aligned} \dot{T} &\approx \frac{E_{R,\text{ir}}}{k_B} \frac{h_{\text{ir}} E_{R,\text{ir}}}{k_B |u_{\text{ir}}|} (s + \kappa g) \\ &\approx 2.9(s + 65g) \text{ nK/s} \end{aligned} \quad (\text{A.55})$$

where, once again, s is the lattice depth in IR recoils, and g is the compensation, also in IR recoils. It becomes obvious that our heating rate is completely dominated by the compensating beams. Typical values are $s = 7.0$ and $g = 2.9$.

Note that the large difference in the heating rate between green and IR can be mostly attributed to the density of states factor and the recoil energy. The density of states factor is $(\omega_L/\omega_0)^3 = (\lambda_0/\lambda)^3$, which is ~ 2 for green and ~ 0.25 for IR, giving a factor of 8. The recoil scales as λ^{-2} which gives another factor of 4. This accounts for a factor of 32, the remaining factor of 2 is due to the different heating rates for a traveling wave and a standing wave.

A.8 Total heating rate in the compensated lattice

In dimple configuration ($\alpha = 1$), and using Eq. A.46 to relate s and the input power P_i , the 1D heating rate is

$$\dot{E} = E_{R,\text{ir}} = \frac{h_{\text{ir}} E_{R,\text{ir}}}{k_B u_{\text{ir}}} \frac{s}{\sqrt{R}} \quad (\text{A.56})$$

Note that

$$\frac{1}{\sqrt{R}} \approx \frac{1+R}{2\sqrt{R}}$$

for the values of R that we deal with. This means that Eq. A.55 is still valid for the heating rate in dimple configuration.

BIBLIOGRAPHY

- [1] X. Wen, *Quantum Field Theory of Many-Body Systems: From the Origin of Sound to an Origin of Light and Electrons, Oxford Graduate Texts* (OUP Oxford, 2004). 1
- [2] A. Altland and B. Simons, *Condensed Matter Field Theory* (Cambridge University Press, 2010). 2
- [3] N. Ashcroft and N. Mermin, *Solid state physics* (Saunders College, 1976). 2, 35
- [4] L. Landau, *Collected papers of L. D. Landau* (Gordon and Breach, 1965). 2
- [5] K. Andres, J. E. Graebner, and H. R. Ott, “4f-Virtual-Bound-State Formation in CeAl₃ at Low Temperatures,” Phys. Rev. Lett. **35**, 1779–1782 (1975). 2
- [6] F. Steglich, J. Aarts, C. D. Bredl, W. Lieke, D. Meschede, W. Franz, and H. Schäfer, “Superconductivity in the Presence of Strong Pauli Paramagnetism: CeCu₂Si₂,” Phys. Rev. Lett. **43**, 1892–1896 (1979). 2
- [7] D. C. Tsui, H. L. Stormer, and A. C. Gossard, “Two-Dimensional Magnetotransport in the Extreme Quantum Limit,” Phys. Rev. Lett. **48**, 1559–1562 (1982). 2
- [8] R. B. Laughlin, “Anomalous Quantum Hall Effect: An Incompressible Quantum Fluid with Fractionally Charged Excitations,” Phys. Rev. Lett. **50**, 1395–1398 (1983). 2, 3
- [9] J. Bednorz and K. Müller, “Possible high- T_c superconductivity in the Ba-La-Cu-O system,” Zeitschrift für Physik B Condensed Matter **64**, 189–193 (1986). 2
- [10] P. Coleman, “Many Body Physics: Unfinished Revolution,” in *International Conference on Theoretical Physics*, D. Iagolnitzer, V. Rivasseau, and J. Zinn-Justin, eds., (Birkhäuser Basel, 2004), pp. 559–580. 2

- [11] P. W. Anderson, “More Is Different,” *Science* **177**, 393–396 (1972). 2
- [12] X. Wen, “Topological orders in rigid states,” *International Journal of Modern Physics B* **04**, 239–271 (1990). 3
- [13] J. A. Hertz, “Quantum critical phenomena,” *Phys. Rev. B* **14**, 1165–1184 (1976). 3
- [14] S. Sachdev, *Quantum Phase Transitions, Quantum Phase Transitions* (Cambridge University Press, 2011). 3
- [15] “The Hubbard model at half a century,” *Nature Physics* **9**, 523–523 (2013). 4
- [16] J. Hubbard, “Electron Correlations in Narrow Energy Bands. III. An Improved Solution,” *Proceedings of the Royal Society of London. Series A, Mathematical and Physical Sciences* **281**, pp. 401–419 (1964). 4, 37
- [17] J. Quintanilla and C. Hooley, “The strong-correlations puzzle,” *Physics World* **22**, 32–37 (2009). 5
- [18] D. Jaksch, C. Bruder, J. I. Cirac, C. W. Gardiner, and P. Zoller, “Cold Bosonic Atoms in Optical Lattices,” *Phys. Rev. Lett.* **81**, 3108–3111 (1998). 5
- [19] R. P. Feynman, “Simulating physics with computers,” *International journal of theoretical physics* **21**, 467–488 (1982). 5
- [20] M. Greiner, O. Mandel, T. Esslinger, T. Hänsch, and I. Bloch, “Quantum phase transition from a superfluid to a Mott insulator in a gas of ultracold atoms,” *Nature* **415**, 39–44 (2002). 5
- [21] N. Gemelke, X. Zhang, C.-L. Hung, and C. Chin, “In situ observation of incompressible Mott-insulating domains in ultracold atomic gases.,” *Nature* **460**, 995–8 (2009). 5, 182
- [22] K. Jiménez-García, R. L. Compton, Y.-J. Lin, W. D. Phillips, J. V. Porto, and I. B. Spielman, “Phases of a Two-Dimensional Bose Gas in an Optical Lattice,” *Physical Review Letters* **105**, 110401 (2010).

- [23] S. Trotzky, L. Pollet, F. Gerbier, U. Schnorrberger, I. Bloch, N. V. Prokof'ev, B. Svistunov, and M. Troyer, "Suppression of the critical temperature for superfluidity near the Mott transition," *Nature Physics* **6**, 998–1004 (2010).
- [24] M. J. Mark, E. Haller, K. Lauber, J. G. Danzl, a. J. Daley, and H.-C. Nägerl, "Precision Measurements on a Tunable Mott Insulator of Ultracold Atoms," *Physical Review Letters* **107**, 175301 (2011).
- [25] X. Zhang, C.-L. Hung, S.-K. Tung, and C. Chin, "Observation of quantum criticality with ultracold atoms in optical lattices," *Science (New York, N.Y.)* **335**, 1070–2 (2012). 5
- [26] J. K. Freericks and H. Monien, "Phase diagram of the Bose-Hubbard Model," *EPL (Europhysics Letters)* **26**, 545 (1994). 5
- [27] W. Krauth and N. Trivedi, "Mott and Superfluid Transitions in a Strongly Interacting Lattice Boson System," *EPL (Europhysics Letters)* **14**, 627 (1991).
- [28] M. P. A. Fisher, P. B. Weichman, G. Grinstein, and D. S. Fisher, "Boson localization and the superfluid-insulator transition," *Phys. Rev. B* **40**, 546–570 (1989). 5
- [29] T. Fukuhara, P. Schauß, M. Endres, S. Hild, M. Cheneau, I. Bloch, and C. Gross, "Microscopic observation of magnon bound states and their dynamics," *Nature* **502**, 76–9 (2013). 5
- [30] D. Scalapino, "The case for $d_{x^2-y^2}$ pairing in the cuprate superconductors," *Physics Reports* **250**, 329 – 365 (1995). 5
- [31] W. Hofstetter, J. I. Cirac, P. Zoller, E. Demler, and M. D. Lukin, "High-Temperature Superfluidity of Fermionic Atoms in Optical Lattices," *Phys. Rev. Lett.* **89**, 220407 (2002). 5
- [32] Y.-R. Lee, M.-S. Heo, J.-H. Choi, T. T. Wang, C. A. Christensen, T. M. Rvachov, and W. Ketterle, "Compressibility of an ultracold Fermi gas with repulsive interactions," *Phys. Rev. A* **85**, 063615 (2012). 6

- [33] M. Köhl, H. Moritz, T. Stöferle, K. Günter, and T. Esslinger, “Fermionic Atoms in a Three Dimensional Optical Lattice: Observing Fermi Surfaces, Dynamics, and Interactions,” *Physical Review Letters* **94**, 080403 (2005). 6
- [34] R. Jördens, N. Strohmaier, K. Günter, H. Moritz, and T. Esslinger, “A Mott insulator of fermionic atoms in an optical lattice.,” *Nature* **455**, 204–7 (2008). 6, 8, 137, 181
- [35] U. Schneider, L. Hackermüller, S. Will, T. Best, I. Bloch, T. A. Costi, R. W. Helmes, D. Rasch, and A. Rosch, “Metallic and insulating phases of repulsively interacting fermions in a 3D optical lattice.,” *Science (New York, N.Y.)* **322**, 1520–5 (2008). 6, 8, 137, 181
- [36] A. Damascelli, Z. Hussain, and Z. Shen, “Angle-resolved photoemission studies of the cuprate superconductors,” *Reviews of Modern Physics* **75** (2003). 6
- [37] R.-H. He *et al.*, “From a single-band metal to a high-temperature superconductor via two thermal phase transitions.,” *Science (New York, N.Y.)* **331**, 1579–83 (2011). 6
- [38] K. Jin, N. P. Butch, K. Kirshenbaum, J. Paglione, and R. L. Greene, “Link between spin fluctuations and electron pairing in copper oxide superconductors.,” *Nature* **476**, 73–5 (2011). 6
- [39] P. M. Grant, “High-temperature superconductivity: The great quantum conundrum.,” *Nature* **476**, 37–9 (2011). 6, 7
- [40] E. Koch, in *Correlated Electrons: From Models to Materials*, E. Pavarini, E. Koch, F. Anders, and M. Jarrell, eds., (Forschungszentrum Jülich GmbH, Julich, Germany, 2012), Chap. 7. Exchange mechanisms. 7
- [41] J. Milton, “Superconductors come of age,” *Nature News*. doi:10.1038/news.2010.527, 2010. 7
- [42] M. K. Wu, J. R. Ashburn, C. J. Torng, P. H. Hor, R. L. Meng, L. Gao, Z. J. Huang, Y. Q. Wang, and C. W. Chu, “Superconductivity at 93 K in a new mixed-phase

- Y-Ba-Cu-O compound system at ambient pressure,” Phys. Rev. Lett. **58**, 908–910 (1987). 7
- [43] J. M. Tranquada *et al.*, “Antiferromagnetism in $\text{YBa}_2\text{Cu}_3\text{O}_{6+x}$,” Phys. Rev. B **38**, 2477–2485 (1988). 8
- [44] L. Liáng, *YBCO Superconductor Research Progress* (Nova Science Publishers, 2008). 8
- [45] D. Greif, T. Uehlinger, G. Jotzu, L. Tarruell, and T. Esslinger, “Short-Range Quantum Magnetism of Ultracold Fermions in an Optical Lattice,” Science 1307 (2013). 8, 202
- [46] S. Trotzky, P. Cheinet, S. Fölling, M. Feld, U. Schnorrberger, a. M. Rey, a. Polkovnikov, E. a. Demler, M. D. Lukin, and I. Bloch, “Time-resolved observation and control of superexchange interactions with ultracold atoms in optical lattices.,” Science (New York, N.Y.) **319**, 295–9 (2008). 8
- [47] S. Nascimbène, Y.-A. Chen, M. Atala, M. Aidelsburger, S. Trotzky, B. Paredes, and I. Bloch, “Experimental Realization of Plaquette Resonating Valence-Bond States with Ultracold Atoms in Optcal Superlattices,” Phys. Rev. Lett. **108**, 205301 (2012). 8
- [48] K. Kim, M.-S. Chang, S. Korenblit, R. Islam, E. Edwards, J. Freericks, G.-D. Lin, L.-M. Duan, and C. Monroe, “Quantum simulation of frustrated Ising spins with trapped ions,” Nature **465**, 590–593 (2010). 8
- [49] J. W. Britton, B. C. Sawyer, A. C. Keith, C.-C. J. Wang, J. K. Freericks, H. Uys, M. J. Biercuk, and J. J. Bollinger, “Engineered two-dimensional Ising interactions in a trapped-ion quantum simulator with hundreds of spins,” Nature **484**, 489–492 (2012). 8, 9
- [50] J. Simon, W. S. Bakr, R. Ma, M. E. Tai, P. M. Preiss, and M. Greiner, “Quantum simulation of antiferromagnetic spin chains in an optical lattice,” Nature **472**, 307–312 (2011). 8

- [51] J. Struck, C. Ölschläger, R. Le Targat, P. Soltan-Panahi, A. Eckardt, M. Lewenstein, P. Windpassinger, and K. Sengstock, “Quantum Simulation of Frustrated Classical Magnetism in Triangular Optical Lattices,” *Science* **333**, 996–999 (2011). 8
- [52] F. Meinert, M. J. Mark, E. Kirilov, K. Lauber, P. Weinmann, A. J. Daley, and H.-C. Nägerl, “Quantum Quench in an Atomic One-Dimensional Ising Chain,” *Phys. Rev. Lett.* **111**, 053003 (2013). 8
- [53] P. Richerme, Z.-X. Gong, A. Lee, C. Senko, J. Smith, M. Foss-Feig, S. Michalakis, A. V. Gorshkov, and C. Monroe, “Non-local propagation of correlations in quantum systems with long-range interactions,” *Nature* **511**, 198–201 (2014). 8
- [54] T. Paiva, Y. L. Loh, M. Randeria, R. T. Scalettar, and N. Trivedi, “Fermions in 3D Optical Lattices: Cooling Protocol to Obtain Antiferromagnetism,” *Physical Review Letters* **107**, 086401 (2011). 9, 100, 101, 198
- [55] S. Fuchs, E. Gull, L. Pollet, E. Burovski, E. Kozik, T. Pruschke, and M. Troyer, “Thermodynamics of the 3D Hubbard Model on Approaching the Néel Transition,” *Physical Review Letters* **106**, 030401 (2011). 9, 52, 100, 192
- [56] D. C. McKay and B. DeMarco, “Cooling in strongly correlated optical lattices: prospects and challenges,” *Reports on Progress in Physics* **74**, 054401 (2011). 9
- [57] J. Imriška, M. Iazzi, L. Wang, E. Gull, D. Greif, T. Uehlinger, G. Jotzu, L. Tarruell, T. Esslinger, and M. Troyer, “Thermodynamics and Magnetic Properties of the Anisotropic 3D Hubbard Model,” *Phys. Rev. Lett.* **112**, 115301 (2014). 9
- [58] T. A. Corcovilos, S. K. Baur, J. M. Hitchcock, E. J. Mueller, and R. G. Hulet, “Detecting antiferromagnetism of atoms in an optical lattice via optical Bragg scattering,” *Phys. Rev. A* **81**, 013415 (2010). 9, 78, 190, 191
- [59] M. Rigol, T. Bryant, and R. R. P. Singh, “Numerical Linked-Cluster Approach to Quantum Lattice Models,” *Phys. Rev. Lett.* **97**, 187202 (2006). 9, 183

- [60] P. M. Duarte, “Band structure calculations for an optical lattice,” <http://dx.doi.org/10.5281/zenodo.11612>, 2014. 11
- [61] O. Morsch and M. Oberthaler, “Dynamics of Bose-Einstein condensates in optical lattices,” Rev. Mod. Phys. **78**, 179–215 (2006). 11
- [62] J. C. Slater, “A Soluble Problem in Energy Bands,” Phys. Rev. **87**, 807–835 (1952). 14
- [63] C. Salomon, G. Shlyapnikov, and L. Cugliandolo, *Many-Body Physics with Ultracold Gases: Lecture Notes of the Les Houches Summer School: Volume 94, July 2010, Lecture Notes of the Les Houches Summer School* (OUP Oxford, 2013). 15
- [64] W. Kohn, “Analytic Properties of Bloch Waves and Wannier Functions,” Physical Review **115**, 809–821 (1959). 15
- [65] F. Schwabl, *Advanced Quantum Mechanics, Advanced texts in physics* (Springer, 2005). 23
- [66] I. Bloch, J. Dalibard, and W. Zwerger, “Many-body physics with ultracold gases,” Rev. Mod. Phys. **80**, 885–964 (2008). 27, 29, 30, 88
- [67] J. Sakurai and J. Napolitano, *Modern Quantum Mechanics* (Pearson Education, 2014), Chap. 6. Scattering theory. 29
- [68] T. Busch, B. Englert, K. Rzazewski, and M. Wilkens, “Two cold atoms in a harmonic trap,” Foundations of Physics pp. 549–559 (1998). 29
- [69] F. Werner, O. Parcollet, A. Georges, and S. R. Hassan, “Interaction-Induced Adiabatic Cooling and Antiferromagnetism of Cold Fermions in Optical Lattices,” Phys. Rev. Lett. **95**, 056401 (2005). 30, 31, 32, 196
- [70] R. Jördens, Ph.D. thesis, ETH Zürich, 2010. 47, 137
- [71] M. Mark, Ph.D. thesis, Innsbruck, 2012. 30

- [72] K. E. Strecker, G. B. Partridge, and R. G. Hulet, “Conversion of an Atomic Fermi Gas to a Long-Lived Molecular Bose Gas,” *Phys. Rev. Lett.* **91**, 080406 (2003). 32, 138
- [73] G. Zürn, T. Lompe, a. N. Wenz, S. Jochim, P. S. Julienne, and J. M. Hutson, “Precise Characterization of ^6Li Feshbach Resonances Using Trap-Sideband-Resolved RF Spectroscopy of Weakly Bound Molecules,” *Physical Review Letters* **110**, 135301 (2013). 32, 139
- [74] W. Heisenberg, “Zur Theorie des Ferromagnetismus,” *Zeitschrift fü Physik* **49**, 619–636 (1928). 33
- [75] J. Hubbard, “Electron Correlations in Narrow Energy Bands,” *Proceedings of the Royal Society of London. Series A. Mathematical and Physical Sciences* **276**, 238–257 (1963). 34, 35
- [76] M. C. Gutzwiller, “Effect of Correlation on the Ferromagnetism of Transition Metals,” *Phys. Rev. Lett.* **10**, 159–162 (1963). 35
- [77] J. Kanamori, “Electron Correlation and Ferromagnetism of Transition Metals,” *Progress of Theoretical Physics* **30**, 275–289 (1963). 35
- [78] R. Scalettar, “QUEST: QUantum Electron Simulation Toolbox,” <http://quest.ucdavis.edu/tutorial/hubbard7.pdf>, 2013. 35
- [79] N. F. Mott, “The Basis of the Electron Theory of Metals, with Special Reference to the Transition Metals,” *Proceedings of the Physical Society. Section A* **62**, 416 (1949). 38
- [80] N. F. Mott, “Metal-Insulator Transition,” *Rev. Mod. Phys.* **40**, 677–683 (1968). 38
- [81] P. M. Duarte, “A few simple treatments of the Hubbard model,” <http://dx.doi.org/10.5281/zenodo.11558>, 2014. 39

- [82] F. Göhmann and S. Murakami, “Algebraic and analytic properties of the one-dimensional Hubbard model,” Journal of Physics A: Mathematical and General **30**, 5269 (1997). 42
- [83] R. Schumman, “Thermodynamics of a 4-site Hubbard model by analytical diagonalization,” . 43, 44
- [84] A. Leggett, *Quantum Liquids: Bose condensation and Cooper pairing in condensed-matter systems*, Oxford Graduate Texts (OUP Oxford, 2006). 43
- [85] C. C. Tsuei, J. R. Kirtley, Z. F. Ren, J. H. Wang, R. H., and Z. Z. Li, “Pure $d_{x^2-y^2}$ order-parameter symmetry in the tetragonal superconductor $Tl_2Ba_2CuO_{6+\delta}$,” Nature **387**, 481–483 (1997). 43
- [86] C. C. Tsuei and J. R. Kirtley, “Pairing symmetry in cuprate superconductors,” Rev. Mod. Phys. **72**, 969–1016 (2000). 43
- [87] D. J. Scalapino and S. A. Trugman, “Local antiferromagnetic correlations and dx^2-y^2 pairing,” Philosophical Magazine Part B **74**, 607–610 (1996). 44
- [88] G. Mahan, *Many-Particle Physics, Physics of Solids and Liquids* (Springer, 2000). 47
- [89] J. Henderson, J. Oitmaa, and M. Ashley, “High-temperature expansion for the single-band Hubbard model,” Physical Review B **46**, 6328–6337 (1992). 47, 183
- [90] M. Rigol, A. Muramatsu, G. G. Batrouni, and R. T. Scalettar, “Local Quantum Criticality in Confined Fermions on Optical Lattices,” Phys. Rev. Lett. **91**, 130403 (2003). 51
- [91] R. W. Helmes, T. A. Costi, and A. Rosch, “Mott Transition of Fermionic Atoms in a Three-Dimensional Optical Trap,” Phys. Rev. Lett. **100**, 056403 (2008). 52
- [92] S. Chiesa, C. N. Varney, M. Rigol, and R. T. Scalettar, “Magnetism and Pairing of Two-Dimensional Trapped Fermions,” Phys. Rev. Lett. **106**, 035301 (2011). 51

- [93] R. Scalettar, “Computational Quantum Magnetism. Lecture III: Determinant Quantum Monte Carlo,” http://boulder.research.yale.edu/Boulder-2003/reading/scalettar_3.pdf, 2003. 52
- [94] R. Blankenbecler, D. J. Scalapino, and R. L. Sugar, “Monte Carlo calculations of coupled boson-fermion systems. I,” Phys. Rev. D **24**, 2278–2286 (1981). 52, 183
- [95] M. Rigol, T. Bryant, and R. R. P. Singh, “Numerical Linked-Cluster Approach to Quantum Lattice Models,” Phys. Rev. Lett. **97**, 187202 (2006). 53
- [96] B. Tang, E. Khatami, and M. Rigol, “A short introduction to numerical linked-cluster expansions,” Computer Physics Communications **184**, 557 – 564 (2013). 53, 183
- [97] S. Chu, “Nobel Lecture: The manipulation of neutral particles,” Rev. Mod. Phys. **70**, 685–706 (1998). 55
- [98] C. N. Cohen-Tannoudji, “Nobel Lecture: Manipulating atoms with photons,” Rev. Mod. Phys. **70**, 707–719 (1998).
- [99] W. D. Phillips, “Nobel Lecture: Laser cooling and trapping of neutral atoms,” Rev. Mod. Phys. **70**, 721–741 (1998). 55
- [100] C. Chin, R. Grimm, P. Julienne, and E. Tiesinga, “Feshbach resonances in ultracold gases,” Rev. Mod. Phys. **82**, 1225–1286 (2010). 55, 137
- [101] M. Houbiers, H. T. C. Stoof, W. I. McAlexander, and R. G. Hulet, “Elastic and inelastic collisions of ^6Li atoms in magnetic and optical traps,” Phys. Rev. A **57**, R1497–R1500 (1998). 56, 132
- [102] P. M. Duarte, Master’s thesis, Rice University, 2011. 59, 65
- [103] G. Ritt, G. Cennini, C. Geckeler, and M. Weitz, “Laser frequency offset locking using a side of filter technique,” Applied Physics B: Lasers and Optics **79**, 363–365 (2004), 10.1007/s00340-004-1559-6. 59

- [104] G. Ferrari, M.-O. Mewes, F. Schreck, and C. Salomon, “High-power multiple-frequency narrow-linewidth laser source based on a semiconductor tapered amplifier,” *Opt. Lett.* **24**, 151–153 (1999). 59
- [105] R. E. Scholten, “Enhanced laser shutter using a hard disk drive rotary voice-coil actuator,” *Rev. Sci. Instrum.* **78**, 026101 (2007). 61
- [106] P. M. Duarte, R. A. Hart, J. M. Hitchcock, T. A. Corcovilos, T.-L. Yang, A. Reed, and R. G. Hulet, “All-optical production of a lithium quantum gas using narrow-line laser cooling,” *Phys. Rev. A* **84**, 061406 (2011). 63, 67
- [107] M. S. Safronova, B. Arora, and C. W. Clark, “Frequency-dependent polarizabilities of alkali-metal atoms from ultraviolet through infrared spectral regions,” *Phys. Rev. A* **73**, 022505 (2006). 73, 74
- [108] J. Mitroy, M. S. Safronova, and C. W. Clark, “Theory and applications of atomic and ionic polarizabilities,” *Journal of Physics B: Atomic, Molecular and Optical Physics* **43**, 202001 (2010). 73, 74
- [109] T.-L. Yang, Master’s thesis, Rice University, 2014. 78, 169
- [110] J. Liang *et al.*, “1.5% root-mean-square flat-intensity laser beam formed using a binary-amplitude spatial light modulator,” *Applied optics* **48**, 1955–1962 (2009). 83
- [111] A. L. Gaunt, T. F. Schmidutz, I. Gotlibovych, R. P. Smith, and Z. Hadzibabic, “Bose-Einstein Condensation of Atoms in a Uniform Potential,” *Phys. Rev. Lett.* **110**, 200406 (2013). 83
- [112] C. J. M. Mathy, D. a. Huse, and R. G. Hulet, “Enlarging and cooling the Néel state in an optical lattice,” *Physical Review A* **86**, 023606 (2012). 89
- [113] K. M. O’Hara, M. E. Gehm, S. R. Granade, and J. E. Thomas, “Scaling laws for evaporative cooling in time-dependent optical traps,” *Phys. Rev. A* **64**, 051403 (2001). 98, 99, 167

- [114] M. Köhl, “Thermometry of fermionic atoms in an optical lattice,” *Physical Review A* **73**, 031601 (2006). 98, 198
- [115] E. Kozik, E. Burovski, V. W. Scarola, and M. Troyer, “Néel temperature and thermodynamics of the half-filled three-dimensional Hubbard model by diagrammatic determinant Monte Carlo,” *Phys. Rev. B* **87**, 205102 (2013). 100
- [116] P. M. Duarte, “LDA solutions for the Hubbard model in a compensated optical lattice,” <http://dx.doi.org/10.5281/zenodo.11761>, 2014. 110
- [117] W. Ketterle, D. S. Durfee, and S. D. M. Kurn, “Making, probing and understanding Bose-Einstein condensates,” in *Bose-Einstein Condensation in Atomic Gases (Proceedings of the International School of Physics “Enrico Fermi,” Course CXL)*, M. Inguscio, S. Stringari, and C. E. Wieman, eds., (IOS Press, 1999). 111
- [118] W. Ketterle and M. W. Zwierlein, “Making, probing and understanding ultracold Fermi Gases,” *Rivista del Nuovo Cimento* **31**, 247–422 (2008). 111, 129, 136
- [119] C. C. Bradley, C. A. Sackett, and R. G. Hulet, “Bose-Einstein Condensation of Lithium: Observation of Limited Condensate Number,” *Phys. Rev. Lett.* **78**, 985–989 (1997). 112
- [120] D. Dries, Ph.D. thesis, Rice University, 2010. 112
- [121] M. Auzinsh, D. Budker, and S. Rochester, *Optically Polarized Atoms: Understanding Light-atom Interactions* (OUP Oxford, 2010). 114, 116, 117
- [122] A. Edmonds, *Angular Momentum in Quantum Mechanics, Investigations in Physics Series* (Princeton University Press, 1996). 120
- [123] D. Budker, D. Kimball, and D. DeMille, *Atomic Physics: An Exploration Through Problems and Solutions* (Oxford University Press, 2004). 121

- [124] G. Reinaudi, T. Lahaye, Z. Wang, and D. Guéry-Odelin, “Strong saturation absorption imaging of dense clouds of ultracold atoms,” Optics letters **32**, 3143–3145 (2007). 127
- [125] P. M. Duarte and E. Yang, “Analyze density profiles of ultracold Fermionic gases,” , <http://dx.doi.org/10.5281/zenodo.11760>, 2014. 130
- [126] D. A. Butts and D. S. Rokhsar, “Trapped Fermi gases,” Phys. Rev. A **55**, 4346–4350 (1997). 130
- [127] V. W. Scarola, L. Pollet, J. Oitmaa, and M. Troyer, “Discerning Incompressible and Compressible Phases of Cold Atoms in Optical Lattices,” Phys. Rev. Lett. **102**, 135302 (2009). 137
- [128] R. Jördens *et al.*, “Quantitative Determination of Temperature in the Approach to Magnetic Order of Ultracold Fermions in an Optical Lattice,” Physical Review Letters **104**, 180401 (2010). 137
- [129] T. Rom, T. Best, O. Mandel, A. Widera, M. Greiner, T. W. Hänsch, and I. Bloch, “State Selective Production of Molecules in Optical Lattices,” Phys. Rev. Lett. **93**, 073002 (2004). 137
- [130] G. Thalhammer, K. Winkler, F. Lang, S. Schmid, R. Grimm, and J. H. Denschlag, “Long-Lived Feshbach Molecules in a Three-Dimensional Optical Lattice,” Phys. Rev. Lett. **96**, 050402 (2006). 137
- [131] S. Taie, R. Yamazaki, S. Sugawa, and Y. Takahashi, “An SU (6) Mott insulator of an atomic Fermi gas realized by large-spin Pomeranchuk cooling,” Nature Physics **8**, 825–830 (2012). 137
- [132] U. Schneider, Ph.D. thesis, Johannes Gutenberg Univerität in Mainz, 2010. 137
- [133] T. Stöferle, H. Moritz, K. Günter, M. Köhl, and T. Esslinger, “Molecules of Fermionic Atoms in an Optical Lattice,” Phys. Rev. Lett. **96**, 030401 (2006). 138

- [134] E. L. Hazlett, Y. Zhang, R. W. Stites, and K. M. O'Hara, "Realization of a Resonant Fermi Gas with a Large Effective Range," *Phys. Rev. Lett.* **108**, 045304 (2012). 138, 139
- [135] G. Thalhammer, K. Winkler, F. Lang, S. Schmid, R. Grimm, and J. H. Denschlag, "Long-Lived Feshbach Molecules in a Three-Dimensional Optical Lattice," *Physical Review Letters* **96**, 050402 (2006). 139
- [136] H. Miyake, G. A. Siviloglou, G. Puentes, D. E. Pritchard, W. Ketterle, and D. M. Weld, "Bragg Scattering as a Probe of Atomic Wave Functions and Quantum Phase Transitions in Optical Lattices," *Phys. Rev. Lett.* **107**, 175302 (2011). 147, 148
- [137] G. Birkl, M. Gatzke, I. H. Deutsch, S. L. Rolston, and W. D. Phillips, "Bragg Scattering from Atoms in Optical Lattices," *Phys. Rev. Lett.* **75**, 2823–2826 (1995). 148
- [138] M. Weidemüller, A. Hemmerich, A. Görlitz, T. Esslinger, and T. W. Hänsch, "Bragg Diffraction in an Atomic Lattice Bound by Light," *Phys. Rev. Lett.* **75**, 4583–4586 (1995). 148
- [139] F. Cordobes Aguilar, A. F. Ho, and J. Ruostekoski, "Optical Signatures of Antiferromagnetic Ordering of Fermionic Atoms in an Optical Lattice," *Phys. Rev. X* **4**, 031036 (2014). 148
- [140] C. Cohen-Tannoudji, J. Dupont-Roc, and G. Grynberg, *Atom-Photon Interactions: Basic Processes and Applications, A Wiley-Interscience publication* (Wiley, 1998). 149, 152
- [141] J. Ruostekoski, C. J. Foot, and A. B. Deb, "Light Scattering for Thermometry of Fermionic Atoms in an Optical Lattice," *Phys. Rev. Lett.* **103**, 170404 (2009). 149
- [142] L. Luo, B. Clancy, J. Joseph, J. Kinast, A. Turlapov, and J. E. Thomas, "Evaporative cooling of unitary Fermi gas mixtures in optical traps," *New Journal of Physics* **8**, 213 (2006). 167

- [143] T. Paiva, R. Scalettar, M. Randeria, and N. Trivedi, “Fermions in 2D Optical Lattices: Temperature and Entropy Scales for Observing Antiferromagnetism and Superfluidity,” *Phys. Rev. Lett.* **104**, 066406 (2010). 183
- [144] C. J. M. Mathy and D. A. Huse, “Accessing the Néel phase of ultracold fermionic atoms in a simple-cubic optical lattice,” *Phys. Rev. A* **79**, 063412 (2009). 196
- [145] R. Staudt, M. Dzierzawa, and A. Muramatsu, “Phase diagram of the three-dimensional Hubbard model at half filling,” *The European Physical Journal B* **17**, 411–415 (2000). 198
- [146] E. Kozik, E. Burovski, V. W. Scarola, and M. Troyer, “Néel temperature and thermodynamics of the half-filled three-dimensional Hubbard model by diagrammatic determinant Monte Carlo,” *Phys. Rev. B* **87**, 205102 (2013). 198
- [147] T. Gottwald and P. G. J. van Dongen, “Antiferromagnetic order of repulsively interacting fermions on optical lattices,” *Phys. Rev. A* **80**, 033603 (2009). 198
- [148] B. Wunsch, L. Fritz, N. T. Zinner, E. Manousakis, and E. Demler, “Magnetic structure of an imbalanced Fermi gas in an optical lattice,” *Phys. Rev. A* **81**, 013616 (2010). 198
- [149] R. Grimm, M. Weidemüller, and Y. B. Ovchinnikov, “Optical Dipole Traps for Neutral Atoms,” in *Optical Dipole Traps for Neutral Atoms*, Vol. 42 of *Advances In Atomic, Molecular, and Optical Physics*, B. Bederson and H. Walther, eds., (Academic Press, 2000), pp. 95 – 170. 205
- [150] J. P. Gordon and A. Ashkin, “Motion of atoms in a radiation trap,” *Physical Review A* **21**, 1606–1617 (1980). 212, 213
- [151] F. Gerbier and Y. Castin, “Heating rates for an atom in a far-detuned optical lattice,” *Physical Review A* **82**, 013615 (2010). 212

- [152] H. Pichler, a. J. Daley, and P. Zoller, “Nonequilibrium dynamics of bosonic atoms in optical lattices: Decoherence of many-body states due to spontaneous emission,” Physical Review A **82**, 063605 (2010).
- [153] J.-F. Riou, A. Reinhard, L. a. Zundel, and D. S. Weiss, “Spontaneous-emission-induced transition rates between atomic states in optical lattices,” Physical Review A **86**, 033412 (2012). 212